EXPLOTACIÓN SINÉRGICA DE DATOS MULTIESPECTRALES Y RADAR PARA LA ESTIMACIÓN DE VARIABLES BIOFÍSICAS DE LA VEGETACIÓN MEDIANTE TECNOLOGÍAS DE SENSORAMIENTO REMOTO

Gabriel Rodrigo Caballero

Directores
Dr. Jesús Delegido Gómez
Dr. Jochem Verrelst

Doctorado en Teledetección
Abril de 2023

Universitat de València

Facultat de Física
Departament de Física de la Terra i Termodinàmica

Doctorado en Teledetección

Explotación sinérgica de datos multiespectrales y radar para la estimación de variables biofísicas de la vegetación mediante tecnologías de sensoramiento remoto

Tesis Doctoral

Gabriel Rodrigo Caballero

Directores
Dr. Jesús Delegido Gómez
Dr. Jochem Verrelst

JESÚS DELEGIDO GÓMEZ, Profesor Catedrático en el departamento de Física de la Tierra y Termodinámica de la Facultad de Física, Universidad de Valencia.

JOCHEM VERRELST, investigador postdoctoral sénior en el Laboratorio de Procesado de Imágenes de la Universidad de Valencia.

CERTIFICAN:

Que la tesis doctoral **"Explotación sinérgica de datos multiespectrales y radar para la estimación de variables biofísicas de la vegetación mediante tecnologías de sensoramiento remoto"**, presentada por Gabriel Rodrigo Caballero ha sido realizada bajo su dirección y es favorable para optar por el grado de Doctor por la Universidad de Valencia en el programa de doctorado en Teledetección.

Y para que así conste, firman el presente certificado en Burjassot, a 29 de marzo de 2023.

Fdo.: Jesús Delegido Gómez

Fdo.: Jochem Verrelst

Nota introductoria

Esta tesis doctoral se presenta para obtener el título de Doctorado en Teledetección de la Universidad de Valencia.

Según el reglamento vigente sobre depósito, evaluación y defensa de la tesis doctoral de la Universidad de Valencia, la tesis doctoral puede ser presentada de dos formas: 1) tesis tradicional o 2) tesis por compendio de publicaciones. En este caso, la tesis presentada está elaborada por compendio de publicaciones. La tesis de acuerdo con esta opción, tiene que cumplir los siguientes requisitos:

1. Se deben presentar un mínimo de tres artículos, ya publicados o aceptados en revistas indexadas en algún índice internacional como JCR (WoS) y/o SJR (Scopus) y ser el autor de la tesis el primer firmante de cada uno de ellos.
2. La tesis debe presentar un resumen global de la temática, de los principales resultados y de las conclusiones.
3. La tesis debe incluir una copia completa de los trabajos publicados o admitidos para publicación.

Concretamente, esta tesis doctoral está compuesta de las siguientes publicaciones:

Caballero, G.; Pezzola, A.; Winschel, C.; Casella, A.; Sanchez Angonova, P.; Rivera-Caicedo, J.P.; Berger, K.; Verrelst, J.; Delegido, J. Seasonal Mapping of Irrigated Winter Wheat Traits in Argentina with a Hybrid Retrieval Workflow Using Sentinel-2 Imagery. Remote Sens. 2022, 14, 4531. https://doi.org/10.3390/rs14184531

Caballero, G.; Pezzola, A.; Winschel, C.; Casella, A.; Sanchez Angonova, P.; Orden, L.; Berger, K.; Verrelst, J.; Delegido, J. Quantifying Irrigated Winter Wheat LAI in Argentina Using Multiple Sentinel-1 Incidence Angles.

Remote Sens. 2022, 14, 5867. https://doi.org/10.3390/rs14225867

Caballero, G.; Pezzola, A.; Winschel, C.; Sanchez Angonova, P.; Casella, A.; Orden, L.; Salinero-Delgado, M.; Reyes-Muñoz, P.; Berger, K.; Delegido, J.; Verrelst, J. Synergy of Sentinel-1 and Sentinel-2 Time Series for Cloud-Free Vegetation Water Content Mapping with Multi-Output Gaussian Processes. Remote Sens. 2023, 15, 1822. https://doi.org/10.3390/rs15071822

"A Flor, por dar el primer paso aquella vez, y a mi hija Charo, por elegirme desde su nube. A la memoria de mis padres Jorge y Elsa"

Agradecimientos

Bueno, ha llegado la hora de escribir esta sección de la tesis doctoral. Quizás la más compleja de todo el escrito. Son muchos los recuerdos que vienen a mi mente en este momento y los interrogantes que habitan en mí. ¿Cómo, por dónde y por quién empezar?

Siguiendo el orden cronológico de los acontecimientos, todo comenzó cuando me propuse construir un perchero robot. Tenía 6 años de edad y corría el año 1986. Tomé la idea de un libro titulado "*Cómo hacer batería e imanes*", publicado por la editorial Plesa SM en el año 1975. Ese, libro como tantos otros, se encontraba en la biblioteca de mi casa, la cual compartía con mis cuatro hermanos y mis padres. Acudí a mi padre Jorge con dudas relacionadas con el circuito eléctrico de aquél extraño artefacto. Mi padre, sin dudarlo, me enseñó todo lo que sabía acerca del tema y luego de culminar con éxito el primer proyecto, descubrí que aquél pequeño gran logro no era más que el inicio de mi pasión por la ciencia.

Jamás me detuve, al poco tiempo mis cajones, mis armarios y mi habitación toda, estaban llenos de cables, lámparas, baterías, motores e interruptores. Fue entonces cuando me inicié en la electrónica. Con apenas 10 años soldé mi primera plaqueta electrónica. ¡Cómo olvidarla! A partir de ese momento mi madre Elsa se convirtió en experta en componentes electrónicos. Todas las semanas, al salir de su trabajo, me compraba componentes para que yo desarrollara mis proyectos. Siempre tenía alguno nuevo dándome vueltas en la cabeza.

Pasaron los años y mis padres me ofrecieron cambiar de colegio. Con 12 años tomé la decisión de dejar a mis compañeros del icónico colegio Santo Tomás de la provincia de Córdoba, Argentina para comenzar mi aventura en el Instituto Técnico Salesiano (ITS) Villada. En el año 1999 me gradué de técnico electromecánico tras seis intensos años de valioso aprendizaje.

Casi sin darme cuenta, me encontraba cursando la carrera de Ingeniería en Telecomunicaciones y fue entonces cuando conocí al emblemático Ingeniero Riso. Héctor Riso, confió en mi desde el primer momento y son muchos los años de esta historia que hemos compartido. Trabajábamos juntos en la Universidad de la Defensa Nacional y un día mi dijo: "vos a los 40 tenés que ser doctor". Yo me encontraba cursando la maestría en Ingeniería de Sistemas Embebidos, la cual Héctor coordinaba.

Mi amigo y consejero Gabriel Ricardo Platzeck (Günther) me introdujo en el mundo de la teledetección. Compartimos un proyecto apasionante de geolocalización de descargas atmosféricas en la empresa INVAP para cual trabajé durante quince años. Grandes momentos de mi carrera profesional tuvieron lugar en INVAP. En el área Aeroespacial y Gobierno participé de numerosos proyectos relacionados con los satélites de observación de la Tierra y de Telecomunicaciones desarrollados por Argentina.

Mis ganas de aprender, de conocer nuevas culturas y de vivir nuevas experiencias nunca se detuvieron. En el año 2017 gané una beca del ministerio de modernización de la República Argentina para cursar una maestría en España. En septiembre del 2017, nos mudamos a España con mi esposa Florencia y mi hija Charo. Juntos los tres comenzamos una nueva experiencia de vida. En España cursé la maestría en teledetección de la Universitat de València y fue allí donde conocí a mi director de tesis Jesús Delegido y a mi codirector Jochem Verrelst.

Con Jesús, desde aquél entonces, forjamos una relación que continuó creciendo en diversos planos: científico, gastronómico y afectivo. En septiembre del 2021 comencé a transitar el arduo camino de cursar el doctorado en Teledetección con una beca de la fundación Carolina de España. No dudé en pedirle a Jesús que fuese mi director de tesis, él aceptó con gusto. Compartimos muchos momentos de lucidez con Jesús, nos reuníamos a "filosofar", a veces de ciencia, y otras de la vida.

Hoy con 42 años siento el mismo entusiasmo que aquél niño de 6 años, acaricio el sueño de ser Doctor en Ciencias y tengo la certeza de que siempre he sido fiel a mis convicciones, a mi escala de valores y al ejemplo que mis padres me dejaron, sin lugar a dudas mi mayor tesoro.

Ha llegado entonces la hora de dar las gracias. Siguiendo el hilo cronológico, comenzaré por mis padres, Jorge y Elsa, que me dieron la vida y me educaron en el amor de un hogar donde todas las noches se comían exquisitos manjares y se escuchaba buena música. Cómo no mencionar a los centros educativos Santo Tomás e ITS Villada que me formaron desde la niñez hasta la adolescencia, hermosos recuerdos me vienen a la cabeza.

Gracias ingeniero Riso por creer en mí, por animarme a seguir, por darme oportunidades y por hacer que mis años, primero como alumno y luego como investigador, en la Universidad sean inolvidables.

Gracias a la empresa INVAP, mi segunda casa, donde me formé como profesional. Gracias por todos los viajes, por las experiencias transmitidas, por darme las herramientas necesarias para interpretar, diseñar e implementar sistemas tecnológicos complejos, pero sobre todo gracias por enseñarme a compartir el trabajo en equipo, a entender el enfoque de otros compañeros y a valorar el proceso de revisión de pares.

Gracias Günther por tu amistad, por escucharme, por introducirme en el mundo de la teledetección y por todos los momentos profesionales compartidos. Gracias por nuestras largas tertulias derivativas asociativas, por tantas risas y por esos mates de baja impedancia que jamás olvidaré.

Gracias a la Fundación Carolina por concederme la beca doctoral que posibilitó la realización de esta tesis. Seré de ahora en adelante un becario de la ilustre Fundación Carolina de España, gracias.

Gracias Jesús Delegido por guiarme en estos años, tanto en el plano científico como en el personal. Gracias por tus invitaciones a cenar, por los viajes a Latinoamérica que hemos vivido, por sumarme al equipo de difusión del programa Copernicus, por confiar siempre en mí. Gracias por hacer que nuestro aterrizaje en Valencia, nuestro segundo lugar en el mundo, fuese tan agradable.

Gracias Jochem Verrelst y Katja Berger por su compromiso, dedicación y rigurosidad científica. Gracias por hacer de cada revisión un proceso de aprendizaje. Por la paciencia, por el respeto, por el profesionalismo, por todo ello, gracias. Gracias también a mis compañeros del Laboratorio de

Procesado de Imágenes de la Universitat de València. Gracias por los almuerzos compartidos, por conversaciones de todo tipo, por escuchar mis ideas y por alentarme siempre.

Debería dedicar sólo un apartado de agradecimientos para mis colegas y amigos de la Estación Experimental Hilario Ascasubi del Instituto Nacional de Tecnología Agraria (INTA) de Argentina. Gracias Alejandro Pezzola, Cristina Winschel, Luciano Orden y Alejandra Casella por recolectar los datos de campo, por introducirme en el mundo agronómico, por enseñarme tanto, por ser grandes personas y amigos y por tratarme como uno más desde que nos conocimos. Sin su trabajo y amistad esta tesis no hubiese sido posible. Estaré siempre agradecido con ustedes.

Gracias a mis hermanos, familiares y amigos, por atender siempre mis locas ocurrencias, por las risas por la música, por las comilonas y por el afecto incondicional. Los llevo a todos siempre en mi corazón, sin importar la distancia.

Y, como no podía ser de otra manera, lo mejor viene al final. Gracias a mi esposa Florencia y a mi hija Charo por seguir mis sueños, por dejarlo todo atrás sin dudarlo, por la valentía de enfrentar una nueva vida en otro país y por ser el motor de tracción en este camino que juntos los tres hemos emprendido. ¿Cuál será el próximo paso? No lo sé, pero tengo la certeza de que allí estarán ustedes para celebrarlo y de que contaré con su apoyo siempre. A mis compañeras de ruta, a mis mujeres hermosas, simplemente gracias.

Gabriel Rodrigo Caballero, Valencia, 13 de marzo de 2023

Acrónimos

AL Active Learning

ALIA Average Leaf Inclination Angle

CCC Canopy Chlorophyll Content

CONV Convolutional Model

CSM Cross-Spectral Mixture

CV Cross Validation

CWC Canopy Water Content

DW Dry Weight

EBD Euclidean distance-Based Diversity

EEHA Estación Experimental Hilario Ascasubi

EO Earth Observation

ESA European Space Agency

EWT Leaf Equivalent Water Thickness

FAO Food and Agriculture Organization

fCOVER Fractional of Green Vegetation Cover

FW Fresh Weight

GAI Green Area Index

GEE Google Earth Engine

GP Gaussian Processes

GPR Gaussian Processes Regression

GRD Ground Range Detected

INTA Instituto Nacional de Tecnología Agropecuaria

IWS Interferometric Wide Swath

LAI Leaf Area Index

LCC Leaf Chlorophyll Content

LMC Linear Model of Coregionalization

LWC Leaf Water Content

MAE Mean Absolute Error

MAPE Mean Absolute Percentage Error

MLRA Machine Learning Regression Algorithm

MOGP Multi-Output Gaussian Processes

MOSM Multiple-Output Gaussian processes Spectral Mixture

MSI Multi-Spectral Instrument

NIR Near-Infrared

N Nitrógeno

NDVI Normalized Difference Vegetation Index

NRMSE Normalized Root Mean Square Error

ODS Objetivos del Desarrollo Sostenible

PAI Plant Area Index

RCS Radar Cross Section

RMSE Root Mean Square Error

ROI Region of Interest

RVI Radar Vegetation Index

RTM Radiative Transfer Model

SAR Synthetic Aperture Radar

S1 Sentinel-1

S1–A Sentinel-1A

S1–B Sentinel-1B

S2 Sentinel-2

S2–A Sentinel-2A

S2–B Sentinel-2B

SAIL Scattering from Arbitrarily Inclined Leaves

SWIR Shortwave-Infrared

VBRC Valle Bonaerense del Río Colorado

VI Vegetation Indices

VBV Vegetation Biophysical Variables

VH Vertical–Horizontal polarization

VV Vertical–Vertical polarization

VWC Vegetation Water Content

VIS Visible Spectrum

Sinopsis

La agenda 2030 plantea 17 Objetivos del Desarrollo Sostenible (ODS) que se deben alcanzar para garantizar un futuro sustentable que promueva el avance de la sociedad y la economía haciendo uso racional de los recursos naturales. El trigo como alimento universal ampliamente difundido, representa una alternativa atractiva para abordar el ODS "Hambre Cero". Resulta relevante, bajo el concepto de sostenibilidad, mensurar la proporción de las tierras agrícolas destinadas a la producción del trigo, estimar el rendimiento y conocer el estado de salud de las plantas para satisfacer la creciente demanda alimentaria a nivel global. Las variables biofísicas de la vegetación (VBV) son indicadores directos del crecimiento y productividad de los cultivos. La toma de medidas in situ de VBV es un proceso laborioso especialmente en zonas agrícolas donde la variabilidad espacial de los cultivos es significativa. Los sistemas de observación de la Tierra (EO–*Earth observation*) presentan oportunidades sin precedentes para el monitoreo de las variables biofísicas del trigo. En especial, el programa Copernicus de la Agencia Espacial Europea se ha posicionado como un agente principal a nivel mundial, gracias a su política de datos de libre acceso. Sentinel–2 (S2) es una constelación de satélites que forma parte de las misiones Sentinel del programa Copernicus de EO. S2 transporta un instrumento multiespectral capaz de adquirir información de la reflectividad de la superficie con 13 bandas espectrales distribuidas en el intervalo 440–2200 nm y resoluciones espaciales de 10, 20 y 60 m. El período de revisita, así como su resolución espacial y espectral, han convertido a S2 en un sistema de EO trascendental para el monitoreo de variables biofísicas de la vegetación. Los sistemas ópticos de EO se ven limitados con frecuencia por las condiciones climáticas tales como nubosidad o precipitaciones. En este sentido, la tecnología radar, presenta nuevas oportunidades para el monitoreo de VBV que deben explorarse en profundidad. Sentinel–1 (S1) es una constelación radar de la familia Sentinel. Con dos bandas polarimétricas VH & VV en banda C, S1

mapea información de la retrodispersión de la superficie terrestre de forma sistemática. Debido a la complejidad de la interacción de la señal radar con las superficies cultivadas y al ruido aditivo inherente de speckle, la estimación de VBV con tecnología radar aún sigue siendo un desafío. Surge entonces la propuesta de fusionar datos multiespectrales de S2 y radar de S1 con la intención de desarrollar modelos de estimación de VBV que se beneficien de las ventajas que ambas tecnologías de EO presentan. El objetivo de esta tesis doctoral es desarrollar modelos de estimación de variables biofísicas del trigo, en una zona irrigada de cultivo intensivo al sureste de Argentina, basados en medidas in situ de la vegetación, a partir de: i) datos multiespectrales de S2; ii) datos radar de S1; y iii) la sinergia S1 & S2. En la figura 1 se presenta la contextualización del problema a resolver.

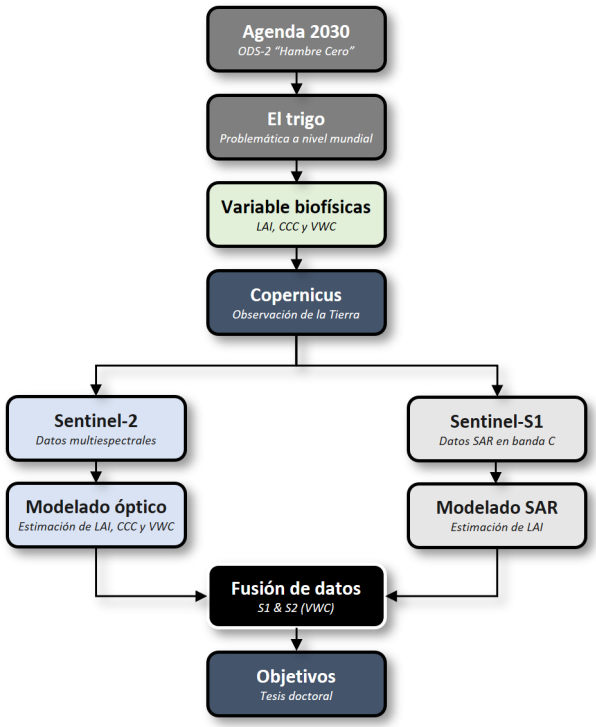

Figura 1: Esquema conceptual de la tesis doctoral

Para abordar la problemática planteada, se desarrollaron en primer lugar,

modelos de estimación del índice de área foliar (LAI–*leaf area index*), del contenido de clorofila de la cubierta vegetal (CCC–*canopy chlorophyll content*) y del contenido de agua del trigo (VWC–*vegetation water content*), utilizando una base de datos multitemporal de VBV tomadas in situ, algoritmos de aprendizaje automático, una base de datos de espectros de reflectividad bidireccional de la vegetación simulados con un modelo de transferencia radiativa y datos multiespectrales de S2. Se obtuvieron modelos híbridos de estimación de estas VBV que se ajustaron con alta precisión a los datos de campo (LAI: R^2 = 0.92, RMSE = 0.43 m^2 m^{-2}, CCC: R^2 = 0.80, RMSE = 0.27 g m^{-2} y VWC: R^2 = 0.75, RMSE = 416 g m^{-2}) y se logró reconstruir con éxito la curva fenológica del cultivo de trigo. En segundo lugar se implementó un modelo de estimación de LAI basado en datos radar de S1 en ambas polarizaciones VH & VV, adquiridos en diferentes geometrías de adquisición. Se probó que la estructura tridimensional de la vegetación cuando es observada desde ángulos de incidencia local diferentes proporciona información muy valiosa que puede ser utilizada para mejorar los modelos existentes (LAI: R^2 = 0.67, RMSE = 0.88 m^2 m^{-2}). Por último, se desarrolló una estrategia de fusión de datos de S1 & S2 para reconstruir series temporales de VWC. Se aplicaron varios modelos de procesos Gaussianos de salidas múltiples (MOGP–*multi-output Gaussian process*) para analizar la correlación cruzada existente, en el dominio de la frecuencia, entre los canales ópticos y radar. Posteriormente, se seleccionó el mejor modelo de MOGP, en términos de precisión, para su aplicación a nivel de pixel posibilitando la reconstrucción espaciotemporal de mapas de VWC a partir de la sinergia S1 & S2. La combinación sinérgica de datos radar y ópticos mostró ser un novedoso enfoque para abordar el monitoreo de variables biofísicas del trigo en regiones intensamente cultivadas con frecuente nubosidad.

Índice general

Parte I
Resumen extenso

CAPÍTULO 1

INTRODUCCIÓN

1.1. Contextualización

Los Objetivos del Desarrollo Sostenible (ODS), planteados en la agenda 2030 aprobada por la Asamblea General de las Naciones Unidas en 2015, proponen un escenario que promueve la igualdad entre las personas asegurando la prosperidad global, a través de un contrato social que persigue proteger los recursos naturales finitos del planeta Tierra y se apoya en el hecho de que la eficiencia en la extracción y explotación de los recursos naturales por parte del ser humano se encuentra en constante crecimiento (UN General Assembly, 2015).

El conocimiento de la geolocalización de los sucesos medioambientales, económicos y sociales como así también su variabilidad temporal, resulta de particular importancia para gestionar eficientemente los ODS y así mejorar el bienestar de las personas (Avtar et al., 2020). Esta información integra un conglomerado de datos digitales que abarca desde mapas topográficos hasta productos de múltiples capas de información geográfica superpuestas y estructuradas por datos complejos obtenidos de fuentes fiables (MacFeely, 2019).

La calidad de vida y la prosperidad de la humanidad están asociadas con el grado de satisfacción de un conjunto de necesidades básicas de los seres humanos (López-Ruiz et al., 2021, Susniene y Jurkauskas, 2009). En primer nivel se encuentran las necesidades fisiológicas innatas de supervivencia que, como individuos, incorporamos desde que nacemos (Reer and Krämer, 2018). Respirar, alimentarse e hidratarse, descansar, evitar el dolor y mantener la temperatura corporal se identifican como necesidades del primer nivel de la pirámide de Maslow (Maslow, 1991). En este contexto, el ODS "Hambre Cero" establece: *"Acabar con el hambre, conseguir la seguridad alimentaria y mejora nutricional y promocionar la agricultura sostenible"*.

En términos de productividad agrícola, la meta 2.3 persigue: *"Para 2030, duplicar la productividad agrícola y los ingresos de los productores de alimentos en pequeña escala, en particular las mujeres, los pueblos indígenas, los agricultores familiares, los pastores y los pescadores, entre otras cosas mediante un acceso seguro y equitativo a las tierras, a otros recursos de producción e insumos, cono-*

cimientos, servicios financieros, mercados y oportunidades para la generación de valor añadido y empleos no agrícolas".

Con base en la sostenibilidad de los sistemas productivos, la meta 2.4 relacionada con este ODS, menciona: *"Para 2030, asegurar la sostenibilidad de los sistemas de producción de alimentos y aplicar prácticas agrícolas resilientes que aumenten la productividad y la producción, contribuyan al mantenimiento de los ecosistemas, fortalezcan la capacidad de adaptación al cambio climático, los fenómenos meteorológicos extremos, las sequías, las inundaciones y otros desastres, y mejoren progresivamente la calidad del suelo y la tierra".*

Para monitorizar el estado y progreso del ODS "Hambre Cero" y de las metas 2.3 y 2.4 propuestos en la agenda 2030 el indicador 2.4.1 hace referencia a mensurar la proporción del área en que se desarrolla una agricultura sostenible y productiva (Kussul et al., 2019).

La demanda mundial de alimentos está aumentando debido a la constante expansión de la población y al crecimiento del ingreso per cápita (Tilman et al., 2011). Dicha demanda implica el uso intensivo de las tierras destinadas a la explotación de cultivos. Es importante comprender y dimensionar los impactos ambientales de la sobreexplotación de recursos naturales para satisfacer la creciente necesidad alimentaria del planeta (Sánchez et al., 2019).

La agricultura es una actividad de gran importancia a nivel global que tiene una estrecha relación con el equilibrio ecológico del planeta y el desarrollo armónico de la naturaleza (Paoletti et al., 1989). La proporción de las superficies intensamente cultivadas y las prácticas agronómicas aplicadas a los cultivos producen un impacto directo sobre el medio ambiente y éste a su vez modula el cambio climático (Kastner et al., 2014). Un adecuado control de la explotación agrícola permite incrementar los niveles de fijación de carbono en el suelo mejorando además la gestión de los recursos hídricos y disminuyendo las emisiones de gases de efecto invernadero (Pachauri y Meyer, 2014, Smith et al., 2014).

El trigo (*Triticum aestivum*) junto con el arroz y el maíz es uno de los tres cereales más cultivados en todo el mundo (Grote et al., 2021). Pertenece a

la familia de las gramíneas y suministra el 20 % del total de calorías consumidas a nivel global. Tiene sus orígenes en la antigua Mesopotamia donde se evidencia el uso de este cereal para la producción de alimentos (Field, 1932). Debido a su alto grado de adaptabilidad a condiciones climáticas diversas y a la disponibilidad de agua para el consumo de las plantas, el trigo ha proliferado a nivel global y forma parte de la dieta básica de gran parte de la población mundial (Acevedo et al., 2018).

Contar con información del rendimiento del cultivo de trigo a escalas local y regional se torna fundamental para el desarrollo de economías sustentables (Luis et al., 2012). El rendimiento del cultivo de trigo está asociado a su genética, manejo y a las condiciones edafoclimáticas de la región (Slafer et al., 2003). Para el cultivo de trigo, el consumo de agua no solo está vinculado con la fotosíntesis, sino también con la tasa de llenado del grano y, en última instancia, con el rendimiento (Alvarez Prado et al., 2013). La fertilización nitrogenada es una práctica de manejo agronómica insustituible cuyo objetivo es cubrir los requerimientos nutricionales del cultivo para conseguir su máxima eficiencia económica y ambiental (Forrestal et al., 2014).

El monitoreo de los efectos de la fertilización nitrogenada sobre el cultivo de trigo se basa en comprender los procesos fisiológicos (fotosíntesis, respiración, transpiración, absorción de nutrientes y translocación) de las plantas (Belete et al., 2018, Hinzman et al., 1986). El estado de salud, productividad, crecimiento y estado fenológico del cultivo de trigo pueden inferirse mediante el conocimiento de las variables biofísicas de la vegetación (VBV–*vegetation biophysical variables*) (Gitelson et al., 2003). Por lo tanto, comprender de forma precisa y oportuna la distribución espaciotemporal de las variables biofísicas de las plantas de trigo resulta indispensable para lograr una gestión eficiente de los recursos naturales destinados a la producción de este cereal y alcanzar los rendimientos esperados en términos de seguridad alimentaria (Dubois et al., 2011).

Estimar y monitorear las variables biofísicas esenciales de la vegetación, como el índice de área foliar (LAI–*leaf area index*), el contenido de clorofila de la cubierta vegetal (CCC–*canopy chlorophyll content*) y el contenido

de agua de la vegetación (VWC–*vegetation water content*) resulta de particular importancia para analizar cuantitativamente el crecimiento de los cultivos dando así soporte a la explotación sostenible de superficies cultivadas (Hanes, 2013, Hank et al., 2015). Las definiciones de estas variables son las siguientes:

El LAI se define como el área foliar total unilateral por unidad de superficie de suelo (m^2 superficie foliar/m^2 suelo). Está fuertemente relacionado con la fotosíntesis y la evapotranspiración de la cubierta vegetal y juega un papel clave en el intercambio de energía y agua entre la biosfera y la atmósfera (Weiss et al., 2004) por este motivo se lo considera una variable climática esencial de tipo estructural (Baret et al., 2013). Otras definiciones del LAI pueden encontrarse en la literatura como el índice de área efectiva de la vegetación (PAI–*plant area index*) que incluye el área de todos los órganos de la planta y asume una distribución aleatoria de las hojas (Leblanc et al., 2005) y el LAI verde (GAI–*green area index*) que describe la transferencia de radiación de los elementos fotosintéticamente activos de la cubierta vegetal (Amin et al., 2021, Duveiller et al., 2011).

El CCC (g de clorofila/m^2 suelo) se define como el producto entre el LAI y el contenido de clorofila de las hojas (LCC–*leaf chlorophill content*) expresado en gramos por unidad de superficie foliar (g de clorofila /m^2 de superficie foliar). Debido a la fuerte correlación que existe entre el LCC y el contenido de nitrógeno (N) a nivel de hoja, es posible utilizar el CCC como proxy para cuantificar el contenido de N de la cubierta vegetal en la etapa de desarrollo vegetativo de las plantas (Baret et al., 2007, Berger et al., 2020a, Delloye et al., 2018).

El VWC se define como la cantidad de agua de la vegetación por unidad de superficie de suelo (g agua/m^2 de suelo) e incluye todos los elementos de la estructura vegetal: tallos, hojas, flores y frutos. El VWC se encuentra asociado a la transpiración, al estrés hídrico y a la productividad de biomasa de la vegetación, por este motivo se lo considera una variable crucial para determinar el estado fisiológico de las plantas (Clevers et al., 2010, Peñuelas et al., 1993, Zhang et al., 2017). El VWC es un indicador significativo del crecimiento de las plantas durante las diferentes etapas de de-

sarrollo (Hanes, 2013). Conocer la distribución espacial del VWC permite además dimensionar la cantidad de agua demandada para fines de riego, lo cual es imprescindible para estimar los costes asociados de producción agrícola en términos económicos y ambientales (Ingram et al., 2008).

Tradicionalmente, el contenido de agua de la vegetación ha sido determinado cosechando de modo manual una superficie cultivada y calculando a posteriori la diferencia entre el peso húmedo y el peso seco de esa muestra (Han et al., 2019). Para determinar el LAI y el CCC existen instrumentos portátiles que pueden ser fácilmente desplegados en campo, no obstante, la recolección de variables biofísicas in situ es un proceso laborioso especialmente en áreas extensas donde la variabilidad espacial es significativa (Rud et al., 2014).

Los sistemas de observación de la Tierra (EO–*Earth observation*) proporcionan una visión sinóptica de las superficies terrestres y, por lo tanto, constituyen una alternativa eficiente para monitorear la heterogeneidad espacial y temporal de las VBV en regiones agrícolas de todo el mundo (Schott, 1989). El programa Copernicus de la Agencia Espacial Europea (ESA–*european space agency*) proporciona datos de observación de la Tierra mediante una serie de misiones satelitales Sentinel y una gama de servicios divididos por áreas temáticas (vigilancia atmosférica, terrestre, ambiental oceánica y meteorológica, cambio climático, emergencias y seguridad). Copernicus ha logrado posicionarse como actor principal en la monitorización de los ODS gracias a su política de datos abiertos de libre acceso (Jutz and Milagro-Pérez, 2018).

Sentinel-2 (S2) es un sistema operacional de EO de órbita baja perteneciente al programa Copernicus. Está formado por una constelación de dos satélites S2-A y S2-B que transportan un instrumento multiespectral (MSI–*multispectral instrument*) capaz de adquirir información global sistemática de la superficie terrestre en las regiones del espectro visible (VIS–*visible spectrum*), infrarrojo cercano (NIR–*near infrared*) e infrarrojo de onda corta (SWIR–*short wave infrared*) con 13 bandas espectrales. Provee imágenes multiespectrales con un tiempo de revisita de 5 días en el ecuador y una resolución espacial de 10 m, 20 m y 60 m (Drusch et al., 2012). S2 es una mi-

sión espacial de gran interés para el desarrollo de servicios de monitoreo en cuasi tiempo real de las superficies agrícolas (Delloye et al., 2018).

En los últimos años, el rápido desarrollo y la constante evolución de las tecnologías de EO, han dado lugar a una copiosa producción de investigación dedicada a explotar los datos multiespectrales de los satélites ópticos para monitorear las VBV en áreas intensamente cultivadas, de forma rápida y precisa (Amin et al., 2021, Berger et al., 2020b, Clevers et al., 2010, Danner et al., 2021, Verrelst et al., 2019, 2013a, 2015b).

Las técnicas utilizadas para estimar las VBV a partir de datos de EO pueden clasificarse en cuatro categorías (Verrelst et al., 2015a, 2019): (1) Métodos paramétricos, típicamente consisten en establecer relaciones entre las VBV y los datos espectrales de EO generalmente transformados en forma de índices (Broge and Leblanc, 2001, Gitelson et al., 2002). (2) Métodos no paramétricos que utilizan algoritmos de regresión de aprendizaje automático (MLRA–*machine learning regression algorithms*) para entrenar modelos de estimación de las VBV y reciben como argumento de entrada datos de reflectividad de la superficie observada y datos de VBV medidos in situ o simulados (Atzberger et al., 2010, Mountrakis et al., 2011, Verger et al., 2011). (3) Inversión de modelos de transferencia radiativa (RTM–*radiative transfer model*) (Houborg and Boegh, 2008, Jacquemoud et al., 1995, 2009, Kimes et al., 1998, Verrelst et al., 2014). Los RTM aplican las leyes de la física para simular la reflectividad espectral de la vegetación modelando los procesos de reflexión, transmisión y absorción de la radiación electromagnética en función de las características físicas y químicas de las hojas y de los parámetros estructurales de las plantas (Féret et al., 2021, Feret et al., 2008, Jacquemoud et al., 2009, Verhoef, 1984, Verhoef and Bach, 2007). (4) Enfoques híbridos, son quizás los más atractivos y novedosos ya que combinan la potencia de simulación de los RTM con la velocidad y eficiencia de los MLRA (Abdelbaki and Udelhoven, 2022, Berger et al., 2020b, Brede et al., 2020, Danner et al., 2021, Verrelst et al., 2019). En este escenario, los datos de entrenamiento son simulados variando los parámetros de entrada de un RTM acoplado (hoja-cobertura vegetal). Posteriormente, se utiliza un MLRA para establecer las relaciones no lineales entre los espectros de reflectividad simulados y las VBV a estimar. Diversos autores han desarro-

llado modelos de estimación de variables biofísicas del trigo basados en datos de EO y en MLRA o regresiones paramétricas (Amin et al., 2021, Delegido et al., 2015, Estévez et al., 2021, Pasqualotto et al., 2019, Zhang et al., 2017, 2016).

Del conjunto de MLRA se distingue la regresión de procesos Gaussianos (GPR–*Gaussian process regression*) (Camps-Valls et al., 2016, Rasmussen and Williams, 2006) que es un método probabilístico no paramétrico ampliamente adoptado en estudios dedicados a inferir VBV utilizando datos de EO (Abdelbaki and Udelhoven, 2022, Adeluyi et al., 2021, Camps-Valls et al., 2016, Estévez et al., 2022, Estévez et al., 2021, Pascual-Venteo et al., 2022, Reyes-Muñoz et al., 2022, Salinero-Delgado et al., 2021, Van Wittenberghe et al., 2014, Verrelst et al., 2012, 2016, Xie et al., 2021). GPR proporciona un mecanismo fiable para construir y calibrar la incertidumbre de las estimaciones, lo que permite evaluar la fidelidad de los modelos de estimación de VBV y transferirlos espaciotemporalmente a otras regiones cultivadas del mundo (Verrelst et al., 2013b).

Monitorear la evolución temporal de las variables biofísicas del trigo mediante datos de S2 en las etapas de desarrollo vegetativo, brinda oportunidades sin precedentes para dar respuesta al análisis causa-efecto de las prácticas agrícolas implementadas durante el manejo del cultivo (Cavalaris et al., 2021). Sin embargo, en regiones de latitudes altas donde las condiciones climáticas como la nubosidad persistente imposibilita el uso de las escenas de S2, el monitoreo de las regiones intensamente cultivadas se ve restringido a intervalos de corta duración, razón por la cual resulta difícil monitorear las VBV a lo largo del ciclo fenológico del cultivo de trigo. En este sentido la EO basada en datos de radar provee la tecnología para mitigar esta limitación (Valero et al., 2021).

Sentinel-1 (S1) es otra misión espacial de la ESA perteneciente al programa Copernicus, que transporta un sensor radar de apertura sintética (SAR–*synthetic aperture radar*). El sensor SAR de banda C de S1 permite la adquisición de imágenes radar en modo ascendente y descendente tanto de día como de noche en toda condición climática (Torres et al., 2012). La constelación S1 comprendida por los satélites S1-A, lanzado el 3 de abril de

2014, y S1-B, lanzado el 25 de abril de 2016, predefine el modo interferométrico (IWS–*interferometric wide swath*) para observaciones sobre tierra. El modo IWS consiste en imágenes de polarización dual (VV & VH) a 10 m de resolución espacial con un tiempo de revisita de 3 días en el ecuador que pueden utilizarse para monitorear la evolución de las regiones agrícolas. El 3 de agosto del 2022 la ESA comunicó que debido a una anomalía (producida el 23 de diciembre del 2021) en el subsistema de potencia que alimenta la antena SAR de S1-B, la misión se había perdido por completo. El lanzamiento del tercer miembro de la familia de radares S1-C está previsto para la segunda mitad de 2023, no obstante, se cuenta con varios años de datos de S1-A y S1-B operando de forma simultánea. Las densas series temporales de datos polarimétricos de S1 ofrecen nuevas perspectivas para abordar problemáticas de índole agrícola (SenSAgri, 2020).

La biomasa y la estructura tridimensional de la vegetación modifican el coeficiente de retrodispersión de la señal SAR (Karam et al., 1992) que, en función de la longitud de onda, puede penetrar la cubierta vegetal de los cultivos. Esto resulta conveniente para monitorear las VBV (Gao et al., 2013, McNairn et al., 2014, Zhang et al., 2014). Numerosos estudios han abordado la estimación de VBV del cultivo de trigo con datos SAR (Kaplan et al., 2021, Nasrallah et al., 2019, Ouaadi et al., 2021, Vavlas et al., 2020). Las series temporales de datos SAR se han utilizado además para el seguimiento de la VBV del trigo y de otros cultivos a lo largo de su ciclo fenológico. Mattia et al. (2003) y Ouaadi et al. (2021), estudiaron la variabilidad temporal del coeficiente de retrodispersión radar en banda C para cultivos de trigo. Veloso et al. (2017), descubrieron una fuerte correlación entre el índice de vegetación de diferencia normalizada (NDVI–*normalized difference vegetation index*), el LAI verde, la biomasa fresca y la relación VH/VV de S1 para cultivos de trigo, maíz y cebada. La explotación de los datos satelitales de sensores de tipo SAR, así como el análisis de series temporales, constituyen un claro diferenciador y plantean un nuevo paradigma en el campo del sensoramiento remoto (Liu et al., 2019). A diferencia de los sensores ópticos, la geometría de adquisición de las imágenes radar sobre regiones de cultivos, juega un papel determinante (Bousbih et al., 2017, Rozenstein et al., 2016). Para cultivos como el trigo, que evidencian una

amplia evolución de la estructura tridimensional de las plantas a lo largo del ciclo fenológico, el valor del coeficiente de retrodispersión radar en banda C se ve significativamente alterado por el ángulo de incidencia local de la señal radar (Ulaby et al., 1982).

En la actualidad, la mayoría de los productos de teledetección basados en datos de las misiones satelitales Sentinel, hacen uso de los datos de S1 y de S2 de forma independiente. El próximo paso es explotar la sinergia de múltiples fuentes de datos, es decir, combinar datos ópticos con datos de radar. La cobertura global y las observaciones sistemáticas de S1 y S2 plantean un escenario de aplicaciones de monitoreo de cultivos, detección de cambios y mapeo de las coberturas de las superficies terrestres basadas en fusión de datos radar y ópticos que merece ser explotado en los próximos años (Mattia et al., 2018, Satalino et al., 2018). Algunos esfuerzos de investigación han hecho uso de la alta calidad radiométrica de S1 y de la resolución espectral de S2 de forma sinérgica para monitorear VBV (Caballero et al., 2018a, Druce et al., 2021, Mercier et al., 2020, Pipia et al., 2019, Veloso et al., 2017). En el contexto de EO, el desarrollo de modelos que exploten las dependencias entre flujos de datos SAR y ópticos resulta conveniente cuando las escenas observadas están contaminadas por nubes (Pipia et al., 2019).

GPR puede ser extendido a modelos de múltiples salidas dando origen al concepto de procesos Gaussianos de salida múltiple (MOGP–*multi-output Gaussian process*). Los modelos de MOGP son capaces de computar la correlación cruzada existente entre datos de series temporales de S1 & S2 (Wolff et al., 2020). Por este motivo, MOGP representa una estrategia de aprendizaje automático particularmente atractiva para abordar aplicaciones de fusión de datos radar y ópticos. El uso de MOGP para explotar de forma sinérgica la información de S1 & S2, ha sido escasamente explorado. Pipia et al. (2019), utilizaron series temporales del índice de vegetación radar (RVI–*radar vegetation index*) derivado a partir de datos de S1 y de LAI basado en un modelo óptico presentado por Amin et al. (2021), con el propósito de reconstruir datos de LAI sobre una región agrícola ubicada al noroeste de la península Ibérica. La fusión de datos de radar y ópticos para el monitoreo de las VBV es por lo tanto un campo novedoso de investigación y merece especial atención.

Habiendo analizado las ventajas que los sistemas de EO presentan para monitorear espaciotemporalmente las VBV de forma eficiente y expeditiva, la política de datos abiertos y de libre acceso que promueve el programa Copernicus, la importancia del trigo como alimento global y los enfoques de fusión de datos de radar y ópticos que permiten abordar el monitoreo de cultivos en regiones nubosas, no cabe lugar a dudas de que los sistemas de EO tales como S1 y S2 constituyen una herramienta imprescindible para hacer frente a las problemáticas de seguridad alimentaria planteadas por la agenda 2030 a diferentes escalas, tanto a nivel local como global, mejorar la productividad agrícola y asegurar la sostenibilidad ambiental (Masó et al., 2020). Este concepto es reconocido dentro del programa "ESA Earth Observation Living Planet" a través del servicio "Copernicus Land Monitoring" (ESA, 2018).

1.2. Objetivos

El objetivo de esta tesis doctoral es explotar la información multiespectral del sensor óptico de S2, la información radiométrica del sensor radar en banda C de S1, y la sinergia S1 & S2 utilizando bases de datos de medidas in situ y algoritmos de aprendizaje automático, para desarrollar modelos de estimación de variables biofísicas del trigo en una zona irrigada intensamente cultivada, que contribuyan a la implementación de prácticas agronómicas sustentables, orientadas a realizar un uso eficiente de los recursos naturales.

Del objetivo principal se desprenden los siguientes objetivos específicos:

1. Diseñar un protocolo para la toma de medidas in situ de variables biofísicas del trigo de invierno en diferentes lotes de un área irrigada de cultivo intensivo localizada al Sur de la Provincia de Buenos Aires, Argentina.
2. Realizar campañas de campo de acuerdo con la metodología definida en el protocolo de medición de variables biofísicas del trigo.
3. Construir una base de datos multitemporal de medidas in situ que incluya valores de LAI, fCOVER (*fraction of green vegetation cover*), biomasa fresca y seca y CCC, para las campañas de cultivo 2020 y 2021 de trigo irrigado en la región de estudio.
4. Implementar un enfoque híbrido basado en un modelo acoplado de transferencia radiativa, datos multiespectrales de S2 a 10 y 20 m de resolución espacial, VBV medidas in situ y GPR para el desarrollo de modelos de estimación de LAI, CCC y VWC del trigo de invierno.
5. Generar un modelo de estimación de LAI dedicado al cultivo de trigo de invierno con datos polarimétricos del sensor radar de S1 adquiridos a diferentes ángulos de incidencia local, medidas in situ y GPR.
6. Evaluar la capacidad de distintos modelos de MOGP para fusionar series temporales de S1 & S2.

7. Estimar el contenido de agua del trigo de invierno explotando de forma sinérgica la información proveniente de los satélites de observación de la Tierra S1 y S2 en sitios que se vean afectados por la presencia de nubes.

1.3. Estructura de la tesis

La tesis doctoral se estructura de la siguiente manera:

En el Capítulo 1 se presenta una introducción general al tema de investigación, se brinda el contexto de la problemática abordada, se realiza una exploración del estado del arte en el campo del sensoramiento remoto tanto en el dominio óptico como en el campo de los sensores radar y se plantean los objetivos de la tesis doctoral. En el Capítulo 2 se describen los materiales y métodos utilizados para llevar adelante la investigación. Se realiza una descripción del área de estudio y de los enfoques utilizados para desarrollar modelos de estimación de variables biofísicas de la vegetación a partir de datos ópticos de S2, radar de S1 y de la fusión S1 & S2. En el Capítulo 3 se presenta un resumen de los resultados obtenidos y una breve discusión sobre los aportes originales realizados al campo de la teledetección. En el Capítulo 4 se exponen las conclusiones y limitaciones encontradas. A continuación se anexan los tres artículos que componen esta tesis.

CAPÍTULO 2

MATERIALES Y MÉTODOS

2.1. Área de estudio

El área de estudio está ubicada en el valle Bonaerense del Río Colorado (VBRC) al sureste de la provincia de Buenos Aires, Argentina. El VBRC presenta dos agroambientes claramente diferenciables: un área de secano y un área irrigada por las aguas del río Colorado. Se encuentra entre los paralelos 39º y 40º de latitud Sur y los meridianos de 62º y 63º de longitud Oeste. Es posible encontrar una amplia variedad de cultivos en la zona. En el área irrigada, se realizan riegos por gravedad en diferentes estadíos fenológicos de los cultivos. En la década de los sesenta, se produjeron grandes transformaciones del paisaje natural en la región de estudio. Se construyó una extensa red de canales de riego y de drenaje que transporta el agua del río Colorado a la zona priorizada de cultivo intensivo del VBRC. El desarrollo de las actividades agropecuarias en la zona tiene lugar gracias al riego artificial. El área total de cultivos bajo riego es aproximadamente 90.000 ha, las cuales se destinan principalmente a la producción de: (1) horticultura especializada en papa, zapallo y cebolla; (2) producción de alfalfa para semilla y henificación; (3) maíz para semilla y ensilaje; (4) girasol para semilla; (5) cereales de invierno como avena y trigo; y (6) pasturas polifíticas. En la zona de secano se cultivan principalmente cereales de invierno entre los cuales se destacan: avena, trigo, cebada y centeno (Caballero et al., 2020). El sitio de ensayo se ubica en la Estación Experimental Agropecuaria Hilario Ascasubi del Instituto Nacional de Tecnología Agropecuaria (EEHA - INTA) de Argentina. Esta tesis se focaliza en tres lotes de trigo de invierno pertenecientes a la campaña de cultivo 2020 y en un lote de trigo de la campaña 2021 del VBRC.

2.1.1 Caracterización ambiental de la región de estudio

El segmento Sur de la provincia de Buenos Aires está compuesto por los partidos de Patagones y Villarino. Con un clima Mediterráneo, la región de estudio presenta un paisaje árido de estepa. Las precipitaciones son mayores en otoño generalmente y decrecen desde el Norte hacia el suroeste. El déficit de agua anual medio para el cultivo de trigo es de 322 mm en

la zona de regadío, mientras que en la zona de secano puede superar los 400 mm (Sanchez y Matarazzo, 1983). El régimen de precipitaciones oscila entre períodos de extrema sequía y períodos con abundantes lluvias. La temperatura anual media es de 14.8 ºC, los valores más bajos se registran en el mes de julio ($<$ 2 ºC) mientras que en enero la temperatura durante el día puede ser mayor de 30 ºC. El período anual libre de heladas es de 240 días máximo hacia el Este del VBRC. En el área de estudio el suelo experimenta dos fenómenos que afectan negativamente la productividad de los cultivos. El primero es la alta salinidad del suelo, la cual está asociada a una baja capacidad de drenaje del agua utilizada para riego. El segundo es la pérdida de suelo que se origina durante las tareas de laboreo agrícola (vinculadas con la nivelación de los lotes para el posterior riego por gravedad) y da lugar a una disminución importante de nutrientes de origen orgánico. En términos generales, los suelos tienen una textura arenosa o franco-arenosa con 1 % de materia orgánica. Debido a la textura del suelo, el riesgo de erosión ocasionada por los fuertes vientos de origen Patagónico es alto y la capacidad de retención de agua es por lo tanto baja. La región de estudio presenta una ligera pendiente descendiente (20 m de altura s.n.m. en 8 km) en sentido Oeste-Este.

2.1.2 Propiedades del trigo de invierno en la región de estudio

El cultivo de trigo requiere de suelos con baja salinidad ($<$ 4 dS m^{-1}), pH neutro, alta concentración de fósforo (P$>$ 20 ppm) y un buen porcentaje de materia orgánica (M.O.$>$ 1.5 %) (Agamennoni et al., 1996). Cuando las plantas de trigo se enfrentan a períodos de sequía en las etapas iniciales de desarrollo, se puede apreciar que las parcelas cultivadas no son uniformes lo cual es atribuible a la composición físico-química del suelo (Sanchez y Matarazzo, 1983). El trigo de ciclo largo se siembra desde mediados de mayo a finales de junio y se cosecha desde mediados de diciembre a principios de enero. Se requiere un riego presiembra para garantizar que el perfil de suelo se encuentre con un alto contenido de humedad al momento de implantar las semillas. Se recomienda ajustar la densidad de siembra entre 250 y 350 plantas/m^2. El cultivo de trigo requiere entre 500 a 550 mm de

agua durante su ciclo fenológico. Si el perfil de suelo se encuentra recargado de agua al momento de la siembra, las plantas de trigo alcanzan la etapa de macollaje sin sufrir déficit hídrico. En el período de encañazón comienza el aumento de la demanda hídrica (3–4 mm/día) que llega a ser máxima durante la fase de llenado del grano (5–6 mm/día).

2.1.3 Manejo del cultivo de trigo

La siembra del trigo se realizó el 25 de junio de 2020 con una densidad de semillas de 95 kg ha^{-1} en tres lotes del área priorizada de la EEHA en el VBRC. Durante la siembra se suministró una dosis de 80 kg ha^{-1} de fosfato diamónico de acuerdo con la formulación 18-46-00 (18 % N, 46 % P2O5, 0 % K2O). En el transcurso de las labores previas a la siembra se conformaron bordos espaciados 14 m para facilitar el riego por gravedad. Además del riego presiembra, el cultivo de trigo se irrigó artificialmente en tres estadíos fenológicos diferentes: macollaje, encañazón y llenado del grano. La calidad promedio del agua utilizada para riego, en la campaña 2020, fue de: pH = 8.23, conductividad eléctrica (C.E.) = 1.37 dS m^{-1}, relación de absorción de sodio (R.A.S.) = 3.52 (Laboratorio de Suelos y Aguas EEHA INTA-Ascasubi) (Casella et al., 2022). Los lotes de trigo de la campaña 2020 en el VBRC recibieron fertilización nitrogenada con Urea granulada uniformemente distribuida (150–200 kg ha^{-1}) en dos momentos de la etapa de macollaje: principios de agosto y mediados de septiembre Z2.3 y Z2.4 respectivamente según la escala de Zadoks (Zadoks et al., 1974). Al inicio de la etapa de macollaje la densidad de plantas fue de 243 plantas m^{-2} y la separación entre hileras de 17.5 cm. La composición físico-química del suelo en el muestreo inicial fue analizada en el Laboratorio de Suelos y Aguas EEHA INTA-Ascasubi y presentó los siguientes valores: pH = 7.8; C.E. = 0.70 dS m^{-1}, M.O. = 1.35 %, N = 0.35 %, P = 13 mg kg^{-1}.

2.1.4 Medidas in situ de variables biofísicas del trigo de invierno

Los lotes de trigo seleccionados para la medición in situ de variables biofísicas se visitaron periódicamente a lo largo del ciclo fenológico del cultivo.

Buscando que las fechas de muestreo en campo coincidieran en $\pm$ 6 días con el paso de S2 y en función de las condiciones climáticas en la región de estudio, se realizaron 8 muestreos durante la campaña de cultivo 2020 desde principios de agosto hasta finales de diciembre. Las medidas in situ de las VBV fueron tomadas por un grupo de profesionales del laboratorio de teledetección y sistemas de información geográfica (SIG) de la EEHA del INTA, Argentina. En cada muestreo se tomaron las medidas in situ de LAI, LCC, fCOVER y biomasa fresca del trigo sobre un total de 9 puntos georreferenciados (tres por cada lote). Para la medición no destructiva del LAI se utilizó la aplicación PocketLai (Confalonieri et al., 2013). Los valores de LCC fueron medidos con el instrumento SPAD 502 Minolta y el fCOVER con la aplicación Canopeo (Patrignani y Ochsner, 2015) siguiendo el protocolo definido por Casella et al. (2022). En cada punto de muestreo se realizaron 5 medidas de cada VBV y luego se calculó el valor promedio. Para obtener los valores de biomasa fresca, se cosechó un área de 0.02 m^2 y se pesó la muestra compuesta de tallos, hojas, flores y frutos en laboratorio (FW–*fresh weight*). Los valores de biomasa seca se obtuvieron luego de secar las muestras de biomasa fresca en un horno a temperatura constante (60 ºC) durante 24 hs y de determinar su peso seco (DW–*Dry weight*) (Gamiely et al., 1991). La base de datos multitemporal de variables biofísicas del trigo está compuestas por un total de 72 entradas (8 muestreos x 9 puntos) que contienen valores de LAI, LCC, fCOVER, FW y DW. Por último, se acoplaron los valores de reflectividad de la superficie terrestre de las 10 bandas espectrales de S2 a 10 y 20 m de resolución espacial, obtenidos de las imágenes de S2 en nivel L2A, a la base de datos de medidas in situ. En el artículo de Caballero et al. (2022a) se brinda una explicación detallada del área de estudio, del diseño experimental, del manejo del cultivo de trigo, de las fechas de muestreo coincidentes con las adquisiciones de S2 y del procedimiento utilizado para la toma de medidas in situ de las variables biofísicas del trigo para la campaña 2020 del VBRC, así como también del cálculo de los valores de CCC y de VWC.

2.2. Esquema general metodológico

En esta sección se presentan los métodos utilizados para implementar los modelos de estimación de variables biofísicas del trigo a partir de datos ópticos de S2 (Sección 2.2.1), de datos SAR de S1 (Sección 2.2.2) y de la fusión de datos S1 & S2 (Sección 2.2.3). El esquema metodológico de trabajo se presenta en la Figura 2.1, donde pueden diferenciarse cuatro bloques conceptuales. En primer lugar, la recolección en campo de variables biofísicas del trigo en la zona de estudio (ver Sección 2.1.4) y posterior procesamiento de la base de datos de medidas in situ y la construcción de una base de datos de espectros simulados utilizando un RTM acoplado. En segundo lugar, el desarrollo de un enfoque híbrido basado en un RTM acoplado, Gaussian process, medidas in situ y datos ópticos de S2 para la obtención de modelos de estimación de LAI, CCC y VWC del cultivo de trigo. En tercer lugar, la estimación del LAI del trigo de invierno basada en datos SAR de S1 adquiridos en diferentes geometrías de observación, Gaussian process y medidas in situ. Por último, la implementación de un modelo de reconstrucción de series temporales de VWC basado en la fusión de datos S1 & S2.

2.2.1 Modelos de estimación de variables biofísicas del trigo basados en datos multiespectrales de Sentinel–2

Con el objetivo de desarrollar modelos híbridos optimizados de estimación de variables biofísicas del trigo, el punto de partida del flujo de trabajo fue la simulación de una base de datos de entrenamiento. Para el desarrollo de la base de datos de espectros de reflectividad simulados se utilizó un RTM acoplado basado en los modelos PROSPECT–PRO (Féret et al., 2021) y 4SAIL (Verhoef and Bach, 2007). El RTM acoplado PROSAIL-PRO fue utilizado para simular la reflectividad bidireccional de la vegetación en función de diversas variables bioquímicas de las hojas como por ejemplo: contenido de clorofila (C_{ab}), contenido de proteína (C_p), carotenoides (C_{xc}) o contenido de agua (C_w) y variables biofísicas de las plantas como el LAI y el ángulo medio de inclinación de las hojas (ALIA–*average leaf inclination*

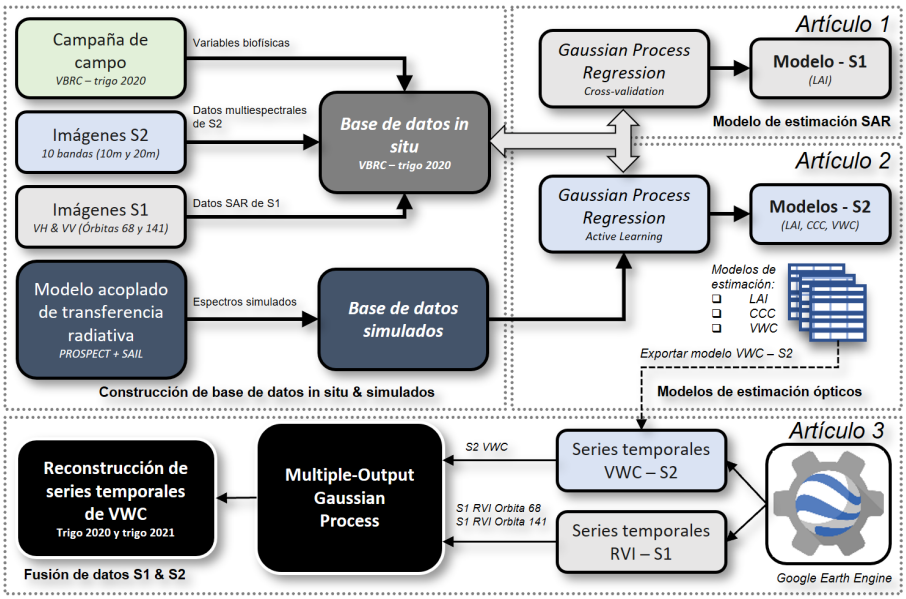

Figura 2.1: Esquema metodológico del trabajo

angle) entre otros. Se generó una base de datos sintética de 1000 espectros de reflectividad bidireccional (usando la configuración espectral de las 10 bandas de S2 a 10 y 20 m de resolución espacial) de la cubierta vegetal. Los parámetros bioquímicos y biofísicos de entrada del modelo acoplado PROSAIL–PRO se configuraron tomando como referencia los valores utilizados por otros autores (Berger et al., 2020b, Danner et al., 2019, Estévez et al., 2021). Con la finalidad de reducir la dimensión de la base de datos simulados y de obtener un conjunto óptimo de datos para entrenar los modelos de estimación de variables biofísicas del trigo, se utilizó una estrategia de aprendizaje activo (AL–*active learning*) (Verrelst et al., 2016). AL realiza el muestreo y evaluación del conjunto de datos de entrada de forma iterativa a través de un proceso inteligente (Berger et al., 2021). Para cuantificar las disimilitudes en el conjunto de datos de entrenamiento se empleó un algoritmo basado en la distancia euclídea (EBD–*euclidean distance-based diversity*). Para obtener los modelos de estimación de variables biofísicas del trigo (LAI, CCC y VWC) se entrenaron modelos de Gaussian process

regression utilizando las bases de datos de espectros de reflectividad de la cubierta vegetal simulados y de medidas in situ, relacionadas a la reflectividad de la superficie observada por S2 en el punto de muestreo específico, correspondientes a la campaña de trigo 2020. Se realizaron 1000 iteraciones para entrenar los modelos de GPR. Cada muestra de la base de datos de espectros simulados fue comparada utilizando AL–EBD, contra el conjunto de datos de medidas in situ y espectros de reflectividad de S2. Esta estrategia plantea una alternativa eficiente para reducir la dimensión del espacio muestral, ya que cuando el valor del error cuadrático medio (RMSE–*root mean square error*) de GPR disminuye, la muestra analizada es agregada al subconjunto optimizado de datos de entrenamiento (Verrelst et al., 2016, 2021). Posteriormente se procedió a aplicar los modelos de LAI, CCC y VWC a una serie temporal de 15 imágenes libres de nubes de S2 (nivel L2A) sobre la zona de estudio. Por último, se analizó la evolución temporal de las variables biofísicas estimadas y su correspondencia con la fenología del cultivo y con los datos medidos in situ para la campaña de trigo 2020 del VBRC. En el artículo de Caballero et al. (2022a) se brinda una explicación detallada de la metodología híbrida utilizada para desarrollar los modelos de estimación de las variables biofísicas LAI, CCC y VWC del trigo de invierno basados en datos multiespectrales de S2 y medidas in situ.

2.2.2 Modelo de estimación de LAI del trigo basado en datos radar de Sentinel–1 adquiridos en múltiples ángulos de observación

La estrategia de observación de la constelación Sentinel–1 define la adquisición en modo descendente sobre la región de estudio. Dos órbitas relativas (órbitas 141 y 68) se encuentran disponibles para la zona priorizada de cultivos del VBRC, lo cual permite monitorear el desarrollo de las plantas de trigo con diferentes ángulos de incidencia local. Para la órbita 141 se cuenta con datos de S1-A adquiridos a un ángulo de incidencia local medio de 33º, mientras que para la órbita 68, tanto S1-A como S1-B, adquieren imágenes de la región de estudio con un ángulo de incidencia local medio de 43º. Debido a que la estructura tridimensional de la vegetación, observada por un sensor radar, modifica la amplitud del coeficiente de retrodisper-

sión en banda C, la geometría de adquisición juega un papel determinante en el desarrollo de modelos de estimación de variables biofísicas del trigo basados en datos SAR. Con la finalidad de explotar la información multitemporal de S1 adquirida en distintos ángulos de incidencia local para la estimación de LAI del trigo, se planteó una estrategia basada en GPR para fusionar los datos SAR provenientes de distintas órbitas descendentes de adquisición. Se utilizaron imágenes de S1 de modo interferométrico enfocadas y proyectadas sobre el terreno (GRD–*ground range detected*) que fueron procesadas aplicando una cadena de procesamiento estándar (En el artículo de Caballero et al. (2022b) se brinda una revisión detallada de la cadena de procesamiento implementada para preprocesar las imágenes de S1) (aplicar datos de órbita, eliminar el ruido térmico electrónico, calibración radiométrica, filtrado de speckle y proyección sobre el terreno) para obtener valores de coeficiente de retrodispersión calibrados y normalizados sobre el área de estudio (Filipponi, 2019). Buscando maximizar la respuesta del modelo de LAI para trigo basado en datos SAR de S1, se acotó la base de datos de medidas in situ entre el 3 de septiembre y el 2 de noviembre de 2020, período que se corresponde con las etapas de desarrollo vegetativo del cultivo en la región de estudio. Se realizaron diferentes ensayos para encontrar el modelo de LAI que mejor se ajustara a los datos de campo. En primer lugar, se entrenaron modelos de GPR con los datos polarimétricos (VH & VV) de S1–A y S1–B adquiridos en diferentes geometrías de observación correspondientes a las órbitas 68 y 141 sobre la región de estudio y VBV tomadas in situ del cultivo de trigo. Se obtuvieron tres modelos de LAI basados en datos de S1 (LAI–S1): (1) modelo de LAI para datos de S1 adquiridos en la órbita 141; (2) modelo de LAI para los datos de S1 correspondientes a la órbita 68; y (3) modelo de LAI para los datos de S1 adquiridos en ambas órbitas 68 y 141. El comportamiento de los modelos de LAI–S1 fue evaluado utilizando diversas métricas de bondad de ajuste: el coeficiente de determinación (R^2), el error medio absoluto (MAE–*mean absolute error*), el RMSE y el error cuadrático medio normalizado (NRMSE–*normalized root mean square error*). Para el segundo grupo de pruebas se aplicó el interpolador de Whittaker (Whittaker, 1922) a las series temporales de datos SAR de S1 adquiridas en ambas geometrías de observación. De esta manera, se obtuvieron valores de coeficiente de retrodispersión en banda C

para ambas polarizaciones (VH & VV) con resolución temporal de 1 día. Se evaluaron entonces 3 modelos de LAI basados en datos SAR interpolados de S1 de acuerdo con las geometrías de observación provistas por las órbitas relativas 68 y 141 y por la fusión de ambas fuentes de datos. Por último se aplicó una estrategia de validación cruzada (CV–*cross–validation*) (Snee, 1977) para entrenar los algoritmos de estimación de LAI basados en GPR, datos SAR de S1 y medidas in situ del trigo. El modelo de mayor precisión en términos del NRMSE, fue aplicado a una serie temporal de productos preprocesados de S1 con la finalidad de demostrar la capacidad de la tecnología radar en banda C para monitorear la distribución espaciotemporal de los cultivos de trigo en la zona de estudio. En el artículo de Caballero et al. (2022b) se brinda una explicación detallada de la metodología utilizada para desarrollar el modelo de estimación de LAI del trigo de invierno basados en datos radiométricos de S1 adquiridos en ángulos de incidencia local diferentes y medidas in situ.

2.2.3 Reconstrucción de series temporales del contenido de agua del trigo basada en la sinergia de Sentinel–1 & Sentinel–2

Para implementar un modelo de fusión de datos SAR de S1 y ópticos de S2 capaz de reconstruir series temporales de VWC del trigo, se exploraron 4 algoritmos de multiple-output Gaussian process: i) spectral mixture kernels for multiple-output Gaussian processes (MOSM) (Parra and Tobar, 2017), ii) cross-spectral mixture (CSM) (Ulrich et al., 2015), iii) linear model of coregionalization (LMC) (Álvarez et al., 2012, Goovaerts and Goovaerts, 1997), y iv) convolutional model (CONV) (Alvarez and Lawrence, 2008, van der Wilk et al., 2017) con distintas configuraciones de entrada (Para una revisión detallada de la parametrización de los modelos de MOGP consulte el artículo de Caballero et al. (2023)). Los modelos de MOGP utilizados analizan la similitud, en términos de correlación cruzada, de las señales de entrada en el dominio de la frecuencia. En primer lugar se estudió la correlación entre el índice de vegetación radar, derivado de datos SAR de S1, y el contenido de agua de la vegetación, estimado a partir de datos multiespectrales de S2 con el modelo de VWC desarrollado por Caballero

et al. (2022a). Para acceder a los catálogos de S1 y de S2 de forma expeditiva se abordó una estrategia de procesamiento en la nube utilizando la plataforma Google Earth Engine (GEE). GEE posibilita el análisis y visualización de datos geoespaciales a escala global poniendo a disposición de los usuarios un catálogo con petabytes de imágenes de los satélites más utilizados para propósitos de EO. El modelo de VWC desarrollado por Caballero et al. (2022a) fue adaptado para que fuese escalable en el entorno provisto por GEE siguiendo la metodología propuesta por Pipia et al. (2021). Para construir series temporales de RVI se utilizaron las órbitas 68 y 141 de S1 que permiten la observación de la zona de cultivo de trigo desde diferentes ángulos de incidencia local (ver Sección 2.2.2). Los modelos de MOGP fueron entrenados con tres canales de datos: i) VWC–S2 (canal–1), ii) RVI–S1 órbita 68 (canal–2) y iii) RVI–S1 órbita 141 (canal–3). Para la evaluación de los modelos de MOGP se seleccionaron dos regiones de interés (ROI–*region of interest*) ubicadas en la zona de estudio y se calculó el valor promedio de VWC–S2 y de RVI–S1 a lo largo de una serie temporal de 3 años aproximadamente. La ROI-1 (superficie: 1.2 ha) pertenece a un lote de trigo de la campaña de cultivos 2020, mientras que la ROI-2 (superficie: 1.56 ha) corresponde a un campo de trigo de la campaña 2021. Con la finalidad de evaluar la capacidad de los modelos de MOGP para fusionar datos de S1 & S2, se evaluaron las siguientes métricas: el RMSE, el NRMSE, el MAE, el error de porcentaje medio absoluto (MAPE–*mean absolute percentage error*) y el tiempo de entrenamiento. En función de la posible combinación de entradas de datos de S1 & S2, se evaluaron tres escenarios de entrenamiento para cada ROI por cada modelo de MOGP: i) RVI–$S1_{\text{órbita 68}}$ & VWC–S2, ii) RVI–$S1_{\text{órbita 141}}$ & VWC–S2 y iii) RVI–$S1_{\text{órbita 68}}$ & RVI–$S1_{\text{órbita 141}}$ & VWC–S2. El modelo que presentó los mejores resultados en términos de precisión de las predicciones para ambas ROIs fue aplicado en dos regiones de mayores dimensiones, pertenecientes a las campañas de cultivo 2020 y 2021 del VBRC, con el objetivo de reconstruir espaciotemporalmente valores de VWC, a nivel de píxel, basados en la sinergia de S1 & S2. En el artículo de Caballero et al. (2023) se brinda una explicación detallada de la metodología utilizada para reconstruir series temporales de VWC del trigo de invierno mediante la fusión S1 & S2.

CAPÍTULO 3

RESULTADOS Y DISCUSIÓN

3.1. Preámbulo

Los resultados que se presentan en esta sección constituyen un resumen de los principales hallazgos alcanzados durante el desarrollo de los artículos que componen esta tesis doctoral. El Artículo 1 **(Caballero et al., 2022a)**, en primer lugar, presenta el desarrollo de modelos de estimación de LAI, CCC y VWC para el cultivo de trigo basados en la implementación de un enfoque híbrido que combina un modelo acoplado de transferencia radiativa, datos multiespectrales de S2, medidas in situ de la vegetación y Gaussian process regression. En segundo lugar, el Artículo 2 **(Caballero et al., 2022b)** aborda una estrategia de estimación del índice de área foliar basada en adquisiciones de S1 en diferentes ángulos de observación y medidas biofísicas del trigo medidas en campo y, finalmente, el Artículo 3 **(Caballero et al., 2023)** explota la sinergia de series temporales de S1 & S2 para la reconstrucción de mapas de contenido de agua de las plantas de trigo de invierno utilizando algoritmos de MOGP. Los artículos que componen esta tesis doctoral se encuentran anexados al final de este documento.

3.2. Artículo 1. Modelos de estimación de variables biofísical del trigo con datos multiespectrales de Sentinel–2

3.2.1 Contexto

Los resultados que se presentan en esta sección de la tesis doctoral constituyen un resumen de los principales hallazgos publicados en el siguiente artículo:

- **Caballero, G., Pezzola, A., Winschel, C., Casella, A., Sanchez Angonova, P., Berger, K., Rivera-Caicedo, J. P., Verrelst, J., and Delegido, J. (2022a). Seasonal Mapping of Irrigated Winter Wheat Traits in Argentina with a Hybrid Retrieval Workflow Using Sentinel-2 Imagery.** ***Remote Sens.*****, 14(18):4531**

3.2.2 Antecedentes

Como complemento de la investigación realizada durante el período doctoral en materia de desarrollo de modelos de estimación de variables biofísicas de la vegetación con datos multiespectrales de Sentinel–2, se destaca a modo de antecedente, la siguiente publicación:

- Casella, A., Orden, L., Pezzola, N. A., Bellaccomo, C., Winschel, C. I., Caballero, G. R., Delegido, J., Gracia, L. M. N., and Verrelst, J. (2022). Analysis of Biophysical Variables in an Onion Crop (Allium cepa L.) with Nitrogen Fertilization by Sentinel-2 Observations. *Agronomy*, 12(8):1884

3.2.3 Justificación y aportaciones

El primer paso del desarrollo de esta tesis doctoral ha sido la implementación de modelos híbridos de estimación de variables biofísicas de la vegetación basados en datos multiespectrales de Sentinel–2. En los últimos años, se han desarrollado numerosas investigaciones que abordan la temática planteada (ver Sección 1.1), sin embargo, aún existe la necesidad de probar y adaptar métodos híbridos bajo condiciones ambientales diversas, en diferentes regiones geográficas y sobre distintos tipos de cultivos. Las características ambientales de la región de estudio (ver Sección 2.1.1), las propiedades fisiológicas del trigo irrigado (ver Sección 2.1.2), el manejo característico del cultivo en el valle Bonaerense del río Colorado (ver Sección 2.1.3) y la multitemporalidad de la base de datos de VBV medidas in situ (ver Sección 2.1.4), constituyen la originalidad de la investigación abordada. Con la finalidad de explotar la capacidad de los datos del sensor óptico de S2, el primer artículo que compone esta tesis doctoral **(Caballero et al., 2022a)**, plantea un enfoque híbrido que permite desarrollar modelos de estimación de LAI, CCC y VWC del trigo de invierno en una región de cultivo intensivo ubicada al sureste de Argentina. Sin lugar a dudas el concepto de VWC utilizado en esta tesis, que tiene en cuenta la cantidad de agua disponible en todos los órganos de las plantas, representa un claro diferenciador. Los valores de VWC de las plantas de trigo, fueron calculados teniendo en cuenta la diferencia entre el peso húmedo y el peso seco de la vegetación en g m^{-2} tras referir esta diferencia a la superficie del área de la vegetación cosechada y multiplicando el resultado por el valor del fCOVER medido in situ. En el trabajo de Pasqualotto et al. (2018), se definieron dos nuevos índices para estimar el contenido de agua de la cubierta vegetal (CWC–*canopy water content*) de zonas de cultivo heterogéneas. Los autores encontraron que la precisión de las estimaciones realizadas con estos índices disminuye para cultivos cuya fracción de cobertura vegetal es menor al 30 %, y pusieron en relevancia la contribución del suelo al extrapolar el contenido de agua de las hojas al nivel de la cubierta vegetal. En las etapas tempranas de desarrollo del cultivo de trigo la contribución del suelo desnudo en cada píxel observado por S2 es predominante, razón por la cual, resulta particularmente conveniente incorporar el valor del fCOVER

medido in situ para determinar el contenido de agua de las plantas.

3.2.4 Base de datos multitemporal de variables biofísicas del trigo medidas in situ

El diseño de una metodología de medición in situ de variables biofísicas del trigo condujo a la obtención de una base de datos de campo multitemporal. La base de datos de medidas in situ cubre diferentes estados vegetativos de las plantas de trigo. Si bien el proceso de recolección de medidas in situ fue realizado siguiendo un protocolo específicamente diseñado para tal fin, el error de los instrumentos y métodos utilizados no fueron considerados al evaluar la precisión global de los modelos de estimación de VBV desarrollados. Trabajos futuros deberían incorporar el error de las medidas de campo. Debido a las condiciones edafoclimáticas de la región de estudio (ver Sección 2.1.1), la variación temporal del fCOVER del trigo medido in situ manifiesta un comportamiento particular. Desde la emergencia de las plántulas hasta la etapa de macollaje el fCOVER aumenta de forma constante, siguiendo la curva fenológica característica de este cultivo, sin embargo cuando el trigo llega a la etapa de antesis, el valor del fCOVER disminuye considerablemente debido a que las plantas de trigo presentan un cambio estructural significativo. Este ha sido el principal hallazgo en relación con la obtención de la base de datos de VBV medidas in situ del cultivo de trigo en el VBRC. Asimismo, los valores de LAI del trigo tomados in situ se correlacionan con los efectos producidos por las fertilizaciones y los riegos posteriormente realizados para fijar la Urea (N) granulada. Las medidas de campo en este sentido permiten inferir cómo ha sido el manejo del cultivo en la región de estudio gracias a que las fechas de muestreo de la campaña de trigo 2020 fueron definidas en función de los cambios que se producen durante la fase de desarrollo de las plantas.

3.2.5 Modelos de estimación de variables biofísicas del trigo basados en datos ópticos de Sentinel–2

Con el propósito de optimizar el conjunto de datos de entrenamiento de espectros de reflectividad simulados para el cultivo de trigo, se realizó una exploración intensiva de la parametrización del modelo acoplado PROSAIL-PRO. El valor del espesor equivalente de agua de las hojas (EWT–*Leaf equivalent water thickness*) mostró ser un parámetro determinante, no solo de la capacidad de predicción del modelo de VWC, sino también de la precisión de las estimaciones obtenidas de los modelos de LAI y CCC. Esto se debe mayoritariamente a que el EWT tiene en cuenta el contenido de agua relacionado con el área foliar, mientras que las muestras tomadas in situ, incluyen además tallos, flores y frutos de las plantas de trigo. Se realizaron múltiples ensayos para determinar el rango óptimo de valores de EWT resultando el intervalo más conveniente: 0.0002–0.05 g cm^{-2}. Los modelos de estimación de las VBV fueron validados con los datos de campo medidos in situ de la campaña de trigo 2020 del VBRC. Se obtuvieron resultados de validación de alta precisión; LAI: R^2 = 0.92, RMSE = 0.43 m^2 m^{-2}, CCC: R^2 = 0.80, RMSE = 0.27 g m^{-2} y VWC: R^2 = 0.75, RMSE = 416 g m^{-2}. Gracias a que se utilizó la regresión de procesos Gaussianos para encontrar las relaciones no paramétricas entre las 10 bandas a 10 y 20 m de resolución espacial de S2 y las VBV de la base de datos optimizada de entrenamiento, fue posible construir mapas de la incertidumbre asociada a las estimaciones para cada una de las variables analizadas, lo cual representa una ventaja del esquema híbrido de estimación de VBV implementado. La información de incertidumbre de las estimaciones, puede ser usada para cuantificar el grado de portabilidad espaciotemporal de los modelos, lo cual resulta particularmente útil cuando éstos son aplicados sobre diferentes cultivos y agroambientes. Los modelos de LAI, CCC y VWC desarrollados fueron posteriormente aplicados a una serie temporal de 15 imágenes de S2. Fue posible reproducir la curva fenológica del cultivo de trigo y analizar los efectos del riego artificial y la fertilización en la etapa de desarrollo vegetativo de las plantas. El estudio se llevó a cabo analizando los datos de manejo del cultivo, la fase de desarrollo según la escala

de Zadoks[1], las VBV medidas in situ y los valores de LAI, CCC y VWC estimados por los modelos híbridos. Desde el punto de vista agronómico, el monitoreo de las VBV del trigo mediante modelos de estimación basados en datos multiespectrales de S2, proporciona información de alto valor agregado para realizar una gestión eficiente de los riegos y fertilizaciones que son factores determinantes del rendimiento de este cultivo.

[1] En Caballero et al. (2022a) se brinda un detalle exhaustivo de las fases de desarrollo del cultivo de trigo determinadas in situ según la escala de Zadoks.

3.3. Artículo 2. Cuantificación del LAI del trigo con datos SAR de Sentinel–1 adquiridos en diferentes geometrías de observación

3.3.1 Contexto

Los resultados que se presentan en esta sección de la tesis doctoral constituyen un resumen de los principales hallazgos publicados en el siguiente artículo:

- **Caballero, G., Pezzola, A., Winschel, C., Casella, A., Sanchez Angonova, P., Orden, L., Berger, K., Verrelst, J., and Delegido, J. (2022b). Quantifying Irrigated Winter Wheat LAI in Argentina Using Multiple Sentinel-1 Incidence Angles.** ***Remote Sens.*****, 14(22):5867**

3.3.2 Antecedentes

Como complemento de la investigación realizada durante el período doctoral en materia de procesamiento de imágenes SAR de Sentinel–1, se destacan a modo de antecedentes una publicación y dos comunicaciones enviadas a congresos:

- Caballero, G. R., Platzeck, G., Pezzola, A., Casella, A., Winschel, C., Silva, S. S., Ludueña, E., Pasqualotto, N., and Delegido, J. (2020). Assessment of Multi-Date Sentinel-1 Polarizations and GLCM Texture Features Capacity for Onion and Sunflower Classification in an Irrigated Valley: An Object Level Approach. *Agronomy*, 10(6):845
- Caballero, G., Pezzola, A., Casella, A. A., and Delegido, J. (2018b). Clasificación de cobertura de suelo para un valle irrigado a partir de series temporales de datos SAR en banda C con Sentinel-1. *XVIII Simposio Internacional en Percepción Remota y Sistemas de Información Geográfica (SELPER). 6-9 noviembre, 2018. La Habana, Cuba.*

- Ayala, J., Jara, C., Lozano, P., Van Wittenberghe, S., Verrelst, J., Caballero, G., and Delegido, J. (2022). Estimación del Carbono Orgánico del Suelo usando datos de Teledetección y SIG en dos Ecosistemas alto Andinos del Ecuador. *XX Simposio Internacional en Percepción Remota y Sistemas de Información Geográfica (SELPER).26-28 de octubre de 2022, Monterrey, Nuevo León, México.*

3.3.3 Justificación y aportaciones

En segundo lugar, en el marco de la presente tesis doctoral se planteó desarrollar una metodología para estimar el LAI del trigo a partir de datos SAR de Sentinel–1. El LAI además de ser un indicador directo del estado fisiológico de las plantas, es una variable biofísica de tipo estructural que permite escalar el contenido de agua y de clorofila de las hojas al nivel de la cubierta vegetal, lo cual cobra valor desde el punto de vista del manejo agronómico realizado sobre el cultivo de trigo (ver Sección 2.1.3). Múltiples estudios han explorado la interacción de la señal radar con la estructura tridimensional de las plantas de trigo (Kaplan et al., 2021, Mattia et al., 2003, Nasrallah et al., 2019, Ouaadi et al., 2021, Pipia et al., 2021, Vavlas et al., 2020). Cuando se trata de la viabilidad de generar mapas de variables biofísicas de la vegetación a partir de series temporales de S1, varios estudios experimentales han utilizado la amplitud del coeficiente de retrodispersión en banda C observado desde una única órbita relativa (Bousbih et al., 2017, Hosseini et al., 2015). Veloso et al. (2017), por ejemplo, utilizaron series temporales de datos SAR de Sentinel–1 para monitorear el ciclo fenológico de cultivos de verano (girasol, maíz y soja) y de cultivos de invierno (cebada, colza y trigo). Sin embargo, la variación de la retrodispersión radar observada desde distintos ángulos de incidencia local para el monitoreo de variables biofísicas de los cultivos no ha sido explorada en profundidad aún. Con la ambición de investigar la capacidad de los datos SAR del sensor radar en banda C de S1 para monitorear las VBV del trigo, el segundo artículo que compone esta tesis doctoral **(Caballero et al., 2022b)**, presenta un enfoque novedoso basado en observaciones de S1 realizadas en diferentes ángulos de incidencia local, para monitorear espaciotemporalmente el LAI del trigo de invierno en un valle irrigado. En este artículo se pone de manifiesto que las estimaciones de LAI basadas en datos SAR de S1 pueden dar soporte al monitoreo de cultivos en regiones agrícolas propensas a nubes, donde los modelos de estimación de variables biofísicas de la vegetación basados en datos ópticos multiespectrales se ven limitados por esta condición climática.

3.3.4 Modelo de estimación de LAI del trigo basado en datos de radar de apertura sintética de Sentinel–1

Los modelos de LAI fueron entrenados con datos SAR de S1 adquiridos en diferentes geometrías de observación. En relación al ángulo de incidencia local, se obtuvieron mejores resultados para el modelo de LAI del trigo entrenado con datos de S1 adquiridos desde la órbita descendente 68. Debido a que el valor medio del ángulo de incidencia local sobre la zona de estudio para la órbita descendente 68 es de 43º, aumenta el trayecto de la señal radar que atraviesa los cultivos de trigo lo cual maximiza la retrodispersión volumétrica proveniente de la vegetación y atenúa la contribución del suelo. Los datos SAR adquiridos desde la órbita 141 tienen un ángulo de incidencia local promedio de 33º, razón por la cual aumenta la retrodispersión superficial relacionada principalmente con la humedad y la rugosidad del suelo. Cuando se utilizaron los datos de ambas órbitas para entrenar el modelo de estimación de LAI se produjo un considerable aumento del valor del R^2 y una consistente disminución del RMSE. El proceso de interpolación de Whittaker permitió obtener series temporales de datos SAR en ambas polarizaciones (VH & VV) para las órbitas 68 y 141 con una resolución temporal de 1 día, lo cual derivó en una mejora significativa del rendimiento del modelo de LAI en términos de R^2 y de RMSE. Esto se fundamenta en el incremento de información de la estructura tridimensional de la vegetación que supone la observación del cultivo en diferentes geometrías de adquisición. El modelo de LAI basado en S1 fue validado con los datos de campo de la campaña de trigo 2020 del VBRC utilizando una estrategia de validación cruzada. Se obtuvo una fuerte correlación entre los valores estimados y medidos de LAI del trigo: $R^2 = 0.67$ y una aceptable precisión global media: RMSE = 0.88 m^2 m^{-2}. En el artículo de Caballero et al. (2022b) se proporciona un exhaustivo detalle de los resultados estadísticos obtenidos durante la fase de implementación de los modelos de LAI basados en datos SAR de S1. Posteriormente, el modelo entrenado se aplicó a una serie temporal de productos preprocesados de S1 y se generaron mapas de LAI multitemporales que reflejaron adecuadamente el ciclo de crecimiento del cultivo del trigo. El modelo de LAI–S1 mostró ser sensible a los cambios estructurales de las plantas de trigo en la región de estudio. Otros factores

como el contenido de agua de la vegetación y la humedad del suelo tienen influencia sobre el valor del coeficiente de retrodispersión en banda C observado por S1. En la etapa de senescencia, el contenido de humedad de las plantas de trigo disminuye hasta alcanzar el estado de grano maduro. Las plantas se encuentran completamente secas, sin embargo, permanecen de pie y la estructura tridimensional de la vegetación remanente representa una sección transversal radar (RCS–*radar cross section)* perceptible a la señal SAR de S1. A diferencia de los modelos ópticos de estimación de LAI, que son capaces de detectar el cambio de coloración y pigmentación de la vegetación que ocurre en la etapa de senescencia, el modelo desarrollado basado en datos SAR resultó más adecuado para estimar el LAI total de la vegetación compuesto por el área foliar de las hojas fotosintéticamente activas y senescentes referido a unidades de superficie. La orientación espacial de las hileras del cultivo de trigo en las etapas tempranas de desarrollo, demostró ser un factor determinante para el modelo de estimación de LAI basado en datos de S1. Desde la emergencia de las plántulas hasta los primeros estadíos de la etapa de macollaje el suelo no está completamente cubierto de vegetación y la retrodispersión superficial es gobernada por la humedad y rugosidad del suelo que varía de un lote de cultivo a otro y depende además de la geometría de adquisición de S1.

3.4. Artículo 3. Sinergia de S1 & S2 para la reconstrucción de series temporales de VWC del trigo

3.4.1 Contexto

Los resultados que se presentan en esta sección de la tesis doctoral constituyen un resumen de los principales hallazgos publicados en el siguiente artículo:

- **Caballero, G., Pezzola, A., Winschel, C., Sanchez Angonova, P., Casella, A., Orden, L., Salinero-Delgado, M., Reyes-Muñoz, P., Berger, K., Delegido, J., and Verrelst, J. (2023). Synergy of Sentinel-1 and Sentinel-2 Time Series for Cloud-Free Vegetation Water Content Mapping with Multi-Output Gaussian Processes.** ***Remote Sens.*****, 15(7):1822**

3.4.2 Antecedentes

Como complemento de la investigación realizada durante el período doctoral en materia de fusión de datos SAR de Sentinel–1 y multiespectrales de Sentinel–2, se destacan a modo de antecedentes una comunicación enviada a congresos y una tesis de máster en Teledetección de la Universitat de València:

- Caballero, G., Delegido, J., and Verrelst, J. (2018a). Estimación del LAI de la vegetación a partir de la sinergia Sentinel 1 -Sentinel 2. *XVIII Simposio Internacional en Percepción Remota y Sistemas de Información Geográfica (SELPER). 6-9 noviembre, 2018. La Habana, Cuba.*
- Caballero, G. (2018). Estimación del LAI de la vegetación a partir de la sinergia Sentinel–1 & Sentinel–2. *Trabajo de fin de máster de la Universitat de Valencia. Octubre, 2018. Valencia, España.*

3.4.3 Justificación y aportaciones

El tercer estudio que compone esta tesis consistió en desarrollar una estrategia de fusión de datos SAR de Sentinel–1 y multiespectrales de Sentinel–2 para reconstruir series temporales de contenido de agua de la vegetación. La comunidad científica, dedicada al monitoreo de cultivos por medio de datos de observación de la Tierra, cuenta con una basta experiencia en el campo de la teledetección óptica. Numerosas investigaciones han utilizado los datos del sensor MSI a bordo de S2 para el desarrollo de modelos de estimación de VBV haciendo uso de diferentes metodologías (ver Sección 1.1). La desventaja de estos enfoques radica principalmente en que la teledetección óptica depende fuertemente de las condiciones climáticas, siendo inviable ante la presencia de nubes sobre las regiones particulares de estudio. Se han implementado regresiones no paramétricas de procesos Gaussianos para reconstruir series temporales de VBV estimadas a partir de datos de EO ópticos buscando mitigar esta limitación (Belda et al., 2020, Pipia et al., 2021). Sin embargo, en regiones de altas latitudes donde la persistencia de nubes imposibilita la adquisición de imágenes multiespectrales a lo largo del ciclo fenológico de los cultivos, ésta alternativa no representa una solución factible. El radar de apertura sintética de S1 ofrece nuevas oportunidades para abordar el desarrollo de modelos de estimación de VBV en regiones nubosas. Debido a que la longitud de onda de la señal electromagnética en banda C es mayor que el tamaño de las moléculas de vapor de agua, las nubes no alteran el valor de amplitud del coeficiente de retrodispersión radar de las imágenes de nivel GRD adquiridas por S1 en modo IWS. No obstante, dos consideraciones deben ser analizadas cuidadosamente: i) la interacción de la señal radar con la superficie terrestre es compleja y depende no solo de la estructura tridimensional y contenido de agua de la vegetación, sino también de la humedad y rugosidad del suelo y de la geometría de observación y ii) El ruido inherente de speckle, presente en las imágenes de radar, corrompe la información de la superficie terrestre observada dificultando la interpretación de la variabilidad espacial de las zonas de cultivos. En este contexto resulta imperioso explorar modelos de fusión de datos SAR y multiespectrales que se beneficien de las ventajas de ambos sistemas de EO. El tercer artículo que compone esta

tesis doctoral **(Caballero et al., 2023)**, presenta una metodología enfocada en regresiones de procesos Gaussianos de salida múltiple, para estimar el contenido de agua del trigo de invierno fusionando sinérgicamente series temporales del índice de vegetación radar de S1 y de un modelo óptico, presentado en Caballero et al. (2022a), basado en GPR, datos multiespectrales de S2 y VBV medidas in situ. El principal hallazgo del tercer apartado que compone esta tesis demuestra que la sinergia de series temporales de S1 & S2 puede ser usada para reconstruir mapas de contenido de agua del trigo en regiones nubosas de altas latitudes.

3.4.4 Modelos de fusión de datos de S1 & S2 basados en MOGP para la reconstrucción de series temporales de VWC del trigo

Las series temporales de RVI–S1 & VWC–S2 demostraron estar fuertemente correlacionadas sobre el área de estudio. Tanto para los lotes de trigo de la campaña 2020 (ROI–1) como para el lote de la campaña 2021 (ROI–2) del VBRC (ver la Figura 1 y la Tabla 1 en Caballero et al. (2023)), fue posible inferir tres ciclos fenológicos correspondientes a la rotación típica de cultivos de la zona de estudio (maíz–girasol–trigo), a partir del análisis multitemporal de los datos de S1 & S2. Del conjunto de algoritmos de MOGP utilizados para analizar la correlación de las señales en el dominio de la frecuencia, el modelo Gaussiano convolucional resultó ser el mejor en términos de precisión de fusión de datos. El modelo CONV utiliza el teorema de la convolución para modelar la correlación en el dominio de la frecuencia de los canales del conjunto de datos de S1 & S2. Se evaluaron modelos de fusión de dos y tres canales de entrada (canal–1: VWC–S2; canal–2: RVI–S1 órbita 68 y canal–3: RVI–S1 órbita 141). Al evaluar los modelos de dos canales de entrada (óptico + radar), se obtuvieron mejores resultados cuando se utilizaron datos de S1 correspondientes a la órbita 68, ya que para esta geometría de observación, la componente volumétrica de la retrodispersión radar es maximizada ($NRMSE_{\text{(S2\&S1–órbita 68)}}$ = 14.97 % ; $NRMSE_{\text{(S2\&S1–órbita 141)}}$ = 20.05 % para el ROI-1 y de la misma manera, $NRMSE_{\text{(S2\&S1–órbita 68)}}$ = 14.61 % ; $NRMSE_{\text{(S2\&S1–órbita 141)}}$ = 15.68 % para el ROI-2). La evaluación de los modelos de fusión de tres canales (óptico +

radar + radar) plantea los siguientes escenarios: i) la precisión del modelo CONV aumenta para el ROI–2 (trigo 2021) cuando se utiliza la información de ambas órbitas (68 y 141), $NRMSE_{(\text{S2\&S1–órbitas 68\&141})}$ = 10.1 % y; ii) la precisión del modelo CONV disminuye levemente para el ROI–1 (trigo 2020), $NRMSE_{(\text{S2\&S1–órbitas 68\&141})}$ = 16.1 %. Esto se debe a que la cantidad de imágenes disponibles de S2 difiere cada año y está definida por las condiciones climáticas del área de estudio. Además, las observaciones de S2 para ambos períodos, están desigualmente espaciadas en tiempo, razón por la cual, las series temporales VWC de S2 tienen espectros de frecuencia disímiles y el modelo CONV responde de forma diferente en cada caso. Con la finalidad de simular la presencia de nubes sobre la región de estudio, se eliminaron observaciones de S2 del conjunto de datos S1 & S2, correspondientes a dos ciclos fenológicos completos (campañas 2020 y 2021) del trigo de invierno desde septiembre hasta finales de diciembre, y se aplicó el modelo CONV a nivel de píxel para la reconstrucción espaciotemporal de mapas de contenido de agua del cultivo de trigo sobre dos regiones de mayores dimensiones del VBRC. La primera región de fusión de datos S1 & S2 contiene los lotes de trigo de la campaña de cultivos 2020, mientras que la segunda región, sobre la cual se aplicó el modelo CONV, contiene al lote de trigo de la campaña 2021. Tras implementar la estrategia de fusión de datos de S1 & S2 se logró recuperar con éxito el perfil temporal de la curva fenológica del trigo de invierno. Para cada fecha evaluada a lo largo de los ciclos fenológicos 2020 y 2021 se obtuvieron fuertes correlaciones entre los mapas de VWC obtenidos a partir de datos multiespectrales de S2 y el modelo de VWC presentado en Caballero et al. (2022a) y los reconstruidos a partir de la sinergia S1 & S2 ($\overline{R^2}_{trigo-2020}$ = 0.95, $\overline{R^2}_{trigo-2021}$ = 0.96). En el artículo de Caballero et al. (2023) se brinda una detallada revisión de los resultados de la fusión de datos de S1 & S2.

CAPÍTULO 4

CONCLUSIONES

Las principales conclusiones extraídas de los diferentes análisis realizados en esta tesis doctoral se resumen a continuación:

1. La planificación de los muestreos de campo, basada en realizar las medidas in situ en los momentos que se corresponden con los cambios fenológicos durante el desarrollo vegetativo de las plantas, resultó adecuada. Siguiendo la metodología de muestreo propuesta, se obtuvieron seis medidas de campo que reflejaron de forma representativa la fenología del trigo en la zona de estudio y permitieron analizar las relaciones causa–efecto de los riegos y las fertilizaciones realizados durante el manejo del cultivo.

2. Los valores de fCOVER del trigo medidos in situ reflejan un comportamiento temporal particular, que es atribuido a las condiciones edafoclimáticas de la región de estudio. El fCOVER aumenta constantemente desde la etapa de emergencia de las plántulas hasta la etapa de macollaje, sin embargo, cuando las plantas de trigo se encuentran en el estado de antesis, a mediados de octubre, el valor de fCOVER disminuye de forma repentina. Superada la etapa de antesis, las plantas de trigo manifiestan un cambio estructural que se ve reflejado en los valores de fCOVER medidos in situ, cercanos al 80 %.

3. La proporción de suelo desnudo, produce una variación de los valores de reflectividad espectral de las superficies cultivadas observadas por S2, e influye en mayor medida durante las etapas tempranas de desarrollo del trigo. Por este motivo, los valores de fCOVER deben ser tenidos en cuenta en el cálculo del contenido de agua de la vegetación.

4. La implementación de un enfoque híbrido para el desarrollo de los modelos de estimación de LAI, CCC y VWC del trigo, a partir de datos multiespectrales de S2, es una estrategia robusta para abordar el monitoreo de las VBV del trigo en la zona de estudio. La flexibilidad de parametrización del modelo de transferencia radiativa acoplado PROSAIL-PRO y al mismo tiempo la escalabilidad y velocidad computacional que proporciona Gaussian process, constituyen la principal fortaleza del enfoque híbrido implementado.

5. El valor del espesor equivalente de agua de las hojas es un parámetro determinante en la parametrización del modelo de transferencia radiativa acoplado PROSAIL-PRO. Debido a la relación directa entre el EWT y los valores de contenido de agua a nivel de la cubierta vegetal, el modelo híbrido de VWC resulta particularmente sensible a este parámetro. Para el caso del cultivo de trigo resulta conveniente configurar el RTM PROSAIL-PRO con valores de EWT comprendidos entre: 0.0002 y 0.05 g cm^{-2}.

6. El uso de GPR, como sólido algoritmo probabilístico de regresión, para encontrar las relaciones no paramétricas en el conjunto de datos de entrenamiento, proporciona la ventaja adicional de suministrar la incertidumbre de las estimaciones a nivel de píxel. Los mapas de incertidumbre ayudan a evaluar la fidelidad de los mapas de VBV del trigo y además permiten explorar la transferibilidad de los modelos a otras regiones dedicadas a la explotación intensiva de este cultivo.

7. Los modelos híbridos de estimación de las variables biofísicas del trigo se ajustaron con alta precisión a los datos de campo (LAI: R^2 = 0.92, RMSE = 0.43 m^2 m^{-2}, CCC: R^2 = 0.80, RMSE = 0.27 g m^{-2} y VWC: R^2 = 0.75, RMSE = 416 g m^{-2}.)

8. Los modelos de estimación de LAI, CCC y VWC del trigo aplicados a una serie temporal de 15 imágenes de S2, reproducen la curva fenológica del cultivo. La incertidumbre de las estimaciones es menor durante el desarrollo vegetativo de las plantas, de septiembre a noviembre. En la etapa de senescencia, de mediados de noviembre a fines de diciembre, la incertidumbre es mayor debido a que los modelos han sido entrenados con datos multitemporales medidos in situ que corresponden a la etapa de crecimiento y desarrollo de las plantas de trigo.

9. La combinación de datos SAR en banda C de S1 adquiridos en distintos geometrías de observación, ofrece nuevas oportunidades para el monitoreo de las regiones agrícolas. Especialmente, en áreas para las cuales se encuentran disponibles las órbitas ascendentes y descendentes de S1.

10. La amplitud del coeficiente de retrodispersión radar en banda C, presenta una fuerte dependencia con la estructura tridimensional de la vegetación y con el ángulo de incidencia local de la señal radar. Múltiples observaciones en distintas configuraciones geométricas conducen a un aumento de la información relacionada con el desarrollo vegetativo de las plantas de trigo y por lo tanto, pueden respaldar de manera eficiente la implementación de modelos de estimación de variables biofísicas del trigo particularmente en áreas agrícolas propensas a nubes como el valle Bonaerense del río Colorado.

11. Otros factores como el contenido de agua de la vegetación y la humedad del suelo tienen influencia sobre el valor del coeficiente de retrodispersión en banda C de S1, ya que modifican el valor de la constante dieléctrica de los elementos de dispersión que se encuentran en la celda de resolución de las superficies observadas. Estas variables deberán ser tenidas en cuenta en futuros estudios.

12. La variabilidad espacial de los mapas de LAI derivados a partir de datos SAR de S1 se ve afectada por el ruido inherente de speckle del sensor radar. De todos modos, es posible recuperar el perfil temporal del ciclo fenológico del trigo cuando el modelo de estimación de LAI es aplicado a una serie temporal de productos preprocesados de S1. Esta valiosa información puede dar soporte al análisis agronómico de la fenología del trigo de invierno en la región de estudio.

13. El modelo de estimación de LAI basado en datos de S1 presenta una fuerte correlación entre los valores estimados y medidos de LAI del trigo: R^2 = 0.67 y una aceptable precisión global media: RMSE = 0.88 m^2 m^{-2}. El modelo, es además sensible a los cambios estructurales de las plantas de trigo en la región de estudio.

14. La orientación espacial de las hileras del cultivo en las primeras etapas de desarrollo de las plantas de trigo, juega un papel determinante en la precisión del modelo de LAI basado en datos SAR de S1. Esto se debe a que la retrodispersión radar superficial es alterada en función de la rugosidad de las superficies observadas. Cuando las hileras del cultivo son perpendiculares a la señal radar la retrodisper-

sión es máxima debido a que los surcos realizados durante el laboreo de las tierras agrícolas incrementan la sección transversal radar. Por el contrario cuando las hileras se orientan en sentido longitudinal, la retrodispersión superficial es mínima y predomina la componente volumétrica proveniente de la vegetación.

15. Las imágenes ópticas de EO se ven afectadas por la presencia de nubes. El monitoreo de cultivos con esta tecnología se ve entonces restringido a diferentes momentos del ciclo fenológico, que no necesariamente aportan información relevante. Para analizar las relaciones causa-efecto de las prácticas agrícolas implementadas durante el manejo del cultivo, es necesario monitorear la evolución de las plantas de trigo en momentos clave a lo largo del ciclo fenológico.

16. Las series temporales del índice de vegetación radar derivado a partir de datos SAR de S1 en banda C y de VWC obtenidas a partir de datos multiespectrales de S2 están fuertemente correlacionadas cuando son analizadas sobre la región de estudio. Es posible reconocer los ciclos de los cultivos e interpretar la rotación: maíz–girasol–trigo, típica del VBRC.

17. Los modelos de MOGP pueden explotar la información de correlación cruzada, en el dominio de la frecuencia, entre las series temporales de datos SAR de S1 y ópticos de S2. Del conjunto de modelos de MOGP aplicados sobre la zona de estudio, el convolucional Gaussiano (CONV) resulta el más preciso, en términos de NRMSE, para reconstruir series temporales de VWC a partir de la fusión de datos de S1 & S2.

18. Las series temporales de RVI de S1 en distintas geometrías de adquisición pueden ser utilizadas para complementar la información provista por el sensor óptico de S2. Los esquemas multicanal pueden ser extrapolados a otras aplicaciones y sensores de EO. Los modelos de MOGP resultan además propicios para la fusión de datos provenientes de distintas fuentes de información, como datos medidos in situ, datos multiespectrales y datos radar.

19. La sinergia de series temporales de datos SAR de S1 y multiespectrales de S2 propone una prometedora alternativa para monitorear las zonas agrícolas, incluso en presencia de nubosidad persistente.

20. El mapeo sistemático de las variables biofísicas del trigo como el LAI, el CCC y el VWC mediante datos multiespectrales de S2, datos SAR de S1 o datos fusionados de S1 & S2, ofrece nuevas oportunidades para monitorear la variabilidad espacial y temporal del desarrollo del trigo en el Valle Bonaerense del Río Colorado.

21. Gracias al uso de GPR como algoritmo de aprendizaje automático, los modelos implementados de estimación de variables biofísicas del trigo, basados en datos de S1, de S2 y de S1 & S2 y ajustado para datos de campo del VBRC, pueden ser extrapolados a otros agroambientes, con la finalidad de gestionar la producción agrícola de forma sostenible y garantizar así la seguridad alimentaria.

Bibliografía

Álvarez, M. A., Rosasco, L., and Lawrence, N. D. (2012). Kernels for Vector-Valued Functions: A Review. *MAL*, 4(3):195–266.

Abdelbaki, A. and Udelhoven, T. (2022). A Review of Hybrid Approaches for Quantitative Assessment of Crop Traits Using Optical Remote Sensing: Research Trends and Future Directions. *Remote Sens.*, 14(15):3515.

Acevedo, M., Zurn, J. D., Molero, G., Singh, P., He, X., Aoun, M., Juliana, P., Bockleman, H., Bonman, M., El-Sohl, M., Amri, A., Coffman, R., and McCandless, L. (2018). The role of wheat in global food security. In *Agricultural Development and Sustainable Intensification*, pages 81–110. Routledge, New York, NY, USA.

Adeluyi, O., Harris, A., Verrelst, J., Foster, T., and Clay, G. D. (2021). Estimating the phenological dynamics of irrigated rice leaf area index using the combination of PROSAIL and Gaussian Process Regression. *Int. J. Appl. Earth Obs. Geoinf.*, 102:102454.

Agamennoni, R., Matarazzo, R., and Rivas, J. (1996). Producción de trigo bajo riego. *Boletín de Divulgación, EEA Hilario Ascasubi*, pages 10–16.

Alvarez, M. and Lawrence, N. (2008). Sparse Convolved Gaussian Processes for Multi-output Regression. *Advances in Neural Information Processing Systems*, 21.

Alvarez Prado, S., Gallardo, J. M., Serrago, R. A., Kruk, B. C., and Miralles, D. J. (2013). Comparative behavior of wheat and barley associated with field release and grain weight determination. *Field Crops Research*, 144:28–33.

Amin, E., Verrelst, J., Rivera-Caicedo, J. P., Pipia, L., Ruiz-Verdú, A., and Moreno, J. (2021). Prototyping Sentinel-2 green LAI and brown LAI products for cropland monitoring. *Remote Sens. Environ.*, 255:112168.

Atzberger, C., Guérif, M., Baret, F., and Werner, W. (2010). Comparative analysis of three chemometric techniques for the spectroradiometric assessment of canopy chlorophyll content in winter wheat. *Computers and electronics in agriculture*, 73(2):165–173.

Avtar, R., Aggarwal, R., Kharrazi, A., Kumar, P., and Kurniawan, T. A. (2020). Utilizing geospatial information to implement SDGs and monitor their Progress. *Environ. Monit. Assess.*, 192(1):1–21.

Ayala, J., Jara, C., Lozano, P., Van Wittenberghe, S., Verrelst, J., Caballero, G., and Delegido, J. (2022). Estimación del Carbono Orgánico del Suelo usando datos de Teledetección y SIG en dos Ecosistemas alto Andinos del Ecuador. *XX Simposio Internacional en Percepción Remota y Sistemas de Información Geográfica (SELPER).26-28 de octubre de 2022, Monterrey, Nuevo León, México.*

Baret, F., Houles, V., and Guérif, M. (2007). Quantification of plant stress using remote sensing observations and crop models: the case of nitrogen management. *Journal of Experimental Botany*, 58(4):869–880.

Baret, F., Weiss, M., Lacaze, R., Camacho, F., Makhmara, H., Pacholcyzk, P., and Smets, B. (2013). GEOV1: LAI and FAPAR essential climate variables and FCOVER global time series capitalizing over existing products. Part1: Principles of development and production. *Remote Sens. Environ.*, 137:299–309.

Belda, S., Pipia, L., Morcillo-Pallarés, P., and Verrelst, J. (2020). Optimizing Gaussian Process Regression for Image Time Series Gap-Filling and Crop Monitoring. *Agronomy*, 10(5):618.

Belete, F., Dechassa, N., Molla, A., and Tana, T. (2018). Effect of nitrogen fertilizer rates on grain yield and nitrogen uptake and use efficiency of bread wheat (Triticum aestivum L.) varieties on the Vertisols of central highlands of Ethiopia. *Agric. Food Secur.*, 7(1):1–12.

Berger, K., Rivera-Caicedo, J., Martino, L., Wocher, M., Hank, T., and Verrelst, J. (2021). A survey of active learning for quantifying vegetation traits from terrestrial earth observation data. *Remote Sensing*, accepted:...

Berger, K., Verrelst, J., Féret, J.-B., Wang, Z., Wocher, M., Strathmann, M.,

Danner, M., Mauser, W., and Hank, T. (2020a). Crop nitrogen monitoring: Recent progress and principal developments in the context of imaging spectroscopy missions. *Remote Sens. Environ.*, 242:111758.

Berger, K., Verrelst, J., Féret, J.-B., Hank, T., Wocher, M., Mauser, W., and Camps-Valls, G. (2020b). Retrieval of aboveground crop nitrogen content with a hybrid machine learning method. *International Journal of Applied Earth Observation and Geoinformation*, 92:102174.

Bousbih, S., Zribi, M., Lili-Chabaane, Z., Baghdadi, N., El Hajj, M., Gao, Q., and Mougenot, B. (2017). Potential of Sentinel-1 Radar Data for the Assessment of Soil and Cereal Cover Parameters. *Sensors*, 17(11):2617.

Brede, B., Verrelst, J., Gastellu-Etchegorry, J.-P., Clevers, J. G., Goudzwaard, L., den Ouden, J., Verbesselt, J., and Herold, M. (2020). Assessment of workflow feature selection on forest LAI prediction with sentinel-2A MSI, landsat 7 ETM+ and Landsat 8 OLI. *Remote Sensing*, 12(6):915.

Broge, N. H. and Leblanc, E. (2001). Comparing prediction power and stability of broadband and hyperspectral vegetation indices for estimation of green leaf area index and canopy chlorophyll density. *Remote Sens. Environ.*, 76(2):156–172.

Caballero, G. (2018). Estimación del LAI de la vegetación a partir de la sinergia Sentinel–1 & Sentinel–2. *Trabajo de fin de máster de la Universitat de Valencia. Octubre, 2018. Valencia, España.*

Caballero, G., Delegido, J., and Verrelst, J. (2018a). Estimación del LAI de la vegetación a partir de la sinergia Sentinel 1 -Sentinel 2. *XVIII Simposio Internacional en Percepción Remota y Sistemas de Información Geográfica (SELPER). 6-9 noviembre, 2018. La Habana, Cuba.*

Caballero, G., Pezzola, A., Casella, A. A., and Delegido, J. (2018b). Clasificación de cobertura de suelo para un valle irrigado a partir de series temporales de datos SAR en banda C con Sentinel-1. *XVIII Simposio Internacional en Percepción Remota y Sistemas de Información Geográfica (SELPER). 6-9 noviembre, 2018. La Habana, Cuba.*

Caballero, G., Pezzola, A., Winschel, C., Casella, A., Sanchez Angonova, P., Berger, K., Rivera-Caicedo, J. P., Verrelst, J., and Delegido, J. (2022a).

Seasonal Mapping of Irrigated Winter Wheat Traits in Argentina with a Hybrid Retrieval Workflow Using Sentinel-2 Imagery. *Remote Sens.*, 14(18):4531.

Caballero, G., Pezzola, A., Winschel, C., Casella, A., Sanchez Angonova, P., Orden, L., Berger, K., Verrelst, J., and Delegido, J. (2022b). Quantifying Irrigated Winter Wheat LAI in Argentina Using Multiple Sentinel-1 Incidence Angles. *Remote Sens.*, 14(22):5867.

Caballero, G., Pezzola, A., Winschel, C., Sanchez Angonova, P., Casella, A., Orden, L., Salinero-Delgado, M., Reyes-Muñoz, P., Berger, K., Delegido, J., and Verrelst, J. (2023). Synergy of Sentinel-1 and Sentinel-2 Time Series for Cloud-Free Vegetation Water Content Mapping with Multi-Output Gaussian Processes. *Remote Sens.*, 15(7):1822.

Caballero, G. R., Platzeck, G., Pezzola, A., Casella, A., Winschel, C., Silva, S. S., Ludueña, E., Pasqualotto, N., and Delegido, J. (2020). Assessment of Multi-Date Sentinel-1 Polarizations and GLCM Texture Features Capacity for Onion and Sunflower Classification in an Irrigated Valley: An Object Level Approach. *Agronomy*, 10(6):845.

Camps-Valls, G., Verrelst, J., Munoz-Mari, J., Laparra, V., Mateo-Jimenez, F., and Gomez-Dans, J. (2016). A survey on gaussian processes for earth-observation data analysis: A comprehensive investigation. *IEEE Geoscience and Remote Sensing Magazine*, 4(2):58–78.

Casella, A., Orden, L., Pezzola, N. A., Bellaccomo, C., Winschel, C. I., Caballero, G. R., Delegido, J., Gracia, L. M. N., and Verrelst, J. (2022). Analysis of Biophysical Variables in an Onion Crop (Allium cepa L.) with Nitrogen Fertilization by Sentinel-2 Observations. *Agronomy*, 12(8):1884.

Cavalaris, C., Megoudi, S., Maxouri, M., Anatolitis, K., Sifakis, M., Levizou, E., and Kyparissis, A. (2021). Modeling of Durum Wheat Yield Based on Sentinel-2 Imagery. *Agronomy*, 11(8):1486.

Clevers, J. G. P. W., Kooistra, L., and Schaepman, M. E. (2010). Estimating canopy water content using hyperspectral remote sensing data. *Int. J. Appl. Earth Obs. Geoinf.*, 12(2):119–125.

Confalonieri, R., Foi, M., Casa, R., Aquaro, S., Tona, E., Peterle, M., Boldi-

ni, A., De Carli, G., Ferrari, A., Finotto, G., Guarneri, T., Manzoni, V., Movedi, E., Nisoli, A., Paleari, L., Radici, I., Suardi, M., Veronesi, D., Bregaglio, S., Cappelli, G., Chiodini, M. E., Dominoni, P., Francone, C., Frasso, N., Stella, T., and Acutis, M. (2013). Development of an app for estimating leaf area index using a smartphone. Trueness and precision determination and comparison with other indirect methods. *Comput. Electron. Agric.*, 96:67–74.

Danner, M., Berger, K., Wocher, M., Mauser, W., and Hank, T. (2019). Fitted prosail parameterization of leaf inclinations, water content and brown pigment content for winter wheat and maize canopies. *Remote Sensing*, 11(10):1150.

Danner, M., Berger, K., Wocher, M., Mauser, W., and Hank, T. (2021). Efficient RTM-based training of machine learning regression algorithms to quantify biophysical & biochemical traits of agricultural crops. *ISPRS J. Photogramm. Remote Sens.*, accepted:...

Delegido, J., Verrelst, J., Rivera, J. P., Ruiz-Verdú, A., and Moreno, J. (2015). Brown and green LAI mapping through spectral indices. *Int. J. Appl. Earth Obs. Geoinf.*, 35:350–358.

Delloye, C., Weiss, M., and Defourny, P. (2018). Retrieval of the canopy chlorophyll content from Sentinel-2 spectral bands to estimate nitrogen uptake in intensive winter wheat cropping systems. *Remote Sens. Environ.*, 216:245–261.

Druce, D., Tong, X., Lei, X., Guo, T., Kittel, C. M. M., Grogan, K., and Tottrup, C. (2021). An Optical and SAR Based Fusion Approach for Mapping Surface Water Dynamics over Mainland China. *Remote Sens.*, 13(9):1663.

Drusch, M., Del Bello, U., Carlier, S., Colin, O., Fernandez, V., Gascon, F., Hoersch, B., Isola, C., Laberinti, P., Martimort, P., Meygret, A., Spoto, F., Sy, O., Marchese, F., and Bargellini, P. (2012). Sentinel-2: ESA's Optical High-Resolution Mission for GMES Operational Services. *Remote Sensing of Environment*, 120:25–36.

Dubois, O. et al. (2011). *The state of the world's land and water resources for*

food and agriculture: managing systems at risk. Earthscan.

Duveiller, G., Weiss, M., Baret, F., and Defourny, P. (2011). Retrieving wheat Green Area Index during the growing season from optical time series measurements based on neural network radiative transfer inversion. *Remote Sens. Environ.*, 115(3):887–896.

ESA (2018). FutureEO. https://www.esa.int/Applications/Observing_the_Earth/FutureEO (accessed on 20 march 2023).

Estévez, J., Salinero-Delgado, M., Berger, K., Pipia, L., Rivera-Caicedo, J. P., Wocher, M., Reyes-Muñoz, P., Tagliabue, G., Boschetti, M., and Verrelst, J. (2022). Gaussian processes retrieval of crop traits in google earth engine based on sentinel-2 top-of-atmosphere data. *Remote Sensing of Environment*, 273:112958.

Estévez, J., Berger, K., Vicent, J., Rivera-Caicedo, J. P., Wocher, M., and Verrelst, J. (2021). Top-of-atmosphere retrieval of multiple crop traits using variational heteroscedastic gaussian processes within a hybrid workflow. *Remote Sensing*, 13(8).

Féret, J.-B., Berger, K., de Boissieu, F., and Malenovskỳ, Z. (2021). PROSPECT-PRO for estimating content of nitrogen-containing leaf proteins and other carbon-based constituents. *Remote Sensing of Environment*, 252:112173.

Feret, J. B., François, C., Asner, G. P., Gitelson, A. A., Martin, R. E., Bidel, L. P. R., Ustin, S. L., le Maire, G., and Jacquemoud, S. (2008). PROSPECT-4 and 5: Advances in the leaf optical properties model separating photosynthetic pigments. *Remote Sensing of Environment*, 112(6):3030–3043.

Field, H. (1932). Ancient Wheat and Barley from Kish, Mesopotamia on JSTOR. *American Anthropologist*, 34(2):303–309.

Filipponi, F. (2019). Sentinel-1 GRD Preprocessing Workflow. *Proceedings*, 18(1):11.

Forrestal, P., Meisinger, J., and Kratochvil, R. (2014). Winter Wheat Starter Nitrogen Management: A Preplant Soil Nitrate Test and Site-Specific Nitrogen Loss Potential. *Soil Sci. Soc. Am. J.*, 78(3):1021–1034.

Gamiely, S., Randle, W. M., Mills, H. A., and Smittle, D. A. (1991). A Rapid and Nondestructive Method for Estimating Leaf Area of Onions. *HortScience*, 26(2):206.

Gao, S., Niu, Z., Huang, N., and Hou, X. (2013). Estimating the Leaf Area Index, height and biomass of maize using HJ-1 and RADARSAT-2. *Int. J. Appl. Earth Obs. Geoinf.*, 24:1–8.

Gitelson, A., Gritz, Y., and Merzlyak, M. (2003). Relationships between leaf chlorophyll content and spectral reflectance and algorithms for non-destructive chlorophyll assessment in higher plant leaves. *Journal of Plant Physiology*, 160(3):271–282.

Gitelson, A., Zur, Y., Chivkunova, O., and Merzlyak, M. (2002). Assessing carotenoid content in plant leaves with reflectance spectroscopy. *Photochemistry and Photobiology*, 75(3):272–281.

Goovaerts, P. and Goovaerts, D. C. E. E. P. (1997). *Geostatistics for Natural Resources Evaluation*. Oxford University Press, Oxford, England, UK.

Grote, U., Fasse, A., Nguyen, T. T., and Erenstein, O. (2021). Food Security and the Dynamics of Wheat and Maize Value Chains in Africa and Asia. *Front. Sustainable Food Syst.*, 4.

Han, D., Liu, S., Du, Y., Xie, X., Fan, L., Lei, L., Li, Z., Yang, H., and Yang, G. (2019). Crop Water Content of Winter Wheat Revealed with Sentinel-1 and Sentinel-2 Imagery. *Sensors*, 19(18):4013.

Hanes, J. (2013). *Biophysical Applications of Satellite Remote Sensing*. Springer, Berlin, Germany.

Hank, T. B., Bach, H., and Mauser, W. (2015). Using a Remote Sensing-Supported Hydro-Agroecological Model for Field-Scale Simulation of Heterogeneous Crop Growth and Yield: Application for Wheat in Central Europe. *Remote Sens.*, 7(4):3934–3965.

Hinzman, L. D., Bauer, M. E., and Daughtry, C. S. T. (1986). Effects of nitrogen fertilization on growth and reflectance characteristics of winter wheat. *Remote Sens. Environ.*, 19(1):47–61.

Hosseini, M., McNairn, H., Merzouki, A., and Pacheco, A. (2015). Es-

timation of Leaf Area Index (LAI) in corn and soybeans using multi-polarization C- and L-band radar data. *Remote Sens. Environ.*, 170:77–89.

Houborg, R. and Boegh, E. (2008). Mapping leaf chlorophyll and leaf area index using inverse and forward canopy reflectance modeling and spot reflectance data. *Remote Sensing of Environment*, 112(1):186–202.

Ingram, J. S. I., Gregory, P. J., and Izac, A.-M. (2008). The role of agronomic research in climate change and food security policy. *Agric. Ecosyst. Environ.*, 126(1):4–12.

Jacquemoud, S., Baret, F., Andrieu, B., Danson, F. M., and Jaggard, K. (1995). Extraction of vegetation biophysical parameters by inversion of the PROSPECT+SAIL models on sugar beet canopy reflectance data. Application to TM and AVIRIS sensors. *Remote Sensing of Environment*, 52(3):163–172.

Jacquemoud, S., Verhoef, W., Baret, F., Bacour, C., Zarco-Tejada, P., Asner, G., François, C., and Ustin, S. (2009). PROSPECT + SAIL models: A review of use for vegetation characterization. *Remote Sensing of Environment*, 113(SUPPL. 1):S56–S66.

Jutz, S. and Milagro-Pérez, M. P. (2018). 1.06 - Copernicus Program. In *Comprehensive Remote Sensing*, volume 1, pages 150–191. Elsevier, Walthm, MA, USA.

Kaplan, G., Fine, L., Lukyanov, V., Manivasagam, V. S., Tanny, J., and Rozenstein, O. (2021). Normalizing the Local Incidence Angle in Sentinel-1 Imagery to Improve Leaf Area Index, Vegetation Height, and Crop Coefficient Estimations. *Land*, 10(7):680.

Karam, M. A., Fung, A. K., Lang, R. H., and Chauhan, N. S. (1992). A microwave scattering model for layered vegetation. *IEEE Trans. Geosci. Remote Sens.*, 30(4):767–784.

Kastner, T., Erb, K.-H., and Haberl, H. (2014). Rapid growth in agricultural trade: effects on global area efficiency and the role of management. *Environ. Res. Lett.*, 9(3):034015.

Kimes, D. S., Nelson, R. F., Manry, M. T., and Fung, A. K. (1998). Attributes

of neural networks for extracting continuous vegetation variables from optical and radar measurements. *International Journal of Remote Sensing*, 19(14):2639–2662.

Kussul, N., Lavreniuk, M., Shumilo, L., and Kolotii, A. (2019). Nexus Approach for Calculating SDG Indicator 2.4.1 Using Remote Sensing and Biophysical Modeling. In *IGARSS 2019 - 2019 IEEE International Geoscience and Remote Sensing Symposium*, pages 6425–6428. IEEE.

Leblanc, S. G., Chen, J. M., Fernandes, R., Deering, D. W., and Conley, A. (2005). Methodology comparison for canopy structure parameters extraction from digital hemispherical photography in boreal forests. *Agric. For. Meteorol.*, 129(3):187–207.

Liu, C.-a., Chen, Z.-x., Shao, Y., Chen, J.-s., Hasi, T., and Pan, H.-z. (2019). Research advances of SAR remote sensing for agriculture applications: A review. *Journal of Integrative Agriculture*, 18(3):506–525.

López-Ruiz, V.-R., Huete-Alcocer, N., Alfaro-Navarro, J.-L., and Nevado-Peña, D. (2021). The relationship between happiness and quality of life: A model for Spanish society. *PLoS One*, 16(11).

Luis, V., Sainz, R., Eduardo, E., and Andrés, B. (2012). Optimizing fertilizer nitrogen use efficiency by intensively managed spring wheat in humid regions: Effect of split application. *Can. J. Plant Sci.*

MacFeely, S. (2019). The Big (data) Bang: Opportunities and Challenges for Compiling SDG Indicators. *Glob. Policy*, 10(S1):121–133.

Maslow, A. H. (1991). *Motivación y personalidad*. Díaz de Santos, Spain.

Masó, J., Serral, I., Domingo-Marimon, C., and Zabala, A. (2020). Earth observations for sustainable development goals monitoring based on essential variables and driver-pressure-state-impact-response indicators. *Int. J. Digital Earth*, 13(2):217–235.

Mattia, F., Balenzano, A., Satalino, G., Lovergine, F., Peng, J., Wegmuller, U., Cartus, O., Davidson, M. W. J., Kim, S., Johnson, J., Walker, J., Wu, X., Pauwels, V. R. N., McNairn, H., Caldwell, T., Cosh, M., and Jackson, T. (2018). Sentinel-1 & Sentinel-2 for SOIL Moisture Retrieval at Field

Scale. In *IGARSS 2018 - 2018 IEEE International Geoscience and Remote Sensing Symposium*, pages 6143–6146. IEEE.

Mattia, F., Le Toan, T., Picard, G., Posa, F. I., D'Alessio, A., Notarnicola, C., Gatti, A. M., Rinaldi, M., Satalino, G., and Pasquariello, G. (2003). Multitemporal C-band radar measurements on wheat fields. *IEEE Trans. Geosci. Remote Sens.*, 41(7):1551–1560.

McNairn, H., Kross, A., Lapen, D., Caves, R., and Shang, J. (2014). Early season monitoring of corn and soybeans with TerraSAR-X and RADARSAT-2. *Int. J. Appl. Earth Obs. Geoinf.*, 28:252–259.

Mercier, A., Betbeder, J., Baudry, J., Le Roux, V., Spicher, F., Lacoux, J., Roger, D., and Hubert-Moy, L. (2020). Evaluation of Sentinel-1 & 2 time series for predicting wheat and rapeseed phenological stages. *ISPRS J. Photogramm. Remote Sens.*, 163:231–256.

Mountrakis, G., Im, J., and Ogole, C. (2011). Support vector machines in remote sensing: A review. *ISPRS Journal of Photogrammetry and Remote Sensing*, 66(3):247–259.

Nasrallah, A., Baghdadi, N., El Hajj, M., Darwish, T., Belhouchette, H., Faour, G., Darwich, S., and Mhawej, M. (2019). Sentinel-1 Data for Winter Wheat Phenology Monitoring and Mapping. *Remote Sens.*, 11(19):2228.

Ouaadi, N., Ezzahar, J., Khabba, S., Er-Raki, S., Chakir, A., Hssaine, B. A., Le Dantec, V., Rafi, Z., Beaumont, A., Kasbani, M., and Jarlan, L. (2021). C-band radar data and in situ measurements for the monitoring of wheat crops in a semi-arid area (center of Morocco). *Earth Syst. Sci. Data*, 13:3707–3731.

Pachauri y Meyer (2014). *Climate Change 2014: Synthesis Report. Contribution of Working Groups I, II and III to the Fifth Assessment Report of the Intergovernmental Panel on Climate Change*. IPCC.

Paoletti, M. G., Stinner, B. R., and Lorenzoni, G. G. (1989). *Agricultural Ecology and Environment*. Elsevier Science, Walthm, MA, USA.

Parra, G. and Tobar, F. (2017). Spectral Mixture Kernels for Multi-Output Gaussian Processes. *arXiv*.

Pascual-Venteo, A. B., Portalés, E., Berger, K., Tagliabue, G., Garcia, J. L., Pérez-Suay, A., Rivera-Caicedo, J. P., and Verrelst, J. (2022). Prototyping Crop Traits Retrieval Models for CHIME: Dimensionality Reduction Strategies Applied to PRISMA Data. *Remote Sens.*, 14(10):2448.

Pasqualotto, N., Delegido, J., Van Wittenberghe, S., Verrelst, J., Rivera, J. P., and Moreno, J. (2018). Retrieval of canopy water content of different crop types with two new hyperspectral indices: Water Absorption Area Index and Depth Water Index. *Int. J. Appl. Earth Obs. Geoinf.*, 67:69–78.

Pasqualotto, N., D'Urso, G., Bolognesi, S. F., Belfiore, O. R., Van Wittenberghe, S., Delegido, J., Pezzola, A., Winschel, C., and Moreno, J. (2019). Retrieval of Evapotranspiration from Sentinel-2: Comparison of Vegetation Indices, Semi-Empirical Models and SNAP Biophysical Processor Approach. *Agronomy*, 9(10):663.

Patrignani y Ochsner (2015). Canopeo: A Powerful New Tool for Measuring Fractional Green Canopy Cover. *Agron. J.*, 107(6):2312–2320.

Peñuelas, J., Filella, I., Biel, C., Serrano, L., and Savé, R. (1993). The reflectance at the 950–970 nm region as an indicator of plant water status. *Int. J. Remote Sens.*, 14(10):1887–1905.

Pipia, L., Amin, E., Belda, S., Salinero-Delgado, M., and Verrelst, J. (2021). Green LAI Mapping and Cloud Gap-Filling Using Gaussian Process Regression in Google Earth Engine. *Remote Sensing*, 13(3):403.

Pipia, L., Muñoz-Marí, J., Amin, E., Belda, S., Camps-Valls, G., and Verrelst, J. (2019). Fusing optical and SAR time series for LAI gap filling with multioutput Gaussian processes. *Remote Sens. Environ.*, 235:111452.

Rasmussen, C. E. and Williams, C. K. I. (2006). *Gaussian Processes for Machine Learning*. The MIT Press, New York.

Reer, F. and Krämer, N. C. (2018). Psychological need satisfaction and well-being in first-person shooter clans: Investigating underlying factors. *Computers in Human Behavior*, 84:383–391.

Reyes-Muñoz, P., Pipia, L., Salinero-Delgado, M., Belda, S., Berger, K., Estévez, J., Morata, M., Rivera-Caicedo, J. P., and Verrelst, J. (2022). Quan-

tifying Fundamental Vegetation Traits over Europe Using the Sentinel-3 OLCI Catalogue in Google Earth Engine. *Remote Sens.*, 14(6):1347.

Rozenstein, O., Siegal, Z., Blumberg, D. G., and Adamowski, J. (2016). Investigating the backscatter contrast anomaly in synthetic aperture radar (SAR) imagery of the dunes along the Israel–Egypt border. *Int. J. Appl. Earth Obs. Geoinf.*, 46:13–21.

Rud, R., Cohen, Y., Alchanatis, V., Levi, A., Brikman, R., Shenderey, C., Heuer, B., Markovitch, T., Dar, Z., Rosen, C., Mulla, D., and Nigon, T. (2014). Crop water stress index derived from multi-year ground and aerial thermal images as an indicator of potato water status. *Precis. Agric.*, 15(3):273–289.

Sánchez, J., Domínguez, R., León, M., Samaniego, J., and Sunkel, O. (2019). *Recursos naturales, medio ambiente y sostenibilidad: 70 años de pensamiento de la CEPAL*. CEPAL.

Salinero-Delgado, M., Estévez, J., Pipia, L., Belda, S., Berger, K., Paredes Gómez, V., and Verrelst, J. (2021). Monitoring Cropland Phenology on Google Earth Engine Using Gaussian Process Regression. *Remote Sens.*, 14(1):146.

Sanchez y Matarazzo (1983). Caracterización y descripción de las causas edáficas que provocan efectos negativos en el cultivo de trigo (Patagones – Buenos Aires). *Informe Técnico 27, EEA Hilario Ascasubi*, pages 1–8.

Satalino, G., Mattia, F., Balenzano, A., Lovergine, F. P., Rinaldi, M., De Santis, A. P., Ruggieri, S., García, D. A. N., Gómez, V. P., Ceschia, E., Planells, M., Le Toan, T., Ruiz, A., and Moreno, J. F. (2018). Sentinel-1 & Sentinel-2 Data for Soil Tillage Change Detection. In *IGARSS 2018 - 2018 IEEE International Geoscience and Remote Sensing Symposium*, pages 6627–6630. IEEE.

Schott, J. W. (1989). Remote Sensing Of The Earth: A Synoptic View. *undefined*.

SenSAgri, P. (2020). SENSAGRI - Sentinels Synergy for Agriculture. [accessed on 5 March 2023].

Slafer, G., Miralles, D., Savin, R., Whitechurch, E., and González, F. (2003). Ciclo ontogénico, dinámica del desarrollo y generación del rendimiento y la calidad en trigo. *Editorial Facultad de agronomía, Universidad de Buenos Aires, Buenos Aires, 2003. pp. 101-132.*

Smith, P., Clark, H., Dong, H., Elsiddig, E., Haberl, H., Harper, R., House, J., Jafari, M., Masera, O., Mbow, C., et al. (2014). Agriculture, forestry and other land use (afolu).

Snee, R. D. (1977). Validation of Regression Models: Methods and Examples. *Technometrics*, 19(4):415–428.

Susniene y Jurkauskas (2009). The Concepts of Quality of Life and Happiness – Correlation and Differences. *EE*, 63(3).

Tilman, D., Balzer, C., Hill, J., and Befort, B. L. (2011). Global food demand and the sustainable intensification of agriculture. *Proc. Natl. Acad. Sci. U.S.A.*, 108(50):20260–20264.

Torres, R., Snoeij, P., Geudtner, D., Bibby, D., Davidson, M., Attema, E., Potin, P., Rommen, B., Floury, N., Brown, M., Traver, I. N., Deghaye, P., Duesmann, B., Rosich, B., Miranda, N., Bruno, C., L'Abbate, M., Croci, R., Pietropaolo, A., Huchler, M., and Rostan, F. (2012). Gmes sentinel-1 mission. *Remote Sensing of Environment*, 120(0):9 – 24. The Sentinel Missions - New Opportunities for Science.

Ulaby, F. T., Aslam, A., and Dobson, M. C. (1982). Effects of Vegetation Cover on the Radar Sensitivity to Soil Moisture. *IEEE Trans. Geosci. Remote Sens.*, GE-20(4):476–481.

Ulrich, K. R., Carlson, D. E., Dzirasa, K., and Carin, L. (2015). GP Kernels for Cross-Spectrum Analysis. *Advances in Neural Information Processing Systems*, 28.

UN General Assembly, . (2015). Resolution Adopted by the General Assembly on 25 September 2015. Transforming Our World The 2030 Agenda for Sustainable Development.

Valero, S., Arnaud, L., Planells, M., and Ceschia, E. (2021). Synergy of Sentinel-1 and Sentinel-2 Imagery for Early Seasonal Agricultural Crop

Mapping. *Remote Sens.*, 13(23):4891.

van der Wilk, M., Rasmussen, C. E., and Hensman, J. (2017). Convolutional Gaussian Processes. *arXiv*.

Van Wittenberghe, S., Verrelst, J., Rivera, J. P., Alonso, L., Moreno, J., and Samson, R. (2014). Gaussian processes retrieval of leaf parameters from a multi-species reflectance, absorbance and fluorescence dataset. *J. Photochem. Photobiol., B*, 134:37–48.

Vavlas, N.-C., Waine, T. W., Meersmans, J., Burgess, P. J., Fontanelli, G., and Richter, G. M. (2020). Deriving Wheat Crop Productivity Indicators Using Sentinel-1 Time Series. *Remote Sens.*, 12(15):2385.

Veloso, A., Mermoz, S., Bouvet, A., Le Toan, T., Planells, M., Dejoux, J.-F., and Ceschia, E. (2017). Understanding the temporal behavior of crops using Sentinel-1 and Sentinel-2-like data for agricultural applications. *Remote Sens. Environ.*, 199:415–426.

Verger, A., Baret, F., and Camacho, F. (2011). Optimal modalities for radiative transfer-neural network estimation of canopy biophysical characteristics: Evaluation over an agricultural area with CHRIS/PROBA observations. *Remote Sensing of Environment*, 115(2):415–426.

Verhoef, W. (1984). Light scattering by leaf layers with application to canopy reflectance modeling: The SAIL model. *Remote Sensing of Environment*, 16(2):125–141.

Verhoef, W. and Bach, H. (2007). Coupled soil–leaf-canopy and atmosphere radiative transfer modeling to simulate hyperspectral multi-angular surface reflectance and TOA radiance data. *Remote Sensing of Environment*, 109(2):166–182.

Verrelst, J., Alonso, L., Camps-Valls, G., Delegido, J., and Moreno, J. (2012). Retrieval of vegetation biophysical parameters using Gaussian process techniques. *IEEE Transactions on Geoscience and Remote Sensing*, 50(5 PART 2):1832–1843.

Verrelst, J., Camps-Valls, G., Muñoz Marí, J., Rivera, J., Veroustraete, F., Clevers, J., and Moreno, J. (2015a). Optical remote sensing and the retrie-

val of terrestrial vegetation bio-geophysical properties - a review. *ISPRS Journal of Photogrammetry and Remote Sensing*, 108:273–290.

Verrelst, J., Malenovskỳ, Z., Van der Tol, C., Camps-Valls, G., Gastellu-Etchegorry, J.-P., Lewis, P., North, P., and Moreno, J. (2019). Quantifying vegetation biophysical variables from imaging spectroscopy data: a review on retrieval methods. *Surveys in Geophysics*, 40(3):589–629.

Verrelst, J., Rivera, J., Camps-Valls, G., and Moreno, J. (2013a). Recent advances in biophysical parameter retrieval methods - opportunites for sentinel-2. ESA Living Planet Symposium 2013, 09-13 September, Edinbrugh, UK.

Verrelst, J., Rivera, J., Moreno, J., and Camps-Valls, G. (2013b). Gaussian processes uncertainty estimates in experimental Sentinel-2 LAI and leaf chlorophyll content retrieval. *ISPRS Journal of Photogrammetry and Remote Sensing*, 86:157–167.

Verrelst, J., Rivera, J., Tol, C., Magnani, F., Mohammed, G., and Moreno, J. (2015b). Global sensitivity analysis of the SCOPE model: What drives simulated canopy-leaving sun-induced fluorescence. *Remote Sensing of Environment*, 166:8–21.

Verrelst, J., Rivera, J., van der Tol, C., Magnani, F., Mohammed, G., and Moreno, J. (2014). Global sensitivity Analysis of the A-SCOPE model in support of future FLEX fluorescence retrievals. 5th International Workshop on Remote Sensing of Vegetation Fluorescence, 22 - 24 April 2014, Paris, France.

Verrelst, J., Rivera, J. P., Gitelson, A., Delegido, J., Moreno, J., and Camps-Valls, G. (2016). Spectral band selection for vegetation properties retrieval using Gaussian processes regression. *Int. J. Appl. Earth Obs. Geoinf.*, 52:554–567.

Verrelst, J., Rivera-Caicedo, J. P., Reyes-Muñoz, P., Morata, M., Amin, E., Tagliabue, G., Panigada, C., Hank, T., and Berger, K. (2021). Mapping landscape canopy nitrogen content from space using prisma data. *ISPRS Journal of Photogrammetry and Remote Sensing*, 178:382–395.

Weiss, M., Frederic, B., Smith, G., Jonckheere, I., and Coppin, P. (2004). Re-

view of methods for in situ leaf area index (lai) determination: Part ii. estimation of lai, errors and sampling. *Agricultural and Forest Meteorology*, 121:37–53.

Whittaker, E. T. (1922). On a New Method of Graduation. *Proc. Edinburgh Math. Soc.*, 41:63–75.

Wolff, T., Cuevas, A., and Tobar, F. (2020). MOGPTK: The Multi-Output Gaussian Process Toolkit. *ResearchGate*.

Xie, R., Darvishzadeh, R., Skidmore, A. K., Heurich, M., Holzwarth, S., Gara, T. W., and Reusen, I. (2021). Mapping leaf area index in a mixed temperate forest using Fenix airborne hyperspectral data and Gaussian processes regression. *Int. J. Appl. Earth Obs. Geoinf.*, 95:102242.

Zadoks, J. C., Chang, T. T., and Konzak, C. F. (1974). A decimal code for the growth stages of cereals. *Weed Res.*, 14(6):415–421.

Zhang, C., Pattey, E., Liu, J., Cai, H., Shang, J., and Dong, T. (2017). Retrieving Leaf and Canopy Water Content of Winter Wheat Using Vegetation Water Indices. *IEEE J. Sel. Top. Appl. Earth Obs. Remote Sens.*, 11(1):112–126.

Zhang, J., Han, W., Huang, L., Zhang, Z., Ma, Y., and Hu, Y. (2016). Leaf Chlorophyll Content Estimation of Winter Wheat Based on Visible and Near-Infrared Sensors. *Sensors*, 16(4):437.

Zhang, Y., Venkatachalam, A. S., Huston, D., and Xia, T. (2014). Advanced signal processing method for ground penetrating radar feature detection and enhancement. In *Proceedings Volume 9063, Nondestructive Characterization for Composite Materials, Aerospace Engineering, Civil Infrastructure, and Homeland Security 2014*, volume 9063, pages 276–289. SPIE.

Parte II
Listado de Publicaciones

ARTÍCULO 1

"Seasonal Mapping of Irrigated Winter Wheat Traits in Argentina with a Hybrid Retrieval Workflow Using Sentinel-2 Imagery"

This article belongs to the Special Issue Cropland Phenology Monitoring Based on Cloud-Computing Platforms of the Remote Sensing Journal. Journal Rank: JCR - Q1 (Geosciences, Multidisciplinary) / Cite Score - Q1 (General Earth and Planetary Sciences). The article was published in September 2022. This journal had an impact factor of 5.349 in 2022.

remote sensing

MDPI

Article

Seasonal Mapping of Irrigated Winter Wheat Traits in Argentina with a Hybrid Retrieval Workflow Using Sentinel-2 Imagery

Gabriel Caballero [1,2,*], Alejandro Pezzola [3], Cristina Winschel [3], Alejandra Casella [4], Paolo Sanchez Angonova [3], Juan Pablo Rivera-Caicedo [5], Katja Berger [2,6], Jochem Verrelst [2] and Jesus Delegido [2]

1 Agri-Environmental Engineering, Technological University of Uruguay (UTEC), Av. Italia 6201, Montevideo 11500, Uruguay
2 Image Processing Laboratory (IPL), University of Valencia, C/Catedrático José Beltrán 2, 46980 Paterna, Spain
3 Remote Sensing and SIG Laboratory, Hilario Ascasubi Agricultural Experimental Station, National Institute of Agricultural Technology (INTA), Hilario Ascasubi 8142, Argentina
4 Permanent Observatory of Agro-Ecosystems, Climate and Water Institute-National Agricultural Research Centre (ICyA-CNIA), National Institute of Agricultural Technology (INTA), Nicolás Repetto s/n, Hurlingham 1686, Argentina
5 Secretary of Research and Graduate Studies, CONACYT-UAN, Tepic 63155, Mexico
6 Mantle Labs GmbH, Grünentorgasse 19/4, 1090 Vienna, Austria
* Correspondence: gabriel.caballero@utec.edu.uy; Tel.: +34-685-829-332

Citation: Caballero, G.; Pezzola, A.; Winschel, C.; Casella, A.; Sanchez Angonova, P.; Rivera-Caicedo, J.P.; Berger, K.; Verrelst, J.; Delegido, J. Seasonal Mapping of Irrigated Winter Wheat Traits in Argentina with a Hybrid Retrieval Workflow Using Sentinel-2 Imagery. *Remote Sens.* **2022**, *14*, 4531. https://doi.org/10.3390/rs14184531

Academic Editor: Roshanak Darvishzadeh

Received: 9 August 2022
Accepted: 7 September 2022
Published: 10 September 2022

Abstract: Earth observation offers an unprecedented opportunity to monitor intensively cultivated areas providing key support to assess fertilizer needs and crop water uptake. Routinely, vegetation traits mapping can help farmers to monitor plant development along the crop's phenological cycle, which is particularly relevant for irrigated agricultural areas. The high spatial and temporal resolution of the Sentinel-2 (S2) multispectral instrument leverages the possibility to estimate leaf area index (LAI), canopy chlorophyll content (CCC), and vegetation water content (VWC) from space. Therefore, our study presents a hybrid retrieval workflow combining a physically-based strategy with a machine learning regression algorithm, i.e., Gaussian processes regression, and an active learning technique to estimate LAI, CCC and VWC of irrigated winter wheat. The established hybrid models of the three traits were validated against in-situ data of a wheat campaign in the Bonaerense valley, South of the Buenos Aires Province, Argentina, in the year 2020. We obtained good to highly accurate validation results with LAI: R^2 = 0.92, RMSE = 0.43 m^2 m^{-2}, CCC: R^2 = 0.80, RMSE = 0.27 g m^{-2} and VWC: R^2 = 0.75, RMSE = 416 g m^{-2}. The retrieval models were also applied to a series of S2 images, producing time series along the seasonal cycle, which reflected the effects of fertilizer and irrigation on crop growth. The associated uncertainties along with the obtained maps underlined the robustness of the hybrid retrieval workflow. We conclude that processing S2 imagery with optimised hybrid models allows accurate space-based crop traits mapping over large irrigated areas and thus can support agricultural management decisions.

Keywords: leaf area index; vegetation water and chlorophyll content; Gaussian processes regression; hybrid retrieval workflow; dimensionality reduction; active learning

1. Introduction

Wheat is a worldwide cultivated grain crop providing nearly 20% of all calories consumed due to its strong adaptability to various temperature and water conditions [1]. As an important global food crop, wheat yield information is essential in terms of food security [2]. Good agronomic practices and natural resource usage become fundamental for winter wheat grain development and crop yield. These practices have an important significance for modern precision agriculture [3]. Irrigated valleys, although representing

only 20% of the world's croplands, produce 40% of the global crop harvest [4]. In arid and semi-arid intensively cultivated areas, irrigation improves economic returns and can boost food production by up to 400% [4,5]. Hence, accurate and timely mapping of winter wheat biophysical and biochemical variable, or crop traits, results in being indispensable for enhancing crop management, food security, and agriculture structure adjustment [6–8]. The estimation and monitoring of crucial crop variables, such as leaf area index (LAI), canopy chlorophyll content (CCC), and vegetation water content (VWC), are key for agricultural applications including crop growth modelling and yield estimation supporting sustainable management of cultivated areas [6,9]. Definitions of these variables are given as follows.

LAI is defined as the total one-sided leaf area per soil unit (m^2 leaf area per m^2 soil). It is strongly related to canopy photosynthesis and evapotranspiration and plays a key role in the exchange of energy and water between the biosphere and atmosphere [10]. Varying definitions of LAI have been presented, such as effective plant area index [11], which includes the area from all plant organs and assumes random distributions of leaves. The green LAI (GAI) is probably the most relevant term describing the radiation transfer in vegetated canopies, i.e., the green photosynthetically active elements of the canopy [12,13]. Here, we refer mainly to GAI being most closely related to the signal actually recorded by satellite instruments. Nonetheless, for the sake of simplicity, we use the term LAI throughout this study. CCC is defined as the product of LAI and leaf chlorophyll content (C_{ab}) expressed in grams per unit leaf area (g/m^2). Hence, CCC represents the optical path in the vegetated canopy where absorption by chlorophyll pigments dominates the radiometric signal [14]. In addition, due to its strong relationship with nitrogen (N) content, often C_{ab} is considered a proxy for leaf N status. Therefore, CCC can be considered for quantifying canopy-level N content [15,16], although restricted to vegetative growth stages [17]. Due to its strong association with plant transpiration, vegetation stress, and biomass productivity, VWC has been widely considered a crucial variable for crop physiological status [18–20]. VWC of wheat crops is also a significant growth indicator during different development stages [6]. Water availability not only affects wheat photosynthesis, but also the grain filling rate and, ultimately, yield [21,22]. Traditionally, wheat crop water content has been determined by manually sampling plants to obtain fresh weight and dry weight and then calculating crop water content [2]. However, conventional field measurements are destructive and labour-intensive, especially across large areas with significant within-field spatial variability in soil infiltration, drainage, and conductivity characteristics [23]. The same holds true for destructive sampling of other crop variables. Earth observation (EO) technology can be used as an appealing alternative, providing a synoptic view of the Earth's surface by making use of the complex interactions between radiation and the environment [24]. Nowadays, an attractive operational EO system with the capability to capture the visible (VIS), near-infrared (NIR), red-edge and short-wave infrared (SWIR) spectral domains involves the Sentinel-2 (S2) mission [25]. The recent S2 constellation that combines a high revisit frequency (5-day) and spatial resolution (10–20 m) with systematic global acquisition and an open access policy is promising in the development of operational farming services in near-real-time [16]. In recent years, the rapid development of EO technology has produced an unprecedented amount of research applying satellite data for monitoring crop traits across large areas, in a quick and accurate way e.g., [13,19,26–30].

With respect to the retrieval of crop traits from EO data, a multitude of techniques have been developed, which can be categorized into four main categories [30,31]: (1) Parametric regression approaches typically consist of relations between the traits and spectral data transformed into spectral indices e.g., [32,33]. (2) The second category of regression approaches obtains these variables from reflectance data using linear or nonlinear nonparametric approaches, i.e., chemometrics or machine learning regression algorithms (MLRA) e.g., [34–36]. (3) The category of physically-based retrieval methods refers to the inversion of radiative transfer models (RTMs) e.g., [37–41]. RTMs apply physical laws to explain the cause–effect relationships between radiation–photon interactions and plant constituents. The most prominent one-dimensional, (1D) turbid medium RTM for sim-

ulating vegetation reflectance is PROSAIL [42]. PROSAIL is composed of a leaf optical properties model, typically from the PROSPECT family [43,44], and, (b) the Scattering of Arbitrarily Inclined Leaves canopy architecture model (SAIL, 4SAIL) [45,46]. The last category of retrieval methods (4) is presented by hybrid approaches, being perhaps of most interest within current research lines and also for operational contexts [26,27,30,47,48]. Hybrid methods blend physics described by RTMs with the speed and efficiency of MLRAs. Within hybrid scenarios, training datasets are simulated by varying the input parameter space of coupled leaf-canopy RTMs. The nonlinear relationships between simulated reflectance and vegetation properties are then learned by an MLRA. Ideally, these training databases represent the canopy states realistically and at the same time are small enough to avoid exhaustive processing times. Regarding these strategies, a diversity of MLRAs have been successfully applied for retrieval tasks during the last few decades, e.g., artificial neural networks, decision trees or kernel-based methods [30,31]. As part of the latter family, especially Gaussian processes, regression (GPR) [49] emerged as a competitive retrieval algorithm e.g., [50–52], and has been widely adopted in studies inferring traits from EO data e.g., [48,53–64].

GPR received special attention also thanks to associated uncertainty estimates provided along with the predictions. This special feature enables assessing the fidelity of the models when transferring them into other spaces and times [28]. Moreover, to enhance mapping performance and processing speed, active learning (AL) techniques can be incorporated into hybrid workflows. AL aims to optimize training datasets through intelligent sampling using an iterative procedure devoted to exploiting samples during the design of the regression model [65–67].

Time-series of multiple quantitative traits over irrigated winter wheat present a captivating tool to address crop management questions and improve agricultural practises. Multiple authors have developed satellite-based retrieval models for wheat traits mapping using MLRA or parametric regressions [3,13,20,59,68,69]. Hybrid retrieval workflows may outperform these simpler empirical approaches due to their appealing property of combining physical awareness (RTMs) with flexibility of machine learning algorithms. Hence, they are an appealing alternative to be explored in our context. Several experimental studies have already demonstrated the feasibility of producing accurate vegetation traits maps from multispectral data, including S2 [59,70–73]. However, there is still the need to further test and adapt hybrid methods under diverse environmental conditions, at different locations and to multiple crop types.

In an attempt to demonstrate the possibilities of space-based cropland trait monitoring, this study presents the development of an optimised hybrid retrieval workflow dedicated to irrigated winter wheat monitoring in Argentina. Given the above-sketched general framework, this study aims to reach the following objectives: (1) to develop independent hybrid models optimised with AL and GPR for an explicit quantification of winter wheat LAI, CCC, and VWC from S2 data; (2) to generate accurate S2-based maps of the wheat traits with the inclusion of associated uncertainties over an intensive irrigated agroecosystem; and (3) to evaluate LAI, CCC, and VWC time series identifying seasonal trends over the selected study site.

2. Materials and Methods

2.1. Generation of Training Data Sets

Aiming to develop optimised hybrid models, the workflow initiates with simulating a training database using the coupled PROSPECT-PRO [44] and 4SAIL models, further referred to as PROSAIL-PRO. The models simulate bi-directional reflectance as a function of diverse leaf biochemical input variables, e.g., C_{ab}, leaf protein content (C_p), leaf carotenoid content (C_{xc}) or leaf equivalent water thickness (EWT) and biophysical variables, i.e., LAI and average leaf inclination angle (ALIA). The synthetic training database was generated by using Latin Hypercube Sampling (LHS) to randomly select samples from the multi-spectral input space. For this, 1000 combinations were drawn from all PROSAIL-PRO parameters.

The selected size of the training dataset may appear rather small compared to classical retrieval approaches, for instance using lookup-table approaches or neural networks. Note that a standard implementation of GPR struggles to cope with thousands of samples within reasonable time intervals. Hence, as suggested by prior studies, e.g., [67,74], successfully training GP models with data sets of rather small sizes, we also restrict here to 1000 samples.

An overview of all included PROSAIL-PRO parameters including sampling, mean values, distributions and ranges is given in Table 1 (see also the study by Berger et al. [26] for full information about the generation of the training database). *VWC* can then be directly calculated from *EWT* with a (unit) conversion factor of 10'000 upscaling from leaf to canopy level through *LAI*. Fractional vegetation cover (*FVC*) was used to introduce the crop-bare-soil relationship (see Equation (1)). *CCC* was also obtained through extrapolating from C_{ab} to canopy level by means of *LAI* (see Equation (2)). Finally, simulated *VWC* and *CCC* both in [g m^{-2}] were added to the training database:

$$VWC_s = (EWT \times LAI \times FVC) \times 10000 \left[\mathrm{g/m^2}\right] \quad (1)$$

$$CCC_s = (C_{ab} \times LAI)/100 \left[\mathrm{g/m^2}\right] \quad (2)$$

Table 1. Parameter ranges for PROSPECT-PRO and 4SAIL (PROSAIL-PRO). Specified ranges are uniformly distributed in LHS sampling.

Leaf Optical Properties			Canopy Reflectance Model		
PROSPECT-PRO Parameters	**Notation [Unit]**	**Range**	**4SAIL Parameters**	**Notation [Unit]**	**Range**
Leaf chlorophyll a+b content	*Cab* [µg cm^{-2}]	5–75	Leaf area index	*LAI* [m^2 m^{-2}]	0.1–7.0
Leaf structure parameter	*Nstruct , no dim.*	1.0–2.0	Average leaf inclination angle	*ALIA* [°]	30–70
Leaf carotenoid content	*Cxc* [µg cm^{-2}]	0–15	Soil brightness	*soil, no dim.*	0–1
Leaf equivalent water thickness	*EWT* [cm]	0.0002–0.05	Sun zenith angle	*SZA* [°]	20–40
Carbon-based constituents	*CBC* [g cm^{-2}]	0.001–0.01	Hot spot effect	*Hot* [m m^{-1}]	0.01
Leaf anthocyanin content	*Canth* [µg cm^{-2}]	0–2	Observer zenith angle	*OZA* [°]	0
Leaf protein content	*Cp* [µg cm^{-2}]	0.001–0.0025	Diffuse/direct radiation	*DDR* [%]	80
Leaf mass per area	*Cm* [µg cm^{-2}]	0.0001–0.03	Relative azimuth angle	*rAA* [°]	0
Brown pigment content	*Cbrown, no dim.*	0			

Finally, bi-directional canopy reflectance was calculated using S2 spectral configuration and excluding low-resolution bands of 60 m since their focus is on cloud screening and atmospheric corrections. For instance, Estévez et al. [59] analyzed the contribution of the S2 spectral bands covering 10–20 m pixel resolutions for LAI retrieval purposes. The authors concluded to keep all ten bands (with S2 central wavelengths of 493 nm, 560 nm, 665 nm, 704 nm, 740 nm, 783 nm, 833 nm, 865 nm, 1610 nm, and 2190 nm) for further processing. To assure a maximum of spectral information required for the retrieval of multiple crop traits, we also decided to explore the ten S2 bands.

2.2. Gaussian Processes Regression

GPR is used as core MLRA in the hybrid model development. GPR modeling is flexible enough to fit many types of data, including geospatial and time-series data. GP is a Gaussian distribution over functions, which means that, instead of inferring the distribution of a parameter, GP can be then used to infer a distribution over functions directly under the premise that the function values are themselves random variables. At the inference stage, every time a new observation is made, the model hypothesis (prior probability distribution) is updated in light of the new observations. After having observed some function values, prior distribution over functions can be converted into posterior over functions. A Gaussian Process is a collection of random variables any finite number of which have (consistent) joint Gaussian distributions [49].

Notationally, GP can be deployed as follows: we observe training dataset $\mathfrak{D} = \{(x_i, f_i(x_i))|i = 1, \ldots, N\}$, where $x_i \in \mathbb{R}^{\mathcal{B}}$ (being $\mathcal{B}$ the number of sensor spectral bands) and $X = \{x_i\}_{i=1}^{N}$, GP aims to provide a suitable model to predict the function outputs f_* given a test dataset X_* of size $N_* \times \mathfrak{D}$ unknown by the model. In a noise-free environment, the joint distribution under GP is:

$$\begin{pmatrix} f \\ f_* \end{pmatrix} \sim \mathcal{N}\left(\begin{bmatrix} \mu \\ \mu_* \end{bmatrix}, \begin{bmatrix} k(X,X) & k(X,X_*) \\ k(X_*,X) & k(X_*,X_*) \end{bmatrix}\right) \tag{3}$$

where μ and μ_* are the means of the functions f and f_*, which can be assumed as 0, $K = k(X, X)$ is the matrix of self-similarities in the training dataset, $K_* = k(X, X_*)$ and $K_*^T = k(X_*, X)$ represents the similarities between training and test datasets, and $K_{**} = k(X_*, X_*)$ express the self-similarities in the test dataset. The mean μ_* (expectation of f_*) and the co-variance Σ_* of the test dataset X_* can be calculated as follows:

$$\mu_* = \mathbb{E}(f_*) = K_*^T K^{-1} f \tag{4}$$

$$\Sigma_* = K_{**} - K_*^T K^{-1} K_* \tag{5}$$

To compute the measures of similarity between two points x_i and x_j, a positive definite kernel (or covariance function) that describes the covariance of the GP random variables should be implemented. The squared exponential kernel, also known as a radial basis function (RBF), which arises from taking the exponent of the scaled squared Euclidean distance between the data locations, is one of the most popular kernels used in GP modeling. It can be computed as:

$$k(x_i, x_j) = \sigma_f^2 e^{-\frac{1}{2\ell^2}\left\|x_i - x_j\right\|^2} \tag{6}$$

where σ_f^2 is the overall variance (σ_f^2 that is also known as amplitude), and the parameter ℓ is the variance of the Gaussians (length scale) that controls the smoothness and confidence of the regression process. Thus, a Gaussian process is a distribution over functions whose smoothness is defined by the kernel k. RBF is a linear combination of basis functions; wherever there is data, we place a basis function scaled by the term σ_f^2. Consequently, f_* is the sum of basis functions scaled by σ_f^2. There are several manners to find the optimal ℓ value, cross-validation, maximum likelihood estimation (MLE), and Bayesian Learning are examples of different methods that can be implemented in the stage of learning the kernel parameters.

The key concept regarding GP is the fact that given two points x_i and x_j that are similar (similarity determined by the kernel k), the function values $f(x_i)$ and $f(x_j)$, should be expected to be similar too. Straight away, the kernel function parameters have been optimised using a training dataset, and the kernel matrix can be plugged into the predictive equations for the mean μ_* and co-variance Σ_* of the test data x_* to obtain predictions f_* on the whole test dataset X_*. The process of making predictions is only computing the posterior distribution $p(f_*|X_*, X, f)$ of x_* given $f$and the previous x, we can condition on the observations, to obtain:

$$f_*|X_*, X, f \sim \mathcal{N}\Big(f_*; k(X,X_*)k(X,X)^{-1}f, k(X_*,X_*) - k(X,X_*)k(X,X)^{-1}k(X_*,X)\Big) \tag{7}$$

Conditioning a Gaussian gives another Gaussian:

$$p(f_*|X_*, X, f) \sim \mathcal{N}\big(f_*|\mu_*, \textstyle\sum_*\big) \tag{8}$$

where Σ_* models the co-variances and cross-covariances between all combinations of train and test data. Predictions made using GP are not just point predictions: they are whole probability distributions.

More commonly, we have access to noisy observations $\{x_i, y_i\}_{i=1}^{N}$ with $y_i = f_i(x_i) + \mathcal{E}$, where $\mathcal{E}$ is the noise of the observations. Assuming that the noise is Gaussian distributed with zero mean and variance σ_n^2, the noise can be therefore expressed as $\mathcal{E} \sim \mathcal{N}(0, \sigma_n^2)$. The value of σ_n^2 can be estimated from data utilizing the MLE principle. Assuming independently added Gaussian noise to each observation, the joint distribution of observations and test predictions is given by:

$$\begin{pmatrix} y \\ f_* \end{pmatrix} \sim \mathcal{N}\left([0], \begin{bmatrix} k(X,X) + \sigma_n^2 I & k(X,X_*) \\ k(X_*,X) & k(X_*,X_*) \end{bmatrix}\right) \tag{9}$$

To make predictions from a noisy GP, the only thing to do is to establish a conditioning on the observation:

$$f_*|X_*, X, y \sim \mathcal{N}\left(k(X,X_*)\left[k(X,X) + \sigma_n^2 I\right]^{-1} y, k(X_*,X_*) - k(X,X_*)\left[k(X,X) + \sigma_n^2 I\right]^{-1} k(X_*,X)\right) \tag{10}$$

The mean is linear in two ways:

$$\mu_* = k(X_*,X)\left[k(X,X) + \sigma_n^2\right]^{-1} y \tag{11}$$

The predictive co-variance (confidence intervals) is the difference between two terms:

$$\Sigma_* = k(X_*,X_*) - k(X_*,X)\left[k(X,X) + \sigma_n^2 I\right]^{-1} k(X,X_*) \tag{12}$$

The first term is the prior variance, from which we subtract a (positive) term, telling how much the data X has explained. It is worth mentioning that the variance is independent of the observed outputs y. Although the posterior distribution $p(f_*|X_*, X, y)$ covers noise in training data, it is still a distribution over noise-free predictions f_*. To additionally include noise ε into predictions y_*, we must add σ_n^2 to the diagonal of Σ_*:

$$p(y_*|X_*, X, y) \sim \mathcal{N}\left(y_*|\mu_*, \sum\nolimits_* + \sigma_n^2 I\right) \tag{13}$$

Summarizing, as a Bayesian approach, GPR provides a natural and automatic mechanism to construct and calibrate uncertainties.

2.3. Active Learning Principles

GPR as a kernel-based regression method permits an enlarged number of input variables to be scanned and can be particularly convenient to deal with regression uncertainties since the confidence interval for the predictions is provided. Even though GPR offer a suitable alternative to processing large training datasets, processing large simulated training datasets could become computationally inefficient. Consequently, a reduction in the sampling domain, which specifies the size of the training dataset, is needed. A solution to the sampling reduction issue is given by semi-supervised approaches, and these techniques are also known as active learning [66]. AL aims to provide a strategy to efficiently reduce massive training datasets into an optimal dataset by sampling and evaluating the data pool iteratively through an intelligent process [67]. In AL, new informative samples are labeled based on the knowledge acquired during the exploration of the data input space.

Solving regression problems with AL can be addressed through a diversity framework. Diversity-based AL strategies create a reduced training dataset by selecting new samples from the input space, according to their dissimilarities [75]. Euclidean distance-based diversity (EBD) selects those samples out of the pool being distant from the already included ones in the training set, using squared Euclidean distance:

$$d_E = \|x_u - x_l\|_2^2 \tag{14}$$

where x_u is a sample from the candidate set, and x_l is a sample from the training dataset. All distances between samples are computed and then the farthest are selected.

With the purpose to decrease the GPR training time, the EBD sampling method was performed in order to reduce the size of the input data space. Accordingly, 1% of the 1000 labeled samples (pairs of simulated bi-directional reflectance and vegetation traits) was randomly selected as the initial data set. The GPR training process was iteratively repeated up to 1000 times. At each iteration, the sample from the input data set with the largest distance between the pool of the 1000 labeled samples was selected by the EBD and added to the training data only when performance improved as evaluated by the root mean square error (RMSE) against the in-situ data [66,72].

2.4. Study Site

The Bonaerense Valley of Colorado River (BVCR) is located in the South of the Buenos Aires Province, Argentina, between the 39° and 40°S parallels and the 62° and 63°W meridians. Two different cropping systems can be well distinguished in the region: irrigated and non-irrigated crops. From the productive point of view, irrigation presents the highest productivity and contribution to the regional socio-economic movement. The area has a surface of 500,000 ha, of which 140,000 ha are irrigated by an extensive irrigation network based on uncoated drainage channels. Gravity irrigation has made the most of the agricultural activities in the area possible. The implanted crops under irrigation conditions occupy 91163 ha in the BVCR, including horticulture, pastures, and cereals. This study focused on three wheat paddocks of the BVCR in the Villarino district (see Figure 1).

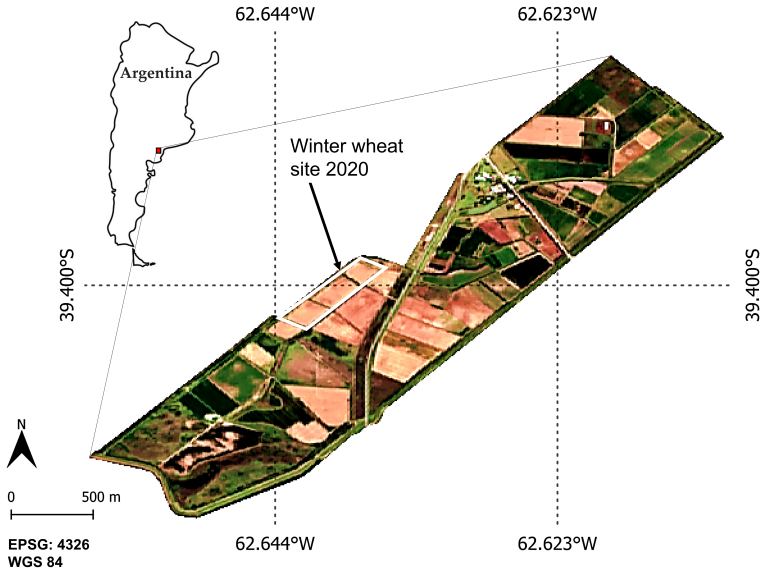

Figure 1. Overview of the Bonaerense Valley of Colorado River study site with test fields for the winter wheat campaign of the year 2020. True colour S2 image (R = B4, G = B3, B = B2) of 27 December 2020. Reference system: WGS84 (EPSG 4326).

2.5. Wheat Crop Experimental Design

A total of three repetitions were set up for each of the wheat paddocks. The position of nine elementary sampling units (ESU) was measured with a differential global positioning system (GPS) and recorded as point sample references in the field campaign database. The ESUs were revisited at each date corresponding to cloud-free S2 acquisitions to guarantee solid time-series. If there was a coincidence in ±6 days related to the S2 acquisition, the traits of the wheat crop were sampled.

The measurements were performed following a defined field protocol for the BVCR 2020 wheat campaign; see Figure 2. Hereby, the sampling strategy consisted of defining ESUs of 10 m × 10 m size for each wheat paddock in order to comply with the S2 spatial resolution (10 m). In addition, a minimum distance of 30 m from the parcels' edges was kept. Sampling points were distributed within the ESUs following a five-measurements square spatial sampling strategy providing a statistically averaged LAI estimate per ESU [69]. The centre of the ESUs (sampling point A) was georeferenced using the S2 pixel grid to assure correspondence to the S2 reflectance data.

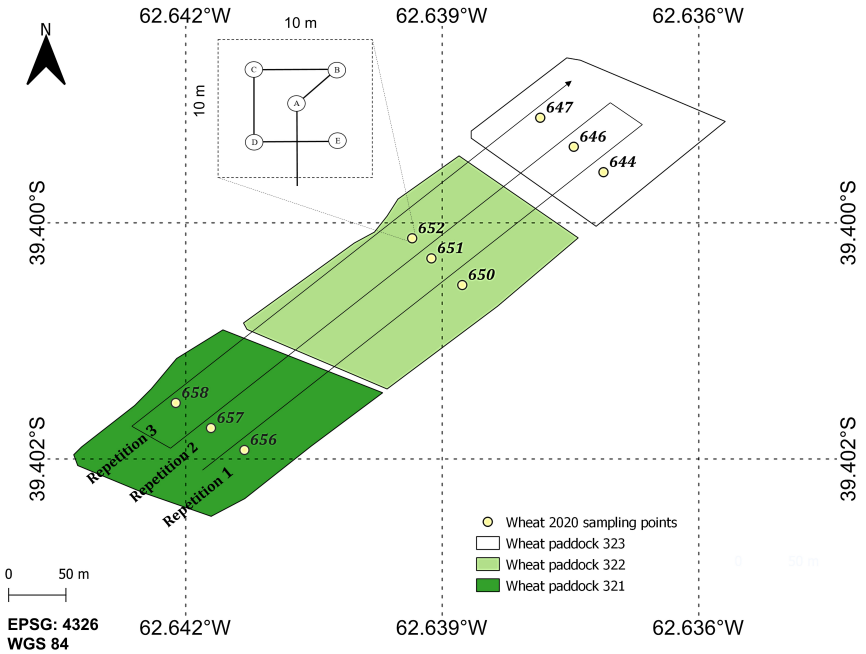

Figure 2. Layout of measurement design for the 2020 campaign at the BVCR study site: three ESUs were defined per wheat paddock and sampling approach for each elementary sampling unit, partly adapted from [69]. Reference system: WGS84 (EPSG 4326).

The in-situ measurement protocol used to carry out the field campaigns involved the collection of four main traits: LAI, fractional vegetation cover (FVC), C_{ab}, and above-ground fresh biomass (AGFB). The crop phenological stage and field data observations were also registered in the in-situ measurements database. The phenology was determined according to secondary growth stages of the Zadoks-scale [76].

Wheat Crop Management and Field Data Collection

The wheat crop was sown on 25 June 2020 at three different paddocks in the study site, a uniform seed density was established at 95 kg ha^{-1}, and the weight of 1000 seeds was 45.8 g on average. At the wheat sowed stage, 80 kg ha^{-1} of diammonium phosphate was used as a fertilizer considering the formulation 18-46-00 (18% N, 46% P_2O_5, and K_2O 0%). Phosphorus fertilization is a key factor in replenishing soil nutrients and obtaining more vigorous plants. Moreover, a rapid formation and growth of the root system are promoted making plants more resistant to water deficit. A system of ground edges separated by 14 m was implemented at the pre-sowing labour stage to ensure water embankments during the irrigation processes. Sunflower hybrid seed was the predecessor crop. At the beginning of the tillering stage, a value of 243 wheat plants per square meter (plant density) was measured. The distance between rows (rows spacing) was set as 17.5 cm according

to wheat crop management recommendations in the region of the Colorado river valley. Wheat fertilization took place in two instances throughout the phenological cycle, first on 31 August 2020 and second by the middle of September. The dose of nitrogen (Urea) supplied was distributed uniformly and ranged between 150–200 kg ha^{-1}. It is reasonable to expect that wheat plants start to receive nutrients from Urea up to one week later of fertilization. Three gravity irrigations were performed at different instances of the crop cycle between late August and November.

A collection of field data was obtained from the study area of the BVCR. In the year 2020, the test site was visited regularly during the growing periods from August to December. Data were collected on wheat fields belonging to the communal farmlands of BVCR by a group of expert professionals and technicians of HAEE-INTA, Argentina. The exact sampling sites were the same across the wheat 2020 field campaign. Each site was confined to a 10 × 10 m area, corresponding to the average S2 pixel size.

LAI measurements were taken using the PocketLAI R Smart-App [77]. Six observations were made-up per ESU and averaged giving a total of 54 LAI values for the entire campaign.

The FVC was measured utilizing the "Canopeo®" App [78]. The app uses the RGB camera of the smart devices applying the relations R/G, B/G, and 2G-R-B to determine the crop canopy coverage percentage related to the soil.

To determine the AGFB value, five wheat plants per ESU were cut at soil level at each sampling date throughout the growing season. A sowing track or an area of 0.02 m^2 was considered to obtain the AGFB samples. Each fresh biomass sample made up of wheat leaf, stalk, and fruit was enclosed in a sealed plastic bag and brought to the laboratory inside of a cooler for the fresh weight (FW) and dry weight (DW) measurements (see Table 2). The AGFB samples were weighed in the fresh state and oven-dried until reached constant weight for 24 h at 60 °C before dry weight was determined [79]. The DW corresponds to the above-ground dry biomass (AGDB) vegetation biophysical variable expressed in g units.

Table 2. Database of in-situ wheat traits with dates, ranges, mean values as well as standard deviations (SD) of the measurements.

Wheat Variable	Date	Range	Mean	SD
LAI (m^2 m^{-2})	03-09-2020	0.16–0.30	0.23	0.05
	17-09-2020	0.56–1.54	0.94	0.29
	02-10-2020	1.59–3.81	2.57	0.66
	19-10-2020	1.53–3.27	2.62	0.51
	02-11-2020	2.78–5.05	4.12	0.63
	16-11-2020	3.31–5.39	4.02	0.80
	30-11-2020	3.29–4.75	4.08	0.50
	16-12-2020	3.97–5.64	4.68	0.43
FVC (%)	10-08-2020	6.2–9.1	7.63	1.00
	03-09-2020	23.0–48.0	34.94	8.32
	17-09-2020	22.1–80.2	44.21	22.73
	02-10-2020	32.7–69.2	48.30	13.28
	19-10-2020	23.6–69.5	46.15	12.97
	02-11-2020	11.1–29.3	20.92	5.07
	16-11-2020	74.4–92.0	87.44	4.83
	30-11-2020	80.0–90.8	88.22	3.06
C_{ab} (μg cm^{-2})	03-09-2020	38.23–44.82	41.96	2.23
	17-09-2020	36.49–52.61	42.21	4.91
	02-10-2020	38.12–52.02	45.33	4.46
	19-10-2020	39.64–45.12	43.08	1.84
	02-11-2020	33.63–42.44	38.29	2.89
	16-11-2020	35.72–44.92	39.41	2.85
	30-11-2020	13.93–48.31	35.32	9.59

Table 2. *Cont.*

Wheat Variable	Date	Range	Mean	SD
AGFB (g)	03-09-2020	15–25	19.67	3.59
	17-09-2020	31–54	42.00	6.83
	02-10-2020	76–175	112.67	27.23
	19-10-2020	47–94	66.00	13.61
	02-11-2020	131–296	213.67	42.41
	16-11-2020	57–101	81.78	15.84
	30-11-2020	73–184	121.60	38.45
AGDB (g)	03-09-2020	2.00–6.00	3.56	1.17
	17-09-2020	9.00–15.00	11.67	2.00
	02-10-2020	23.00–48.00	33.22	8.23
	19-10-2020	8.00–15.00	12.11	2.42
	02-11-2020	38–62	45.67	7.86
	16-11-2020	17–32	26.00	4.22
	30-11-2020	23–70	46.67	14.04

The SPAD-502 instrument (Minolta r) was used to perform C_{ab} measurements. Six leaves per wheat plant were selected randomly at each ESU, and five SPAD values were registered per wheat leaf and then averaged giving a total of 54 C_{ab} values. To extrapolate from SPAD non-dimensional values to C_{ab} values expressed in μg cm^{-2}, the following Equation (15) was implemented:

$$C_{ab}\left[\frac{\mu g}{cm^2}\right] = 12.23e^{0.0279.SPAD} \quad (15)$$

LAI was used to upscale from C_{ab} to *CCC*. Factor 100 led to the correct ground surface unit by upscaling from leaf [μg cm^{-2}] to canopy level [g m^{-2}]:

$$CCC\left[\frac{g}{m^2}\right] = C_{ab}\left[\frac{\mu g}{cm^2}\right] \times LAI \times \frac{1}{100} \quad (16)$$

Plant leaf water content is commonly expressed as equivalent water thickness corresponding to a hypothetical thickness of a single layer of water averaged over the whole leaf area [80]. *EWT* relates the leaf's water content to the leaf's area (*Al*), so it is usually expressed in μg cm^{-2} as follows:

$$EWT = \frac{(FW - DW)}{Al} \left[\mu g\ cm^{-2}\right] \quad (17)$$

Canopy water content (*CWC*) is commonly derived through extrapolation by means of the *LAI*:

$$CWC = EWT \times LAI \left[g\ m^{-2}\right] \quad (18)$$

Due to the linkage of *LAI* to the area of leaves, *CWC* may neglect the water content contained in other organs, such as stalks and fruits. To monitor the total amounts of water stored in wheat plants, leaves, stalks, and fruits were included in our analysis. The *FW* and *DW* values determined in the laboratory per each ESU of the study site (consisting of wheat fresh and dry organic matter) were used as a proxy for the determination of *VWC* expressed in g m^{-2} units. The *VWC* values were then obtained by calculating the difference between the *FW* [g] and *DW* [g] and referring it to the sowing area *A*, implicated in the field data collection process:

$$VWC_h = \frac{(FW - DW)}{A} \left[g\ m^{-2}\right] \quad (19)$$

Equation (19) assumes a wheat plant homogeneously distributed in one square meter of soil, hence we refer here to VWC_h, with the subscript *h* standing for homogeneous.

However, this approach can lead to errors in the estimation of total *VWC* values. During the first growing stages, plants are separated by rows leading to a proportion of the soil visible to the sensor. Since the S2 sensor acquires surface reflectance in a 10 m × 10 m ground sampling distance (GSD), the spectral value of each band summarizes both the soil and vegetation contributions. Only when the wheat crops reach the maximum greenness stage is the soil completely covered by vegetation. Hence, to be more precise in the determination of the *VWC*, we introduced a modification considering in-situ measured *FVC* in the calculation of plant water content per square meter of sowed wheat:

$$VWC = VWC_h \times FVC = \frac{(FW - DW)}{A} \times FVC \ \left[\mathrm{g\ m^{-2}}\right] \quad (20)$$

The calculated wheat *CCC* and *VWC* values were recorded as new inputs of the field campaign database as shown in Table 3.

Table 3. Dates, ranges, mean values, and standard deviations (SD) for calculated variables (CCC and VWC).

Wheat Variable	Date	Range	Mean	SD
CCC ($\mathrm{g\ m^{-2}}$)	03-09-2020	0.06–0.12	0.10	0.02
	17-09-2020	0.22–0.71	0.41	0.16
	02-10-2020	0.74–1.61	1.16	0.29
	19-10-2020	0.60–1.44	1.13	0.23
	02-11-2020	1.18–1.74	1.56	0.17
	16-11-2020	1.22–2.10	1.59	0.34
	30-11-2020	0.64–1.70	1.40	0.29
VWC ($\mathrm{g\ m^{-2}}$)	03-09-2020	207–455	284	70
	17-09-2020	315–1554	666	360
	02-10-2020	868–3021	1996	693
	19-10-2020	494–2240	1315	554
	02-11-2020	944–3083	1777	629
	16-11-2020	1481–3275	2399	589
	30-11-2020	2016–5079	3287	1113

The wheat phenological stage was registered along the BVCR campaign from August to December 2020 (see Figure 3 and Table 4).

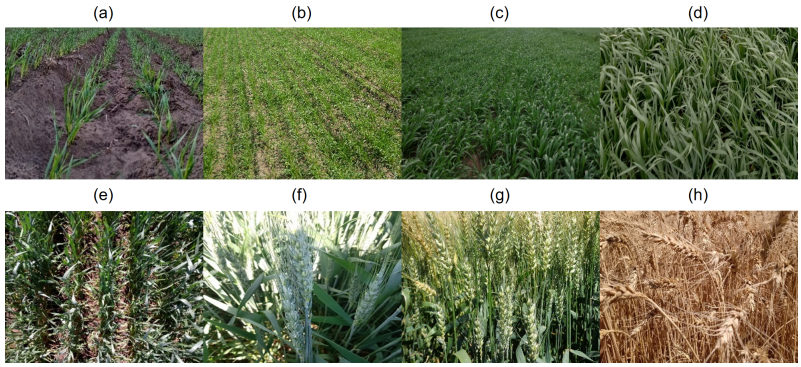

Figure 3. Photographic documentation of wheat crop growing period from August to November 2020, BVCR campaign, corresponding to LAI, FVC, C_{ab}, and AGFB sampling dates. With (**a**) seedling stage at 10 August 2020; (**b**) tillering stage at 4 September 2020; (**c**) tillering stage at 17 September 2020; (**d**) tillering stage at 2 Ocotber 2020; (**e**) ear emergence from boot at 19 October 2020; (**f**) anthesis stage at 2 November 2020; (**g**) dough development at 30 November 2020, first appearance of senescence; (**h**) ripening stage at 16 December 2020, complete senescence.

Table 4. Winter wheat field campaign observations with in-situ sampling dates, crop growth stages and details of the field observations.

In-Situ Measurements Date	Wheat Growth Stage	Field Observations
10-08-2020	Seedling growth Z1.3—Three leaves emerged	Plant density: 248 plants m^{-2} (on average), previous crop: sunflower for seed
03-09-2020	Tillering, 2–3 tillers, Z2.3—Main stem and three tillers	Leaves per tiller 2 + 1 flag leaf
17-09-2020	Tillering, 4 tillers Z2.4—Main stem and four tillers	Leaves per tiller: 3 Irrigation date: 17/09/2020 Fertilization date: 16/09/2020
02-10-2020	Tillering, 5 tillers 4—Booting Z4.3—Boots just visible swollen	Plants height 22 cm from the base to the second node Leaves per tiller: 4
19-10-2020	Ear emergence from boot Z5.5—Ear half emerged	Plants height 71 cm (on average) Plants stem nodes: 5
02-11-2020	Anthesis (flowering) Z6.1—Beginning of anthesis (few anthers at the middle of ear)	Plants height 80 cm (on average)
16-11-2020	Milk development Z7.5—Medium milk	Plants height 80 cm (on average) Start of the senescence
30-11-2020	Dough development Z8.7—Hard dough	Senescence process
16-12-2020	Ripening Z9.7—Seed not dormant	Complete senescence Distance between rows: 19 cm Number of ears at 0.50 cm: 72 on average

2.6. Sentinel-2 Image Acquisitions

A series of S2 images consisting of 15 cloud-free L1C products from 29 August to 11 January 2020 was downloaded from ESA's web server https://scihub.copernicus.eu/ (accessed on 20 June 2022).The S2 images were atmospherically corrected using the Sen2cor plugin [81] to obtain bottom-of-atmosphere (BOA) reflectance data from top-of-atmosphere (TOA) L1C products. As a result, 15 level 2A (L2A) S2 images were obtained, coinciding with ±6 days of in-situ sampling. The images were resampled to 10 m GSD and cropped according to the study site in the SNAP 7.0 software https://step.esa.int/main/snap-7-0-released/ (accessed on 18 July 2022).Bands B1 (443 nm), B9 (940 nm), and B10 (1375 nm) were excluded from the resulting products due to their low GSD of 60 m, being in correspondence to the simulations. Finally, the S2 products composed of ten spectral bands were used for further analysis within the AL optimization process (see Table 5).

Table 5. Field campaign and Sentinel-2 acquisition dates.

In-Situ Measurements Date	S2 Acquisition	±Δ Days
10-08-2020	NA	NA
03-09-2020	29-08-2020	−5
17-09-2020	18-09-2020	+1
02-10-2020	28-09-2020	−4
19-10-2020	13-10-2020	−6
02-11-2020	02-11-2020	0
16-11-2020	17-11-2020	+1
30-11-2020	NA	NA
16-12-2020	22-12-2020	+6

2.7. Delineation of the Hybrid Retrieval Workflow

An overview of the complete hybrid retrieval workflow is given in Figure 4. Three well-distinguished conceptual blocks are detailed, starting with an RTM section, followed by in-situ data collection, and the retrieval of biochemical and biophysical traits. In summary, the implemented retrieval workflow consisted of the following four main steps:

1. generation of the training database, i.e., simulated TOC reflectance with corresponding traits using the PROSAIL-PRO model;
2. building the in-situ database containing multitemporal field measurements from the BVCR site and S2 spectra;
3. optimizing the training database with AL-EBD and GPR, applying retrieval models to obtain wheat LAI, CCC, and VWC; and
4. seasonal mapping of the three crop traits over irrigated wheat fields and corresponding uncertainties using S2 scenes.

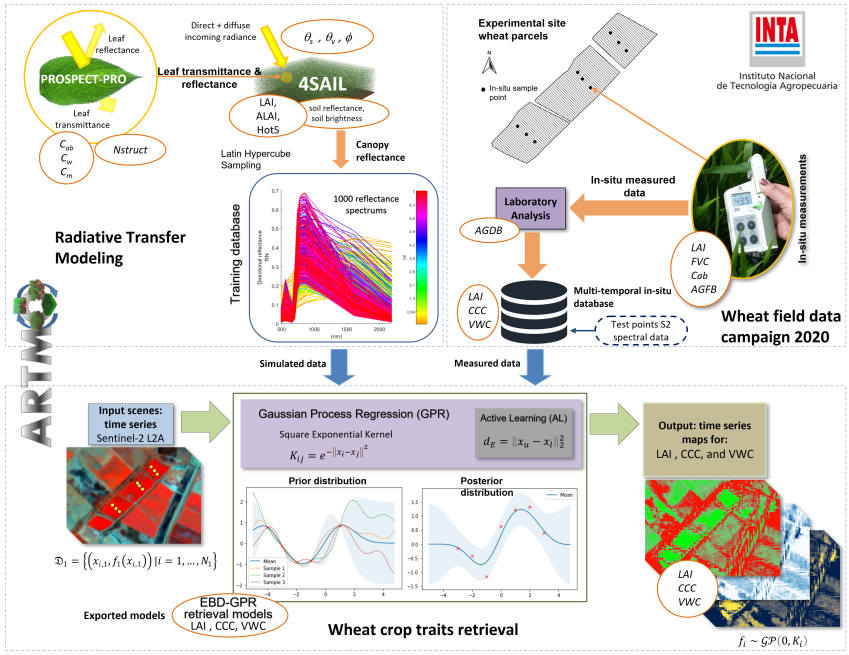

Figure 4. Illustration of the hybrid retrieval workflow using the coupled PROSAIL-PRO models to establish a training database for the GPR, partly adapted from [82]. The output maps show our vegetation traits modeling over the BVCR area in Argentina.

Note that, according to the 2020 wheat campaign observations (see Table 4), the senescence of the crops started on 16 November 2020. In order to prioritize the retrieval models' response within the vegetation greenness period, the in-situ database was restricted from 3 September to 16 November 2020. Additionally, 12 non-vegetated and 27 senescent crop samples were added to the database aiming to improve the robustness of the crop traits retrieval models after starting yellowing and senescing crop growth stages (see Appendix A for more information on the training database). For model evaluation, the coefficient of determination (R^2), the RMSE, the normalized root mean square error (NRMSE), the mean absolute error (MAE), and the mean absolute percentage error (MAPE) were registered for each crop trait model.

The hybrid workflow was entirely built within the Automated Radiative Transfer Models Operator (ARTMO) toolbox [83]. ARTMO was developed as a modular graphical user interface in Matlab, to automate the simulation of RTMs [84]. The toolbox brings multiple RTMs together with essential tools required for the retrieval of a diversity of biophysical and biochemical vegetation traits. ARTMO has been expanded over the years with all kinds of RTMs and image processing options, such as the MLRA toolbox [85] with included AL module [74], emulation, sensitivity analysis, and scene generation. More information can be found at: http://artmotoolbox.com/ (accessed on 18 July 2022).

3. Results

3.1. Optimized Sample Selection for LAI, CCC and VWC Modeling

In order to build efficient GPR-based retrieval models for wheat traits, at first, the AL EBD technique was explored for optimizing the training samples. In Figure 5, we demonstrate the results of training database reduction through EBD as a function of RMSE (left y-axis) and R^2 (right y-axis). For all three variables, an initial dataset of 10 samples was used as starting point for the AL procedure.

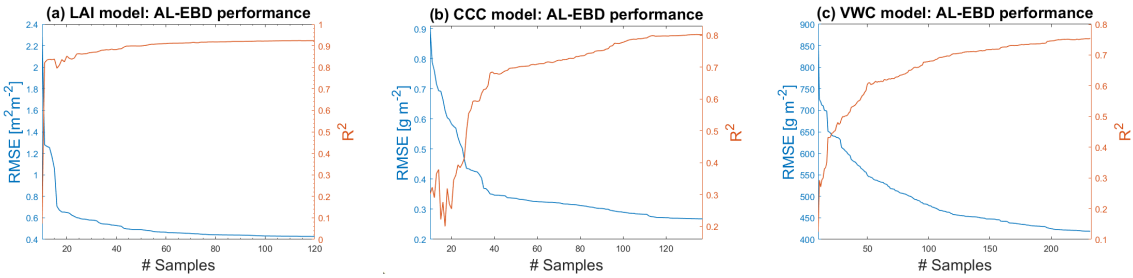

Figure 5. Goodness-of-fit results (RMSE, R^2) using AL (EBD) against validation data. (**a**) LAI model; (**b**) CCC model; (**c**) VWC model.

Figure 5a shows the effect of the training data size on the LAI models' accuracy, with optimal results obtained after adding 112 samples (RMSE: 0.42 m^2 m^{-2}; R^2: 0.92). For CCC, the highest accuracy was obtained after adding 137 samples reaching RMSE: 0.27 g m^{-2} and R^2: 0.8 (see Figure 5b). Figure 5c, shows that the optimal accuracy of the VWC model was achieved after adding 232 samples (RMSE: 416 g m^{-2}; R^2: 0.76). Note hereby that lowering the RMSE does not necessarily go along with an improvement of R^2, as can be read on the right y-axis of Figure 5. Although it follows the same general trends as RMSE, the pattern provided by R^2 is more irregular, indicating it as a less reliable measure than RMSE for AL testing [72].

Figure 6 presents the scatter plots of estimated against in-situ measured LAI, CCC and VWC samples. Overall, values for R^2 and RMSE indicate relatively high agreements between modelled and measured wheat traits. In addition, uncertainties are provided as standard deviation (SD) expressed by the colour table. The SD of LAI, ranging from 0.62 to 1.23 m^2 m^{-2}, provides a proxy of the model's uncertainty and is indicated by the

colour bar close to the regression graph (see Figure 6a). Figure 6b shows the resulting optimised CCC model, with uncertainty interval ranging from 0.2 to 0.48 g m^{-2}. In Figure 6c, the optimised VWC model are displayed, with uncertainty interval ranging from 370 to 542 g m^{-2}.

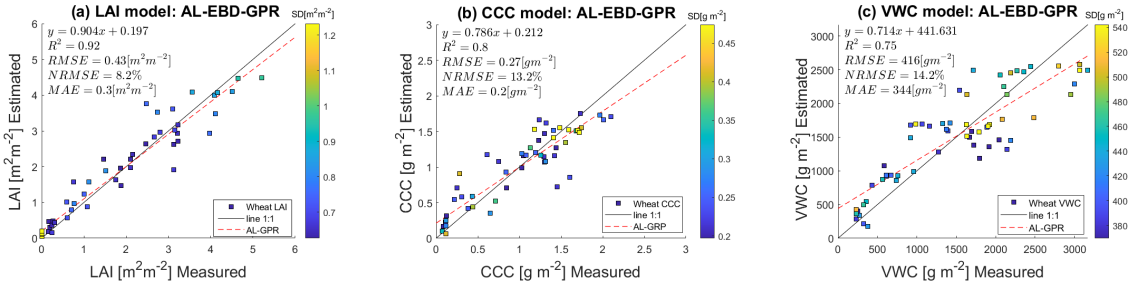

Figure 6. Measuredvs. estimated wheat traits along 1:1-line including uncertainty intervals, using the EBD-optimised training data set. (**a**) LAI model estimates; (**b**) CCC model estimates; (**c**) VWC model estimates.

3.2. Lai, CCC, and VWC Mapping

Next, the optimally trained hybrid GPR models were applied to the six selected dates of the 2020 BVCR wheat campaign. The scenes cover a variety of crop types, including the wheat paddocks selected for this study. Non-vegetated land covers, comprising bare soils, water bodies, and man-made surfaces, were removed from the scenes by applying a vectorial mask.

Figure 7 displays the six S2-derived LAI maps over the BVCR site during the growing season of 2020 (ending 01/2021). All grey-coloured areas correspond to fallow or harvested fields or dried-out natural vegetation. In contrast, LAI distribution of the intensively cultivated crops may vary during the whole growing cycles of the BVCR 2020 campaign. The wheat crop was sown in late June 2020, leading to the emergence of the main wheat stem and three tillers in late August. The highest LAI values during the growing season are identified: LAI reaches a maximum greenness stage at the beginning of November 2020 with 4.12 m^2 m^{-2}. Wheat senescence starts in the middle of November and harvest takes place by the first days of January 2021. Figure 8 shows the multitemporal maps resulting from the CCC estimates for the BVCR study site. The CCC values oscillate between 0 and 2 g m^{-2} being the maximum detected on 2 November. Later in the growing season, from around 16 November 2020 onwards, all wheat parcels exhibited a markedly low CCC driving toward senescence. Due to the linkage between LAI and CCC, both variables are strongly correlated across the whole wheat's growing cycle.

VWC maps are displayed in Figure 9 for the six selected dates of the 2020 BVCR wheat campaign. These maps show spatio-temporal changes in VWC for all crop parcels at the BVCR study site, which were in parity with expected changes in VWC, as driven by rainfall conditions and irrigation management operations during the whole wheat's phenological cycle. Since the VWC was calculated with FVC (see Equation (20)), VWC strongly depends on the percentage of bare soil present in the scene's pixel observed by S2. FVC values widely vary during the vegetation growing period determined primarily by the crop development and structure as well as the implemented crop management practices. Typical VWC values for wheat crop vary from close to 0 g m^{-2} at the start and end of the season to around 2500 g m^{-2} in late November 2020.

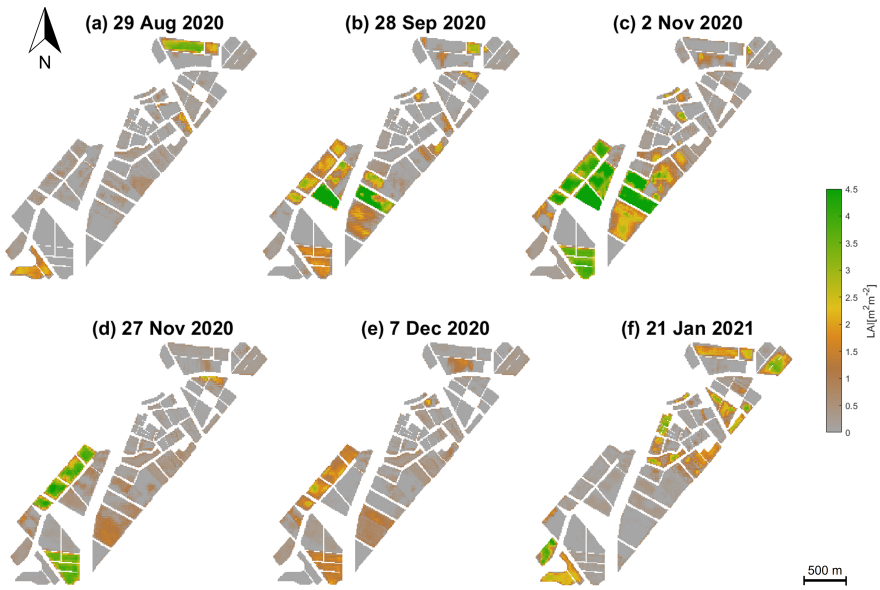

Figure 7. LAI [m^2 m^{-2}] of different crops in the study site, retrieved by the GPR model using simulated vegetation reflectance spectra, in-situ traits measurements and S2 surface multi-spectral reflectance data. Data obtained from BVCR wheat campaign 2020. (**a**) wheat tillering stage at 29 August 2020; (**b**) wheat booting stage at 28 September 2020; (**c**) wheat anthesis-flowering stage at 2 November 2020; (**d**) wheat dough development stage at 27 November 2020; (**e**) wheat ripening stage at 7 December 2020; (**f**) harvested wheat at 21 January 2021.

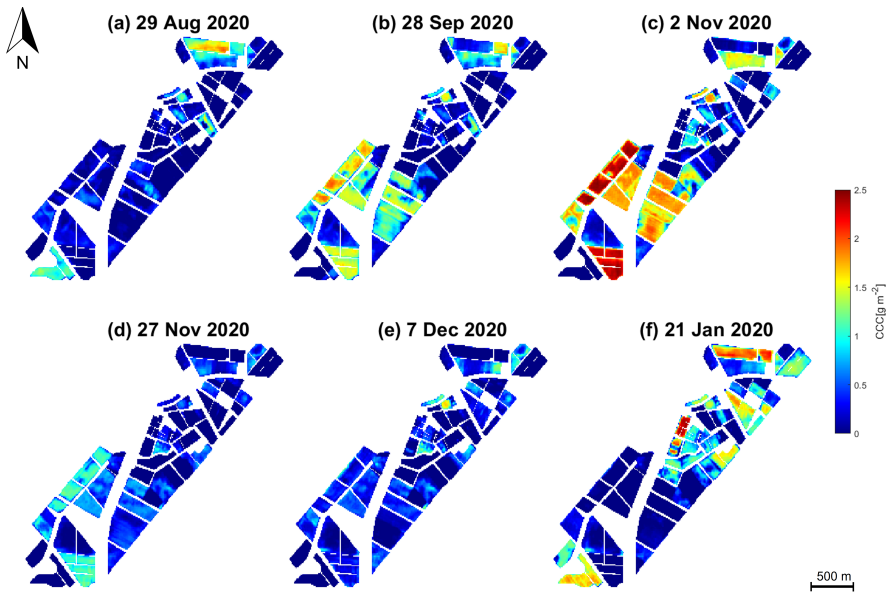

Figure 8. CCC[g m^{-2}] of different crops in the study site, retrieved by the GPR model using simulated vegetation reflectance spectra, in-situ biophysical/biochemical measurements and S2 surface multi-spectral reflectance data. Data obtained from BVCR wheat campaign 2020. (**a**) wheat tillering stage at 29 August 2020; (**b**) wheat booting stage at 28 September 2020; (**c**) wheat anthesis-flowering stage at 2 November 2020; (**d**) wheat dough development stage at 27 November 2020; (**e**) wheat ripening stage at 7 December 2020; (**f**) harvested wheat at 21 January 2021.

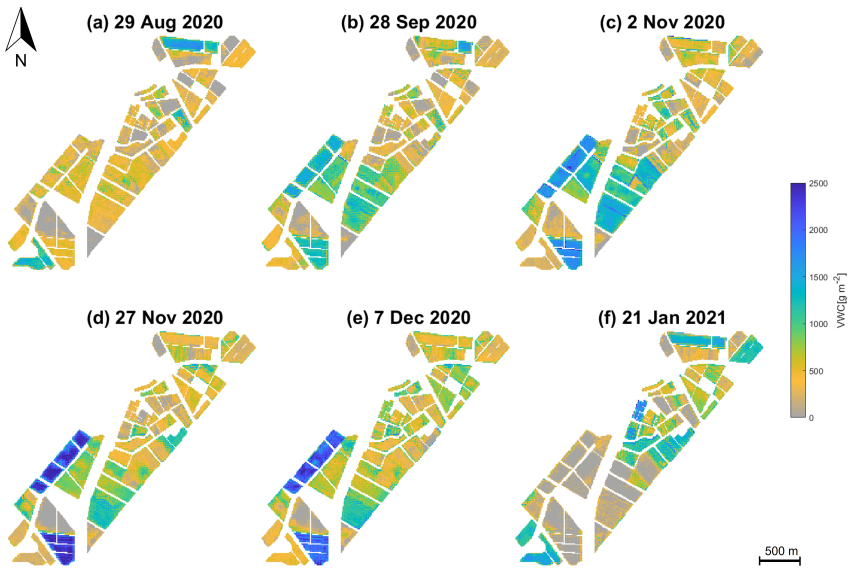

Figure 9. VWC [g m^{-2}] of different crops in the study site, retrieved by the GPR model using simulated vegetation reflectance spectra, in-situ biophysical/biochemical measurements and S2 surface multi-spectral reflectance data. Data obtained from BVCR wheat campaign 2020. (**a**) wheat tillering stage at 29 August 2020; (**b**) wheat booting stage at 28 September 2020; (**c**) wheat anthesis-flowering stage at 2 November 2020; (**d**) wheat dough development stage at 27 November 2020; (**e**) wheat ripening stage at 7 December 2020; (**f**) harvested wheat at 21 January 2021.

3.3. Wheat Phenology Based on Multi-Temporal LAI Maps

According to the Z1.3 state of the Zadoks' scale and collected field data, three leaves of wheat plants emerged in August 2020. Hence, most of the wheat pixels in the S2-observed scene have LAI < 0.5 m^2 m^{-2}. This is clearly noticeable in the LAI map produced for the date 29 August 2020 (see Figure 7a and Table 4). Later in the growing season, around 28 September 2020 (Z4.3, wheat at the tillering stage), all crop parcels revealed distinct LAI growing curves due to field irrigation and fertilization which took place by the third week of September. The S2-derived LAI map for the date 28 September 2020 reveals LAI values of about 2.5 m^2 m^{-2} for the wheat crop (see Figure 7b).

Wheat plants were at the flowering stage on November 2 (Z6.1—few anthers at the middle of the ear) and the plants reached a height of around 80 cm. Hence, LAI ranged from 3.5 to 4.5 m^2 m^{-2} by this date and almost all the cropped pixels at each paddock have experienced the beginning of the anthesis, resulting in higher LAI values (see Figure 7c). Note that some distinct heterogeneities are visible principally in paddock 322; it had a variety of vegetation vigor. In the anthesis stage, the wheat ear arises from the plant stalk, implying that all wheat paddocks are in the flowering stage.

The milk development stage started once the flowering is completed during the month of November, and wheat plants also reached their maximum greenness on 16 November 2020 (Z7.5—Medium milk). Moreover, senescence starts at this time and young leaves may become yellowish. Accordingly, wheat parcels had LAI > 4 m^2 m^{-2}, which represents the LAI curve's inflection point hence from this date onwards LAI decreases until wheat harvest. The wheat traits maps show the early kernel formation stage which occurs one to two weeks after pollination. Once the plants' dehydration period has begun the dough development stage starts. On 30 November (Z8.7—Hard dough), most of the kernel dry weight (starch and protein content) accumulates and therefore LAI < 3.5 m^2 m^{-2} on average, this stage is also known as physiological maturity. The LAI map generated for the date 27 November 2020 displays the decrease of this biophysical variable over the BVCR study site (see Figure 7d) indicating the end of plant growth.

Finally, by the middle of December 2020, wheat parcels revealed complete senescence, and the seed moisture decreased down to 13 to 14%, which corresponds to the ripening stage. The wheat seeds could have been harvested at the end of this stage on 16 December 2020; however, wheat plants remained standing until the first days of January 2021. This can be appreciated in the LAI maps produced for the date 7 December 2020 where (green) LAI values oscillate between 1.5 and 2 m^2 m^{-2} (see Figure 7e). At the end of the ripening stage, the seeds were harvested, which resulted in pronounced decrease in LAI on 4 January 2021 (see Figure 7f).

3.4. Seasonal Analysis of Retrieved Traits

This section explores the seasonal evolution of LAI, CCC and VWC along the wheat 2020 campaign. The trait models were applied to a total of 15 free-cloud L2A S2 scenes to obtain sufficiently dense time series along the wheat seasonal cycle. We also explored the GPR model uncertainty during the course of the season. The uncertainties are mapped in the form of SD to describe the variation of LAI, CCC and VWC values. LAI, CCC and VWC temporal gaps correspond to S2 cloudy acquisitions. Figure 10a displays the temporal profile of retrieved LAI and Figure 10b the LAI SD profiles of the nine in-situ measurement points corresponding to the three paddocks of wheat cropland in the BVCR study site. The figure shows the temporal evolution of the averaged nine ESUs (solid line), and the mean of the in-situ measured LAI values (yellow dots). Figure 10c,d show the temporal profile of the retrieved CCC, the SD, and the mean of the in-situ measured values of all ESUs. Figure 10e,f illustrate the VWC and SD trends. Seasonal patterns of LAI, CCC and VWC reproduce the typical phenological stages of the wheat crop. LAI, CCC and VWC increase steadily, reaching a maximum peak in November 2020. By that time, a plant's dehydration process also emerges, and senescence starts. During the senescence stage, plant water content drops significantly, leading to the wilting of leaves and thus causing

LAI to decrease [86]. Abrupt drops of LAI, CCC and VWC in January 2021 suggest the harvest event.

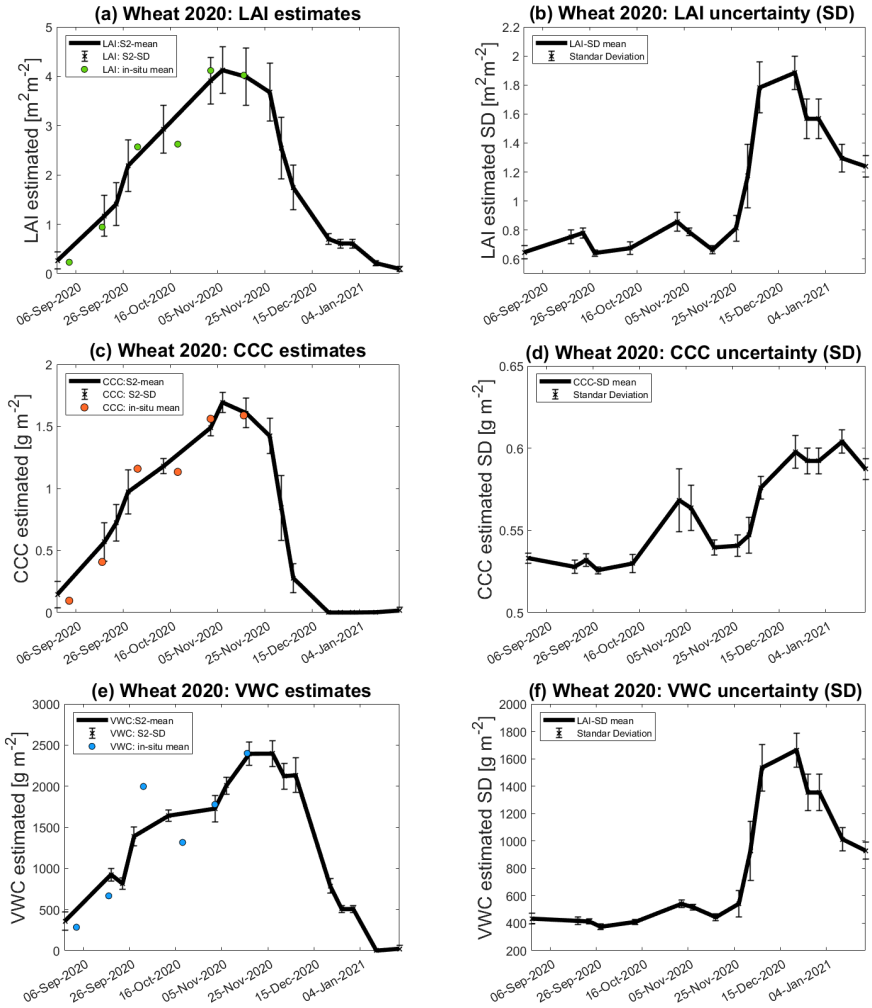

Figure 10. Seasonal evolution of wheat cropland over the three paddocks at the BVCR study sites described by LAI, CCC, and VWC mean values of nice ESUs within the crop limits and the associated uncertainty, plotted as vertical bars. (**a**) LAI estimates; (**b**) LAI uncertainty (SD); (**c**) CCC estimates; (**d**) CCC uncertainty (SD); (**e**) VWC estimates; (**f**) VWC uncertainty (SD).

3.4.1. In-Situ Measured FVC Time Series Analysis of Irrigated Winter Wheat Crops

In the course of wheat tillering, plants reach 10–20 cm height on 17 September and FVC values oscillate between 25–45% (see Figures 3c and 11). The crop leaves remain horizontal during the tillering stage with four leaves per tiller leading to increase of vegetation coverage to FVC about 30–65% on October 2 (see Figure 3d). From the booting stage onwards, the wheat FVC decreases due to plants' stem elongation up to a minimum of 22% on average on November 2. Figure 12b, showing the seasonal patterns of the retrieved LAI vs. the in-situ measured FVC, reflects this behavior: a strong dropping of FVC at the beginning of November (minimum on 2 November), while LAI values remain high in this period (around 3.7 m^2 m^{-2}) and only decrease at the end of November with starting

senescence. This specific behavior of FVC can be explained by the fact that the Canopeo® application uses only the RGB spectral bands to determine the crop canopy coverage.

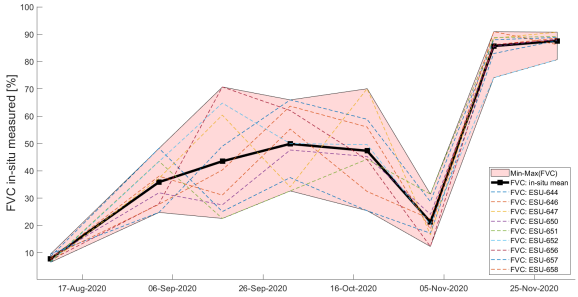

Figure 11. Temporal evolution of wheat crop over the three paddocks at the BVCR study sites described by FVC mean measured values of nine ESUs within the crop limits and the associated SD, which is plotted as shadowed areas.

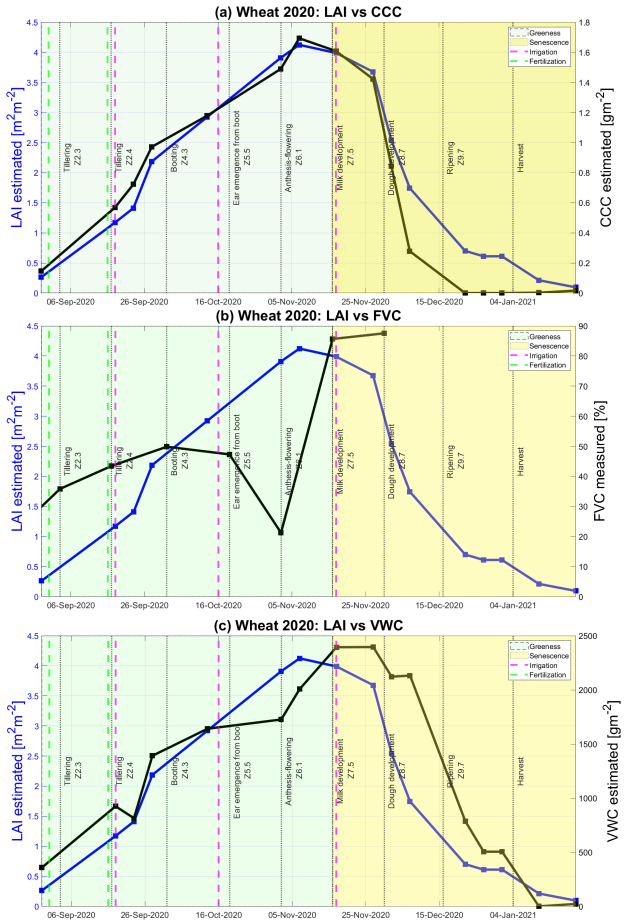

Figure 12. Temporal evolution of wheat cropland over the three paddocks at the BVCR study sites described by LAI, CCC and VWC mean values of nine ESUs within the crop limits and the associated SD, which is plotted as vertical bars. (**a**) LAI vs. CCC temporal estimates; (**b**) LAI temporal estimates vs. FVC in-situ measured values; (**c**) LAI vs. VWC temporal estimates.

Later on in the growing season, by November 16, the FVC values increase up to 86% (see Figure 11). During the senescence period, the FVC values remain high; wheat plants remain standing, and the FVC in-situ measured values range from 80 to 90.8% (see Table 2).

3.4.2. Seasonal Analysis of S2-Retrieved CCC and LAI

Figure 12a presents the temporal profiles of the mean estimated CCC and LAI values along the wheat's seasonal cycle. A strong positive correlation between LAI and CCC temporal profiles can be seen as C_{ab} values have been upscaled with LAI to obtain CCC. CCC retrieved values along the seasonal cycle of winter wheat range from 0 to 1.7 g m^{-2} approximately. At the start of the crop growing season and during the greenness phase, the CCC curve follows the LAI's trend until 27 November. After the vegetation has reached the maximum greenness, which typically corresponds to the LAI peak value, the senescence phase begins until crops are ultimately harvested throughout January 2021. From 27 November onwards, during cropland senescence, the difference between LAI and CCC profiles starts to become more noticeable. On 7 December, $1.5 < LAI < 2$ m^2 m^{-2} indicates the presence of vegetation structures, while $0.2 < CCC < 0.4$ g m^{-2} suggests that the chlorophyll content of wheat plants is declining until, finally, the crop turns yellowish due to the absence of the pigments. According to the in-situ collected notes (see Table 4), the complete senescence for the BVCR 2020 campaign of winter wheat crop at the study site took place by 16 December. Figure 12a shows how the CCC curve drops to zero from 22 December until 21 January. The agreement between both data sources confirms the capability of S2 to retrieve the CCC for monitoring winter wheat croplands.

3.4.3. Seasonal Analysis of S2-Retrieved VWC and LAI

Figure 12c shows the seasonal evolution of the mean estimated value of VWC against LAI. As the VWC model is correlated to FVC in-situ measured values instead of LAI ones, a notorious time shift can be appreciated between the two curves. While the LAI curve describes the leaves' surface per square meter of soil, VWC involves not only the leaves but also the stem and spikes of wheat plants. In addition, third wheat irrigation occurred on 17 November to boost the grain development. Consequently, although senescence had started on 16 November, the VWC values remain high at around 2300 to 2400 g m^{-2} until 27 November. Once the wheat plants have reached the complete senescence by the middle of December 2020, the mature stems remain with a certain level of humidity, thus VWC = 750 g m^{-2} approximately on 22 December.

4. Discussion

With the ambition to develop retrieval models for mapping the diversity of Argentinian winter wheat traits, time-series of S2 imagery was processed to obtain LAI, CCC and VWC maps along the phenological crop cycle in an irrigated, intensively cultivated area. This research is built upon a hybrid retrieval workflow using an optimised simulated training dataset and in-situ measurements of vegetation traits from the BVCR 2020 campaign. In the following, advantages and limitations of the RTMs (Section 4.1), performance of GPR models (Section 4.2), potential of the temporal vegetation traits mapping for wheat agronomic management (Section 4.3), study limitations (Section 4.4), and finally operational monitoring opportunities (Section 4.5) are discussed.

4.1. Advantages and Limitations of Coupled RTMs

Physically-based models simulating the influence of water content and pigments on the obtained signal acquired by satellite sensors potentially lead to improved predictions of crop traits compared to empirical approaches. Regarding the leaf level, we chose the PROSPECT model (i.e., the actual PROSPECT-PRO version), being perhaps the most widely applied leaf RTM in EO vegetation studies. PROSPECT had been first introduced in the 1990s by Jacquemoud et al. [87] and was continuously updated, with for instance improved calibration of the specific absorption coefficients of C_{ab} (introduced in PROSPECT-D [88])

and separation of dry matter content into leaf protein content and carbon-based constituents in PROSPECT-PRO [44]. Although results may not change significantly, the usage of the most actual model version is always recommended. Still, improvements to the model may be required, such as the inclusion of specular reflection [88].

To upscale from leaf to canopy level, C_{ab} and EWT were multiplied by LAI simulated with the SAIL model to obtain CCC and VWC, respectively. The SAIL model assumes that the horizontal direction of the canopy is infinite [45]. Therefore, it is mainly suitable for estimating LAI and other traits of rather continuous and homogeneous crops [89]. Winter wheat is not a pronounced row crop (like maize) but belongs to the grass family (Poaceae). Hence, with its turbid medium assumptions, the choice of SAIL (or PROSAIL when combined with PROSPECT) is justified for our analysis. In addition, we used the simulated FVC data for driving calculations of the VWC training dataset (see Equation (1)). This approach differs from previous studies, e.g., [90,91] where canopy water content was obtained by upscaling EWT by LAI (see Equation (18)).

To optimise the simulated training dataset, we extensively explored the parameterization of winter wheat. Multiple settings were tested to achieve the final VWC model minimising the RMSE. The EWT values ranged from 0.0001 to 0.182 g cm^{-2}, being the most convenient interval presented in Table 1. The in-situ collected variables, LAI, AGFB and AGDB, allowed us to calculate the EWT for winter wheat, involving plant leaves, stalks, and fruits. The calculated EWT values from the campaign data oscillated between 0.019 to 0.175 g cm^{-2}, leading to an uncertainty increase in the final built model (RMSE = 587 g m^{-2}). This can be argued by the fact that EWT implies only water content at the leaf level, whereas field measured data include the water content of all plant organs. Varying the EWT in the PROSAIL-PRO training dataset generation not only affected the VWC model statistics but also the R^2 and RMSE of the LAI and CCC obtained models, which highlighted the sensitivity of PROSAIL-PRO to this leaf variable.

4.2. Performance of Hybrid GPR Models

The proposed workflow is built on the following fundamental factors. First, the careful design of the in-situ measurements methodology led to a collection of high-quality field wheat traits data. Second, the in-situ database covered multi-temporal vegetative stages. In this respect, the GPR models achieved high accuracy for the studied traits, with trustful estimates along the crop greenness phase. Third, we added non-vegetated spectra to the training dataset, i.e., from bare soils, man-made surfaces, and senescent crops as the retrieval models needed to be adapted to the spectral variability of actual land covers of the scenes. Note that, with these additional spectra in the learning process, a slight decrease in the validation may occur; however, more generic wheat traits models can be obtained [58,72].

Active learning provides a powerful and smart sampling method to decrease the redundancy of the training dataset maintaining the spectral variability and thus information content. Finally, from a total of 1000, 112 samples of LAI, 137 samples for CCC, and 232 samples for VWC were intelligently chosen to train the retrieval algorithms. In general terms, the three traits GPR models performed well in learning the nonlinear relationship between the reflectance of S2 spectral bands and LAI, CCC and VWC. This confirms the results of other hybrid studies [59,60,62], where these traits were successfully estimated from S2 data with a GPR model.

The provision of per-pixel associated uncertainty information helps to understand how trustful results are, required to appropriately use the information obtained through a model or measurement [92]. Such information can further indicate the portability of the methods in space and time and is important when the models are being tested across different crops or sites.

The seasonal analysis of LAI, CCC, and VWC revealed differences in the uncertainty for both green and senescent development phases of winter wheat. Generally, low uncertainties refer to spectra that were well represented during the learning phase, whereas retrievals

with high uncertainties refer to spectral information that deviates from what has been represented during the training stage of the models [26]. During the growing season, the availability of in-situ measured traits renders the models more robust and confident. Additionally, the reasonably low uncertainty provided by the GPR retrieval models during this period for most paddocks at the study site suggests reliability in the mapping results. From 16 November onwards, the senescence started, and consequently, winter wheat spectra changed drastically. Additionally, field data were absent for this period; therefore, the uncertainty of the GPR models increased considerably (see Figure 10).

4.3. Potential of Seasonal Traits Mapping for Wheat Agronomic Management

Monitoring of winter wheat traits provides valuable information on the life cycle of the plants needed for efficient crop irrigation and fertilization management being critical factors to crop yield. Winter wheat in our study site was irrigated in the transition between phenological stages. Dates of fertilization were close to those of irrigation since the urea is incorporated into the soil with water, and fertilization occurs first followed by irrigation (see Figure 12). Wheat water absorption depends on the previous hydric stress condition as well as plants' phenological stage. Effects on the vegetation water content can be noticed up to 4 or 5 days after crop irrigation [93–95]. Nitrogen fertilization increases the crop water use efficiency (WUE) due to the higher concentration of nitrogen in plants, leading to improved radiation use efficiency. C_{ab} is positively correlated to photosynthetic activity [96]; consequently, C_{ab} is an indirect indicator of plants' total nitrogen content [97]. Plant stress conditions may affect the photosynthetic process generating nitrogen assimilation and carbon fixation reduction. The leaf chlorophyll content is a genetic attribute of wheat plants; consequently, it remains almost constant during most crop growth stages [3].

CCC monitoring is crucial to understanding plants' photosynthetic activity. Repetitive LAI mapping of winter wheat can provide not only valuable information about plants' leaf area but also a proxy for C_{ab} upscaling to canopy level. CCC monitoring provides useful information to infer plants' salinity and water stress [98,99], as well for the early detection of nitrogen absorption deficiencies and decrease yield associated with plant stress conditions [14,100].

In Figure 12a, the winter wheat fertilization and irrigation dates are presented against the LAI and CCC trends throughout the crop season. The first and second irrigation take place during the tillering stage (Z2.3 and Z2.4 according to the Zadoks growth scale); as a consequence, the slope of the LAI and CCC curves increase. This analysis reveals the potential of the seasonal mapping of irrigated winter wheat traits in Argentina to manage the natural resource usage in arid and semi-arid regions.

The WUE of crops can only be roughly estimated, since, under field conditions, it is arduous to know precisely how much water has been consumed by plants and their growth in accumulated biomass [101]. Consequently, water consumption is usually estimated from indirect data on precipitation and the volume of water lost through runoff, percolation, or direct evaporation from the soil and which has never been consumed by plants [102,103].

Third irrigation occurs during the wheat's milk development stage to boost grain yield (Z7.5 according to Table 4). Figure 12c shows the VWC curve response to this irrigation while LAI has started to decrease by the middle of November 2020.

Well-adjusted VWC models represent an easy-access tool for helping to obtain a response to the most fundamental questions: when and how much to irrigate winter wheat crops in arid and semi-arid regions. To support this analysis, one of the most tested and widespread tools is the hydric balance, which allows for estimating the water content in the soil and deciding the optimal moments of irrigation.

The data fusion of LAI, CCC, and VWC temporal profiles presented in our research constitutes a differentiating element in the field of remote sensing monitoring of irrigated winter wheat development at the study site. (see Sections 3.4.2 and 3.4.3). The potential yield generated by irrigated wheat in the arid region of the focused study site can be compared with the grain production of the harvested winter wheat crops from the agricultural

core area of Argentina. Consequently, monitoring crop traits results is crucial to reducing fertilizer and irrigation water uptake assuring high yields. All these statements point toward the potential of the vegetation traits retrieval models to address the agronomic analysis of irrigated winter wheat crops.

4.4. Study Limitations

Even though the in-situ collected data process was conscientiously carried out, the uncertainty of the measurements and used instruments were not considered in the analysis. However, uncertainty coming from field data has to be kept in mind when assessing the overall accuracy of the retrieval models.

From early August to mid-November, winter wheat plants remain green; thereby, the in-situ LAI samples correspond to the crop's growing season. During this period green, LAI (i.e., GAI) increases as the wheat plants grow. Once crop senescence arrives, plants remain standing and the share of brown leaves increases [13,68]. Each of the winter wheat paddocks was revisited periodically from 10 August to 16 December 2020. The in-situ LAI values were taken from 3 September to the end of the BVCR 2020 wheat campaign; nevertheless, only the green LAI samples were considered to train the LAI model (from 3 September to 16 November). From 16 November to 16 December, in-situ LAI values continue to rise although the cropland has become senescent (see Table 2).

Since in-situ LAI values were used to tune the GPR retrieval models with the AL-EBD techniques, the final LAI retrieval model is better adapted toward green vegetation states. Hence, the uncertainty of the developed models will increase during later (mature/senescent) growing stages.

Finally, it must be noted that our study was conducted with data coming from one single growing season. Thus, temporal transferability to other seasons remains an open question. However, since GPR models provide associated uncertainty estimates, the fidelity of temporal and spatial transferability of the retrieval models to other regions with different cropping environments can be assessed to some degree [104].

4.5. Opportunities for Operational Monitoring

The possibility to estimate the irrigated winter wheat traits at 10 m or 20 m GSD would offer important opportunities for operational precision farming applications. The promising line of hybrid retrieval workflows opens some new branches to be explored in the field of agricultural applications using EO data [105]. The following questions arise: (1) Can we extrapolate the traits models for winter wheat crops to other regions and times? (2) Are the crop traits models sufficiently generic to be applied to other crop types in arid and semi-arid intensively cultivated areas? (3) Are the outcomes of this research useful to address the management of the crops more efficiently, for instance determining when to irrigate and to fertilize optimally?

In this context, the availability of the winter wheat in-situ database obtained from the BVCR 2021 campaign represents an excellent opportunity for the validation and refinement of the developed models and will be explored in a future study.

With respect to the implementation of the GPR models into operational processing, recent possibilities are opened thanks to cloud computing technologies. In a pioneering study, [106] presented an approach on how to integrate GPR models into Google Earth Engine (GEE), e.g., for S2 processing. In this way, the GPR models can be applied anywhere and anytime in the world. Pursuing this approach, first applications already emerged regarding multiple crop traits mapping and monitoring of key growing cycle events (e.g., start/end-of-season) [60] or for wide-scale S2 cropland traits mapping, e.g., over the entirety of Germany [62]. GPR models developed here can be likewise implemented into GEE for monitoring applications. For instance, such a straightforward monitoring interface can help users to understand the appropriate rates and timing of fertilization and irrigation.

5. Conclusions

We presented a hybrid retrieval workflow for operational mapping of LAI, CCC, and VWC that was optimised for an irrigated winter wheat cropland.

The implemented hybrid retrieval method used the advantages of the radiation-surface physics interaction being considered by the RTM and at the same time flexibility, scalability, and computational speed that are provided by GPR. The usage of GPR as a solid probabilistic regression algorithm provides the additional advantage of delivering associated uncertainties along with the trait estimates, helping to assess the fidelity of the mapping results.

The hybrid models for the winter wheat traits were validated with relative high accuracies against in-situ data (LAI: RMSE = 0.43 m^2 m^{-2}; CCC: RMSE = 0.27 g m^{-2}; VWC: RMSE = 416 g m^{-2}). They were subsequently applied to a series S2 imagery during the growing season of 2020 over the South of Buenos Aires Province, Argentina. All produced winter wheat maps showed consistent spatiotemporal performance and relatively low associated uncertainty intervals. The seasonal evolution of the winter wheat crops was quantified by correlating in-situ collected data and interpreting crop growth stages of the S2-derived maps. We conclude that routine mapping of wheat LAI, CCC and VWC constitutes a unique opportunity to monitor irrigated winter wheat development, which will contribute to managing sustainable agricultural production and thus assuring food security.

Author Contributions: G.C., J.D. and J.V. proposed the general objectives and goals of the research; A.P., C.W., P.S.A. and A.C. designed the field campaigns and collected the in-situ data; G.C., J.V. and J.P.R.-C. analyzed the data and obtained the results; G.C. and K.B. wrote the paper; K.B., J.V. and J.D. reviewed the paper and supervised all the procedures. All authors have read and agreed to the published version of the manuscript.

Funding: This research was funded by the European Research Council (ERC) under the ERC-2017-STG SENTIFLEX project (Grant No. 755617) (K.B.) and Ramón y Cajal Contract (Spanish Ministry of Science, Innovation and Universities) (J.V.).

Data Availability Statement: Not applicable.

Acknowledgments: We would especially like to thank the Hilario Ascasubi Agricultural Experimental Station of the National Institute of Agricultural Technology of Argentina for the experimental datasets used in this study. This publication is also the result of the project implementation: "Scientific support of climate change adaptation in agriculture and mitigation of soil degradation" (ITMS2014 + 313011W580) supported by the Integrated Infrastructure Operational Programme funded by the ERDF. The research was also supported by the Action CA17134 SENSECO (Optical synergies for spatiotemporal sensing of scalable ecophysiological traits) funded by COST (European Cooperation in Science and Technology, www.cost.eu (accessed on 22 July 2022)).

Conflicts of Interest: The authors declare no conflict of interest.

Appendix A. EBD-Reduced Final Training Dataset versus Validation Dataset

With the purpose of observing the spectral similarity between the final training data set (Composed of couples of wheat traits and vegetation spectral reflectance simulated by the RTM PROSAIL-PRO) and validation dataset (Composed of wheat traits associated with S2 surface spectral reflectance) from BVCR campaign, both data sets were statistically compared. Figure A1 illustrates averaged training and validation spectra, with standard deviation and ranges in partly transparent colours. It can be observed that the training data match closely with the validation data in the red-edge region and from the NIR on, the difference between them increases. In the visible region of the electromagnetic spectrum, a difference in both training and validation means curves can be appreciated, this phenomenon is attributed to the fact that the MSI on board of S2 satellite integrates vegetation and bare soil reflectance in a 10 × 10 m pixel. The proportionality between vegetation and bare soil for each pixel varies with the fractional vegetation cover. The broader range of the validation data is due to the senescent vegetation and bare soil added spectrums, which

implies a sufficient degree of generalization to ensure that the model is applicable to S2 time series data and able to retrieve the vegetation traits across the complete phenological cycle.

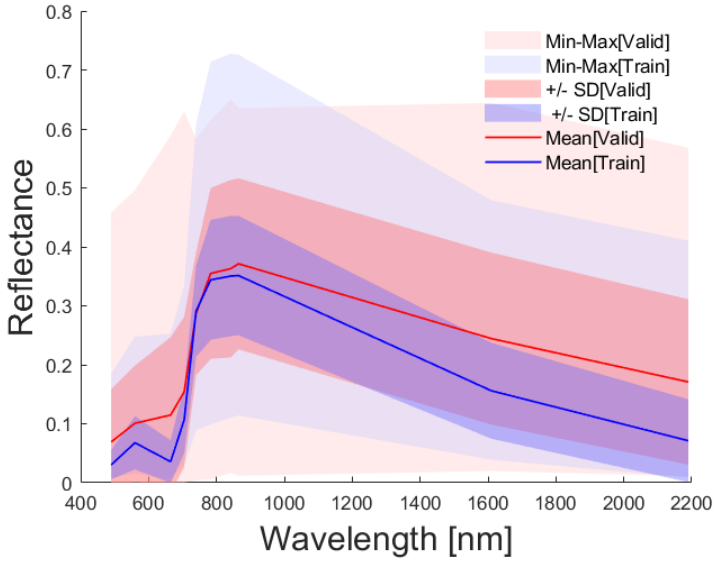

Figure A1. Statistics(mean, standard deviation, min–max) of EBD-reduced final training dataset (blue) vs. validation dataset (red). Training data base was simulated with PROSAIL-PRO.).

References

1. Shiferaw, B.; Smale, M.; Braun, H.J.; Duveiller, E.; Reynolds, M.; Muricho, G. Crops that feed the world 10. Past successes and future challenges to the role played by wheat in global food security. *Food Secur.* **2013**, *5*, 291–317. [CrossRef]
2. Han, D.; Liu, S.; Du, Y.; Xie, X.; Fan, L.; Lei, L.; Li, Z.; Yang, H.; Yang, G. Crop Water Content of Winter Wheat Revealed with Sentinel-1 and Sentinel-2 Imagery. *Sensors* **2019**, *19*, 4013. [CrossRef]
3. Zhang, J.; Han, W.; Huang, L.; Zhang, Z.; Ma, Y.; Hu, Y. Leaf Chlorophyll Content Estimation of Winter Wheat Based on Visible and Near-Infrared Sensors. *Sensors* **2016**, *16*, 437. [CrossRef]
4. Caballero, G.R.; Platzeck, G.; Pezzola, A.; Casella, A.; Winschel, C.; Silva, S.S.; Ludueña, E.; Pasqualotto, N.; Delegido, J. Assessment of Multi-Date Sentinel-1 Polarizations and GLCM Texture Features Capacity for Onion and Sunflower Classification in an Irrigated Valley: An Object Level Approach. *Agronomy* **2020**, *10*, 845. [CrossRef]
5. Fernández-Cirelli, A.; Arumí, J.L.; Rivera, D.; Boochs, P.W. Environmental effects of irrigation in arid and semi-arid regions. *Chil. J. Agric. Res.* **2009**, *69* (Suppl. S1), 27–40. [CrossRef]
6. Hanes, J. *Biophysical Applications of Satellite Remote Sensing*; Springer: Berlin, Germany, 2013.
7. Dong, Q.; Chen, X.; Chen, J.; Zhang, C.; Liu, L.; Cao, X.; Zang, Y.; Zhu, X.; Cui, X. Mapping Winter Wheat in North China Using Sentinel 2A/B Data: A Method Based on Phenology-Time Weighted Dynamic Time Warping. *Remote Sens.* **2020**, *12*, 1274. [CrossRef]
8. Ingram, J.S.I.; Gregory, P.J.; Izac, A.M. The role of agronomic research in climate change and food security policy. *Agric. Ecosyst. Environ.* **2008**, *126*, 4–12. [CrossRef]
9. Hank, T.B.; Bach, H.; Mauser, W. Using a Remote Sensing-Supported Hydro-Agroecological Model for Field-Scale Simulation of Heterogeneous Crop Growth and Yield: Application for Wheat in Central Europe. *Remote Sens.* **2015**, *7*, 3934–3965. [CrossRef]
10. Weiss, M.; Frederic, B.; Smith, G.; Jonckheere, I.; Coppin, P. Review of methods for in situ leaf area index (LAI) determination: Part II. Estimation of LAI, errors and sampling. *Agric. For. Meteorol.* **2004**, *121*, 37–53. [CrossRef]
11. Leblanc, S.G.; Chen, J.M.; Fernandes, R.; Deering, D.W.; Conley, A. Methodology comparison for canopy structure parameters extraction from digital hemispherical photography in boreal forests. *Agric. For. Meteorol.* **2005**, *129*, 187–207. [CrossRef]
12. Duveiller, G.; Weiss, M.; Baret, F.; Defourny, P. Retrieving wheat Green Area Index during the growing season from optical time series measurements based on neural network radiative transfer inversion. *Remote Sens. Environ.* **2011**, *115*, 887–896. [CrossRef]
13. Amin, E.; Verrelst, J.; Rivera-Caicedo, J.P.; Pipia, L.; Ruiz-Verdú, A.; Moreno, J. Prototyping Sentinel-2 green LAI and brown LAI products for cropland monitoring. *Remote Sens. Environ.* **2021**, *255*, 112168. [CrossRef] [PubMed]
14. Schlemmer, M.; Gitelson, A.; Schepers, J.; Ferguson, R.; Peng, Y.; Shanahan, J.; Rundquist, D. Remote estimation of nitrogen and chlorophyll contents in maize at leaf and canopy levels. *Int. J. Appl. Earth Obs. Geoinf.* **2013**, *25*, 47–54. [CrossRef]

15. Baret, F.; Houles, V.; Guérif, M. Quantification of plant stress using remote sensing observations and crop models: The case of nitrogen management. *J. Exp. Bot.* **2007**, *58*, 869–880. [CrossRef] [PubMed]
16. Delloye, C.; Weiss, M.; Defourny, P. Retrieval of the canopy chlorophyll content from Sentinel-2 spectral bands to estimate nitrogen uptake in intensive winter wheat cropping systems. *Remote Sens. Environ.* **2018**, *216*, 245–261. [CrossRef]
17. Berger, K.; Verrelst, J.; Féret, J.B.; Wang, Z.; Wocher, M.; Strathmann, M.; Danner, M.; Mauser, W.; Hank, T. Crop nitrogen monitoring: Recent progress and principal developments in the context of imaging spectroscopy missions. *Remote Sens. Environ.* **2020**, *242*, 111758. [CrossRef]
18. Peñuelas, J.; Filella, I.; Biel, C.; Serrano, L.; Savé, R. The reflectance at the 950–970 nm region as an indicator of plant water status. *Int. J. Remote Sens.* **1993**, *14*, 1887–1905. [CrossRef]
19. Clevers, J.G.P.W.; Kooistra, L.; Schaepman, M.E. Estimating canopy water content using hyperspectral remote sensing data. *Int. J. Appl. Earth Obs. Geoinf.* **2010**, *12*, 119–125. [CrossRef]
20. Zhang, C.; Pattey, E.; Liu, J.; Cai, H.; Shang, J.; Dong, T. Retrieving Leaf and Canopy Water Content of Winter Wheat Using Vegetation Water Indices. *IEEE J. Sel. Top. Appl. Earth Obs. Remote Sens.* **2017**, *11*, 112–126. [CrossRef]
21. Fensholt, R.; Sandholt, I. Derivation of a shortwave infrared water stress index from MODIS near- and shortwave infrared data in a semiarid environment. *Remote Sens. Environ.* **2003**, *87*, 111–121. [CrossRef]
22. Raj, R.; Walker, J.P.; Vinod, V.; Pingale, R.; Naik, B.; Jagarlapudi, A. Leaf water content estimation using top-of-canopy airborne hyperspectral data. *Int. J. Appl. Earth Obs. Geoinf.* **2021**, *102*, 102393. [CrossRef]
23. Rud, R.; Cohen, Y.; Alchanatis, V.; Levi, A.; Brikman, R.; Shenderey, C.; Heuer, B.; Markovitch, T.; Dar, Z.; Rosen, C.; et al. Crop water stress index derived from multi-year ground and aerial thermal images as an indicator of potato water status. *Precis. Agric.* **2014**, *15*, 273–289. [CrossRef]
24. Schott, J.W. Remote Sensing Of The Earth: A Synoptic View. *Phys. Today* **1989**, *42*, 72. [CrossRef]
25. Drusch, M.; Del Bello, U.; Carlier, S.; Colin, O.; Fernandez, V.; Gascon, F.; Hoersch, B.; Isola, C.; Laberinti, P.; Martimort, P.; et al. Sentinel-2: ESA's Optical High-Resolution Mission for GMES Operational Services. *Remote Sens. Environ.* **2012**, *120*, 25–36. [CrossRef]
26. Berger, K.; Verrelst, J.; Féret, J.B.; Hank, T.; Wocher, M.; Mauser, W.; Camps-Valls, G. Retrieval of aboveground crop nitrogen content with a hybrid machine learning method. *Int. J. Appl. Earth Obs. Geoinf.* **2020**, *92*, 102174. [CrossRef]
27. Danner, M.; Berger, K.; Wocher, M.; Mauser, W.; Hank, T. Efficient RTM-based training of machine learning regression algorithms to quantify biophysical & biochemical traits of agricultural crops. *ISPRS J. Photogramm. Remote Sens.* **2021**, *173*, 278–296.
28. Verrelst, J.; Rivera, J.; Camps-Valls, G.; Moreno, J. Recent advances in biophysical parameter retrieval methods—Opportunites for Sentinel-2. In Proceedings of the ESA Living Planet Symposium 2013, Edinbrugh, UK, 9–13 September, 2013.
29. Verrelst, J.; Rivera, J.; Tol, C.; Magnani, F.; Mohammed, G.; Moreno, J. Global sensitivity analysis of the SCOPE model: What drives simulated canopy-leaving sun-induced fluorescence? *Remote Sens. Environ.* **2015**, *166*, 8–21. [CrossRef]
30. Verrelst, J.; Malenovskỳ, Z.; Van der Tol, C.; Camps-Valls, G.; Gastellu-Etchegorry, J.P.; Lewis, P.; North, P.; Moreno, J. Quantifying vegetation biophysical variables from imaging spectroscopy data: A review on retrieval methods. *Surv. Geophys.* **2019**, *40*, 589–629. [CrossRef]
31. Verrelst, J.; Camps-Valls, G.; Muñoz Marí, J.; Rivera, J.; Veroustraete, F.; Clevers, J.; Moreno, J. Optical remote sensing and the retrieval of terrestrial vegetation bio-geophysical properties - A review. *ISPRS J. Photogramm. Remote Sens.* **2015**, *108*, 273–290. [CrossRef]
32. Gitelson, A.; Zur, Y.; Chivkunova, O.; Merzlyak, M. Assessing carotenoid content in plant leaves with reflectance spectroscopy. *Photochem. Photobiol.* **2002**, *75*, 272–281. [CrossRef]
33. Broge, N.H.; Leblanc, E. Comparing prediction power and stability of broadband and hyperspectral vegetation indices for estimation of green leaf area index and canopy chlorophyll density. *Remote Sens. Environ.* **2001**, *76*, 156–172. [CrossRef]
34. Atzberger, C.; Guérif, M.; Baret, F.; Werner, W. Comparative analysis of three chemometric techniques for the spectroradiometric assessment of canopy chlorophyll content in winter wheat. *Comput. Electron. Agric.* **2010**, *73*, 165–173. [CrossRef]
35. Mountrakis, G.; Im, J.; Ogole, C. Support vector machines in remote sensing: A review. *ISPRS J. Photogramm. Remote Sens.* **2011**, *66*, 247–259. [CrossRef]
36. Verger, A.; Baret, F.; Camacho, F. Optimal modalities for radiative transfer-neural network estimation of canopy biophysical characteristics: Evaluation over an agricultural area with CHRIS/PROBA observations. *Remote Sens. Environ.* **2011**, *115*, 415–426. [CrossRef]
37. Jacquemoud, S.; Baret, F.; Andrieu, B.; Danson, F.M.; Jaggard, K. Extraction of vegetation biophysical parameters by inversion of the PROSPECT+SAIL models on sugar beet canopy reflectance data. Application to TM and AVIRIS sensors. *Remote Sens. Environ.* **1995**, *52*, 163–172. [CrossRef]
38. Jacquemoud, S.; Verhoef, W.; Baret, F.; Bacour, C.; Zarco-Tejada, P.; Asner, G.; François, C.; Ustin, S. PROSPECT + SAIL models: A review of use for vegetation characterization. *Remote Sens. Environ.* **2009**, *113*, S56–S66. [CrossRef]
39. Kimes, D.S.; Nelson, R.F.; Manry, M.T.; Fung, A.K. Attributes of neural networks for extracting continuous vegetation variables from optical and radar measurements. *Int. J. Remote Sens.* **1998**, *19*, 2639–2662. [CrossRef]
40. Houborg, R.; Boegh, E. Mapping leaf chlorophyll and leaf area index using inverse and forward canopy reflectance modeling and SPOT reflectance data. *Remote Sens. Environ.* **2008**, *112*, 186–202. [CrossRef]

41. Verrelst, J.; Rivera, J.; van der Tol, C.; Magnani, F.; Mohammed, G.; Moreno, J. Global sensitivity Analysis of the A-SCOPE model in support of future FLEX fluorescence retrievals. In Proceedings of the 5th International Workshop on Remote Sensing of Vegetation Fluorescence, Paris, France, 22–24 April 2014.
42. Jacquemoud, S. PROSPECT + SAIL models: A review of use for vegetation characterization. *Remote Sens. Environ* **2009**, *113*, 56– 66. [CrossRef]
43. Feret, J.B.; François, C.; Asner, G.P.; Gitelson, A.A.; Martin, R.E.; Bidel, L.P.R.; Ustin, S.L.; le Maire, G.; Jacquemoud, S. PROSPECT-4 and 5: Advances in the leaf optical properties model separating photosynthetic pigments. *Remote Sens. Environ.* **2008**, *112*, 3030–3043. [CrossRef]
44. Féret, J.B.; Berger, K.; de Boissieu, F.; Malenovskỳ, Z. PROSPECT-PRO for estimating content of nitrogen-containing leaf proteins and other carbon-based constituents. *Remote Sens. Environ.* **2021**, *252*, 112173. [CrossRef]
45. Verhoef, W. Light scattering by leaf layers with application to canopy reflectance modeling: The SAIL model. *Remote Sens. Environ.* **1984**, *16*, 125–141. [CrossRef]
46. Verhoef, W.; Bach, H. Coupled soil–leaf-canopy and atmosphere radiative transfer modeling to simulate hyperspectral multi-angular surface reflectance and TOA radiance data. *Remote Sens. Environ.* **2007**, *109*, 166–182. [CrossRef]
47. Brede, B.; Verrelst, J.; Gastellu-Etchegorry, J.P.; Clevers, J.G.; Goudzwaard, L.; den Ouden, J.; Verbesselt, J.; Herold, M. Assessment of workflow feature selection on forest LAI prediction with sentinel-2A MSI, landsat 7 ETM+ and Landsat 8 OLI. *Remote Sens.* **2020**, *12*, 915. [CrossRef]
48. Abdelbaki, A.; Udelhoven, T. A Review of Hybrid Approaches for Quantitative Assessment of Crop Traits Using Optical Remote Sensing: Research Trends and Future Directions. *Remote Sens.* **2022**, *14*, 3515. [CrossRef]
49. Rasmussen, C.E.; Williams, C.K.I. *Gaussian Processes for Machine Learning*; The MIT Press: New York, NY, USA, 2006.
50. Verrelst, J.; Muñoz, J.; Alonso, L.; Delegido, J.; Rivera, J.P.; Camps-Valls, G.; Moreno, J. Machine learning regression algorithms for biophysical parameter retrieval: Opportunities for Sentinel-2 and-3. *Remote Sens. Environ.* **2012**, *118*, 127–139. [CrossRef]
51. Verrelst, J.; Rivera, J.; Veroustraete, F.; Muñoz Marí, J.; Clevers, J.; Camps-Valls, G.; Moreno, J. Experimental Sentinel-2 LAI estimation using parametric, non-parametric and physical retrieval methods—A comparison. *ISPRS J. Photogramm. Remote Sens.* **2015**, *108*, 260–272. [CrossRef]
52. Sinha, S.K.; Padalia, H.; Dasgupta, A.; Verrelst, J.; Rivera, J.P. Estimation of leaf area index using PROSAIL based LUT inversion, MLRA-GPR and empirical models: Case study of tropical deciduous forest plantation, North India. *Int. J. Appl. Earth Obs. Geoinf.* **2020**, *86*, 102027. [CrossRef]
53. Verrelst, J.; Alonso, L.; Camps-Valls, G.; Delegido, J.; Moreno, J. Retrieval of Vegetation Biophysical Parameters Using Gaussian Process Techniques. *IEEE Trans. Geosci. Remote Sens.* **2012**, *50*, 1832–1843. [CrossRef]
54. Van Wittenberghe, S.; Verrelst, J.; Rivera, J.P.; Alonso, L.; Moreno, J.; Samson, R. Gaussian processes retrieval of leaf parameters from a multi-species reflectance, absorbance and fluorescence dataset. *J. Photochem. Photobiol. B Biol.* **2014**, *134*, 37–48. [CrossRef]
55. Verrelst, J.; Rivera, J.P.; Gitelson, A.; Delegido, J.; Moreno, J.; Camps-Valls, G. Spectral band selection for vegetation properties retrieval using Gaussian processes regression. *Int. J. Appl. Earth Obs. Geoinf.* **2016**, *52*, 554 – 567. [CrossRef]
56. Xie, R.; Darvishzadeh, R.; Skidmore, A.K.; Heurich, M.; Holzwarth, S.; Gara, T.W.; Reusen, I. Mapping leaf area index in a mixed temperate forest using Fenix airborne hyperspectral data and Gaussian processes regression. *Int. J. Appl. Earth Obs. Geoinf.* **2021**, *95*, 102242. [CrossRef]
57. Camps-Valls, G.; Verrelst, J.; Munoz-Mari, J.; Laparra, V.; Mateo-Jimenez, F.; Gomez-Dans, J. A survey on Gaussian processes for earth-observation data analysis: A comprehensive investigation. *IEEE Geosci. Remote Sens. Mag.* **2016**, *4*, 58–78. [CrossRef]
58. Pascual-Venteo, A.B.; Portalés, E.; Berger, K.; Tagliabue, G.; Garcia, J.L.; Pérez-Suay, A.; Rivera-Caicedo, J.P.; Verrelst, J. Prototyping Crop Traits Retrieval Models for CHIME: Dimensionality Reduction Strategies Applied to PRISMA Data. *Remote Sens.* **2022**, *14*, 2448. [CrossRef]
59. Estévez, J.; Berger, K.; Vicent, J.; Rivera-Caicedo, J.P.; Wocher, M.; Verrelst, J. Top-of-Atmosphere Retrieval of Multiple Crop Traits Using Variational Heteroscedastic Gaussian Processes within a Hybrid Workflow. *Remote Sens.* **2021**, *13*, 1589. [CrossRef]
60. Salinero-Delgado, M.; Estévez, J.; Pipia, L.; Belda, S.; Berger, K.; Paredes Gómez, V.; Verrelst, J. Monitoring Cropland Phenology on Google Earth Engine Using Gaussian Process Regression. *Remote Sens.* **2021**, *14*, 146. [CrossRef]
61. Reyes-Muñoz, P.; Pipia, L.; Salinero-Delgado, M.; Belda, S.; Berger, K.; Estévez, J.; Morata, M.; Rivera-Caicedo, J.P.; Verrelst, J. Quantifying Fundamental Vegetation Traits over Europe Using the Sentinel-3 OLCI Catalogue in Google Earth Engine. *Remote Sens.* **2022**, *14*, 1347. [CrossRef]
62. Estévez, J.; Salinero-Delgado, M.; Berger, K.; Pipia, L.; Rivera-Caicedo, J.P.; Wocher, M.; Reyes-Muñoz, P.; Tagliabue, G.; Boschetti, M.; Verrelst, J. Gaussian processes retrieval of crop traits in Google Earth Engine based on Sentinel-2 top-of-atmosphere data. *Remote Sens. Environ.* **2022**, *273*, 112958. [CrossRef]
63. Adeluyi, O.; Harris, A.; Verrelst, J.; Foster, T.; Clay, G.D. Estimating the phenological dynamics of irrigated rice leaf area index using the combination of PROSAIL and Gaussian Process Regression. *Int. J. Appl. Earth Obs. Geoinf.* **2021**, *102*, 102454. [CrossRef]
64. Perich, G.; Aasen, H.; Verrelst, J.; Argento, F.; Walter, A.; Liebisch, F. Crop Nitrogen Retrieval Methods for Simulated Sentinel-2 Data Using In-Field Spectrometer Data. *Remote Sens.* **2021**, *13*, 2404. [CrossRef]
65. Settles, B. *Active Learning Literature Survey*; University of Wisconsin-Madison Department of Computer Sciences: Madison, WI, USA, 2009.

66. Verrelst, J.; Dethier, S.; Rivera, J.P.; Munoz-Mari, J.; Camps-Valls, G.; Moreno, J. Active learning methods for efficient hybrid biophysical variable retrieval. *IEEE Geosci. Remote Sens. Lett.* **2016**, *13*, 1012–1016. [CrossRef]
67. Berger, K.; Rivera Caicedo, J.P.; Martino, L.; Wocher, M.; Hank, T.; Verrelst, J. A Survey of Active Learning for Quantifying Vegetation Traits from Terrestrial Earth Observation Data. *Remote Sens.* **2021**, *13*, 287. [CrossRef]
68. Delegido, J.; Verrelst, J.; Rivera, J.P.; Ruiz-Verdú, A.; Moreno, J. Brown and green LAI mapping through spectral indices. *Int. J. Appl. Earth Obs. Geoinf.* **2015**, *35*, 350–358. [CrossRef]
69. Pasqualotto, N.; D'Urso, G.; Bolognesi, S.F.; Belfiore, O.R.; Van Wittenberghe, S.; Delegido, J.; Pezzola, A.; Winschel, C.; Moreno, J. Retrieval of Evapotranspiration from Sentinel-2: Comparison of Vegetation Indices, Semi-Empirical Models and SNAP Biophysical Processor Approach. *Agronomy* **2019**, *9*, 663. [CrossRef]
70. Locherer, M.; Hank, T.; Danner, M.; Mauser, W. Retrieval of Seasonal Leaf Area Index from Simulated EnMAP Data through Optimized LUT-Based Inversion of the PROSAIL Model. *Remote Sens.* **2015**, *7*, 10321–10346. [CrossRef]
71. Upreti, D.; Huang, W.; Kong, W.; Pascucci, S.; Pignatti, S.; Zhou, X.; Ye, H.; Casa, R. A comparison of hybrid machine learning algorithms for the retrieval of wheat biophysical variables from sentinel-2. *Remote Sens.* **2019**, *11*, 481. [CrossRef]
72. Verrelst, J.; Rivera-Caicedo, J.P.; Reyes-Muñoz, P.; Morata, M.; Amin, E.; Tagliabue, G.; Panigada, C.; Hank, T.; Berger, K. Mapping landscape canopy nitrogen content from space using PRISMA data. *ISPRS J. Photogramm. Remote Sens.* **2021**, *178*, 382–395. [CrossRef]
73. Liang, L.; Geng, D.; Yan, J.; Qiu, S.; Di, L.; Wang, S.; Xu, L.; Wang, L.; Kang, J.; Li, L. Estimating Crop LAI Using Spectral Feature Extraction and the Hybrid Inversion Method. *Remote Sens.* **2020**, *12*, 3534. [CrossRef]
74. Verrelst, J.; Berger, K.; Rivera-Caicedo, J.P. Intelligent sampling for vegetation nitrogen mapping based on hybrid machine learning algorithms. *IEEE Geosci. Remote Sens. Lett.* **2020**, 18, 2038–2042. [CrossRef]
75. Douak, F.; Melgani, F.; Benoudjit, N. Kernel ridge regression with active learning for wind speed prediction. *Appl. Energy* **2013**, *103*, 328–340. [CrossRef]
76. Zadoks, J.C.; Chang, T.T.; Konzak, C.F. A decimal code for the growth stages of cereals. *Weed Res.* **1974**, *14*, 415–421. [CrossRef]
77. Confalonieri, R.; Foi, M.; Casa, R.; Aquaro, S.; Tona, E.; Peterle, M.; Boldini, A.; De Carli, G.; Ferrari, A.; Finotto, G.; et al. Development of an app for estimating leaf area index using a smartphone. Trueness and precision determination and comparison with other indirect methods. *Comput. Electron. Agric.* **2013**, *96*, 67–74. [CrossRef]
78. Patrignani, A.; Ochsner, T.E. Canopeo: A Powerful New Tool for Measuring Fractional Green Canopy Cover. *Agron. J.* **2015**, *107*, 2312–2320. [CrossRef]
79. Gamiely, S.; Randle, W.M.; Mills, H.A.; Smittle, D.A. A Rapid and Nondestructive Method for Estimating Leaf Area of Onions. *HortScience* **1991**, *26*, 206. [CrossRef]
80. Danson, F.M.; Steven, M.D.; Malthus, T.J.; Clark, J.A. High-spectral resolution data for determining leaf water content. *Int. J. Remote Sens.* **1992**, *13*, 461–470. [CrossRef]
81. Louis, J.; Debaecker, V.; Pflug, B.; Main-Knorn, M.; Bieniarz, J.; Mueller-Wilm, U.; Cadau, E.; Gascon, F. SENTINEL-2 SEN2COR: L2A Processor for Users. In Proceedings of the ESA Living Planet Symposium 2016, Prague, Czech Republic, 9–13 May 2016; Ouwehand, L., Ed.; Spacebooks Online; ESA Special Publications (on CD); Volume SP-740, pp. 1–8.
82. Berger, K.; Atzberger, C.; Danner, M.; Wocher, M.; Mauser, W.; Hank, T. Model-Based Optimization of Spectral Sampling for the Retrieval of Crop Variables with the PROSAIL Model. *Remote Sens.* **2018**, *10*, 2063. [CrossRef]
83. Verrelst, J.; Rivera, J.; Alonso, L.; Moreno, J. ARTMO: An Automated Radiative Transfer Models Operator toolbox for automated retrieval of biophysical parameters through model inversion. In Proceedings of the EARSeL 7th SIG-Imaging Spectroscopy Workshop, Edinburgh, UK, 11–13 April 2011.
84. Verrelst, J.; Romijn, E.; Kooistra, L. Mapping Vegetation Density in a Heterogeneous River Floodplain Ecosystem Using Pointable CHRIS/PROBA Data. *Remote Sens.* **2012**, *4*, 2866–2889. [CrossRef]
85. Caicedo, J.; Verrelst, J.; Munoz-Mari, J.; Moreno, J.; Camps-Valls, G. Toward a semiautomatic machine learning retrieval of biophysical parameters. *IEEE J. Sel. Top. Appl. Earth Obs. Remote Sens.* **2014**, *7*, 1249–1259. [CrossRef]
86. Smit, M.A.; Singels, A. The response of sugarcane canopy development to water stress. *Field Crops Res.* **2006**, *98*, 91–97. [CrossRef]
87. Jacquemoud, S.; Ustin, S.L.; Verdebout, J.; Schmuck, G.; Andreoli, G.; Hosgood, B. Estimating leaf biochemistry using the PROSPECT leaf optical properties model. *Remote Sens. Environ.* **1996**, *56*, 194–202. [CrossRef]
88. Féret, J.B.; Gitelson, A.A.; Noble, S.D.; Jacquemoud, S. PROSPECT-D: Towards modeling leaf optical properties through a complete lifecycle. *Remote Sens. Environ.* **2017**, *193*, 204–215. [CrossRef]
89. Ma, X.; Lu, L.; Ding, J.; Zhang, F.; He, B. Estimating Fractional Vegetation Cover of Row Crops from High Spatial Resolution Image. *Remote Sens.* **2021**, *13*, 3874. [CrossRef]
90. Danner, M.; Berger, K.; Wocher, M.; Mauser, W.; Hank, T. Fitted PROSAIL parameterization of leaf inclinations, water content and brown pigment content for winter wheat and maize canopies. *Remote Sens.* **2019**, *11*, 1150. [CrossRef]
91. Wocher, M.; Berger, K.; Danner, M.; Mauser, W.; Hank, T. Physically-based retrieval of canopy equivalent water thickness using hyperspectral data. *Remote Sens.* **2018**, *10*, 1924. [CrossRef]
92. Povey, A.C.; Grainger, R.G. Known and unknown unknowns: Uncertainty estimation in satellite remote sensing. *Atmos. Meas. Tech.* **2015**, *8*, 4699–4718. [CrossRef]

93. Ali, Z.; Merrium, S.; Habib-ur Rahman, M.; Hakeem, S.; Saddique, M.A.B.; Sher, M.A. Wetting mechanism and morphological adaptation; leaf rolling enhancing atmospheric water acquisition in wheat crop—A review. *Environ. Sci. Pollut. Res.* **2022**, *29*, 30967–30985. [CrossRef] [PubMed]
94. Gil, H.M.; Salort, J.B.; Llompart, J.C.; Sans, J.F.; Carbó, M.R.; León, J.G. Eficiencia en el uso del agua por las plantas. *Investig. Geográficas* **2007**, 63–84. [CrossRef]
95. Sánchez, R.; Pezzola, N.; Cepeda, J. Caracterización edafoclimátia del área de influencia del INTA E.E.A Hilario Ascasubi. *Boletín Divulgación* **1998**, *18*, 72.
96. Delegido, J.; Verrelst, J.; Alonso, L.; Moreno, J. Evaluation of sentinel-2 red-edge bands for empirical estimation of green LAI and chlorophyll content. *Sensors* **2011**, *11*, 7063–7081. [CrossRef]
97. Salisbury, F.B.; Ross, C.W. *Fisiología Vegetal*; Grupo Editorial Iberoamérica: Mexico City, Mexico, 1994.
98. Delegido, J.; Alonso, L.; González, G.; Moreno, J. Estimating chlorophyll content of crops from hyperspectral data using a normalized area over reflectance curve (NAOC). *Int. J. Appl. Earth Obs. Geoinf.* **2010**, *12*, 165–174. [CrossRef]
99. Elarab, M.; Ticlavilca, A.M.; Torres-Rua, A.F.; Maslova, I.; McKee, M. Estimating chlorophyll with thermal and broadband multispectral high resolution imagery from an unmanned aerial system using relevance vector machines for precision agriculture. *Int. J. Appl. Earth Obs. Geoinf.* **2015**, *43*, 32–42. [CrossRef]
100. Cammarano, D.; Fitzgerald, G.; Basso, B.; O'Leary, G.; Chen, D.; Grace, P.; Fiorentino, C. Use of the Canopy Chlorophyl Content Index (CCCI) for Remote Estimation of Wheat Nitrogen Content in Rainfed Environments. *Agron. J.* **2011**, *103*, 1597–1603. [CrossRef]
101. Irmak, S. Evapotranspiration. In *Encyclopedia of Ecology*; Academic Press: Cambridge, MA, USA, 2008; pp. 1432–1438. [CrossRef]
102. Zeleke, K.T.; Wade, L.J. Evapotranspiration Estimation Using Soil Water Balance, Weather and Crop Data. In *Evapotranspiration-Remote Sensing and Modeling*; INTECH: Rijeka, Croatia, 2012; pp. 41–58.
103. Darouich, H.; Ramos, T.B.; Pereira, L.S.; Rabino, D.; Bagagiolo, G.; Capello, G.; Simionesei, L.; Cavallo, E.; Biddoccu, M. Water Use and Soil Water Balance of Mediterranean Vineyards under Rainfed and Drip Irrigation Management: Evapotranspiration Partition and Soil Management Modelling for Resource Conservation. *Water* **2022**, *14*, 554. [CrossRef]
104. Verrelst, J.; Rivera, J.; Moreno, J.; Camps-Valls, G. Gaussian processes uncertainty estimates in experimental Sentinel-2 LAI and leaf chlorophyll content retrieval. *ISPRS J. Photogramm. Remote Sens.* **2013**, *86*, 157–167. [CrossRef]
105. Machwitz, M.; Pieruschka, R.; Berger, K.; Schlerf, M.; Aasen, H.; Fahrner, S.; Jiménez-Berni, J.; Baret, F.; Rascher, U. Bridging the Gap Between Remote Sensing and Plant Phenotyping—Challenges and Opportunities for the Next, Generation of Sustainable Agriculture. *Front. Plant Sci.* **2021**, 2334. [CrossRef] [PubMed]
106. Pipia, L.; Amin, E.; Belda, S.; Salinero-Delgado, M.; Verrelst, J. Green LAI Mapping and Cloud Gap-Filling Using Gaussian Process Regression in Google Earth Engine. *Remote Sens.* **2021**, *13*, 403. [CrossRef] [PubMed]

ARTÍCULO 2

"Quantifying Irrigated Winter Wheat LAI in Argentina Using Multiple Sentinel-1 Incidence Angles"

This article belongs to the Special Issue Remote Sensing of Vegetation Biochemical and Biophysical Parameters of the Remote Sensing Journal. Journal Rank: JCR - Q1 (Geosciences, Multidisciplinary) / Cite Score - Q1 (General Earth and Planetary Sciences). The article was published in November 2022. This journal had an impact factor of 5.349 in 2022.

remote sensing

MDPI

Article

Quantifying Irrigated Winter Wheat LAI in Argentina Using Multiple Sentinel-1 Incidence Angles

Gabriel Caballero [1,2,*], Alejandro Pezzola [3], Cristina Winschel [3], Alejandra Casella [4], Paolo Sanchez Angonova [3], Luciano Orden [3,5], Katja Berger [2,6], Jochem Verrelst [2] and Jesús Delegido [2]

[1] Agri-Environmental Engineering, Technological University of Uruguay (UTEC), Av. Italia 6201, Montevideo 11500, Uruguay
[2] Image Processing Laboratory (IPL), University of Valencia, C/Catedrático José Beltrán 2, Paterna, 46980 Valencia, Spain
[3] Remote Sensing and SIG Laboratory, Hilario Ascasubi Agricultural Experimental Station, National Institute of Agricultural Technology (INTA), Hilario Ascasubi 8142, Argentina
[4] Permanent Observatory of Agro-Ecosystems, Climate and Water Institute-National Agricultural Research Centre (ICyA-CNIA), National Institute of Agricultural Technology (INTA), Nicolás Repetto s/n, Hurlingham, Buenos Aires 1686, Argentina
[5] Centro de Investigación e Innovación Agroalimentaria y Agroambiental (CIAGRO-UMH), GIAAMA Research Group, Universidad Miguel Hernández, Carretera de Beniel Km, 03312 Orihuela, Spain
[6] Mantle Labs GmbH, Grünentorgasse 19/4, 1090 Vienna, Austria
* Correspondence: gabriel.caballero@utec.edu.uy; Tel.: +34-685-829-332

Abstract: Synthetic aperture radar (SAR) data provides an appealing opportunity for all-weather day or night Earth surface monitoring. The European constellation Sentinel-1 (S1) consisting of S1-A and S1-B satellites offers a suitable revisit time and spatial resolution for the observation of croplands from space. The C-band radar backscatter is sensitive to vegetation structure changes and phenology as well as soil moisture and roughness. It also varies depending on the local incidence angle (LIA) of the SAR acquisition's geometry. The LIA backscatter dependency could therefore be exploited to improve the retrieval of the crop biophysical variables. The availability of S1 radar time-series data at distinct observation angles holds the feasibility to retrieve leaf area index (LAI) evolution considering spatiotemporal coverage of intensively cultivated areas. Accordingly, this research presents a workflow merging multi-date S1 smoothed data acquired at distinct LIA with a Gaussian processes regression (GPR) and a cross-validation (CV) strategy to estimate cropland LAI of irrigated winter wheat. The GPR-S1-LAI model was tested against in situ data of the 2020 winter wheat campaign in the irrigated valley of Colorador river, South of Buenos Aires Province, Argentina. We achieved adequate validation results for LAI with R^2_{CV} = 0.67 and $RMSE_{CV}$ = 0.88 m^2 m^{-2}. The trained model was further applied to a series of S1 stacked images, generating temporal LAI maps that well reflect the crop growth cycle. The robustness of the retrieval workflow is supported by the associated uncertainties along with the obtained maps. We found that processing S1 smoothed imagery with distinct acquisition geometries permits accurate radar-based LAI modeling throughout large irrigated areas and in consequence can support agricultural management practices in cloud-prone agri-environments.

Keywords: leaf area index; Sentinel-1; time-series; local incidence angle; Whittaker smoother; Gaussian processes regression

Citation: Caballero, G.; Pezzola, A.; Winschel, C.; Casella, A.; Sanchez Angonova, P.; Orden, L.; Berger, K.; Verrelst, J.; Delegido, J. Quantifying Irrigated Winter Wheat LAI in Argentina Using Multiple Sentinel-1 Incidence Angles. *Remote Sens.* **2022**, *14*, 5867. https://doi.org/10.3390/rs14225867

Academic Editor: Yongshuo Fu

Received: 25 October 2022
Accepted: 14 November 2022
Published: 19 November 2022

1. Introduction

Remote sensing synthetic aperture radar (SAR) satellites have ample potential for the monitoring of vegetation biophysical variables [1–3]. Radar, as a valuable Earth observation (EO) source, allows all-weather image acquisition even during day or night time. In most tropical and cloudy regions, the usage of optical satellite imagery is often restricted to cloud-free acquired scenes typically related to a dry season [4]. This condition makes SAR data

attractive for year-round cropland biophysical variable retrieval [5]. In recent years, the exponential evolution of EO as an applied science has generated an unprecedented amount of research using SAR satellite data for crop trait monitoring over large areas, e.g., [6–12]. At the field scale, various studies have employed radar backscatter to find a relationship between the electromagnetic signal and vegetation dynamics [7]. Ferrazzoli et al. [13] found a strong correlation between C-band HV-polarized backscatter and the biomass of colza, wheat, and alfalfa crops (R^2 = 0.75). Frequently, cross-polarized (CP) radar backscatter is most sensitive to volume scattering mechanisms such as those produced by the vegetation. High correlations have been found between C-Band CP backscatter and crop biophysical variables such as leaf area index (LAI) and biomass [13,14].

The radar backscatter signal is influenced by cropland biomass and the three-dimensional structure of vegetation [15] and also by the ground soil moisture and roughness [16]. The radar acquisition geometry configurations used for the observations play a significant role [17–19]. Regarding vegetation trait retrieval based on radar signals, monitoring of wheat croplands deserves special attention. Multiple studies have explored the backscatter-vegetation structure interaction for winter wheat crops [20–25]. There is consensus that the vegetation backscatter merges the contribution of the soil-canopy interaction (surface scattering) with the backscatter from the canopy layer (volumetric scattering). Regarding wheat plant structure, the following dominant backscatter sources can be distinguished: stem, leaves, and ears [20]. The wheat phenological stage plays a significant role in the vegetation scattering detected by the spaceborne radar instruments [26].

SAR time-series data has been used to track the complete phenological cycle of summer (sunflower, maize, and soybean) and winter (barley, rapeseed, and wheat) crops [27]. SAR imagery for cropland monitoring strongly depends on the radar backscatter incidence angle, thus, it is one of the most critical obstacles [28]. The local incidence angle (LIA) is depicted by the incident radar beam and the normal to the surface, considering local relief, typically derived from a digital elevation model (DEM) [29]. When a homogeneous crop paddock is monitored regularly using radar data, the variability of the backscatter can be attributed, among others, to the LIA of the acquired radar scenes. LIA values between 35º and 40º maximize the vegetation's volumetric scattering increasing the path length of the radar signal [30]. At the other extreme, incidence angles lower than 30º increase the ground surface scattering related mainly to soil moisture and roughness [31]. For scenes observed at shallow incidence angles, the backscatter is lower than those acquired at steeper incidence angles; in consequence, the same backscatter element in a radar resolution cell has distinct and incomparable values of backscatter coefficient for distinct local incidence angles of observation [32,33]. Accounting for angularity, Kaplan et al. [22] studied two transformations that allow the collective usage of Sentinel-1 (S1) imagery for agricultural monitoring of wheat, tomatoes, and cotton in Israel. They normalized the local incidence angle to improve the empirical prediction of LAI.

S1 is a C-band SAR satellite constellation of the Copernicus program belonging to the European Space Agency (ESA). As the pre-defined observation strategy over land, S1 defines the interferometric wide swath (IW) mode. This mode is available for most of the applications in dual-polarization (VV and VH), at 10 × 10 m spatial resolution in a swath of 250 km [34]. S1 mission consisting of S1-A and S1-B satellites provides exhaustive monitoring of Earth's surface once every 6 days at the equator, in a single pass (ascending or descending) for one specific relative orbit. In intensive agriculture sites where several S1 relative orbits lead to multiple-path radar observations, dense time-series of sundry acquisition geometries can be obtained for the same cropland. Vegetation's structure geometry, as a proxy of the radar backscatter, changes as a function of the local incidence angle and plants' growth [16].

The S1 polarimetric bands VH and VV at the C-band provide relevant information on surface scattering (VV polarization) and vegetation volumetric scattering (VH polarization), which allows monitoring of soil moisture and roughness as well as vegetation biophysical parameters. The relationship between the S1 polarimetric bands and the vegetation

traits can be linear or nonlinear. Harfenmeister et al. [35] applied linear and exponential regressions to assess the correlation between absolute and relative vegetation water content, LAI and plant height, and the S1 VH + VV bands. The nonlinear relationship between the S1 polarimetric data and vegetation properties, such as LAI, can be learned by machine learning regression algorithms (MLRA). Considering this strategy, in the last few decades, a variety of MLRAs have been auspiciously applied for recovery tasks mainly on optical data, e.g., decision trees, artificial neural networks, or kernel-based methods [36,37]. Gaussian process regression (GPR) [38] arose as a advantageous kernel-based non-parametric regression and has been broadly utilized in studies retrieving vegetation's traits from EO data [39–47]. GPR as probabilistic MLRA also provides the uncertainty of the estimates making it an appealing option for vegetation trait confidence mapping.

Research in time-series remote sensing data is receiving large attention. The construction of high spatio-temporal data cubes derived from multi-temporal EO images requires the implementation of a data smoothing process to facilitate the processing and analysis of time-series [48]. The Whittaker smoother emerged as an attractive algorithm for filtering EO data in the presence of data gaps [49]. The algorithm is easy and intuitive to use, often gives superior results faster than the widely used Savitzky–Golay smoother [50].

When it comes to the viability of generating vegetation trait maps from S1 time-series data, several experimental studies made use of the polarimetric bands considering the same relative orbit [17,51]. However, the backscatter variation at distinct local incidence angles for crop biophysical variables monitoring has been left largely unexploited. Therefore, and with the ambition to improve vegetation trait retrieval, this research aims to assess the potential of combining S1-A and S1-B C-band high-resolution SAR data acquired at distinct local incidence angles. To assess the possibilities of continuously monitoring cropland's traits with a space-based strategy, this study carries out the development of an S1-based LAI retrieval workflow devoted to irrigated winter wheat cropland monitoring in Argentina. Given the above-sketched general framework, the following three sub-objectives can be defined: (1) to develop a GPR model for an explicit quantification of winter wheat LAI from S1-A and S1-B smoothed data acquired at multiple local incidence angles; (2) to generate accurate S1-based maps of the wheat LAI with the inclusion of associated uncertainties over an intensive irrigated agroecosystem; and (3) to evaluate LAI time-series identifying phenological stages over the selected study site.

2. Materials and Methods

2.1. Theoretical Background

Aiming to describe the theoretical framework implemented in our research, this section presents the mathematical formulations of the Gaussian processes regression algorithm (Section 2.1.1) and the optimized Whittaker smoother (Section 2.1.2).

2.1.1. Gaussian Processes Regression

During the last decade, GPR has been widely adopted for bio-geo science applications [52]. GPR generalizes the Gaussian probability distribution in a function's space. This means an expected covariance between values of the function at a given point [38]. In short, a GPR model establishes a relation between the input (here: S1 polarimetric bands) $x \in \mathrm{R}^{\mathbb{B}}$ and the output variable (vegetation's biophysical variable to be retrieved) $y \in \mathbb{R}$. Being $x = [x^1, \ldots, x^B] \in \mathbb{R}^B$ the S1 polarimetric training dataset and $y \in \mathbb{R}$ the model's output estimates, the mean expected value $\hat{y}$ for a given x_* can be expressed in the form:

$$\widehat{y_*} = f(x_*) = \sum_{i=1}^{N} \alpha_i k_\theta(x_i, x_*) + \alpha_0, \quad (1)$$

where $\{x_i\}_{i=1}^{N}$ are the S1 polarimetric features used in the learning (or training) phase, $\alpha_i \in \mathbb{R}$ is the weight assigned to each one of them, α_0 a constant value (bias) of the regression function, and k_θ is a covariance function (or kernel) assessing the similarity between the

test S1 polarimetric data x_* and all N x_i in the training dataset. The regression kernel is parameterized by a set of parameters $\theta = [v,\ \sigma_n, \sigma_1, \ldots \sigma_B]$.

The core of GPR as a kernel method relies on a convenient definition of the covariance function. We implemented automatic relevance determination (ARD) as a kernel function k_θ, which can be noted as:

$$k(x_i, x_j) = v\ exp\left(-\sum_{b=1}^{B} \frac{\left(x_i^b - x_j^b\right)^2}{2\sigma_b^2}\right) + \sigma_n^2 \delta_{ij}, \tag{2}$$

where x_i^b represents the feature f of the input vector x_i, v is a scaling factor, σ_b is the standard deviation of the observations assumed to be noisy, σ_f is the length scale per S1 input feature (b = 1,..., B), and δ_{ij} is the correlation length scale parameter.

ARD is a widely used covariance function that typically suffices to address most of the remote-sensing-based applications [39]. The weights α_i are obtained by an automatic optimization process. The $1/\sigma_b$ values represent the relevance of the S1 polarimetric feature used to train the GPR model [53,54].

2.1.2. Optimized Whittaker Smoother

Here, we present the Whittaker [55] smoother and interpolator mathematical theory. Whittaker smoother is usually regarded as an example of a non-parametric regression algorithm [56]. He proposed solving a regularized least-squares problem in which a scalar parameter determines the trade-off between fidelity to the data and smoothness of the filtered sequence [57].

Given a sequence of n measurements $\{y_1, y_2, \ldots, y_n\}$, a positive real number λ, and a positive integer $p < n$, find the sequence $\{x_1, x_2, \ldots, x_n\}$ that minimizes:

$$\lambda \sum_{j=1}^{n} \left(y_j - x_j\right)^2 + \sum_{j=1}^{n-p} \left(\Delta^p x_j\right)^2 \tag{3}$$

where Δ is the forward difference operator:

$$\Delta x_j = x_{j+1} - x_j \tag{4}$$

$$\Delta^2 x_j = \Delta\left(\Delta x_j\right) = x_{j+2} - 2x_{j+1} + x_j \tag{5}$$

The first term in the sum in Equation (3) measures fidelity to the data, and the second measures smoothness, in that sense, the polynomial of degree $p-1$ means maximal smoothness. The parameter λ determines the strength of the smoothing. General applications require that λ needs to be tuned over several orders of magnitude (10, 100, 1000). Optimal values of λ should provide a smooth curve that reveals the true nature of the data whilst removing roughness and randomness [58].

Let y^T and x^T be of the form:

$$y^T = [y_1\ y_2 \ldots y_n] \tag{6}$$

$$x^T = [x_1\ x_2 \ldots x_n] \tag{7}$$

The objective function in Equation (3) can be written as:

$$\lambda (y - x)^T (y - x) + x^T M^T M x \tag{8}$$

where M is a $(n-p)xn$ differencing matrix. Given $p = 2$ and $n = 6$, the resulting M matrix looks like follows:

$$M = \begin{pmatrix} 1 & -2 & 1 & 0 & 0 & 0 \\ 0 & 1 & -2 & 1 & 0 & 0 \\ 0 & 0 & 1 & -2 & 1 & 0 \\ 0 & 0 & 0 & 1 & -2 & 1 \end{pmatrix} \tag{9}$$

The minimizer of Equation (8) is the solution of the normal equations:

$$A\hat{x} = \lambda\, y \tag{10}$$

where

$$A = \lambda\, I + M^T M \tag{11}$$

The solution can be obtained via:

$$\hat{x} = \left(I + \lambda^{-1} M^T M\right)^{-1} y \tag{12}$$

or,

$$\hat{x} = y - \lambda^{-1} M^T M \hat{x} \tag{13}$$

As an optional second parameter, the default second-order smoother ($p = 2$) will work fine for almost all signals, and the first p moments of the data are preserved. One popular approach to solve Equation (13) is to perform a search for an optimal criterion over a fine grid of λ values seeking to minimize the loss function. The use of generalized cross-validation (GCV) [59] emerges as an appealing alternative to deal with this issue. With this automatic method of choosing the smoothing parameter, λ is selected to minimize the GCV score:

$$n^{-1} \sum_{j=1}^{n} \left(\frac{y_j - \hat{x}_j}{1 - n^{-1} trace(\lambda A^{-1})} \right)^2 \tag{14}$$

Cross-validation aims to optimize the predictions of miss-out sample data. The prediction accuracy increases when the correlation between neighbor samples is exploited rather than utilizing the values of a smoothed trend [49]. The V-curve was proposed by Frasso and Eilers [60] as a tool to explore the smoothing parameter space. It is a modification on Hutchinson and Hoog [61] L-curve, which is a plot of (ψ,ϕ), evaluated on a fine grid of log λ, with:

$$\psi = \log \sum_j \omega_i \left(y_j - \hat{x_j}\right)^2, \quad \phi = \log \sum_j \left(\Delta_{x_j}^p\right)^2 \tag{15}$$

The Whittaker smoother combined with the V-curve for the optimal selection of the smoothing parameter λ, is a simple, fast, and powerful tool for EO data processing [49].

2.2. Study Site

The study site is located in the South of Buenos Aires Province, Argentina. The Bonaerense valley of the Colorado river (BVCR) is an intensively cultivated and irrigated Agri-environment occupying 91,163 ha, that includes horticulture, pastures, and cereals [62]. Most of the agricultural practices in the study region have been possible thanks to gravity irrigation [63]. To address our study, we selected three winter wheat paddocks belonging to the 2020 crop campaign in the BVCR (see Figure 1).

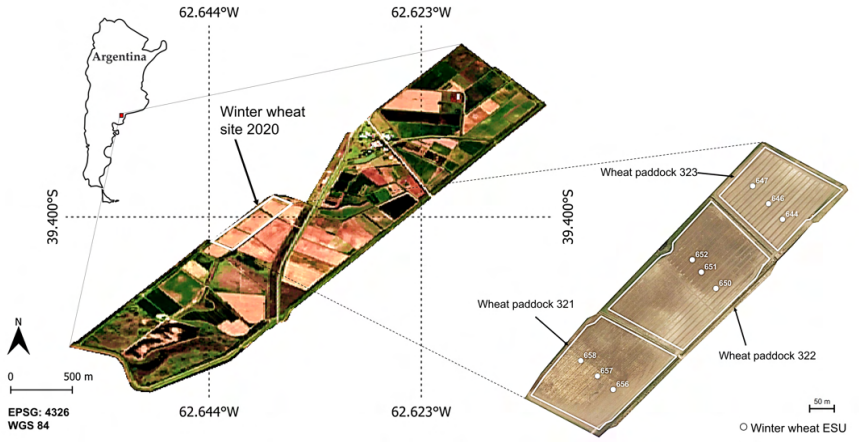

Figure 1. Test fields of irrigated winter wheat in the study site. True color S2 image of 27 December 2020, partly adapted from [63]. Reference system: WGS84 (EPSG 4326).

2.2.1. Characteristics and Environment of the Study Region

The Buenos Aires Province's southern segment made up of the Villarino and Patagones districts, has a temperate Mediterranean arid steppe climate according to the Köppen's climate classification [64]. The landscape presents aridity features in the vicinity of the Río Negro Province. Rainfall is greatest in autumn and decreases from the north to the southwest, with 483.5 mm on average. The estimated annual water deficit in the irrigated area is 322 mm on average, while in the extreme South of the territory it exceeds 400 mm [65]. The rainfall regime alternates between periods with water abundance and extreme droughts. The average annual temperature is 14.8 °C, with the lowest records of 1.6 °C registered in July and the highest values at around 30 °C for January. The annual frost-free period is more than 240 days in the East of the territory.

In the BVCR irrigated area, cropland productivity is affected by two soil issues. Primarily, soil salinity is related to low drainage capacity and soil cutting, which is associated with surface conditioning labors performed to obtain optimal water drainage. In general, the soils are Entic Hapludoll with sandy-to-sandy loam texture according to the USDA Soil Taxonomy classification [66], with levels of organic matter close to 2.3% [67]. Due to its texture, water retention is low, and the risk of erosion is high.

2.2.2. Winter Wheat Cropland Development and Properties in the BVCR

When periods of drought occur in the initial stages of wheat development, lack of crop uniformity is usually observed, attributed to the physio-chemical composition of the soil [68]. In the middle of the booting stage, the color of the cropland is generally darker in the less soil-worn sectors. Wheat croplands require low salinity content soils (<4 dS m^{-1}), neutral pH, high phosphorus concentration (>20 ppm P-soluble), and a good level of organic matter (>1.5%) [69]. The soil must be prepared for the conduction of water, usually under the modality of planks situated every 10 to 14 m [69]. Long-term cycle wheat can be sowed by the end of May, whereas this condition can be extended to the middle of August for short-term cycle wheat [69]. In all cases, it is recommended to take care that the soil profile is recharged with moisture in the planting stage. It is recommended to adjust the seed dose to obtain between 250 and 350 plants m^{-2} during the sowing time. If the profile was effectively recharged for the planting period, the wheat meets the tillering stage without suffering water deficit. After that, at the beginning of the jointing (stem elongation), it is recommended to carry out irrigation when the first visible knot appears, another in pre-flowering (booting), and the third when the heading of the crop has finished.

2.3. Field Data Collection for Training and Validation

Three winter wheat paddocks were sown simultaneously on 25 June 2020. Fertilization was applied in two instances throughout the plants' tillering stage, first by the end of August 2020 and second by the middle of September with 200 kg ha^{-1} of nitrogen (Urea: 46-0-0) manually uniformly distributed. Three gravity irrigations were performed throughout the crop cycle during late August, middle of September, and late November. A comprehensive overview of the BVCR's wheat campaign 2020 and an exhaustive description of the cropland management and experimental design are provided by Caballero et al. [63]. A total of 9 Elementary Sampling Units (ESU) were visited periodically during the wheat development periods from August to December. Each ESU was restricted to a 10 × 10 m area, analogous to the pixel size of the post-processed S1 imagery.

LAI samples were acquired utilizing the PocketLAI R Smart-App [70]. Six observations (n = 6) were performed per ESU and then averaged to boost statistics robustness (See Table 1). Winter wheat phenology was established regarding secondary growth stages defined by the Zadoks-scale [71] and registered in the in situ 2020 database. Winter wheat field data and land use were collected by a group of professionals at the Hilario Ascasubi Experimental Station (HAEE) belonging to the National Institute of Agricultural Technology (INTA), Argentina. The HAEE's land use for the 2020 cropland campaign is displayed in Figure 2.

Table 1. LAI in situ measured database.

Wheat Variable	Sampling Date	Range	Mean	SD
LAI (m^2 m^{-2})	3-Sep-20	0.16–0.30	0.23	0.05
	17-Sep-20	0.56–1.54	0.94	0.29
	2-Oct-20	1.59–3.81	2.57	0.66
	19-Oct-20	1.53–3.27	2.62	0.51
	2-Nov-20	2.78–5.05	4.12	0.63
	16-Nov-20	3.31–5.39	4.02	0.80
	30-Nov-20	3.29–4.75	4.08	0.50
	16-Dec-20	3.97–5.64	4.68	0.43

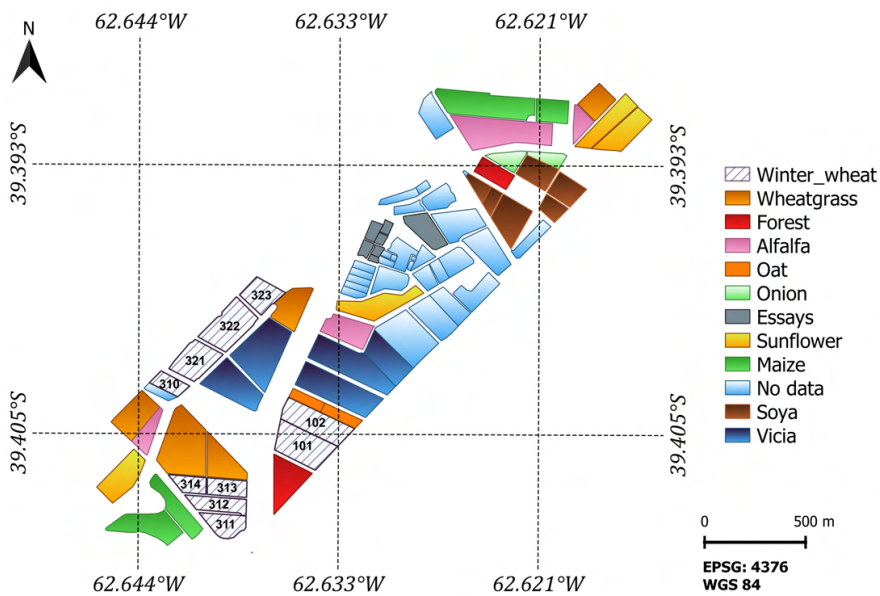

Figure 2. Study site 2020 land use. Reference system: WGS84 (EPSG 4326).

2.3.1. Winter Wheat Phenology and Meteorological Data Trend

The meteorological data were supplied by the INTA-Hilario Ascasubi weather station situated in the study site "39.38ºN, 62.62ºW" (Villarino district—Buenos Aires Province) very close to the wheat crop paddocks selected for this study. Available meteorological stations can be queried through the following website: http://siga.inta.gob.ar/#/ (accessed on 19 September 2022). A time-series consisting of daily soil temperature at 10 cm (ºC) and precipitation (mm) data ranging from the 1 September 2020 to 31 December 2020 were downloaded and analyzed. Figure 3, shows the wheat plant phenological stages evolution (described by the Zadoks-scale), irrigation and fertilization moments, and the meteorological data trend.

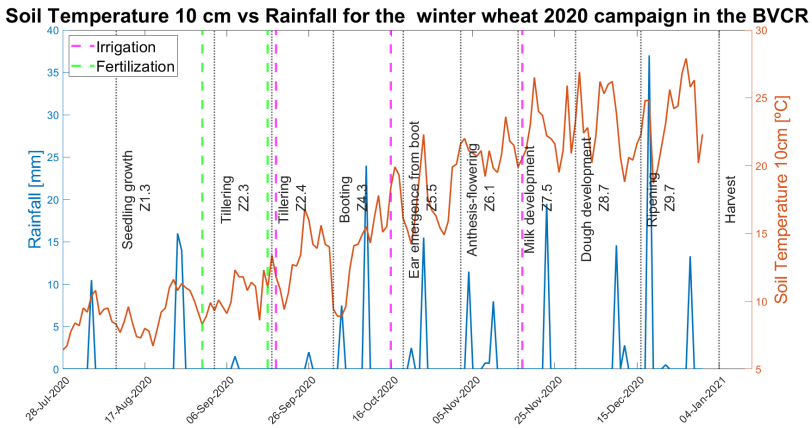

Figure 3. Meteorological data, soil temperature at 10 cm, and rainfall in the BVCR study site against winter wheat phenological stages.

2.4. Sentinel-1 SAR Data Processing

An automatic-processing chain was developed using the Sentinel-1 Toolbox provided by SNAP (Sentinel Application Platform) software version 8.0 https://step.esa.int/main/snap-8-0-released/ (accessed on 20 September 2022). We downloaded from ESA's website https://scihub.copernicus.eu/ (accessed on 19 September 2022), a total of 35 S1-A and S1-B images between 27 August 2020 to 12 January 2021 consisting of Ground Range Detected (GRD) IW products in dual polarization VV+VH, providing a 6-day revisited time over the study site. The selected relative orbit numbers (RON) or S1 paths were 141 for S1-A and 68 for S1-A and S1-B both orbits are descendent. The S1 acquisition time was around 6:20 h local time. The local incidence angle over the winter wheat paddocks varies from roughly 30º to 37º for path 141 and from 40º to 47º for path 68. First, the S1 precise orbits were applied to all S1 images followed by a thermal noise-removing process. Subsequently, the S1 scenes were calibrated radiometrically obtaining the normalized backscatter coefficient γ_0 (Gamma Naught). Afterward, the range doppler terrain correction was utilized to geocode the images precisely using the Shuttle Radar Topography Mission (SRTM) high-resolution DEM. The resulting spatial resolution for the S1 IW-GRD product without multi-looking was set to 10 × 10 m. Following this, the pre-processed S1 images were filtered to minimize the speckle effect. We selected the IDAN filter (Intensity-Driven-Adaptive-Neighborhood) [72] with the following filter configuration parameters: Adaptive Neighbor Size = 5, Number of Looks = 2. Finally, the S1 pre-processed images were spatially filtered by applying a 3 × 3 mean filter and restricted to the study site.

Considering that the S1 images have distinct observation paths, a sub-pixel accurate fine coregistration process is mandatory to ensure that each ground target contributes to the same (range, azimuth) pixel in all the S1 observed scenes [73]. We employed the following fine coregistration configuration parameters: Resampling type = None, Initial offset method = Orbit, Number off ground control points = 2000, RMS threshold (pixel accuracy) = 0.05, Warp polynomial order = 1, Interpolation method = Cubic convolution (6 points). Table 2 shows the correspondence between in situ sampling dates and S1 acquisitions.

Table 2. Field campaign and Sentinel-1 acquisition dates.

Sampling Date	S1-A Path 141	S1-A Path 68	S1-B Path 68	Δ Days (AVG)
3-Sep-20	1-Sep-20	8-Sep-20	2-Sep-20	3
17-Sep-20	13-Sep-20	20-Sep-20	26-Sep-20	5
2-Oct-20	7-Oct-20	2-Oct-20	8-Oct-20	4
19-Oct-20	19-Oct-20	14-Oct-20	20-Oct-20	2
2-Nov-20	31-Oct-20	7-Nov-20	1-Nov-20	3
16-Nov-20	12-Nov-20	19-Nov-20	13-Nov-20	3

2.5. Sentinel-1 Time-Series Smoothing and Interpolation

The Whittaker smoother for time-series interpolation was implemented in Python version 3.6.13 (https://www.python.org/downloads/release/python-3613/, accessed on 22 September 2022) utilizing the vam.whittaker version 2.0.2 (https://github.com/WFP-VAM/vam.whittaker, accessed on 22 September 2022) core functionality used in the MODIS Assimilation and Processing Engine (MODAPE) package version 1.0.0 (https://github.com/WFP-VAM/modape, accessed on 22 September 2022). The algorithm implementation is based on the Whittaker–Eilers smoother exhaustively described by Eilers [74] and Atzberger and Eilers [75]. The use of specific sparse matrix routines makes the smoother fast and memory efficient. We run an optimization process to find the optimal smoothing parameter λ. The amount of smoothing was optimized by applying the V-curve, a variation on the L-curve. The algorithm handles missing data points easily [49] (see Section 2.1.2).

2.6. Experimental Setup

The LAI sample database was bounded between 3 September and 2 November 2020 seeking to prioritize the response of the LAI retrieval model within the vegetation greenness stage [63]. Additionally, 12 samples of non-vegetated surfaces were included in the field data aiming to improve the versatility of the cropland LAI retrieval model. We conducted the following strategies to find the best-fitted model for LAI retrieval based on S1 data. We first divided the tests into two groups to facilitate managing the statistics results. The first group comprises the S1 polarimetric preprocessed data without smoothing and the second set of tests involves the implementation of the optimized Whittaker smoother. We analyzed separately the performance of each S1 single-orbit data (path 141 for S1-A and path 68 for S1-A and S1-B) and then the contribution of merging multiple incidence angles for training the GPR-S1-LAI models and the result of applying it to the band stacked S1 images. Aiming to ensure more robust retrieval results and to use the collected in situ measurements to the fullest, next, a 10-fold cross-validation (CV) [76] sampling scheme was applied. CV splits the available data into k subsets (k = 10). From these k sub-datasets, $k - 1$ sub-datasets are selected as a training dataset (51 data points, 5 on average in each sub-dataset) and a single k sub-dataset (5 data points) is used during the testing stage. The CV process is repeated iteratively k times [37]. The performance of the GPR-S1-LAI models was assessed using diverse goodness-of-fit metrics: the coefficient of determination (R^2), the mean absolute error (*MAE*) (see Equation (17)), the root mean square error (*RMSE*) (see Equation (18)), the normalized root mean square error (*NRMSE*) (see Equation (19)), and the total time (training and validation) for the execution of the MLRA were registered. We present bellow the formulation used for R^2, *MAE*, *RMSE* and *NRMSE* calculations:

$$R^2 = 1 - \frac{\sum_{i=1}^{N}(y_i - \hat{y}_i)^2}{\sum_{i=1}^{N}(y_i - \overline{y})^2} \tag{16}$$

$$MAE = \frac{1}{N}\sum_{i=1}^{N}|y_i - \hat{y}_i| \tag{17}$$

$$RMSE = \sqrt{\frac{1}{N}\sum_{i=1}^{N}(y_i - \hat{y}_i)^2} \tag{18}$$

$$NRMSE = \frac{RMSE}{(y_{max} - y_{min})} \tag{19}$$

where $\{y_i\}_{i=1}^{N}$ are the N winter wheat LAI measured values used for model training, $\{\hat{y}_i\}_{i=1}^{N}$ are the LAI estimated values based on S1 polarimetric data, $(y_{max} - y_{min})$ is the in situ measurement range, and $\overline{y}$ is the mean of the LAI in situ measured values.

2.7. Delineation of Retrieval Workflow

The entire S1-based retrieval workflow is visualized in Figure 4. Three well-differentiated structural blocks are detailed, starting with an S1 preprocessing section, followed by field data collection, and the probabilistic inference of LAI applying GPR models to S1 interpolated data. In brief, the implemented workflow consists of the following four main steps:

1. Pe-processing of the multiple relative orbit number S1 VH+VV polarization imagery: S1-A path 141, 68 and S1-B path 68;
2. Building the in situ database containing multitemporal field LAI measurements from the BVCR site and S1 post-processed interpolated polarimetric data,
3. Training S1 data with GPR algorithms and applying the retrieval model to obtain LAI;
4. seasonal mapping of LAI over irrigated winter wheat fields and corresponding uncertainties using the GPR-S1-LAI model.

The GPR processing was entirely operated within the Automated Radiative Transfer Model Operator (ARTMO) toolbox [77]. ARTMO was developed as a modular graphical user interface in Matlab, to automate the simulation of Radiative Transfer Modeling [40] and mapping applications. More information can be found at: http://artmotoolbox.com/ (accessed 20 September 2022).

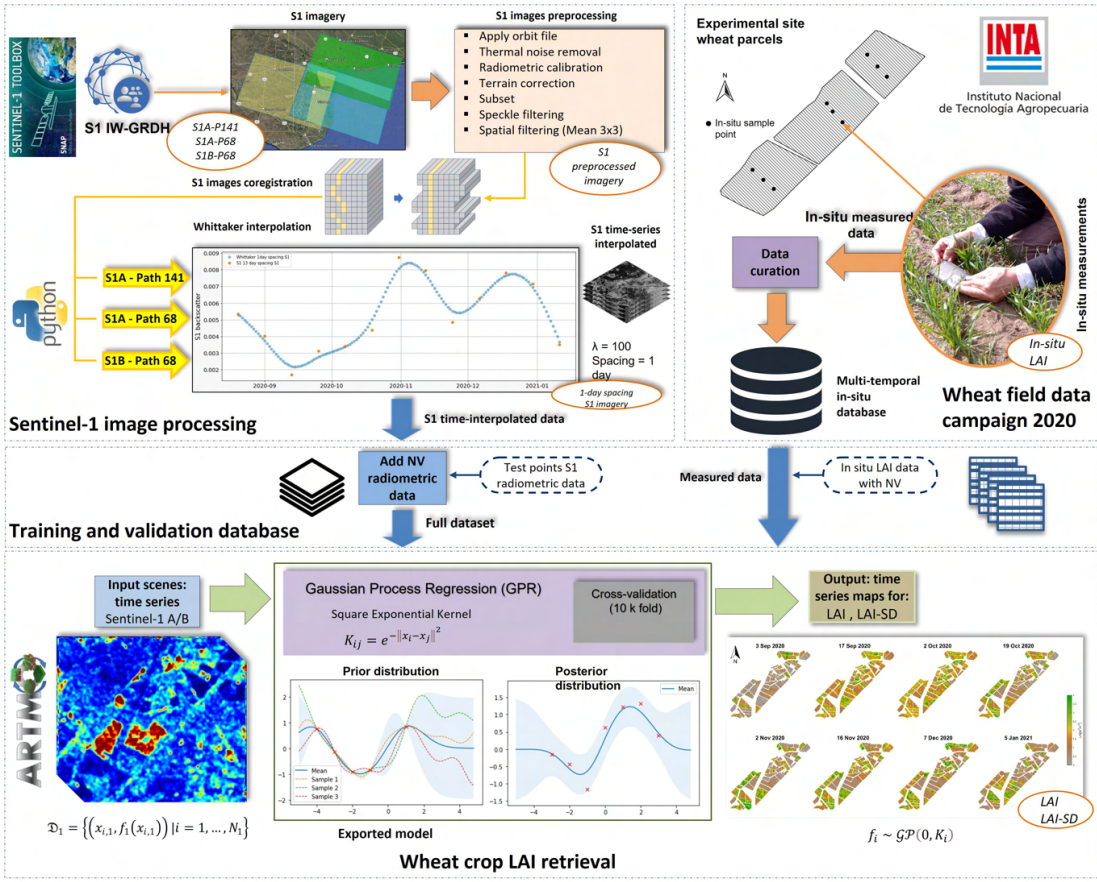

Figure 4. Retrieval workflow for the GPR-S1-LAI modeling using multiple local incidence angles of S1 polarimetric data, partly adapted from [63]. The output maps show our S1-derived LAI maps over the BVCR study area.

3. Results

3.1. Optimized S1 Stack Selection for LAI Modeling

We first explored the contribution of the S1 SAR data at distinct local incidence angles and its effect on the LAI retrieval models' statistics. To do so, the S1 backscatter response for the winter wheat cropland was analyzed by plotting the VV and VH time series of polarimetric data for the distinct S1 local incidences angles. Figure 5a,b displays the S1 VH and VV trend along the crop's phenological development. A noticeable difference can be appreciated when the S1-A path 141 SAR data is plotted against path 68 for both polarizations. Besides the lack of temporal synchronicity between S1-A acquisitions, an amplitude offset can be attributed to the differences in the local incidence angle of both S1 paths. Figure 5c, shows the S1 local incidence angle histograms for all winter wheat pixels at the study site. There is a glaring overlap between S1-A and S1-B LIA values for path 68, this results from the fact that both satellites share the same relative orbit number. The mean LIA value for S1 path 141 is around 33° whereas for path 68 it is approximately 43°.

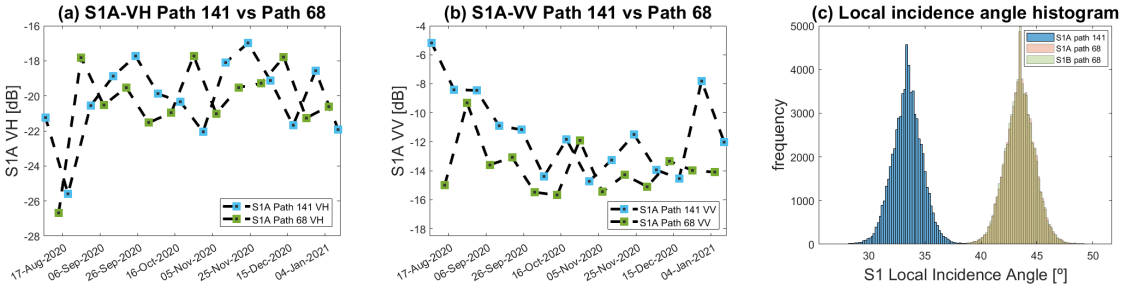

Figure 5. S1-A acquisition trends over the study site. (**a**) Time-series of S1-A VH polarization data for path 141 against path 68. (**b**) Time-series of S1-A VV polarization data for path 141 against path 68. (**c**) S1 Local incidence angle histograms.

Table 3 presents the regression statistics when the S1 original data are used to train the retrieval models in contrast with the case in which the optimized Whittaker smoother is applied to the data. It can be noted that the increase of R^2 and the decrease of MAE, RMSE, and NRMSE values in general terms when all S1 acquisitions at distinct local incidence angles are used to train the LAI retrieval models.

Table 3. Regression statistics for winter wheat LAI retrieval modeling using S1 time-series data.

Regression Statistics for Winter Wheat LAI Retrieval Models Using S1 Time-Series Data						
S1 Data	**MLRA**	**MAE [m^2 m^{-2}]**	**RMSE [m^2 m^{-2}]**	**NRMSE [%]**	**R^2**	**Time [s]**
S1-A-P141	GPR[2B]	1.33	1.48	33.02	0.15	0.1219
S1-A-P68	GPR[2B]	1.16	1.38	30.74	0.34	0.0662
S1-B-P68	GPR[2B]	1.22	1.45	32.30	0.44	0.0893
S1-AB-P141-68	GPR[6B]	0.93	1.04	23.24	0.68	0.1305
Regression statistics for winter wheat LAI retrieval models using S1 time-series smoothed data						
S1-A-P141	GPR[2B]	1.10	1.27	27.28	0.38	0.2638
S1-A-P68	GPR[2B]	0.63	0.86	18.60	0.67	0.0756
S1-B-P68	GPR[2B]	1.20	1.40	30.20	0.13	0.1247
S1-AB-P141-68	GPR[6B]	0.50	0.66	14.21	0.85	0.1525
S1-AB-P141-68	GPR_{CV}[6B]	0.68	0.88	18.91	0.67	0.0117

Figure 6 shows the scatter plots of estimated against in situ measured LAI values. We analyzed three algorithm training scenarios. The first contemplates S1 non-smoothed data for multiple local incidence angle acquisitions (see Figure 6a). In the second, the effect of smoothing the data is studied by training the six bands (6B) GPR-S1-LAI model with 70% of in situ samples (see Figure 6b). Finally, the third scenario investigates the contribution of a 10-fold CV strategy during the model training stage (see Figure 6c). Obtained R^2, MAE, RMSE, and NRMSE statistics denote high agreements between retrieved and measured wheat LAI. The GPR uncertainties are also provided in the standard deviation (SD) form expressed by vertical bars.

3.2. Winter Wheat Seasonal LAI Mapping

The 10-fold GPR_{CV} retrieval model was subsequently applied to the S1 stacked images for LAI mapping purposes. The S1 scenes are characterized by areas of intense agricultural usage covering a variety of crop types (see Figure 2). The wheat croplands are flat, and the vegetation growth is uniform; hence, the S1 backscatter signal is not affected by adverse acquisition geometrical effects, such as radar shadow, foreshortening, and layover. Land covers such as man-made surfaces, water bodies, or bare soil in the study region were excluded from the S1 stacked scenes by applying a vectorial mask.

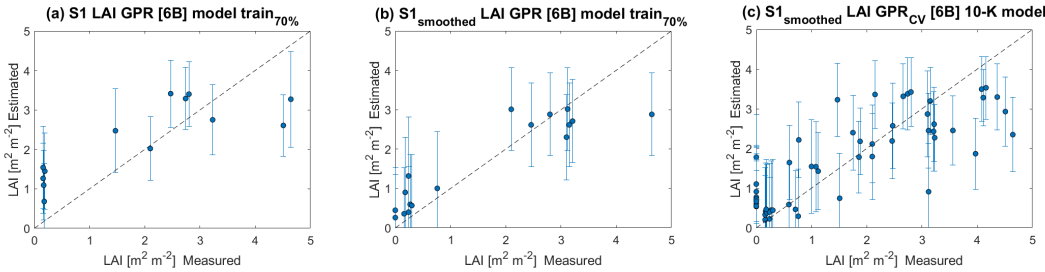

Figure 6. Measured vs. estimated winter wheat LAI along 1:1-line, including uncertainty intervals. (**a**) LAI model estimates using multiple local incidence angles of S1 non-smoothed time-series data; (**b**) LAI model estimates using S1 smoothed time-series data at multiple local incidence angle acquisitions and 70% of the data for model training; (**c**) LAI model estimates using S1 smoothed time-series data at multiple local incidence angle acquisitions and 10-fold CV for model training.

The eight S1-derived maps of winter wheat LAI for the BVCR 2020 campaign are shown in Figure 7. The winter wheat sown in the study site took place by the end of June 2020. The emergence of the plant stem and three tillers was noticeable in late August. By the beginning of November 2020, wheat plants are in the anthesis (flowering) stage, leading to the maximum retrieving values of LAI with 3.78 m^2 m^{-2} on average. The senescence arrives by the middle of November 2020, while harvest takes place by the first days of January 2021.

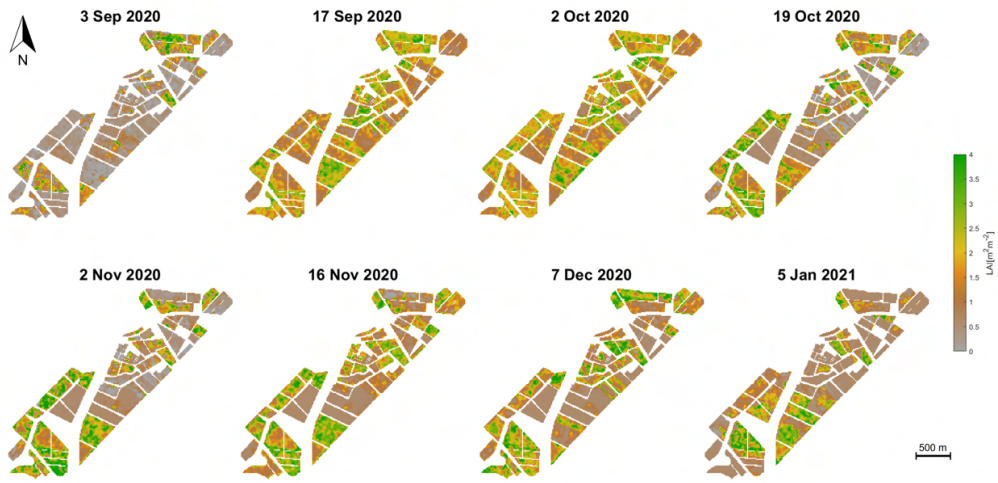

Figure 7. Seasonal mapping of LAI (m^2 m^{-2}) of croplands in the BVCR for the winter wheat campaign 2020, retrieved by the GPR_{CV} model using S1 polarimetric data from multiple local incidence angles acquisitions and in situ measured LAI data.

Absolute uncertainty maps are also provided in the form of SD (see Figure 8). The associated uncertainty maps can serve as a quality layer, e.g., to exclude uncertain areas [78,79]. Generally, the GPR model produced sufficiently low LAI uncertainties (i.e., less than 0.6 m^2 m^{-2} on average) from the start of the season to the maximum greenness, with higher values over the senescence stage, a period in which uncertainty can reach up to 1.25 m^2 m^{-2} values.

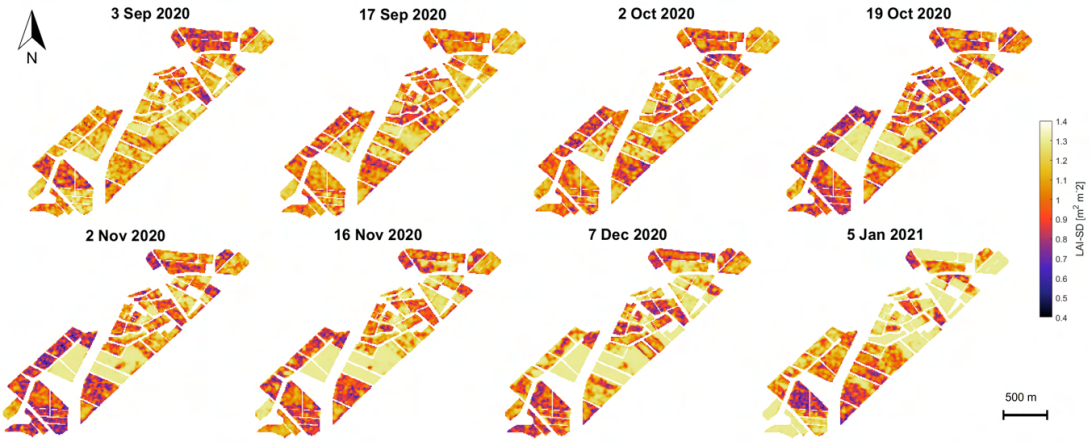

Figure 8. Seasonal mapping of LAI-SD (m^2 m^{-2}) of croplands in the BVCR for the winter wheat campaign 2020, retrieved by the GPR_{CV} model using S1 polarimetric data from multiple local incidence angles acquisitions and in situ measured LAI data.

We computed the histograms of the retrieved LAI values for the winter wheat paddocks pursuing to visualize the dispersion of LAI values and their trend over time. On every date on which the S1-derived LAI map was obtained, we analyze the probability density function (PDF) of all pixels. We focused on paddocks 321, 322, and 323 for the BVCR 2020 field campaign. Two PDFs were explored: Weibull [80] and non-parametric Kernel probability density distribution [81]. We calculated the mean (μ) and the standard deviation (σ) values of the Weibull distribution. The results are shown in Figure 9.

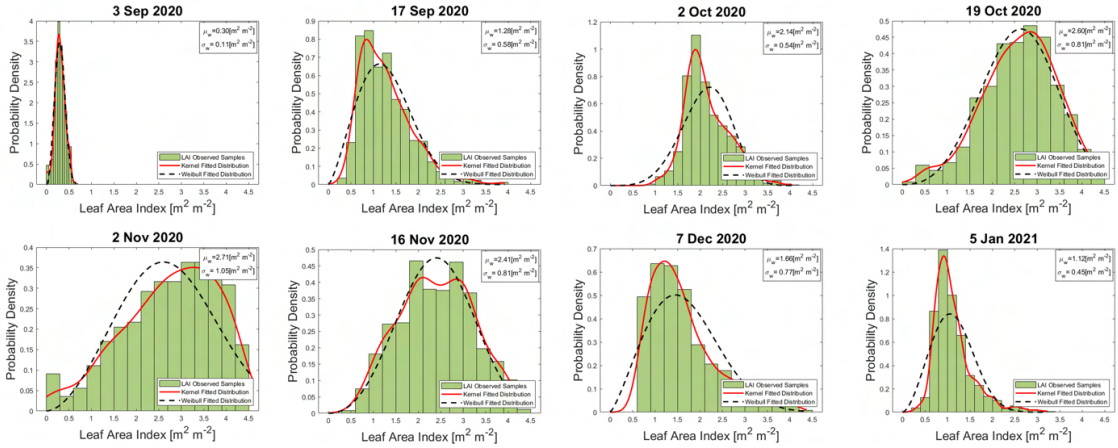

Figure 9. Temporal evolution of probability density function of LAI (m^2 m^{-2}) for the winter wheat paddocks 321, 323, and 323 at the study site. LAI observed samples in each graph correspond to S1-derived LAI estimations.

3.3. Time-Series Trend of Retrieved LAI and Associated Uncertainty

This section explores the winter wheat's LAI seasonal evolution along the BVCR 2020 campaign. The GPR-S1-LAI model was applied to a total of nine S1 stacked scenes with the aim of reproducing, as faithful as possible, the LAI curve of the winter wheat crop. The LAI retrieved curve evolution for the three selected winter paddock in the study region is displayed in Figure 10a. The GPR_{CV} model uncertainties were mapped in the form of

SD to represent the variability of the LAI retrieved values (see Figure 10b). The figures show the temporal LAI and LAI-SD trends of the averaged nine ESUs (solid line), and the mean of the in situ measured LAI values (green dots). Only the first five wheat LAI measurements were plotted, excluding those samples acquired on November 16 and 30 and also 16 December 2020.

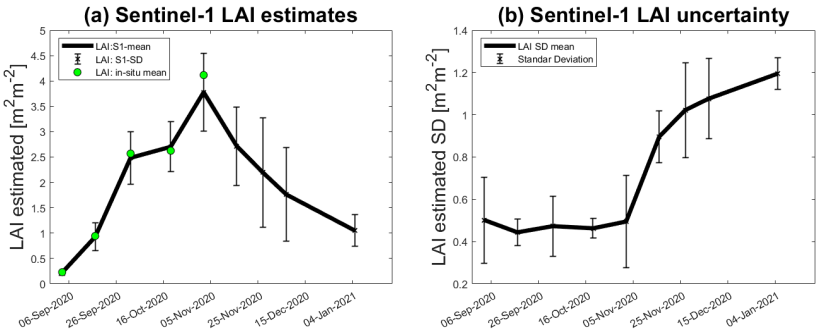

Figure 10. Seasonal evolution of wheat cropland over the three paddocks at the BVCR study sites described by LAI, mean values of nine ESUs within the cropland limits, and the associated uncertainty, plotted as vertical bars. (**a**) LAI estimates; (**b**) LAI uncertainty (SD).

For the three wheat paddocks in the study site, LAI increased from the plants' emergence stage onwards and decreased after tillering. Abrupt drops in LAI in January 2021 suggest a harvest event. Considering the availability of the land use data for the BVCR 2020 campaign presented in Figure 2, the LAI temporal evolution of all wheat paddocks in the study site was determined by averaging all pixels inside each parcel´s bounds. Figure 11 displays the retrieved LAI temporal trend for all the winter paddocks at the study site for the BVCR 2020 campaign. Despite lacking cropland management information for all winter wheat paddocks, the LAI trend over time shows consistency with the development of wheat plants in the study region's environment (see Sections 2.2.1 and 2.2.2).

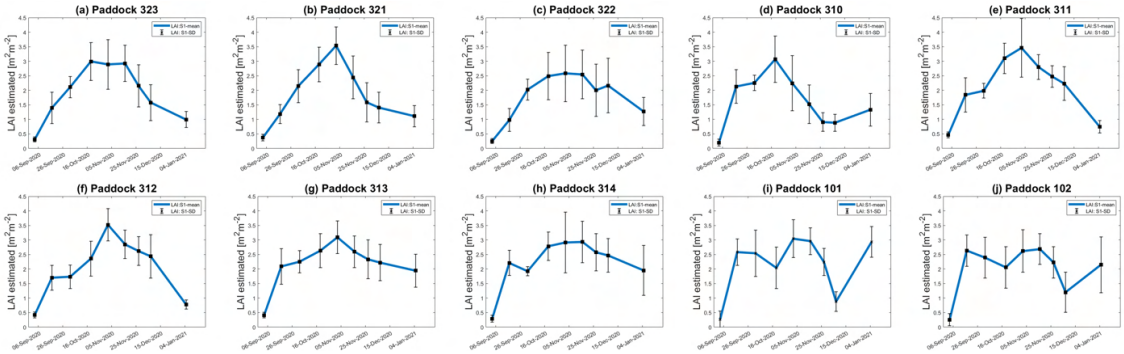

Figure 11. Seasonal evolution of LAI for all winter wheat paddocks in the BVCR study sites. The estimate uncertainty is represented as vertical bars. (**a**) Wheat paddock 323; (**b**) Wheat paddock 321; (**c**) Wheat paddock 322; (**d**) Wheat paddock 310; (**e**) Wheat paddock 311; (**f**) Wheat paddock 312; (**g**) Wheat paddock 313; (**h**) Wheat paddock 314; (**i**) Wheat paddock 101; (**j**) Wheat paddock 102.

4. Discussion

We explored the suitability of multi-S1 data for all-weather LAI wheat monitoring. We aimed to build a radar-based retrieval workflow based on multiple S1-A and S1-B acquisitions at distinct local incidence angles and in situ measurements of irrigated winter wheat LAI from the BVCR 2020 campaign. In the following, LAI retrieval performance and

uncertainties (Section 4.1), sensitivity of S1 backscatter to winter wheat LAI (Section 4.2), the role of S1 acquisition geometry (Section 4.3), and finally the potential of seasonal trends identification based on S1 polarimetric data for wheat agronomic management (Section 4.4) are discussed.

4.1. LAI Retrieval Performance and Uncertainties

In terms of local incidence angles, regressions parameters at 43º (path 68) outperformed those obtained at 33º (path 141). This is in line with the vegetation-acquisition geometry dependency of the radar-acquired scenes (see Figure 5 and Table 3). When both descendent orbits (141 and 68) were used to train the GPR-S1-LAI retrieval model, an appreciable R^2 increase occurred compared to the use of single-orbit polarimetric data. This can be attributed to additional information on the vegetation structure of the different dates and from distinct angles of observation. This achievement is remarkable because mapping winter wheat LAI using multiple S1 observations at distinct local incidence angles has not yet been evaluated so far. We found a significant improvement in the R^2 and RMSE of the GPR-S1-LAI model after applying the data smoothing process based on the optimized Whittaker smoother (see Table 3).

Based on the information presented in Table 3, we can conclude that the best results were obtained for model *S1-AB-P141-68*, with NRMSE < 15% and R^2 of 0.85 m^2 m^{-2}. Nevertheless, and despite achieving these high-accuracy retrieval parameters, we focused on the CV model, seeking to fully exploit the training dataset. The CV strategy provided greater robustness to the LAI retrieval model, while preserving relatively high accuracy. The GPR_{CV}-based LAI model of winter wheat yielded a relatively high R^2 with 0.67 and a low RMSE of 0.88 m^2 m^{-2}.

The LAI estimates based on our approach suggested superior performance over those presented in previous studies. For instance, Bousbih et al. [17] analyzed the potential of S1 radar data for retrieving LAI of cereals in agricultural areas over the Kairouan Plain (Tunisia, North Africa). They achieved R^2 = 0.25 using dual polarimetric radar data acquired from a single angle of observation. Hosseini et al. [51] used full-polarimetric (HH+HV+VH+VV) RADARSAT-2 data for soybean and corn LAI mapping achieving R^2 = 0.64 RMSE = 0.63 m^2 m^{-2} and R^2 = 0.66 and RMSE = 0.75 m^2 m^{-2}, respectively.

Regarding the LAI retrieval uncertainties, two issues deserve to be adequately addressed. First, S1 SAR images are conditioned by the radar's inherent speckle noise, which affects the VH and VV backscatter amplitude of adjacent pixels of homogeneous monitored cropland. This speckle noise, mainly due to the relative phase of individual scatters within a resolution cell, increases the uncertainty of the LAI estimates. Consequently, the S1-based LAI values have high dispersion between retrieving dates (see Figure 9). When a particular scatter element is observed at distinct local incidence angles repeatedly on time, this random speckle effect can be mitigated. Multiple radar observations increase the amount of information, minimizing the entropy of the data and the uncertainty of the estimates. Considering world locations where ascending and descending orbits of S1 are both available, the approach presented in this study constitutes an auspicious line of research. Secondly, the in situ measurements (see Table 1) were collected during the wheat growing season, which renders the models more robust and confident. It can be noticed that in situ LAI sample values show a different pattern than the SAR LAI estimates in late November and December 2020 (see Figure 10), while field trait data show high LAI values, S1-based retrieved LAI show a reduction during this timeframe. After the anthesis, the photosynthetic activity of winter wheat plants decreases leading to the beginning of the senescence process. The moisture content of wheat plant stems, leaves, and ears is considerably reduced by this time affecting the radar backscatter. The in situ measured database was then restricted between 3 September to 2 November 2020 seeking to preserve the consistency of the LAI retrieved values along the green vegetative stages of the winter wheat crop. The final GPR-S1-LAI model is therefore better adapted toward green vege-

tation states. Hence, the uncertainty of the developed models will increase during later (mature/senescent) growing stages.

4.2. Sensitivity of S1 Backscatter to Winter Wheat LAI

LAI can be differentiated into LAI green and LAI brown. The green leaf area index (LAI_G) represents the photosynthetically active leaves of the plants, and is thus also the most common type of LAI [82]. The brown leaf area index (LAI_B), represents the normalized leaf area, which is senescent and losing photosynthetic function [79,83]. During the greenness stage, wheat plant development is usually modeled by LAI_G. From the first days of August to 16 November 2020, winter wheat plants remain green. During this period, LAI_G increased as the wheat plants grow. By 16 November 2020, crop senescence started, and the share of brown leaves increased. From this point on, the LAI_G starts decreasing constantly until reaches zero value at the harvest date. Consequently, the S1 backscatter at VH and VV polarization remained stable at low values (see Figure 5). Additionally, by 16 December 2020, the wheat heads became completely dry, thus, the C-band backscatter decreases to reach the lower monitored values at this stage, the vegetation becomes transparent to the radar signal and the soil moisture is very low because irrigation is stopped. These structural changes in the canopy lead to an increased volume scattering of the ground targets that can be mainly distinguished at VH polarization. Mattia et al. [20] and Satalino et al. [84] found that when the heads of wheat plants emerged, the backscatter changed drastically. They also highlighted the importance of the heading stage as a turning point at which the C-band radar backscatter becomes essentially sensitive to soil moisture rather than wheat plants' biomass variations. During the senescence phase (from the greenness maximum until wheat plants have completed the dehydration process), LAI measurements are indeed represented by the total LAI (LAI_T), thus $LAI_T = LAI_G + LAI_B$, implying that the LAI is defined by green and brown leaf structures [79,83]. The splitting of the analysis into two periods (greenness and senescence) was studied by Che et al. [85], who analyzed the temporal trend of the LAI of vegetation in Shandong Province, China. They set up a breakpoint of two curves (LAI_G and LAI_B) that occurs during the flowering period (anthesis) when the wheat has reached its full height. As radar is sensitive to the canopy's moisture and structure, it implies a certain sensitivity to LAI_T. Nasrallah et al. [24] studied the temporal profiles of the widely known Normalized Difference Vegetation Index (NVDI) based on Sentinel-2 optical data and the S1 backscatter at VH and VV polarizations. The authors remarked on the high sensitivity of the SAR signal to winter wheat phenological cycle, in comparison to the time-series of NDVI [27].

4.3. Role of S1 Acquisition Geometry

The LAI temporal trend for all winter wheat paddocks in the study site is presented in Figure 11. Even though winter wheat croplands are typically homogeneously distributed, the spatial orientation of the rows in the wheat paddocks was not uniform between the cropland locations. For example, in the three selected winter wheat paddocks for in situ data collection (paddocks 321, 322, and 323), the rows were oriented from west-southwest to east-northeast, while in paddocks 101 and 102, the orientation was from north-northwest to south-southeast. In addition, the rows for paddocks 311–314 were from west to east, while in paddock 310, the rows were oriented from west-southwest to east-northeast. This difference in the spatial orientation of rows can be more noticeable during the first development stages of winter wheat plants, such as seedling growth and tillering, when the soil is not yet fully covered by vegetation. The S1 radar signal during this period is governed by the soil moisture dynamic, which differs from one winter wheat paddock to another, giving the difference in soil irrigation conditions and surface roughness. The S1 C-band radar backscatter was affected by the spatial orientation of the rows which varied for the winter wheat paddocks in the study region. This is based on the dependency of the target's radar cross-section (RCS) on the satellite's relative angle [22], thus even minimal changes in the target aspect significantly affect the RCS [18] (see Figure 5). The

descending orbits 141 and 68 were used to perform early morning measurements when dew may become a confounding factor [11,35]. During morning hours of the S1 acquisition, the cropland relative humidity is high and the soil moisture increases causing backscatter alterations of the SAR signal [86,87]. Fortunately, the S1 overpass time was similar for both orbits (around 6:20 h local time), leading to a comparable influence of the dew effect for all S1 acquisitions. After heading had occurred, the soil contribution is considerably reduced and the volumetric backscattering of the vegetation's canopy became more significant at 43º. This finding was noted by several previous studies [20,26,88,89].

Inconsistencies between the trend of the LAI in Figure 11 can be noticed for winter wheat paddocks 101, 102, and most importantly, in paddock 310 (peak LAI is end-of-October and then decreases) and the in situ measurements (highest LAI values were observed throughout November and December). These differences may be attributed to the fact that each crop parcel has been managed by different farmers at the study site regardless of the scope of this research. Other factors accounting for this issue are crop row orientation, the inherent SAR speckle noise, and the tri-dimensional plant structure of winter wheat detected by the S1 radar instrument. In addition, wheat paddocks 101 and 102 were harvested on 18 December 2020, while 321, 322, and 323 on 4 January 2021. Ultimately, the S1-derived LAI decreases suddenly for all winter wheat paddocks between 18 December 2020 and 5 January 2021, which is due to the harvest period. After these dates, there is an increase in LAI values in January for paddocks 101, 102, and 310, which is due to post-harvest land management practices. The sensitivity to surface soil moisture and roughness also increases by this time.

4.4. Potential of Seasonal Trend Identification Based on S1 Polarimetric Data for Wheat Agronomic Management

S1-based LAI mapping represents an attractive all-weather strategy for space-based monitoring of croplands, particularly in cloudy agriculture areas such as the BVCR. Characteristics of the study region were addressed in Section 2.2.1 and the irrigated winter wheat development and properties in Section 2.2.2. This valuable information can support an agronomic analysis of the winter wheat phenology in the study region. A summary of the most important points concerning the previous sections (see Sections 2.2.1, 2.2.2 and 2.3.1), and the innovative S1-based LAI mapping model is given next.

The LAI response was evaluated for a typical wheat extensive crop condition at a productive scale at the BVRC. Agronomic nutritional and water requirement management was performed to enable maximum yield potential. We can appreciate the development of a typical phenological curve concerning each of the sampling dates. A positive evolution was observed in LAI measurements in response to fertilizer and irrigation applications during the vegetative stage of the crop (first five sampling dates). The registered precipitation at the study site along the crop phenological cycle was representative of the expected averaged value of the BVCR semi-arid region (see Section 2.2.1).

In Figure 10a, a noticeable decline in LAI evolution from 5 November (3.78 m^2 m^{-2}) to 25 November 2020 (2.65 m^2 m^{-2}) was observed. This coincides with the stages of the ontogenetic cycle of the wheat crop at the study site and with the warm temperatures recorded for those dates (see Figure 3), thus accelerating the rate of crop development and promoting flowering. In addition, as the photoperiod increases in November in the southern hemisphere, crop stages are shorter [90]. The observed decline is explained by the crop cycle interchange related to changing the apex to the reproductive stage and the beginning of spikelet differentiation [91]. The onset of tillering occurs after the appearance of the terminal spikelet at the apex. The beginning of internode elongation determines a change in assimilate partitioning within the plant, which is mainly destined for the growth of the stem, and consequently, the production of tillers ceases. From that moment on, and depending on the available resources, tiller mortality will occur, defining at the end of this process the number of spikelets per unit area [92]. Therefore, it is possible to make an analogy between the beginning of elongation and the moment when the estimated

S1-derived LAI decreases similar to the results obtained by other authors [24,27]. This evidence confirms the capability of S1 radar data to detect changes that are diagnostic of wheat crop phenology [93], especially over cloud-prone agriculture areas.

5. Conclusions

Merging distinct incidence angle observations of SAR potentially provides a richer source of information related to vegetation structure than single narrow observations, and can thus efficiently support all-weather cropland monitoring applications. Here, we presented an S1-based retrieval workflow for operational mapping of LAI optimized for an irrigated winter wheat cropland located in the South of Buenos Aires Province in Argentina. The implemented retrieval method used the advantages of integrating two distinct S1 descending relative orbits. Physical interaction between the radar signal at distinct acquisition geometries and the vegetation structure provided complementary information for LAI retrieval. We chose GPR as a solid probabilistic MLRA for the retrieval of LAI, given the advantage of delivering associated uncertainties along with the estimates, so assisting in the reliability assessment of the LAI retrieval.

The GPR_{CV} model for retrieving LAI over winter wheat was validated with relatively high accuracy against in situ data RMSE = 0.88 m^2 m^{-2} and R^2 = 0.67. The established GPR_{CV} LAI model was posteriorly applied to a series of S1 stacked imagery of the growing season of 2020 over the BVCR study site. The resulting maps suggest spatiotemporal consistency with winter wheat growth in the region, however, the transferability of the retrieval model to other cropland environments remains to be carefully analyzed. We conclude that dense S1 time-series data at both ascending and descending orbits present an appealing opportunity for year-round monitoring of cultivated areas. Additional research is required to assess if this workflow is applicable to other vegetation structures and environmental conditions.

Author Contributions: G.C., J.D. and J.V. proposed the general objectives and goals of the research; A.P., C.W., P.S.A., A.C. and L.O. designed the field campaigns and collected the in situ data; G.C. and J.V. analyzed the data and obtained the results; G.C. and K.B. wrote the paper; K.B., J.V. and J.D. reviewed the paper and supervised all the procedures. All authors have read and agreed to the published version of the manuscript.

Funding: This research was funded by the European Research Council (ERC) under the ERC-2017-STG SENTIFLEX project (grant agreement 755617) (K.B.) and Ramón y Cajal Contract (Spanish Ministry of Science, Innovation, and Universities) (J.V.).

Data Availability Statement: Not applicable.

Acknowledgments: We would especially like to thank the Hilario Ascasubi Agricultural Experimental Station of the National Institute of Agricultural Technology of Argentina for the experimental datasets used in this study. This publication is also the result of the project implementation: "Scientific support of climate change adaptation in agriculture and mitigation of soil degradation" (ITMS2014+313011W580) supported by the Integrated Infrastructure Operational Programme funded by the ERDF. The research was also supported by the Action CA17134 SENSECO (Optical synergies for spatiotemporal sensing of scalable ecophysiological traits) funded by COST (European Cooperation in Science and Technology www.cost.eu (accessed on 22 July 2022)).

Conflicts of Interest: The authors declare no conflict of interest.

References

1. Gao, S.; Niu, Z.; Huang, N.; Hou, X. Estimating the Leaf Area Index, height and biomass of maize using HJ-1 and RADARSAT-2. *Int. J. Appl. Earth Obs. Geoinf.* **2013**, *24*, 1–8. [CrossRef]
2. McNairn, H.; Kross, A.; Lapen, D.; Caves, R.; Shang, J. Early season monitoring of corn and soybeans with TerraSAR-X and RADARSAT-2. *Int. J. Appl. Earth Obs. Geoinf.* **2014**, *28*, 252–259. [CrossRef]
3. Zhang, Y.; Venkatachalam, A.S.; Huston, D.; Xia, T. Advanced signal processing method for ground penetrating radar feature detection and enhancement. In *Proceedings Volume 9063, Nondestructive Characterization for Composite Materials, Aerospace Engineering, Civil Infrastructure, and Homeland Security 2014*; SPIE: Bellingham, WA, USA, 2014; Volume 9063, pp. 276–289. [CrossRef]

4. Caballero, G.R.; Platzeck, G.; Pezzola, A.; Casella, A.; Winschel, C.; Silva, S.S.; Ludueña, E.; Pasqualotto, N.; Delegido, J. Assessment of Multi-Date Sentinel-1 Polarizations and GLCM Texture Features Capacity for Onion and Sunflower Classification in an Irrigated Valley: An Object Level Approach. *Agronomy* **2020**, *10*, 845. [CrossRef]
5. Ballester-Berman, J.D.; Lopez-Sanchez, J.M.; Fortuny-Guasch, J. Retrieval of biophysical parameters of agricultural crops using polarimetric SAR interferometry. *IEEE Trans. Geosci. Remote Sens.* **2005**, *43*, 683–694. [CrossRef]
6. Vreugdenhil, M.; Navacchi, C.; Bauer-Marschallinger, B.; Hahn, S.; Steele-Dunne, S.; Pfeil, I.; Dorigo, W.; Wagner, W. Sentinel-1 Cross Ratio and Vegetation Optical Depth: A Comparison over Europe. *Remote Sens.* **2020**, *12*, 3404. [CrossRef]
7. Vreugdenhil, M.; Wagner, W.; Bauer-Marschallinger, B.; Pfeil, I.; Teubner, I.; Rüdiger, C.; Strauss, P. Sensitivity of Sentinel-1 Backscatter to Vegetation Dynamics: An Austrian Case Study. *Remote Sens.* **2018**, *10*, 1396. [CrossRef]
8. Mandal, D.; Kumar, V.; Ratha, D.; Dey, S.; Bhattacharya, A.; Lopez-Sanchez, J.M.; McNairn, H.; Rao, Y.S. Dual polarimetric radar vegetation index for crop growth monitoring using sentinel-1 SAR data. *Remote Sens. Environ.* **2020**, *247*, 111954. [CrossRef]
9. Ahmadian, N.; Ullmann, T.; Verrelst, J.; Borg, E.; Zölitz, R.; Conrad, C. Biomass Assessment of Agricultural Crops Using Multi-temporal Dual-Polarimetric TerraSAR-X Data. *PFG* **2019**, *87*, 159–175. [CrossRef]
10. El Hajj, M.; Baghdadi, N.; Wigneron, J.P.; Zribi, M.; Albergel, C.; Calvet, J.C.; Fayad, I. First Vegetation Optical Depth Mapping from Sentinel-1 C-band SAR Data over Crop Fields. *Remote Sens.* **2019**, *11*, 2769. [CrossRef]
11. Khabbazan, S.; Vermunt, P.; Steele-Dunne, S.; Ratering Arntz, L.; Marinetti, C.; van der Valk, D.; Iannini, L.; Molijn, R.; Westerdijk, K.; van der Sande, C. Crop Monitoring Using Sentinel-1 Data: A Case Study from The Netherlands. *Remote Sens.* **2019**, *11*, 1887. [CrossRef]
12. Paloscia, S.; Pettinato, S.; Santi, E.; Notarnicola, C.; Pasolli, L.; Reppucci, A. Soil moisture mapping using Sentinel-1 images: Algorithm and preliminary validation. *Remote Sens. Environ.* **2013**, *134*, 234–248. [CrossRef]
13. Ferrazzoli, P.; Paloscia, S.; Pampaloni, P.; Schiavon, G.; Solimini, D.; Coppo, P. Sensitivity of microwave measurements to vegetation biomass and soil moisture content: A case study. *IEEE Trans. Geosci. Remote Sens.* **1992**, *30*, 750–756. [CrossRef]
14. Paloscia, S.; Macelloni, G.; Pampaloni, P. The relations between backscattering coefficient and biomass of narrow and wide leaf crops. In Proceedings of the 1998 IEEE International Geoscience and Remote Sensing, Seattle, WA, USA, 6–10 July 1998; IEEE: Piscataway, NJ, USA, 1998; Volume 1, pp. 100–102. [CrossRef]
15. Karam, M.A.; Fung, A.K.; Lang, R.H.; Chauhan, N.S. A microwave scattering model for layered vegetation. *IEEE Trans. Geosci. Remote Sens.* **1992**, *30*, 767–784. [CrossRef]
16. Ulaby, F.T.; Aslam, A.; Dobson, M.C. Effects of Vegetation Cover on the Radar Sensitivity to Soil Moisture. *IEEE Trans. Geosci. Remote Sens.* **1982**, *GE-20*, 476–481. [CrossRef]
17. Bousbih, S.; Zribi, M.; Lili-Chabaane, Z.; Baghdadi, N.; El Hajj, M.; Gao, Q.; Mougenot, B. Potential of Sentinel-1 Radar Data for the Assessment of Soil and Cereal Cover Parameters. *Sensors* **2017**, *17*, 2617. [CrossRef] [PubMed]
18. Skolnik, M.I. *Radar Handbook*; McGraw-Hill Education: New York, NY, USA, 2008.
19. Rozenstein, O.; Siegal, Z.; Blumberg, D.G.; Adamowski, J. Investigating the backscatter contrast anomaly in synthetic aperture radar (SAR) imagery of the dunes along the Israel–Egypt border. *Int. J. Appl. Earth Obs. Geoinf.* **2016**, *46*, 13–21. [CrossRef]
20. Mattia, F.; Le Toan, T.; Picard, G.; Posa, F.I.; D'Alessio, A.; Notarnicola, C.; Gatti, A.M.; Rinaldi, M.; Satalino, G.; Pasquariello, G. Multitemporal C-band radar measurements on wheat fields. *IEEE Trans. Geosci. Remote Sens.* **2003**, *41*, 1551–1560. [CrossRef]
21. Ouaadi, N.; Ezzahar, J.; Khabba, S.; Er-Raki, S.; Chakir, A.; Hssaine, B.A.; Le Dantec, V.; Rafi, Z.; Beaumont, A.; Kasbani, M.; et al. C-band radar data and in situ measurements for the monitoring of wheat crops in a semi-arid area (center of Morocco). *Earth Syst. Sci. Data* **2021**, *13*, 3707–3731. [CrossRef]
22. Kaplan, G.; Fine, L.; Lukyanov, V.; Manivasagam, V.S.; Tanny, J.; Rozenstein, O. Normalizing the Local Incidence Angle in Sentinel-1 Imagery to Improve Leaf Area Index, Vegetation Height, and Crop Coefficient Estimations. *Land* **2021**, *10*, 680. [CrossRef]
23. Pipia, L.; Amin, E.; Belda, S.; Salinero-Delgado, M.; Verrelst, J. Green LAI Mapping and Cloud Gap-Filling Using Gaussian Process Regression in Google Earth Engine. *Remote Sens.* **2021**, *13*, 403. [CrossRef]
24. Nasrallah, A.; Baghdadi, N.; El Hajj, M.; Darwish, T.; Belhouchette, H.; Faour, G.; Darwich, S.; Mhawej, M. Sentinel-1 Data for Winter Wheat Phenology Monitoring and Mapping. *Remote Sens.* **2019**, *11*, 2228. [CrossRef]
25. Vavlas, N.C.; Waine, T.W.; Meersmans, J.; Burgess, P.J.; Fontanelli, G.; Richter, G.M. Deriving Wheat Crop Productivity Indicators Using Sentinel-1 Time Series. *Remote Sens.* **2020**, *12*, 2385. [CrossRef]
26. Picard, G.; Le Toan, T.; Mattia, F. Understanding C-band radar backscatter from wheat canopy using a multiple-scattering coherent model. *IEEE Trans. Geosci. Remote Sens.* **2003**, *41*, 1583–1591. [CrossRef]
27. Veloso, A.; Mermoz, S.; Bouvet, A.; Le Toan, T.; Planells, M.; Dejoux, J.F.; Ceschia, E. Understanding the temporal behavior of crops using Sentinel-1 and Sentinel-2-like data for agricultural applications. *Remote Sens. Environ.* **2017**, *199*, 415–426. [CrossRef]
28. Small, D. Flattening Gamma: Radiometric Terrain Correction for SAR Imagery. *IEEE Trans. Geosci. Remote Sens.* **2011**, *49*, 3081–3093. [CrossRef]
29. Marghany, M. Chapter 8—Principle theories of synthetic aperture radar. In *Synthetic Aperture Radar Imaging Mechanism for Oil Spills*; Gulf Professional Publishing: Houston, TX, USA, 2020; pp. 127–150. [CrossRef]
30. Blaes, X.; Defourny, P.; Wegmuller, U.; Vecchia, A.D.; Guerriero, L.; Ferrazzoli, P. C-band polarimetric indexes for maize monitoring based on a validated radiative transfer model. *IEEE Trans. Geosci. Remote Sens.* **2006**, *44*, 791–800. [CrossRef]

31. Mattia, F.; Satalino, G.; Dente, L.; Pasquariello, G. Using a priori information to improve soil moisture retrieval from ENVISAT ASAR AP data in semiarid regions. *IEEE Trans. Geosci. Remote Sens.* **2006**, *44*, 900–912. [CrossRef]
32. Widhalm, B.; Bartsch, A.; Goler, R. Simplified Normalization of C-Band Synthetic Aperture Radar Data for Terrestrial Applications in High Latitude Environments. *Remote Sens.* **2018**, *10*, 551. [CrossRef]
33. Makynen, M.P.; Manninen, A.T.; Simila, M.H.; Karvonen, J.A.; Hallikainen, M.T. Incidence angle dependence of the statistical properties of C-band HH-polarization backscattering signatures of the Baltic Sea ice. *IEEE Trans. Geosci. Remote Sens.* **2002**, *40*, 2593–2605. [CrossRef]
34. Torres, R.; Snoeij, P.; Geudtner, D.; Bibby, D.; Davidson, M.; Attema, E.; Potin, P.; Rommen, B.; Floury, N.; Brown, M.; et al. GMES Sentinel-1 mission. *Remote Sens. Environ.* **2012**, *120*, 9–24. [CrossRef]
35. Harfenmeister, K.; Spengler, D.; Weltzien, C. Analyzing Temporal and Spatial Characteristics of Crop Parameters Using Sentinel-1 Backscatter Data. *Remote Sens.* **2019**, *11*, 1569. [CrossRef]
36. Verrelst, J.; Malenovskỳ, Z.; Van der Tol, C.; Camps-Valls, G.; Gastellu-Etchegorry, J.P.; Lewis, P.; North, P.; Moreno, J. Quantifying vegetation biophysical variables from imaging spectroscopy data: A review on retrieval methods. *Surv. Geophys.* **2019**, *40*, 589–629. [CrossRef] [PubMed]
37. Verrelst, J.; Camps-Valls, G.; Muñoz Marí, J.; Rivera, J.; Veroustraete, F.; Clevers, J.; Moreno, J. Optical remote sensing and the retrieval of terrestrial vegetation bio-geophysical properties—A review. *ISPRS J. Photogramm. Remote Sens.* **2015**, *108*, 273–290. [CrossRef]
38. Rasmussen, C.E.; Williams, C.K.I. *Gaussian Processes for Machine Learning*; The MIT Press: New York, NY, USA, 2006.
39. Camps-Valls, G.; Verrelst, J.; Munoz-Mari, J.; Laparra, V.; Mateo-Jimenez, F.; Gomez-Dans, J. A survey on Gaussian processes for earth-observation data analysis: A comprehensive investigation. *IEEE Geosci. Remote Sens. Mag.* **2016**, *4*, 58–78. [CrossRef]
40. Verrelst, J.; Romijn, E.; Kooistra, L. Mapping Vegetation Density in a Heterogeneous River Floodplain Ecosystem Using Pointable CHRIS/PROBA Data. *Remote Sens.* **2012**, *4*, 2866–2889. [CrossRef]
41. Verrelst, J.; Rivera, J.P.; Gitelson, A.; Delegido, J.; Moreno, J.; Camps-Valls, G. Spectral band selection for vegetation properties retrieval using Gaussian processes regression. *Int. J. Appl. Earth Obs. Geoinf.* **2016**, *52*, 554–567. [CrossRef]
42. Xie, R.; Darvishzadeh, R.; Skidmore, A.K.; Heurich, M.; Holzwarth, S.; Gara, T.W.; Reusen, I. Mapping leaf area index in a mixed temperate forest using Fenix airborne hyperspectral data and Gaussian processes regression. *Int. J. Appl. Earth Obs. Geoinf.* **2021**, *95*, 102242. [CrossRef]
43. Pascual-Venteo, A.B.; Portalés, E.; Berger, K.; Tagliabue, G.; Garcia, J.L.; Pérez-Suay, A.; Rivera-Caicedo, J.P.; Verrelst, J. Prototyping Crop Traits Retrieval Models for CHIME: Dimensionality Reduction Strategies Applied to PRISMA Data. *Remote Sens.* **2022**, *14*, 2448. [CrossRef]
44. Estévez, J.; Berger, K.; Vicent, J.; Rivera-Caicedo, J.P.; Wocher, M.; Verrelst, J. Top-of-Atmosphere Retrieval of Multiple Crop Traits Using Variational Heteroscedastic Gaussian Processes within a Hybrid Workflow. *Remote Sens.* **2021**, *13*, 1589. [CrossRef]
45. Salinero-Delgado, M.; Estévez, J.; Pipia, L.; Belda, S.; Berger, K.; Paredes Gómez, V.; Verrelst, J. Monitoring Cropland Phenology on Google Earth Engine Using Gaussian Process Regression. *Remote Sens.* **2021**, *14*, 146. [CrossRef]
46. Reyes-Muñoz, P.; Pipia, L.; Salinero-Delgado, M.; Belda, S.; Berger, K.; Estévez, J.; Morata, M.; Rivera-Caicedo, J.P.; Verrelst, J. Quantifying Fundamental Vegetation Traits over Europe Using the Sentinel-3 OLCI Catalogue in Google Earth Engine. *Remote Sens.* **2022**, *14*, 1347. [CrossRef] [PubMed]
47. Estévez, J.; Salinero-Delgado, M.; Berger, K.; Pipia, L.; Rivera-Caicedo, J.P.; Wocher, M.; Reyes-Muñoz, P.; Tagliabue, G.; Boschetti, M.; Verrelst, J. Gaussian processes retrieval of crop traits in Google Earth Engine based on Sentinel-2 top-of-atmosphere data. *Remote Sens. Environ.* **2022**, *273*, 112958. [CrossRef] [PubMed]
48. Pan, Z.; Hu, Y.; Cao, B. Construction of smooth daily remote sensing time series data: A higher spatiotemporal resolution perspective. *Open Geospat. Data Softw. Stand.* **2017**, *2*, 1–11. [CrossRef]
49. Eilers, P.H.C.; Pesendorfer, V.; Bonifacio, R. Automatic smoothing of remote sensing data. In Proceedings of the 2017 9th International Workshop on the Analysis of Multitemporal Remote Sensing Images (MultiTemp), Brugge, Belgium, 27–29 June 2017; pp. 1–3. [CrossRef]
50. Savitzky, A.; Golay, M.J.E. Smoothing and Differentiation of Data by Simplified Least Squares Procedures. *Anal. Chem.* **1964**, *36*, 1627–1639. [CrossRef]
51. Hosseini, M.; McNairn, H.; Merzouki, A.; Pacheco, A. Estimation of Leaf Area Index (LAI) in corn and soybeans using multi-polarization C- and L-band radar data. *Remote Sens. Environ.* **2015**, *170*, 77–89. [CrossRef]
52. Camps-Valls, G.; Bruzzone, L. (Eds.) *Kernel Methods for Remote Sensing Data Analysis*; Wiley & Sons: Oxford, UK, 2009.
53. Verrelst, J.; Muñoz, J.; Alonso, L.; Delegido, J.; Rivera, J.; Camps-Valls, G.; Moreno, J. Machine learning regression algorithms for biophysical parameter retrieval: Opportunities for Sentinel-2 and -3. *Remote Sens. Environ.* **2012**, *118*, 127–139. [CrossRef]
54. Verrelst, J.; Alonso, L.; Camps-Valls, G.; Delegido, J.; Moreno, J. Retrieval of vegetation biophysical parameters using Gaussian process techniques. *IEEE Trans. Geosci. Remote Sens.* **2012**, *50*, 1832–1843. [CrossRef]
55. Whittaker, E.T. On a New Method of Graduation. *Proc. Edinburgh Math. Soc.* **1922**, *41*, 63–75. [CrossRef]
56. Verrall, R.J. A state space formulation of Whittaker graduation, with extensions. *Insur. Math. Econ.* **1993**, *13*, 7–14. [CrossRef]
57. Weinert, H.L. Efficient computation for Whittaker–Henderson smoothing. *Comput. Stat. Data Anal.* **2007**, *52*, 959–974. [CrossRef]
58. Zuliana, S.U.; Perperoglou, A. Two dimensional smoothing via an optimised Whittaker smoother. *Big Data Anal.* **2017**, *2*, 1–11. [CrossRef]

59. Craven, P.; Wahba, G. Smoothing noisy data with spline functions. *Numer. Math.* **1978**, *31*, 377–403. [CrossRef]
60. Frasso, G.; Eilers, P.H.C. L- and V-curves for optimal smoothing. *Stat. Model.* **2014**, *15*, 91–111. [CrossRef]
61. Hutchinson, M.F.; Hoog, F.R. Smoothing noisy data with spline functions. *Numer. Math.* **1985**, *47*, 99–106. [CrossRef]
62. Casella, A.; Orden, L.; Pezzola, N.A.; Bellaccomo, C.; Winschel, C.I.; Caballero, G.R.; Delegido, J.; Gracia, L.M.N.; Verrelst, J. Analysis of Biophysical Variables in an Onion Crop (*Allium cepa* L.) with Nitrogen Fertilization by Sentinel-2 Observations. *Agronomy* **2022**, *12*, 1884. [CrossRef] [PubMed]
63. Caballero, G.; Pezzola, A.; Winschel, C.; Casella, A.; Sanchez Angonova, P.; Rivera-Caicedo, J.P.; Berger, K.; Verrelst, J.; Delegido, J. Seasonal Mapping of Irrigated Winter Wheat Traits in Argentina with a Hybrid Retrieval Workflow Using Sentinel-2 Imagery. *Remote Sens.* **2022**, *14*, 4531. [CrossRef]
64. Köppen, W. The thermal zones of the Earth according to the duration of hot, moderate and cold 806 periods and of the impact of heat on the organic world. *Meteorol. Z.* **1884**, *20*, 215–226.
65. Sánchez, R.; Pezzola, N.; Cepeda, J. Caracterización edafoclimátia del área de influencia del INTA E.E.A Hilario Ascasubi. *Boletín de Divulgación* **1998**, *18*, 72.
66. Staff, S.S. *Soil Taxonomy: A Basic System of Soil Classification for Making and Interpreting Soil Surveys*; Natural Resources Conservation Service: Washington, DC, USA, 1999.
67. Orden, L.; Ferreiro, N.; Satti, P.; Navas-Gracia, L.M.; Chico-Santamarta, L.; Rodríguez, R.A. Effects of Onion Residue, Bovine Manure Compost and Compost Tea on Soils and on the Agroecological Production of Onions. *Agriculture* **2021**, *11*, 962. [CrossRef]
68. Sanchez, R.; Matarazzo, R. Caracterización y descripción de las causas edáficas que provocan efectos negativos en el cultivo de trigo (Patagones – Buenos Aires). In *Informe Técnico 27, EEA Hilario Ascasubi*; EEA Hilario Ascasubi: Buenos Aires, Argentina, 1983; pp. 1–8.
69. Agamennoni, R.; Matarazzo, R.; Rivas, J. Producción de trigo bajo riego. In *Boletín de Divulgación*; EEA Hilario Ascasubi: Buenos Aires, Argentina, 1996; pp. 10–16.
70. Confalonieri, R.; Foi, M.; Casa, R.; Aquaro, S.; Tona, E.; Peterle, M.; Boldini, A.; De Carli, G.; Ferrari, A.; Finotto, G.; et al. Development of an app for estimating leaf area index using a smartphone. Trueness and precision determination and comparison with other indirect methods. *Comput. Electron. Agric.* **2013**, *96*, 67–74. [CrossRef]
71. Zadoks, J.C.; Chang, T.T.; Konzak, C.F. A decimal code for the growth stages of cereals. *Weed Res.* **1974**, *14*, 415–421. [CrossRef]
72. Vasile, G.; Trouvé, E.; Ciuc, M.; Bolon, P.; Buzuloiu, V. Intensity-Driven-Adaptive-Neighborhood Technique for POLSAR Parameters Estimation. In Proceedings of the 2005 IEEE International Geoscience and Remote Sensing Symposium, Seoul, Korea, 29 July 2005; pp. 5509–5512.
73. Ye, Y.; Yang, C.; Zhu, B.; Zhou, L.; He, Y.; Jia, H. Improving Co-Registration for Sentinel-1 SAR and Sentinel-2 Optical Images. *Remote Sens.* **2021**, *13*, 928. [CrossRef]
74. Eilers, P.H.C. A Perfect Smoother. *Anal. Chem.* **2003**, *75*, 3631–3636. [CrossRef] [PubMed]
75. Atzberger, C.; Eilers, P.H.C. International Journal of Digital Earth A time series for monitoring vegetation activity and phenology at 10-daily time steps covering large parts of South America. *Int. J. Digit. Earth* **2011**, *4*, 365–386. [CrossRef]
76. Snee, R.D. Validation of Regression Models: Methods and Examples. *Technometrics* **1977**, *19*, 415–428. [CrossRef]
77. Verrelst, J.; Rivera, J.; Alonso, L.; Moreno, J. ARTMO: An Automated Radiative Transfer Models Operator toolbox for automated retrieval of biophysical parameters through model inversion. In Proceedings of the EARSeL 7th SIG-Imaging Spectroscopy Workshop, Edinburgh, UK, 11–13 April 2011.
78. Verrelst, J.; Rivera-Caicedo, J.P.; Reyes-Muñoz, P.; Morata, M.; Amin, E.; Tagliabue, G.; Panigada, C.; Hank, T.; Berger, K. Mapping landscape canopy nitrogen content from space using PRISMA data. *ISPRS J. Photogramm. Remote Sens.* **2021**, *178*, 382–395. [CrossRef]
79. Amin, E.; Verrelst, J.; Rivera-Caicedo, J.P.; Pipia, L.; Ruiz-Verdú, A.; Moreno, J. Prototyping Sentinel-2 green LAI and brown LAI products for cropland monitoring. *Remote Sens. Environ.* **2021**, *255*, 112168. [CrossRef]
80. Weibull, W. A Statistical Distribution Function of Wide Applicability. *J. Appl. Mech.* **1951**, *18*, 293–297. [CrossRef]
81. Rosenblatt, M. Remarks on Some Nonparametric Estimates of a Density Function. *Ann. Math. Stat.* **1956**, *27*, 832–837. [CrossRef]
82. Daughtry, C.S.T.; Gallo, K.P.; Goward, S.N.; Prince, S.D.; Kustas, W.P. Spectral estimates of absorbed radiation and phytomass production in corn and soybean canopies. *Remote Sens. Environ.* **1992**, *39*, 141–152. [CrossRef]
83. Delegido, J.; Verrelst, J.; Rivera, J.P.; Ruiz-Verdú, A.; Moreno, J. Brown and green LAI mapping through spectral indices. *Int. J. Appl. Earth Obs. Geoinf.* **2015**, *35*, 350–358. [CrossRef]
84. Satalino, G.; Balenzano, A.; Mattia, F.; Davidson, M.W.J. C-Band SAR Data for Mapping Crops Dominated by Surface or Volume Scattering. *IEEE Geosci. Remote Sens. Lett.* **2013**, *11*, 384–388. [CrossRef]
85. Che, M.; Chen, B.; Zhang, H.; Fang, S.; Xu, G.; Lin, X.; Wang, Y. A New Equation for Deriving Vegetation Phenophase from Time Series of Leaf Area Index (LAI) Data. *Remote Sens.* **2014**, *6*, 5650–5670. [CrossRef]
86. Shoshany, M.; Svoray, T.; Curran, P.J.; Foody, G.M.; Perevolotsky, A. The relationship between ERS-2 SAR backscatter and soil moisture: Generalization from a humid to semi-arid transect. *Int. J. Remote Sens.* **2000**, *21*, 2337–2343. [CrossRef]
87. Filgueiras, R.; Mantovani, E.C.; Althoff, D.; Fernandes Filho, E.I.; Cunha, F.F.d. Crop NDVI Monitoring Based on Sentinel 1. *Remote Sens.* **2019**, *11*, 1441. [CrossRef]
88. Brown, S.C.M.; Quegan, S.; Morrison, K.; Bennett, J.C.; Cookmartin, G. High-resolution measurements of scattering in wheat canopies-implications for crop parameter retrieval. *IEEE Trans. Geosci. Remote Sens.* **2003**, *41*, 1602–1610. [CrossRef]

89. Balenzano, A.; Mattia, F.; Satalino, G.; Davidson, M.W.J. Dense Temporal Series of C- and L-band SAR Data for Soil Moisture Retrieval Over Agricultural Crops. *IEEE J. Sel. Top. Appl. Earth Obs. Remote Sens.* **2010**, *4*, 439–450. [CrossRef]
90. Miralles, D.J.; Slafer, G.A.; Richards, R.A. *Influence of "Historic" Photoperiod during Stem Elongation on the Number of Fertile Florets in Wheat*; Cambridge University Press: Cambridge, UK, 2003. [CrossRef]
91. Slafer, G.A.; Rawson, H.M. Sensitivity of wheat phasic development to major environmental factors: A re-examination of some assumptions made by physiologists and modellers. *Funct. Plant Biol.* **1994**, *21*, 393–426. [CrossRef]
92. Slafer, G.A.; Abeledo, L.G.; Miralles, D.J.; Gonzalez, F.G.; Whitechurch, E.M. Photoperiod sensitivity during stem elongation as an avenue to raise potential yield in wheat. *Euphytica* **2001**, *119*, 191–197. [CrossRef]
93. Chauhan, S.; Darvishzadeh, R.; Lu, Y.; Boschetti, M.; Nelson, A. Understanding wheat lodging using multi-temporal Sentinel-1 and Sentinel-2 data. *Remote Sens. Environ.* **2020**, *243*, 111804. [CrossRef]

ARTÍCULO 3

"Synergy of Sentinel-1 and Sentinel-2 Time Series for Cloud-free Vegetation Water Content Mapping with Multi-Output Gaussian Processes"

This article belongs to the Special Issue Cropland Phenology Monitoring Based on Cloud-Computing Platforms of the Remote Sensing Journal. Journal Rank: JCR - Q1 (Geosciences, Multidisciplinary) / Cite Score - Q1 (General Earth and Planetary Sciences). The article was published in april 2023. This journal had an impact factor of 5.349 in 2023.

remote sensing

MDPI

Article

Synergy of Sentinel-1 and Sentinel-2 Time Series for Cloud-Free Vegetation Water Content Mapping with Multi-Output Gaussian Processes

Gabriel Caballero [1,*], Alejandro Pezzola [2], Cristina Winschel [2], Paolo Sanchez Angonova [2], Alejandra Casella [3], Luciano Orden [2,4], Matías Salinero-Delgado [1], Pablo Reyes-Muñoz [1], Katja Berger [1,5], Jesús Delegido [1] and Jochem Verrelst [1]

[1] Image Processing Laboratory (IPL), University of Valencia, C/Catedrático José Beltrán 2, Paterna, 46980 Valencia, Spain; jochem.verrelst@uv.es (J.V.)
[2] Remote Sensing and SIG Laboratory, Hilario Ascasubi Agricultural Experimental Station, National Institute of Agricultural Technology (INTA), Hilario Ascasubi 8142, Buenos Aires, Argentina
[3] Permanent Observatory of Agro-Ecosystems, Climate and Water Institute-National Agricultural Research Centre (ICyA-CNIA), National Institute of Agricultural Technology (INTA), Nicolás Repetto s/n, Hurlingham 1686, Buenos Aires, Argentina
[4] Centro de Investigación e Innovación Agroalimentaria y Agroambiental (CIAGRO-UMH), GIAAMA Reseach Group, Universidad Miguel Hernández, Carretera de Beniel Km, 03312 Orihuela, Spain
[5] Mantle Labs GmbH, Grünentorgasse 19/4, 1090 Vienna, Austria
* Correspondence: gabriel.caballero@uv.es; Tel.: +34-685-829-332

Abstract: Optical Earth Observation is often limited by weather conditions such as cloudiness. Radar sensors have the potential to overcome these limitations, however, due to the complex radar-surface interaction, the retrieving of crop biophysical variables using this technology remains an open challenge. Aiming to simultaneously benefit from the optical domain background and the all-weather imagery provided by radar systems, we propose a data fusion approach focused on the cross-correlation between radar and optical data streams. To do so, we analyzed several multiple-output Gaussian processes (MOGP) models and their ability to fuse efficiently Sentinel-1 (S1) Radar Vegetation Index (RVI) and Sentinel-2 (S2) vegetation water content (VWC) time series over a dry agri-environment in southern Argentina. MOGP models not only exploit the auto-correlations of S1 and S2data streams independently but also the inter-channel cross-correlations. The S1 RVI and S2 VWC time series at the selected study sites being the inputs of the MOGP models proved to be closely correlated. Regarding the set of assessed models, the Convolutional Gaussian model (CONV) delivered noteworthy accurate data fusion results over winter wheat croplands belonging to the 2020 and 2021 campaigns ($NRMSE_{wheat\ 2020}$ = 16.1%; $NRMSE_{wheat\ 2021}$ = 10.1%). Posteriorly, we removed S2 observations from the S1 & S2 dataset corresponding to the complete phenological cycles of winter wheat from September to the end of December to simulate the presence of clouds in the scenes and applied the CONV model at the pixel level to reconstruct spatiotemporally-latent VWC maps. After applying the fusion strategy, the phenology of winter wheat was successfully recovered in the absence of optical data. Strong correlations were obtained between S2 VWC and S1 & S2 MOGP VWC reconstructed maps for the assessment dates ($\overline{R^2}_{wheat-2020}$ = 0.95, $\overline{R^2}_{wheat-2021}$ = 0.96). Altogether, the fusion of S1 SAR and S2 optical EO data streams with MOGP offers a powerful innovative approach for cropland trait monitoring over cloudy high-latitude regions.

Keywords: radar vegetation index; time series; irrigated winter wheat; cross-correlation

Citation: Caballero, G.; Pezzola, A.; Winschel, C.; Sanchez Angonova, P.; Casella, A.; Orden, L.; Salinero-Delgado, M.; Reyes-Muñoz, P.; Berger, K.; Delegido, J.; et al. Synergy of Sentinel-1 and Sentinel-2 Time Series for Cloud-Free Vegetation Water Content Mapping with Multi-Output Gaussian Processes. *Remote Sens.* **2023**, *15*, 1822. https://doi.org/10.3390/rs15071822

Academic Editor: Javier J Cancela

Received: 22 February 2023
Revised: 24 March 2023
Accepted: 27 March 2023
Published: 29 March 2023

1. Introduction

Remote sensing (RS) technology offers an appealing opportunity to continuously quantify the health and productivity of croplands [1,2]. One of the key elements that significantly affect crop productivity is water [3]. Sufficient water availability is necessary

for proper plant growth, nutrient uptake, and photosynthesis. Vegetation water content (VWC) is a useful indicator of the water status of crops and can help in monitoring the water needs and ensuring optimal management [4–6]. Climate change has become more pronounced over the past few decades and has caused water scarcity in many regions of the world. Consequently, water stress manifested as among the most critical abiotic stressors, negatively affecting plant growth and crop yield worldwide [7]. Real-time monitoring of the plant water status is urgently required to enable effective management of irrigation scheduling and to prevent waste of water and crop stress. Leaf water content (LWC) is a key variable for vital physiological processes, such as stomatal conductance and transpiration [8]. However, decoupling the spectral contributions of LWC and vegetation's canopy is challenging. Instead, the estimation of VWC, described by LWC $\times$ LAI, is more feasible and often preferred [9].

Today, an unprecedented amount of Earth observation (EO) opportunities emerged from the advent of the European Space Agency's Copernicus programme [10]. The Sentinels satellites guarantee long-term observational commitment and operate a variety of sensors with different spectral configurations and spatial resolutions offering global coverage and synergistic data exploiting possibilities [10]. The flagship land optical operational EO system is the Sentinel-2 (S2) constellation consisting of two polar-orbiting satellites (S2-A and S2-B) [11]. The multi-spectral instrument (MSI) on board S2, combines a relatively high spatial resolution (10–20 m) with a good spectral resolution (13 bands), and the combination of the two satellites ensures a high revisit time (5-day). A remarkable amount of research applying S2 data for crop traits mapping in a quantitative way has been successfully conducted [12–16]. Beyond the well-known benefits that optical RS provides for cropland monitoring, the retrieval of complete vegetation traits time series along the phenological cycle is sometimes hampered by weather conditions in high-latitude areas. In this regard, radar-based RS brings the technology to mitigate this limitation. Sentinel-1 (S1) as a synthetic aperture radar (SAR) sensor permits C-band image acquisition in all-weather conditions during day or night time [17]. The S1 constellation, comprising of S1-A and S1-B satellites, predefines the interferometric wide swath (IW) mode over land consisting of dual-polarized (VV & VH) images, at 10 m of spatial resolution every 6 days in a single pass. Although there is consensus that the vegetation-radar backscatter mechanisms are complex, there is no doubt that the radar signal at C-band is altered by the vegetation's three-dimensional structure and biomass [18,19]. Unlike optical satellites, the observation geometry plays a weighty role in radar acquisitions [20,21]. Multiple studies exploited radar imagery for vegetation biophysical variables monitoring [22–25]. For instance, Caballero et al. [25] presented a novel approach based on S1 radar observations at different local incidence angles for winter wheat LAI monitoring. They achieved satisfactory validation results (R^2 = 0.67 and RMSE = 0.88 m^2 m^{-2}), and proved that S1-based LAI predictions can support cropland monitoring in cloud-prone areas where the optical vegetation traits retrieval models cannot be applied for quantitative crop mapping purposes.

The frequent coverage and the systematic observations of S1 & S2 have opened the door to data-fusion-based RS applications for crop monitoring, land surface change detection and land cover mapping [26,27]. Several research efforts took advantage of the high radiometric quality of S1 in synergy with the improved optical sensor of S2 [28–31]. However, processing S2 optical and S1 radar time series has always been tedious, particularly when a substantial number of preprocessing steps must be implemented for the whole dataset. Downloading S1 and S2 images from the Copernicus data hub [32] usually requires a lot of time and storage space. In this regard, seeking to achieve fully automated preprocessing of EO data streams, migration to cloud-computing platforms offers a solution [33]. Recently, the Google Earth Engine (GEE) platform emerged as a promising, free-access, high-performance computing platform that enables cloud-based processing of petabytes of S1 and S2 satellite data, among others [34]. The GEE platform not only provides the powerful computational capability and access to the Copernicus catalog, but also allows for the integration of machine learning (ML) algorithms [33,35].

Regarding the creation of continuous, cloud-free S1 & S2 time series data streams, ML techniques can be implemented to explicitly learn and exploit the joint relationships of both data streams. Gaussian processes (GP), a nonparametric Bayesian ML regression algorithm, has had a notable impact on the remote sensing community following the pioneering publication by Rasmussen and Williams [36]. GP has been openly and successfully applied for the learning task of analyzing the auto-correlations of single-EO-dataset-channel models [33,37]. GP regression has advanced considerably in recent years, extending the GP concept to multiple-channel models. For computing non-trivial dependencies between multiple and related model outputs, multi-task Gaussian process prediction [38] widely known as multi-output Gaussian process (MOGP) offers a set of kernel models to learn such correlations [39]. The concept of multi-output learning emerged from the field of geostatistics [40]. The MOGP modeling approach can capture valuable information across correlated outputs to provide more accurate predictions than directly modeling these outputs independently [41]. In the context of EO data streams, developing models that exploit the dependencies between optical and radar sensors results particularly convenient when the optical data are affected by cloudy sky conditions leading to gaps in the data stream. Thus, SAR imagery can be used to complement optical sources [29,33,42]. A differentiating attribute of MOGP is the ability of the models to perform multiple channel prediction tasks in the presence of missing input data [43]. This makes MOGP particularly appealing for the fusion of S1 and S2 data streams.

To date, the usage of MOGP to fuse S1 and S2 data streams has only been investigated by Pipia et al. [29] with the purpose of producing continuous LAI time series. Radar-optical data fusion for crop monitoring purposes is a novel field of research that warrants greater attention. For instance, the synergistic usage of S1 & S2 data streams for crop monitoring in a cloud-computing platform by exploiting the cross-correlations of the MOGP model's output channels have yet to be fully explored. Therefore, this study aims to fulfill the following three main objectives: (1) to train several MOGP models with S1 radar vegetation index (RVI) [44] & S2 GP VWC time series data over two irrigated winter wheat paddocks and select the best model for posterior data fusing; (2) to examine if the best-performing MOGP model effectively retrieves crop traits under simulated cloudy conditions; (3) to map the S1 & S2 MOGP-reconstructed VWC values for the gap-filled intervals at the pixel level and evaluate the MOGP's capacity for reconstructing the complete phenological cycle of winter wheat in the absence of optical data.

2. Methodology

2.1. Theoretical Background

In the following, we notationally review the single-output GP and MOGP formulations, adapted to the general requirements of this study.

2.1.1. Single-Output Gaussian Processes Modeling

We refer to the standard GP as a single-output Gaussian process (SOGP). It can be formulated as follows. Let $\mathfrak{D} = \{x_i, y_i\}_{i=1}^{N}$, be a set of N pairs of a $x_i \in \mathbb{R}^{\mathcal{B}}$ point belonging to the training dataset $X = \{x_i\}_{i=1}^{N}$ assigned to a random variable y_i. GP is a random process that uses these pairs to learn the function outputs f_* given a test dataset X_* of size $N_* \times \mathfrak{D}$. Let us assume an additive noise model with a zero mean:

$$y_i = f_i(x_i) + \mathcal{E}_i, \;\; \mathcal{E}_i \sim \mathcal{N}\left(0, \sigma_n^2\right) \tag{1}$$

where σ_n^2 is the variance of the Gaussian noise and f_i is the nonparametric latent function to be found. Assuming independent Gaussian noise, the joint distribution of observations and test predictions is:

$$\begin{pmatrix} y \\ f_* \end{pmatrix} \sim \mathcal{N}\left(\begin{bmatrix} 0 \\ 0 \end{bmatrix}, \begin{bmatrix} \boldsymbol{K}(X,X) + \sigma_n^2 \boldsymbol{I} & \boldsymbol{K}(X,X_*) \\ \boldsymbol{K}(X_*,X) & \boldsymbol{K}(X_*,X_*) \end{bmatrix} \right) \tag{2}$$

where $K(X, X)$ represents the self-similarities in the training set, $K(X, X_*) = K_*$ and $K(X_*, X) = K_*^T$ are the similarities between training and test sets, and $K(X_*, X_*) = K_{**}$ express the self-similarities in the test set. SOGP models are built through parametrizing a covariance kernel that computes the measures of similarity between two points x_i and x_j. Expressive kernels allow the improved representation of complex signals. The squared exponential kernel arises as one of the most used kernels in GP modeling. It can be calculated as:

$$k(x_i, x_j) = \sigma_f^2 e^{-\frac{1}{2\ell^2}\|x_i - x_j\|^2} \tag{3}$$

where σ_f^2 (signal variance) is a scaling factor, and parameter ℓ (variance of the Gaussians) controls the length scale that modules the regression process smoothness and confidence. The model hyperparameters can be learned by maximizing the marginal likelihood of the model [45], through a cross-validation strategy [46], or applying a Bayesian learning process [47]. A SOGP establishes a prior distribution over functions. This can be converted to a posterior probability distribution of X_* given f and the previous X conditioning on the observations, to obtain another Gaussian:

$$p(f_*|X_*, X, y) \sim \mathcal{N}\left(y_*|\mu_{SOGP}, \sigma_{SOGP}^2 + \sigma_n^2 \boldsymbol{I}\right) \tag{4}$$

According to the SOGP formulation, f_* is normally distributed with mean (μ_{SOGP}) and variance (σ_{SOGP}^2) given by:

$$\mu_{SOGP}(x_*) = k(x_*, X)\left[\boldsymbol{K}(X, X) + \sigma_n^2 \boldsymbol{I}\right]^{-1} y \tag{5}$$

$$\sigma_{SOGP}^2(x_*) = k(x_*, x_*) - k(x_*, X)\left[\boldsymbol{K}(X, X) + \sigma_n^2 \boldsymbol{I}\right]^{-1} k(X, x_*) \tag{6}$$

To sum up, SOGP offers a natural mechanism to construct and calibrate uncertainties automatically.

2.1.2. Multi-Output Gaussian Processes Modeling

Let us now assume the S1 and S2 synergy case, where different outputs have different training input points, this model is called heterotopic in the geostatistics literature [48]. For simplicity, we assume an isotopic setting where each model output has the same set of inputs. In the following, we assume that the mean vector of the Gaussian distribution is zero in a free-noise environment. Let $\mathfrak{D}_1 = \{(t_i, f_1(t_i))|i = 1, \ldots, N\}$ be a set of N pairs of RVI random functions f_i extracted from S1 SAR data acquired at times t_i and $\mathfrak{D}_2 = \{(t_i, f_2(t_i))|i = 1, \ldots, N\}$ the corespondent VWC samples derived from S2 optical data, if f_1 and f_2 follow a GP we can write:

$$f_1(t) \sim \mathcal{GP}(0, k_1(t, t_*)) \tag{7}$$

$$f_2(t) \sim \mathcal{GP}(0, k_2(t, t_*)) \tag{8}$$

where k_1 and k_2 are the covariance kernels then the vector valued functions for f_1 and f_2 can be expressed as Gaussian distributions $f_1 \sim \mathcal{N}(0, \boldsymbol{K}_1)$ and $f_2 \sim \mathcal{N}(0, \boldsymbol{K}_2)$ being K_1 and K_2 the covariance kernel matrixes. Now we create a stacked larger vector $\boldsymbol{f}$ containing f_1 and f_2. Assuming that the two processes are independent we can obtain:

$$\begin{bmatrix} f_1 \\ f_2 \end{bmatrix} \sim \mathcal{N}\left(\begin{bmatrix} 0 \\ 0 \end{bmatrix}, \begin{bmatrix} \boldsymbol{K_1} & \boldsymbol{0} \\ \boldsymbol{0} & \boldsymbol{K_2} \end{bmatrix}\right) \tag{9}$$

where the blocks outside the main diagonal are zero because the dependency between f_1 and f_2 was supposed to be zero. The easiest way to extend the SOGP to MOGP cases is to model each of the model's channels singly with a SOGP. If the outputs are correlated, the SOGP approach fails to account for correlations between the outputs of the model impairing regression processes performance [38]. If we want to account for dependencies between the processes, the joint multivariate Gaussian distribution can be written as:

$$\begin{bmatrix} f_1 \\ f_2 \end{bmatrix} = \begin{bmatrix} f_1(t_1) \\ \vdots \\ f_1(t_N) \\ f_2(t_1) \\ \vdots \\ f_2(t_N) \end{bmatrix} \sim \mathcal{N}\left(\begin{bmatrix} 0 \\ 0 \end{bmatrix}, \begin{bmatrix} \boldsymbol{K}_{f_1,f_1} & \boldsymbol{K}_{f_1,f_2} \\ \boldsymbol{K}_{f_2,f_1} & \boldsymbol{K}_{f_2,f_2} \end{bmatrix} \right) \tag{10}$$

Equation (10) can be simplified to $f \sim \mathcal{N}(0, \boldsymbol{K}_{f,f})$. The main challenge of MOGP is to build a cross-covariance function $cov[f_1(t),\ f_2(t_*)]$ such that the matrix $\boldsymbol{K}_{f,f} \in \mathbb{R}^{NxN}$ is positive semi-definite and symmetric [39,41]. The properties of the SOGP are immediately transferred to MOGP because it can straightforwardly be interpreted as SOGP on an extended input space. For a detailed review of the $\boldsymbol{K}_{f,f}$ matrix development see the publication by Álvarez et al. [39].

One particular approach for building the covariance functions is known as process convolution. Each output of the model results from the convolution of a smoothing kernel and a latent random GP. It was firstly introduced by Barry and Hoef [49] to construct covariance functions for SOGP, and later for MOGP [50,51].

2.2. Study Area

The Region of Interest (ROI) selected for the study is an irrigated crop area located in Buenos Aires Province, in the southeast of Argentina (see Figure 1). The extension of the cultivated area of the Bonaerense Valley of Colorado River (BVCR) is approximately 91,163 ha, comprising winter crops such as wheat, barley, forage, and cereals and horticulture [52]. Since 2016, a team of experts from Argentina's National Institute of Agricultural Technology (INTA) Hilario's Ascasubi Experimental Station (HAEE) has been gathering in situ data to create a land cover map each year [25]. The appointed study area mainly corresponds to a dryland agri-environment, and gravity irrigation has enabled most of the agricultural practices in the region [53]. This study focused on two winter wheat fields (*triticum aestivum*) belonging to the BVCR's 2020 and 2021 crop campaigns [54].

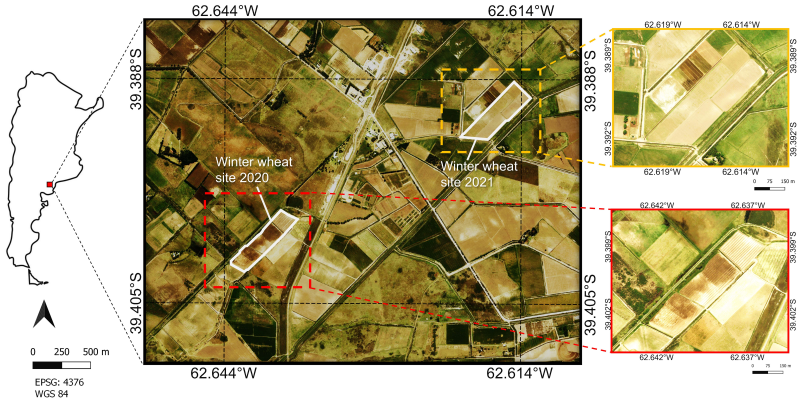

Figure 1. Overview of BVCR test sites (ROI) for the winter wheat campaigns of the years 2020 and 2021. The red and orange dotted rectangles delimit the MOGP subsets analyzed in Section 3.3. Reference system: WGS84 (EPSG 4326). (For interpretation of the references to color in this figure legend, the reader is referred to the Web version of this article).

2.3. Sentinel-2 Time Series Preprocessing

The COPERNICUS/S2_SR image collection over the ROI was assembled using GEE, where the S2 multispectral surface reflectance (S2-L2A) images are available in the form of tiles from December 2018 to current. The cloudy pixel percentage (CPP) was configured to 5 % and the bitmask QA60 band with cloud mask information was used to filter the S2 image collection. The cloud mask permits cloudy and cloud-free pixels to be identified. The 60 m resolution QA60 band includes both cirrus clouds and dense clouds with an indicator specifying the cloud type. Bits 10 and 11 are clouds and cirrus, respectively. The standard GP regression model presented in Caballero et al. [54] was tailored to be scalable into the GEE framework to generate VWC time series at 10 m using the methodology proposed by Pipia et al. [33]. The S2 GP VWC hybrid model was trained with in situ measurements collected in the BVCR during the 2020 crop campaign using Gaussian Processes as a core machine learning regression algorithm (MLRA) and an active learning technique (AL) [55] to estimate VWC of irrigated winter wheat (R^2 = 0.75, RMSE = 416 g m^{-2}). With AL strategies, the number of samples in hybrid modeling can be effectively decreased. Therefore, using an "optimal" statistical technique, the MLRA selects the most representative samples from the training dataset, which leads to the GP hybrid model reaching superior accuracies [56]. Several research efforts have successfully used AL to intelligently reduce the training dataset's size [54,57–59]. The in situ VWC values considered the total amounts of water stored in all wheat plant organs including leaves, fruits, flowers, and stalks. The *VWC* values were then obtained by calculating the difference between the fresh (*FW*) and dry (*DW*) organic matter and referring it to the sowing area (*A*) implicated in the field data collection process. Additionally, seeking to integrate the bare soil contribution, we introduced the fractional vegetation cover (*FVC*) in situ measured values to the calculations of *VWC*:

$$VWC = \frac{(FW - DW)}{A} \times FVC \ \left[g\ m^{-2}\right] \quad (11)$$

FVC is defined as the ratio of green vegetation's vertical projected area to the considered land surface extension [60–64]. This approach arises as a necessity for the improvement of the concept of canopy water content (CWC) defined as the total mass of water in all plants' leaves per surface unit (see Section 2.5.1 of Caballero et al. [54] for a thorough explanation of the formulas used to determine the *VWC* values). The S2 GP VWC hybrid model accepts as input the S2 spectral bands at 10 m and 20 m and predicts VWC along with associated uncertainties. The availability of S2 images strongly depends on sky conditions

over the study site and differs from one crop campaign to other. A total of 44 and 52 cloud-free atmospherically corrected S2 scenes were collected unequally spaced between December 2018 and January 2021 (11 S2 images correspond to the winter wheat 2020 crop campaign from 29 August to 12 December 2020) (see also Caballero et al. [54] for details), and between November 2019 and January 2022 (8 S2 images correspond to the winter wheat 2021 crop campaign from 24 August to 22 December 2021), respectively.

2.4. Sentinel-1 Time Series Preprocessing

Only descendent orbits were found suitable for monitoring the ROI due to the S1 acquisition configuration over the study site. Two relative orbits are thus available for EO purposes: orbits 68 for S1-A and S1-B and 141 for S1-A. A detailed overview of the S1 acquisition over the BVCR at multiple incidence angles is provided by Caballero et al. [25]. In the case of S1, the acquisitions are equally spaced. One S1-A or S1-B descendent pass is available every 6 days over the study site for the relative orbit 68 approximately at 6.20 a.m. local time. The S1-A acquisitions for the relative orbit 141 have a revisit time of 12 days. Radar data was collected from the GEE catalog accessing the COPERNICUS/S1_GRD_FLOAT dataset. It provides S1 Interferometric Wide Swath (IW) Ground Range Detected (GRD) scenes in dual-polarization VH+VV, that have been processed using the Sentinel-1 Toolbox to generate radiometrically calibrated, ortho-corrected products. For each BVCR crop campaign, two completed collections of S1 images were created for the two observation geometries, covering a time span of more than 3 years. From December 2018 to January 2021, there were 64 S1–orbit 141 and 103 S1–orbit 68 images (21 S1–orbit 68 images and 11 S1–orbit 141 images correspond to the 2020 winter wheat crop campaign) and 66 S1–orbit 141 and 115 S1–orbit 68 images from November 2019 to January 2022 (21 S1–orbit 68 images and 10 S1–orbit 141 images correspond to the 2021 winter wheat crop campaign). For each S1 scene, the dual-pol Radar Vegetation Index (RVI) Kim et al. [44], was initially generated as follows:

$$RVI = \frac{4VH}{VH + VV} \tag{12}$$

The coherent integration of signals backscattered from different targets in the resolution cell induces the speckle noise to be generated in the S1 data. The use of local statistics is one of the simplest ways to reduce the speckle noise in SAR data [65]. Spatial speckle filtering 7 × 7 Refined Lee [66] as coded in https://github.com/senbox-org/s1tbx/ (accessed on 11 January 2023), was applied. The refined Lee approach makes use of local gradient data. It does not blur the edges and minute details, and it does not require picture modeling. Depending on how the edge is oriented, the local mean and variance for both the additive and multiplicative noise instances are calculated from a smaller number of pixels. As a result, the edge becomes sharper and the noise around it is reduced [66]. Veloso et al. [28] analyzed the temporal trend of the cross-polarized ratio VH/VV for a variety of winter and summer crops (wheat, rapeseed, maize, soybean and sunflower) in southwest France. They suggested a 7 × 7 window size for filtering the speckle of the cultivated region observed by S1. To recover the essential curve shape, S1 time series smoothing is required [67]. Smoothing has the dual objectives of removing random noise and, ideally, maintaining the true spectral signal. For signal denoising purposes, RVI temporal profiles were filtered using an additional Savitzky–Golay (S–G) smoother [68] (window length = 9, polynomial order = 2) at the pixel level. The S–G smoother whit these predefined parameters, fits a polynomial of order 2 to the 9 RVI samples in the window length to locally smooth a noisy signal employing the least-squares concept. Regarding the S–G parametrization, lower values of the polynomial order can cope with low-rate changing phenomena such as crop rotation in the BVCR. The size of the windows is related to the frequency of the S1 acquisitions. The S–G parameters selection methodology was based on the analysis of the power spectrum associated with the S1–RVI signal. High-frequency components in the power spectrum result from the noise's (if it's genuinely random) ability to shift

unpredictably from pixel to pixel. On the other hand, the lower frequency range has a greater concentration of signal power [69].

2.5. MOGP Models Parametrization

The MOGP processing was entirely conducted within the Multi-Output Gaussian Process Toolkit (MOGPTK) [43] version 0.3.2. The MOGPTK is a Python toolkit for performing multi-output GP regression with kernels utilizing the cross-correlation information between channels to better model time-series signals. The set of MOGP kernels implemented is particularly pertinent for signal reconstruction in the case of missing data. The toolkit provides the functionality for training and interpreting GP models with multiple data channels and includes plotting functions for the case of single input with multiple outputs. More information can be found at: https://github.com/GAMES-UChile/mogptk/ (accessed 11 January 2023).

The preprocessed S1 and S2 time series were first loaded into MOGPTK creating two and three-channel models: (i) S2 GP VWC (CH-1), (ii) S1 orbit 68 RVI (CH-2), (iii) S1 orbit 141 RVI (CH-3). Then we removed a range of data from the CH-1 to simulate the S2 data loss corresponding to the winter wheat cycles (From the beginning of September to the end of December, we removed 9 S2 images for the 2020 campaign and 6 S2 scenes related to the 2021 winter wheat crop campaign) and additionally removed 10% of the data points for CH-2 and CH-3 randomly. Regarding 2020 and 2021 crop campaigns, 35 S2 (CH-1) + 92 S1–orbit 68 (CH-2) + 53 S1–orbit 141 (CH-2) images and 46 S2 (CH-1) + 103 S1–orbit 68 (CH-2) + and 59 S1–orbit 141 (CH-3) images were synergistically used to train the MOGP models, respectively. Aiming to improve training results each data channel was linearly detrended and normalized to have zero mean and unit variance utilizing the transformations provided by the MOGPTK. We analyzed four MOGP spectral kernels: (i) the Spectral Mixture Kernels for Multi-Output Gaussian Processes (MOSM) [70], (ii) the Cross-Spectral Mixture (CSM) [71], (iii) the Linear Model of Coregionalization (LMC) [39,40], and (iv) the Convolutional Model (CONV) [72,73] with four spectral components per channel (Q = 4). The MOGP kernels' parameters were randomly instantiated to establish an initial set of reasonable values for the S1 & S2 dataset using Independent Spectral Mixture (SM) as an estimation method. SM fits an independent GP model for each channel of the dataset with a spectral mixture kernel. Posteriorly it uses the tuned parameters as initial values of the MOGP kernels. For each channel, the noise was initialized with 1/30 of the variance. The MOGP models were then trained using the Adam optimizer [74]. During the training stage, the hyperparameters of the kernel are optimized to approach the training data. The learning rate was set up to 0.1 and the number of iterations for initialization in 500.

In addition, we also considered the SOGP SM kernel using the Bayesian Nonparametric Spectral Estimation (BNSE) [75] as the initialization method to estimate the kernel parameters from the S1 & S2 dataset. BNSE aims to assess the power spectral density of a time series signal and then select the Q greater peaks in the estimated spectrum. The kernel's mean, magnitude, and variance are initialized based on the peak's position, magnitude, and with of the detected spectral components, respectively.

2.6. Experimental Setup

Two distinct ROIs were considered for training the MOGP algorithms and evaluating the S1 and S2 synergy capacity to map VWC over an irrigated area of winter wheat crop. Table 1 shows the geographic boundaries, the dimension in pixels, and the area expressed in hectares for each selected ROI belonging to the winter wheat paddocks of the BVCR 2020 and 2021 crop campaigns. The S2 GP VWC maps were stacked along with S1 orbit 68 and S1 orbit 141 RVI products and the mean for the ROI was then calculated. An exhaustive detail of S1 & S2 acquisition dates for models validation corresponding to the winter wheat 2020 and 2021 crop campaigns is given in Tables A1 and A2 correspondingly. S1 & S2 datasets were used to initialize and train the MOGP models. Aiming to completely reconstruct the VWC cycles over winter wheat cropland, we created artificial S2 GP VWC data gaps (latent

S2 GP VWC data). Seeking to explore the S1-derived RVI capability to reconstruct S2-based VWC maps at distinct acquisition geometries, the MOGP performance was subsequently assessed given models with two and three input channels. Three tests for each ROI were conducted analyzing the following MOGP model input configurations: (i) S2 & S1 orbit 68 (2-channel model), (ii) S2 & S1 orbit 141 (2-channel model), and (iii) (i) S2 & S1 orbits 68 and 141 (3-channel model). Several goodness-of-fit metrics were evaluated to select the best MOGP model: the mean absolute error (*MAE*, Equation (13)), the root mean square error (*RMSE*, Equation (15)), the mean absolute percentage error (*MAPE*, Equation (14)), the normalized root mean square error (*NRMSE*, Equation (16)), and the training time were recorded. Below we display the formulation used for *MAE*, *MAPE*, *RMSE* and *NRMSE* calculations:

$$MAE = \frac{1}{N}\sum_{i=1}^{N}|y_i - \hat{y}_i| \tag{13}$$

$$MAPE = \frac{1}{N}\sum_{i=1}^{N}\frac{|y_i - \hat{y}_i|}{y_i} \tag{14}$$

$$RMSE = \sqrt{\frac{1}{N}\sum_{i=1}^{N}(y_i - \hat{y}_i)^2} \tag{15}$$

$$NRMSE = \frac{RMSE}{(y_{max} - y_{min})} \tag{16}$$

where $\{y_i\}_{i=1}^{N}$ are the S2 GP VWC latent observations used for model assessing, $\{\hat{y}_i\}_{i=1}^{N}$ are the VWC retrieved values based on S1 RVI data, $(y_{max} - y_{min})$ is the S2 GP VWC data range and $\overline{y}$ is the mean of the VWC S2-derived values. To investigate the correlation between each channel of the S1 & S2 dataset, we also plotted the cross-correlation matrix for each evaluated MOGP model. Finally, the best MOGP model was applied to winter wheat 2020 and 2021 sites (see Figure 1). A MOGP model was iteratively trained per pixel using the S1 & S2 three-channel dataset. Each S1 & S2 MOGP VWC reconstructed subset was compared against the latent S2 GP VWC by calculating the coefficient of determination (R^2) and the linear regression.

Table 1. ROI boundaries in geographic coordinates (WGS84), x-pixels quantity (Qty-x), y-pixels quantity (Qty-y), and ROI area selected for training the MOGP models with the S1 & S2 dataset. ROI-1 belongs to the winter wheat 2020 site whereas the ROI-2 to 2021 site.

	North	West	South	East	Qty-x	Qty-y	Area [ha]
ROI-1	−39.398	−62.645	−39.404	−62.636	10	12	1.2
ROI-2	−39.391	−62.618	−39.392	−62.616	12	13	1.56

2.7. Delineation of Retrieval Workflow

Figure 2 gives an overview of the complete processing workflow. Three well-defined processing blocks are depicted, starting with an S2 and S1 imagery acquisition and pre-processing section, followed by MOGP best model selection, and the retrieval of VWC applying MOGP to S1 and S2 time series datasets. To sum up, the implemented processing workflow consisted of the following six main steps:

1. Building of VWC time series applying a GP model trained with in situ data of the BVCR 2020 crop campaign to S2 imagery, and pre-processing of RVI time series for S1 orbit 68 and orbit 141 imagery, respectively;
2. Assembling the S1 & S2 dataset containing multitemporal VWC retrieved values and S1 post-processed RVI data for a specific ROI of the BVCR study site;

3. Setting up the MOGP kernels with Q = 4 and initializing the parameters using SM;
4. Training the MOGP models with the S1 & S2 dataset using the Adam optimizer and assessing the regression statistics error metrics (MAE, MAPE, RMSE, and NRMSE) for best model selection;
5. Multi-seasonal mapping of VWC retrieved given the best evaluated MOGP model and S1 & S2 stacked datasets at pixel level over two distinct bounded fields and corresponding process performance;
6. Reconstructing of artificially removed S2 GP VWC data gaps over winter wheat cropland considering the BVCR 2020 and 2021 crop campaigns.

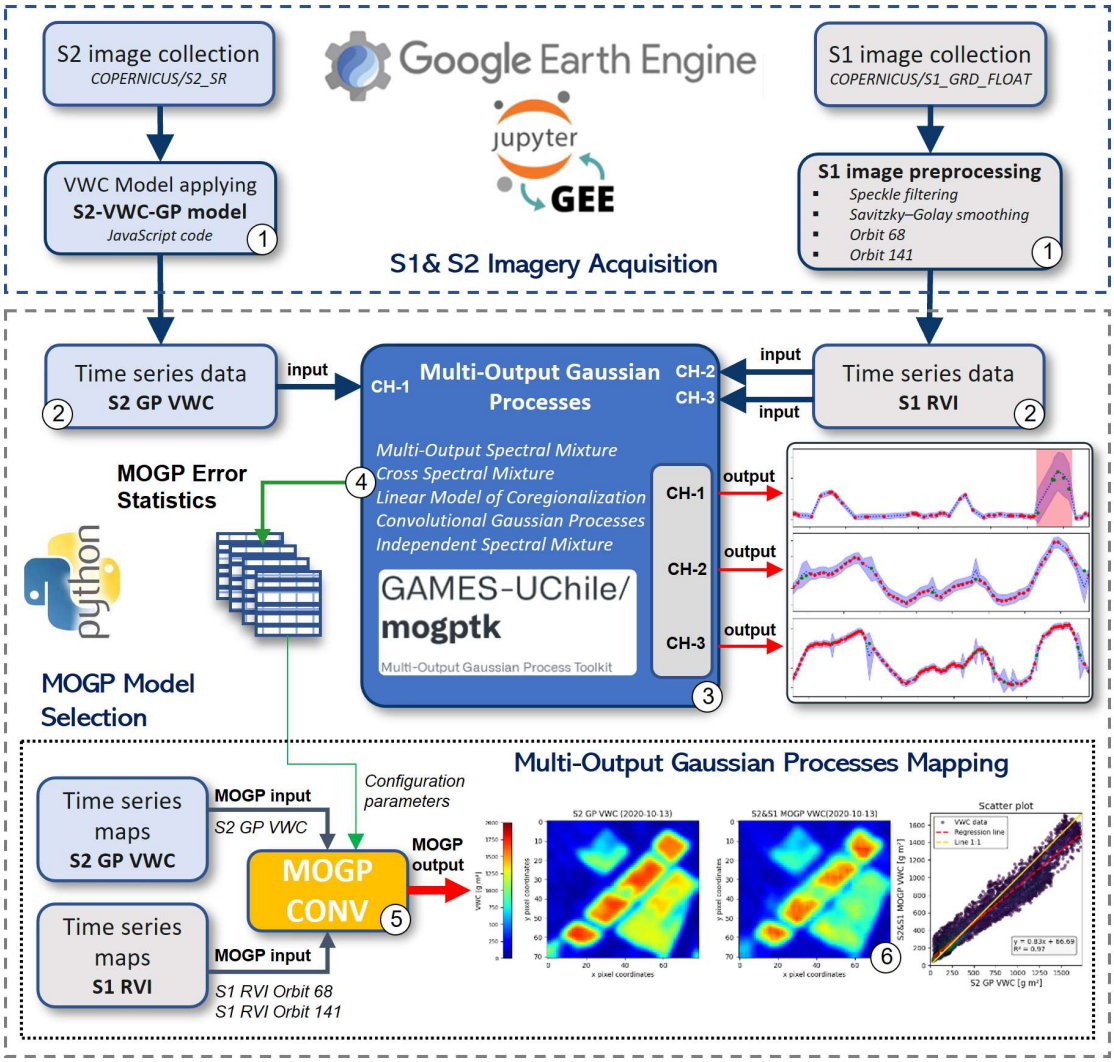

Figure 2. Illustration of the processing workflow to obtain maps of vegetation water content over irrigated winter wheat, as described in Section 2.7. The ordinal numbers in the graph refer to the workflow processing steps. The maps show the output obtained by our MOGP VWC models over the BVCR study site in Argentina.

The entire software framework was implemented in Python version 3.6.13 (https://www.python.org/downloads/release/python-3613/, accessed on 22 September 2022) utilizing the geemap package version 0.19.1 (https://github.com/giswqs/geemap/, accessed on 11 January 2023) for mapping interactively with Google Earth Engine.

3. Results

3.1. S1 SAR RVI & S2 GP VWC Temporal Profiles

In an attempt to analyze multi-seasonal VWC time series over the averaged ROI-1 presented in Table 1, the temporal profiles of S2 GP VWC and S1 RVI orbits 68 and 141 over the irrigated winter wheat sites 2020 are displayed in Figure 3. It is worth highlighting that the typical crop rotation at the study site is: maize-sunflower-wheat [53].

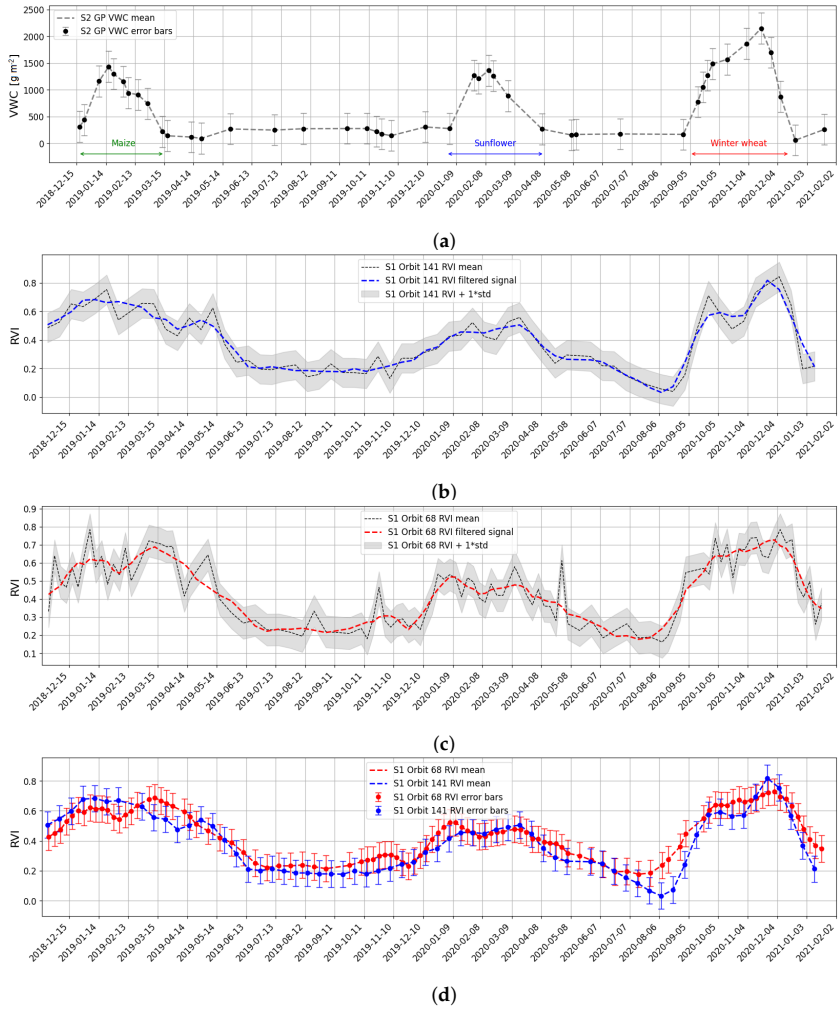

Figure 3. Temporal profiles (mean value and standard deviation) of averaged selected ROI-1 over a winter wheat parcel belonging to the BVCR 2020 crop campaign. S2 GP VWC time series from December 2018 to the end of January 2021 (**a**). S1 RVI orbit 141 smoothed (dashed blue line) and original (dashed black line) time series (**b**). S1 RVI orbit 68 smoothed (dashed red line) and original (dashed black line) time series (**c**). S1 RVI Orbit 68 (red line) and S1 orbit 141 (blue line) RVI time series (**d**).

The temporal profiles for S2 GP VWC and S1 RVI for orbits 68 and 141 for the winter wheat 2021 averaged ROI-2 are shown in Figure 4. Regarding the winter wheat crop for the 2021 campaign, it can be seen that the summer predecessors' crops were sunflower for hybrid seed in 2021 and maize in 2020. An appreciable difference can be distinguished when the S1 RVI for orbits 68 and 141 are plotted jointly (see Figures 3d and 4d). Note that there is a time asynchrony between S1 acquisitions as both satellites S1-A and S1-B share descendent orbit 68. Moreover, the RVI amplitude offset between orbits 68 and 141 is due to the different SAR sensor's acquisition geometry [25]. The mean local incidence angle over the study site for S1 orbit 141 is approximately 33º, whereas for orbit 68 it is around 43º.

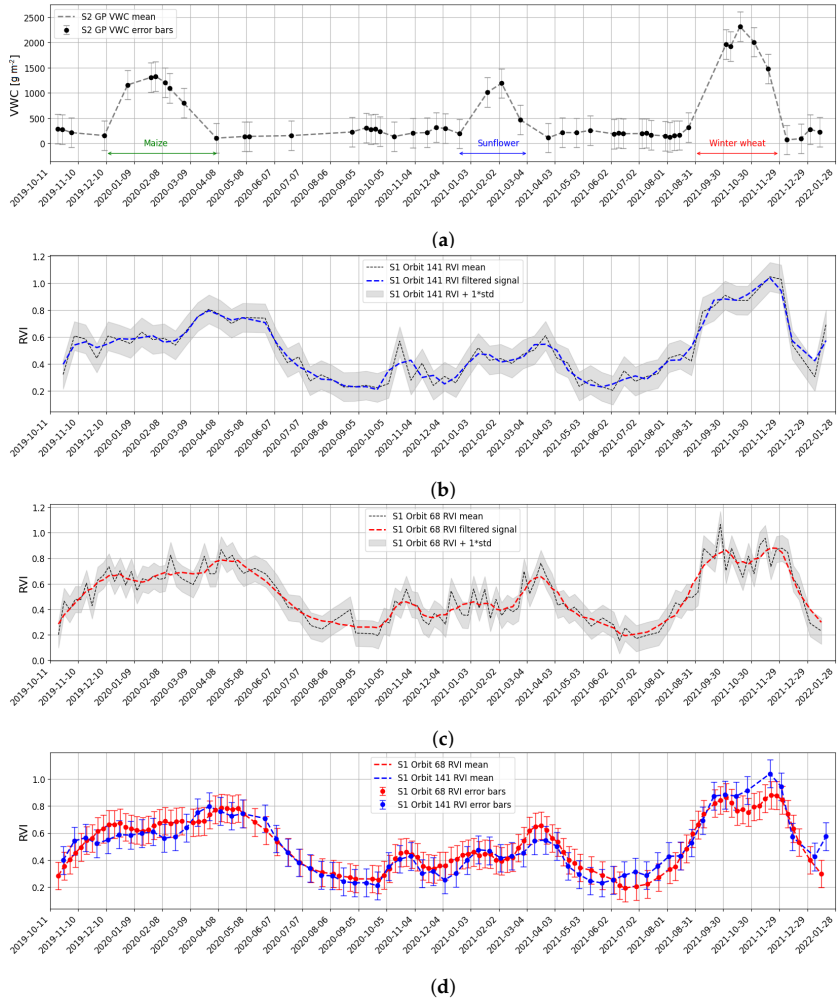

Figure 4. Temporal profiles (mean value and standard deviation) of averaged selected ROI-2 over a winter wheat parcel belonging to the BVCR 2021 crop campaign. S2 GP VWC time series from October 2019 to the end of January 2022 (**a**). S1 RVI orbit 141 smoothed (dashed blue line) and original (dashed black line) time series (**b**). S1 RVI orbit 68 smoothed (dashed red line) and original (dashed black line) time series (**c**). S1 RVI Orbit 68 (red line) and S1 orbit 141 (blue line) RVI time series (**d**).

3.2. Training MOGP Kernels for VWC Time Series Modelling

Two S1 & S2 three-channel datasets were created for training the MOGP models. We first assessed quantitatively the performance of four spectral-mixture kernels for selecting

the best MOGP model and also the outcomes of SOGP to establish a ranking between them. We then explored the contribution of the S1 RVI data at two distinct descendent orbits and its effect on the MOGP models' metrics. To do so, several trials were conducted considering 2 or 3 channels from the S1 & S2 datasets. The space of possible combinations is as follows: (a) S2 GP VWC and S1 RVI orbit 68; (b) S2 GP VWC and S1 RVI orbit 141; and (c) S2 GP VWC, S1 RVI orbit 68 and S1 RVI orbit 141.

Table 2 presents the prediction statistics for the MOGP modeling when the S1 & S2 data streams are used to reconstruct time series data of VWC over the averaged BVCR 2020 winter wheat ROI-1. For each MOGP model and S1 & S2 data stream configuration, we evaluated the following error metrics: MAE, MAPE, RMSE, NRMSE and the training time.

Table 2. Error metrics and training time of the MOGP and SOGP evaluated kernels for the 2020 winter wheat averaged ROI-1.

MOGP Kernel	MAE [g m^{-2}]	MAPE [%]	RMSE [g m^{-2}]	NRMSE [%]	Time [s]
S2 GP VWC and S1 RVI Orbit 68					
MOSM	828.85	56.42	927.56	44.34	10.58
CSM	242.7	15.43	360.55	17.24	17.85
SM-LMC	346.16	22.56	495.49	23.69	12.68
CONV	250.17	19.48	313.11	14.97	21.42
SM	881.4	58.91	1005.71	48.07	6.03
S2 GP VWC and S1 RVI orbit 141					
MOSM	1025.79	69.92	1116.62	53.38	9.37
CSM	283.95	19.76	378.01	18.07	16.06
SM-LMC	482.25	31.99	580.76	27.76	11.49
CONV	255.42	25.25	419.36	20.05	19.25
SM	883.69	59.05	1009.05	48.23	4.98
S2 GP VWC, S1 RVI orbit 68 and S1 RVI orbit 141					
MOSM	907.21	62.61	992.18	47.43	18.56
CSM	472.31	32.75	512.23	24.49	35.18
SM-LMC	463.04	30.75	546.85	26.14	22.67
CONV	249.3	21.83	336.74	16.1	40.27
SM	881.77	58.93	1006.25	48.1	10.29

The MOGP modeling outcomes for the 2021 winter wheat averaged ROI-2 can be visualized in Table 3. A linear increase in runtime can be noted when the three channels are used to train the MOGP regression models.

By eliminating S2 GP VWC samples from the S1 & S2 datasets, we artificially produced data gaps. Subsequently, we used the extracted values as a baseline for the evaluation of the MOGP models' predictions. For that reason, from the S2 GP VWC time series in Figures 3a and 4a, we deleted 9 samples from September 8 to December 12 of 2020 and 6 samples from August 19 to November 27 of 2021, which corresponds to the 2020 and 2021 complete phenological winter wheat cycles, respectively, at the study site. It is noteworthy that the number of S2 acquisitions is different for the 2020 and 2021 crop campaigns due to the cloud coverage dynamic over the study region (see Section 2.3). These latent S2 GP VWC observations exemplify realistically the cloudy image acquisition conditions of S2 at high latitudes. The MOGP regressions for the evaluated models are shown in Figure 5. The MOGP results are also compared to the SM SOGP predictions.

Table 3. Error metrics and training time of the MOGP and SOGP evaluated kernels for the 2021 winter wheat averaged ROI-2.

MOGP Kernel	MAE [g m^{-2}]	MAPE [%]	RMSE [g m^{-2}]	NRMSE [%]	Time [s]
S2 GP VWC and S1 RVI Orbit 68					
MOSM	1606.97	91.26	1746.35	77.76	11.59
CSM	1420.06	79.84	1549.94	69.02	19.85
SM-LMC	1229.57	64.98	1362.06	60.65	13.9
CONV	238.07	41	328.01	14.61	22.31
SM	1408.52	75.06	1550.67	69.05	7.23
S2 GP VWC and S1 RVI orbit 141					
MOSM	1606.95	91.26	1746.33	77.76	9.96
CSM	864.12	54.02	928.28	41.33	18.25
SM-LMC	1262.46	69.72	1378.87	61.4	12.24
CONV	274.33	43.77	352.11	15.68	21.78
SM	1408.52	75.06	1550.67	69.05	6.98
S2 GP VWC, S1 RVI orbit 68 and S1 RVI orbit 141					
MOSM	1640.51	94.6	1778.6	79.2	21
CSM	1446.8	82.65	1576.08	70.18	36.08
SM-LMC	1395.58	74.98	1535.22	68.36	24.21
CONV	190.44	25.69	227.12	10.11	45.02
SM	1408.52	75.06	1550.67	69.05	10.2

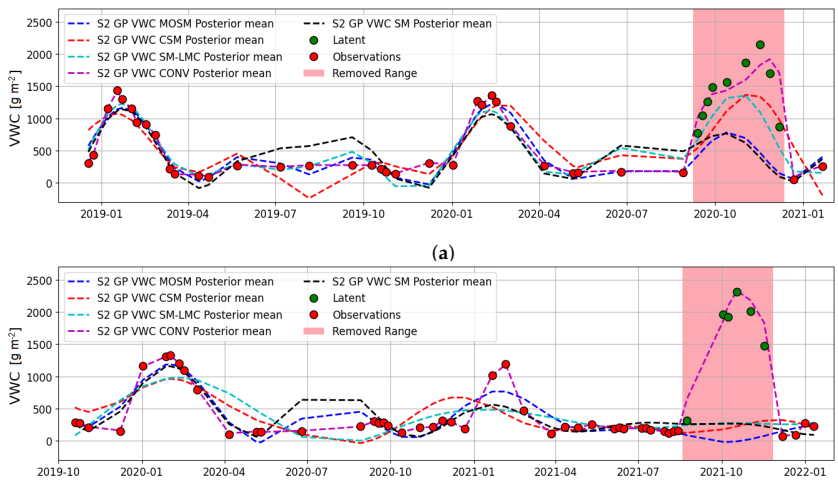

Figure 5. Performance of the SOGP and MOGP models predictions for VWC data reconstruction based on the S1 & S2 synergy. The green dots represent the latent S2 GP VWC data used to compute the error metrics whereas the red dots correspond to the S2 GP VWC cloud-free observations utilized to train the regression models. The red-shaded area represents the artificially created S2 data gap. SOGP and MOGP predictions performance for the selected winter wheat ROI-1 of the year 2020 (**a**) and 2021 (**b**).

As observable in Figure 5, the convolutional model reaches the best results in the predictions of VWC values for both 2020 and 2021 winter wheat test sites. The complete phenological profile of the crop (green dots) is fully recovered, and all latent VWC values are predicted accurately by the CONV model in the absence of optical observations. Consequently, the CONV model is selected for the posterior task of reconstructing VWC at a pixel level. Although CSM and SM-LMC models indeed delivered good results for

the 2020 winter wheat ROI, they have almost zero capacity when applied to the 2021 site. Furthermore, SOGP showed an extremely low capacity to reconstruct VWC in the artificially created gapped windows.

3.2.1. Cross-Correlation Matrixes for the MOGP Trained Kernels

The cross-correlation matrixes for the MOGP evaluated models over the wheat 2020 and 2021 study sites are displayed in Figure 6. The off-diagonal elements represent the dependencies between channels in the S1 & S2 dataset. These dependencies account for cross-spectral coupling among channels in the S1 & S2 dataset.

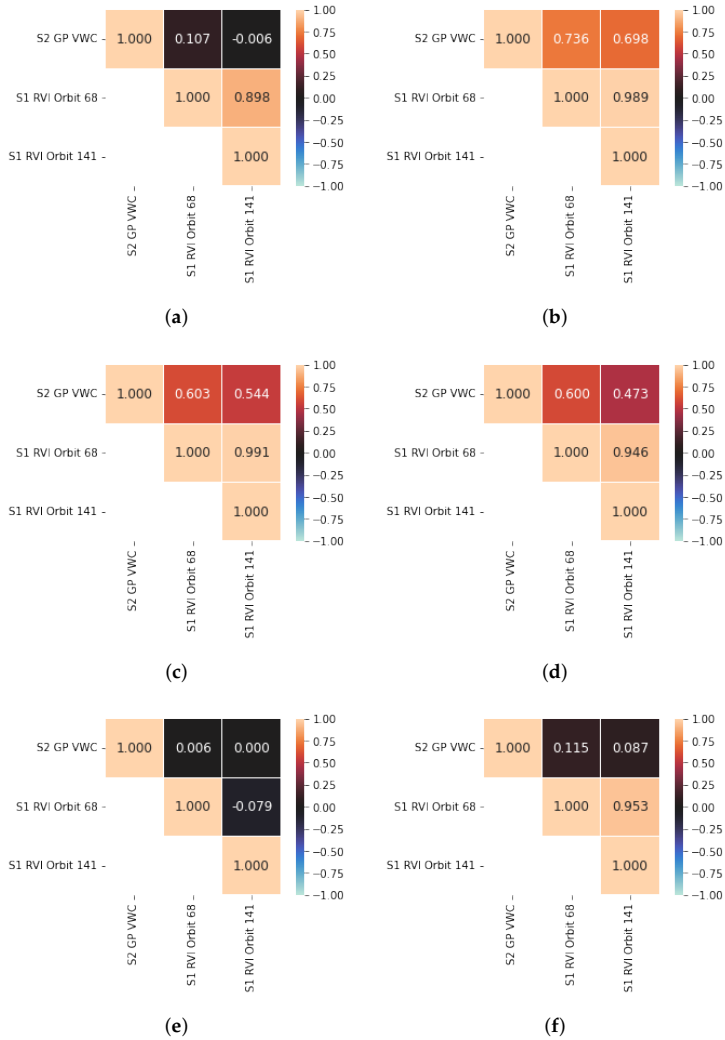

Figure 6. *Cont.*

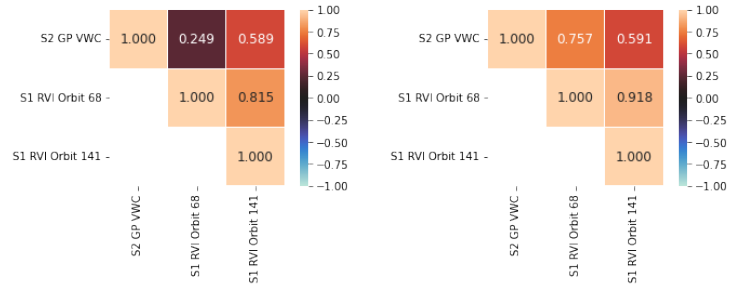

(**g**) (**h**)

Figure 6. Cross-correlation matrix of the S1 & dataset among the channels of the trained MOGP models. The elements of the matrix's diagonal show the auto-correlations of each channel in the dataset. MOSM model for wheat 2020 (**a**). CSM model for wheat 2020 (**b**). SM-LMC model for wheat 2020 (**c**). CONV model for wheat 2020 (**d**). MOSM model for wheat 2021 (**e**). CSM model for wheat 2021 (**f**). SM-LMC model for wheat 2021 (**g**). CONV model for wheat 2021 (**h**).

The empirical cross-correlation matrices in general terms are showing strong correlations between CH-2: S1 RVI orbit 68 and CH-3: S1 RVI orbit 141 in all cases. Nevertheless, the S1-S2 dependencies are determined by the specific MOGP kernel. In some cases CH-1: S2 GP VWC has a negligible correlation with the remaining channels.

3.2.2. Optimized MOGP Kernel for Mapping the VWC of the Winter Wheat 2020 and 2021

In this section, we further explore the CONV model's results. Figure 7 shows the CONV predictions for a three-channel trained model, the S1 & S2 dataset were fused over two different winter wheat ROIs belonging to the BVCR 2020 and 2021 campaigns. It can be noticed that the posterior mean (dashed blue line) for each channel follows the temporal trend of the original observations (red dots). The uncertainty in the form of $\pm \sigma$ is represented by the limited shaded-blue area around the estimations. The S2 GP VWC and S1 RVI curves for orbits 68 and 141 follow similar behavior showing the potential of S1 RVI for crop monitoring purposes. Although the prediction uncertainty increases in the presence of latent data, our trained CONV model is able to recover the more significant trend in the VWC time series for winter wheat 2020 and 2021 minimizing the error (see Tables 2 and 3). The S1 & S2 datasets of Figure 7 are used to optimize the hyperparameters of the CONV model for the wheat site 2020 and 2021. Their values are reported in Appendix B, Tables A3 and A4 correspondingly.

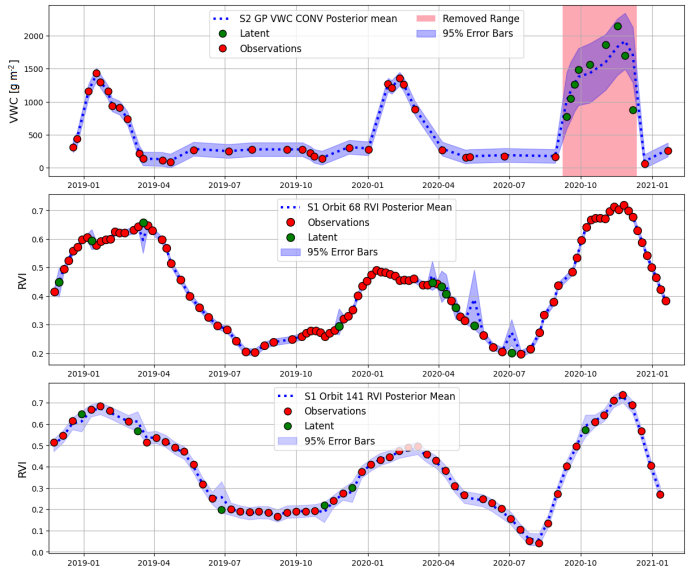

(**a**)

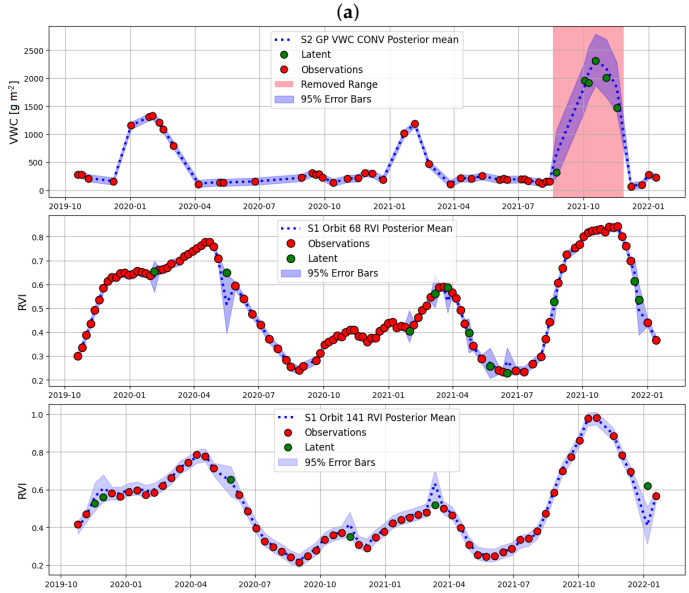

(**b**)

Figure 7. CONV posterior predicted mean for a three-channel model. Red dots indicate the original observations for S2 GP VWC (CH-1), S1 RVI orbit 68 (CH-2), and S1 RVI orbit 141 (CH-3) while the green ones are the latent samples. Winter wheat 2020 ROI-1 (**a**). Winter wheat 2020 ROI-2 (**b**).

3.3. Spatiotemporal Mapping of Reconstructed VWC Based on S1 & S2 Synergy

The S1 & S2 temporal trends presented in Figures 3 and 4 and the best MOGP model selected in Section 3.2.2 were used to demonstrate the feasibility of VWC maps reconstruction based on the S1 & S2 synergy. To accomplish this, we trained an independent CONV model per pixel over two subsets of the BVCR study site. The first subset (red dotted rectangle in Figure 1) contains three winter wheat paddocks that belong to the 2020 crop campaign and its surface is 56 hectares (71 $\times$ 79 pixels at 10 m). The second subset

(orange dotted rectangle in Figure 1) consisted of a large homogeneous parcel of winter wheat from the crop campaign 2021 located not far from the first, its size is 58.5 hectares (76 × 77 pixels at 10 m). For each pixel in the S1 & S2 dataset, a CONV model was initialized with the parameters described in Section 2.5 and then trained using 500 iterations. It is worth pointing out that both spatial subsets selected for the application of the MOGP regression, have had the same crop rotation and management according to the agronomic practices of the HAEE. Winter wheat irrigation has been conducted during three distinct vegetative stages along the phenological cycle. While it is true that we applied the CONV model to the whole S1 & S2 dataset for both spatial subsets reconstructing 44 S1 & S2 MOGP VWC maps for the 2020 winter wheat site and 52 for 2021, we focused on the removed ranges to perform a posterior error metrics analysis. The global R^2 values for the complete spatiotemporal regression were $\overline{R^2}_{subset_1} = 0.72$ and $\overline{R^2}_{subset_2} = 0.67$ and their related processing time: $t_{subset_1} = 70$ h and $t_{subset_2} = 54$ h approximately (processor: 11th Gen Intel(R) Core(TM) i7-1195G7 @ 2.90 GHz 64 bits, RAM: 16 GB). The MOGP technique allowed the reconstruction of each channel in the S1 & S2 dataset independently. It means that, regardless of the acquisition dates of S1 and S2, the CONV model generated a VWC map that coincides with the S2 pass over the study area. Similarly, a reconstructed RVI map was also produced for each S1 acquisition date. The main advantage of MOGP is that there is no need for synchronicity between the acquisitions of S1 and S2. Although the MOGP regression models support the daily temporal resolution (the temporal resolution of each channel can be adjusted independently), we did not modify the S1 and S2 original observation dates. In summary, the temporal resolution of each reconstructed independent channel follows the same pattern as the acquisitions of S1 and S2 over the study area. Consequently, we obtained 44 S1 & S2 MOGP VWC maps for the 2020 wheat campaign and 52 for 2021. Figure 8 show the spatiotemporal reconstruction of VWC maps over the winter wheat paddocks of the BVCR 2020 crop campaign. The vegetation phenology (left) and the scatter plots (right) underpin the S1 & S2 MOGP VWC maps accurately for each assessment date. It is desirable to present the synergy results for the greenness stage of winter wheat at two different locations of the study site. Furthermore, the reconstructed VWC maps for the 2021 winter wheat site are shown in Figure 9. Seeking to prioritize the evaluation of the MOGP within the vegetative development stage of winter wheat plants, we calculated the average R^2 values for the scatter plots presented in Figures 8 and 9, we obtained $\overline{R^2}_{wheat_{2020}} = 0.95$ and $\overline{R^2}_{wheat_{2021}} = 0.96$, which shows the strong correlation of S2 GP VWC and S1 & S2 MOGP VWC maps.

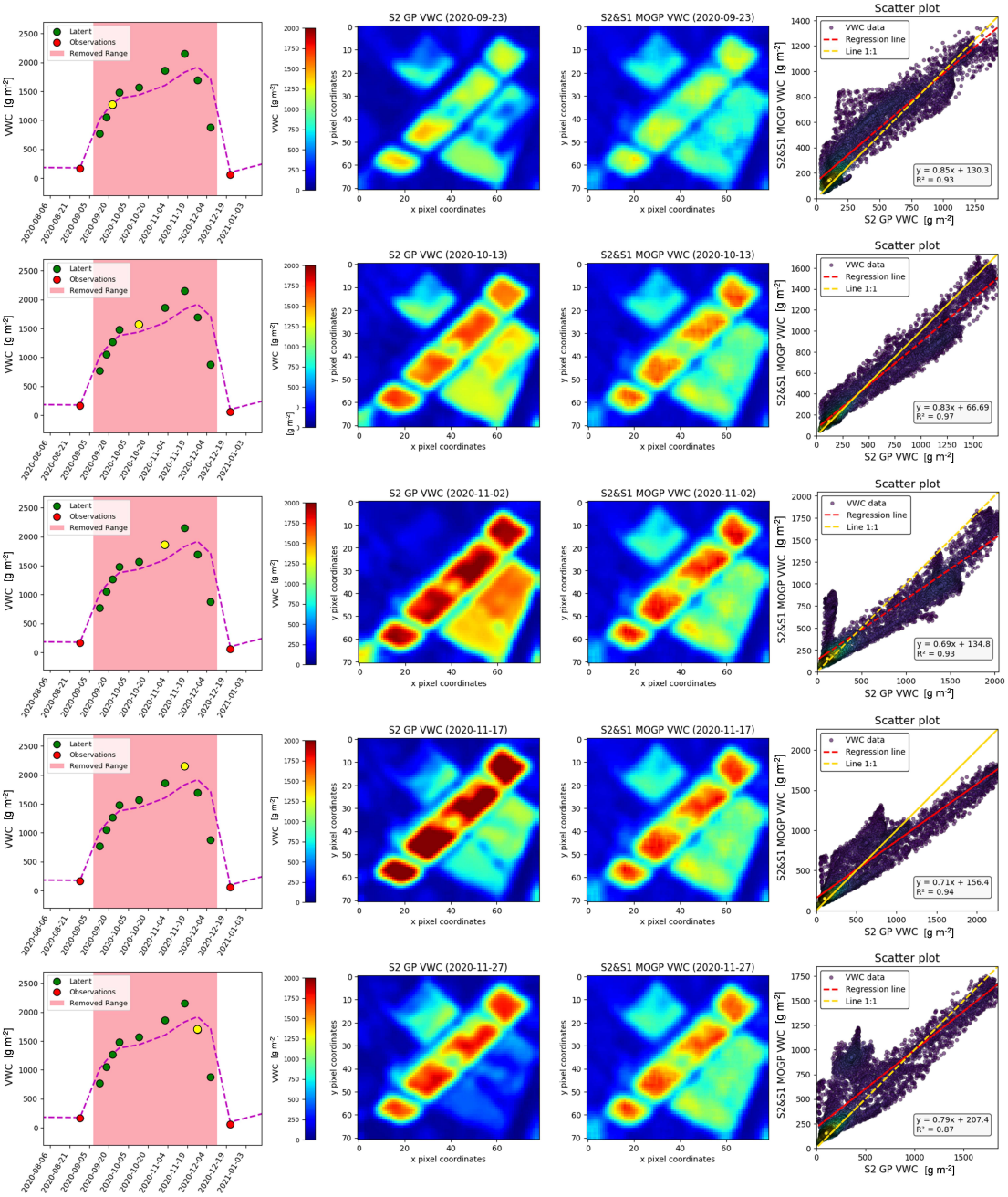

Figure 8. Comparison of S2 GP VWC (original) and S1 & S2 MOGP VWC (reconstructed) maps over a selected subset of the study site (red-dashed rectangle in Figure 1) corresponding to the artificially removed dates: 2020/9/23, 2020/10/13, 2020/11/2, 2020/11/17, and 2020/11/27 of the winter wheat 2020 phenological cycle. For each assessment date, the position of the extracted samples on the phenological curve (yellow dot), the S2 GP VWC map, the reconstructed S1 & S2 MOGP VWC map and the scatterplot between the original and reconstructed VWC maps are shown.

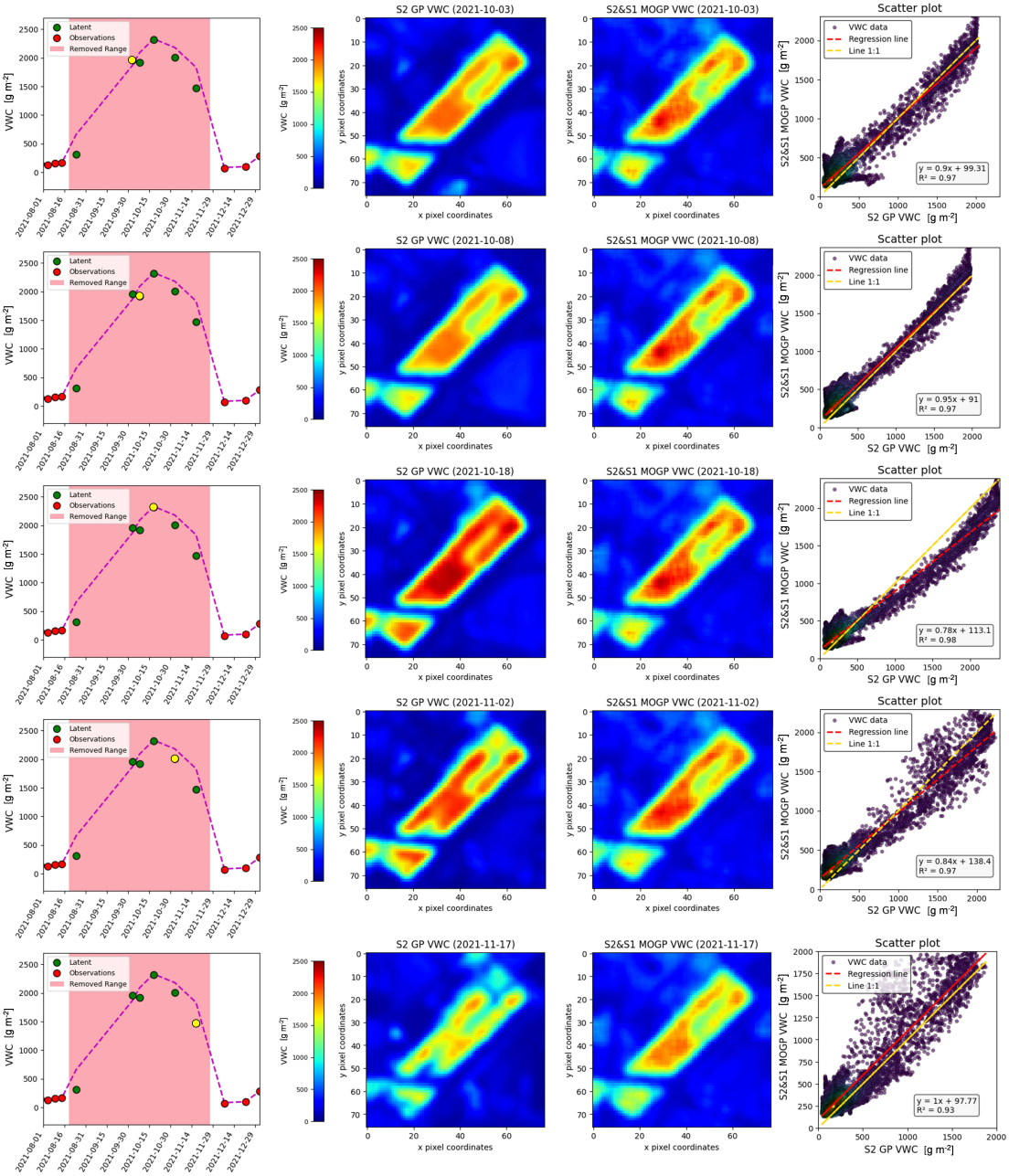

Figure 9. Comparison of S2 GP VWC (original) and S1 & S2 MOGP VWC (reconstructed) maps over a selected subset of the study site (orange-dashed rectangle in Figure 1) corresponding to the artificially removed dates: 2021/10/3, 2021/10/8, 2021/10/18, 2021/11/2, and 2021/11/17 of the winter wheat 2021 phenological cycle. For each assessment date, the position of the extracted samples on the phenological curve (yellow dot), the S2 GP VWC map, the reconstructed S1 & S2 MOGP VWC map and the scatterplot between the original and reconstructed VWC maps are shown.

4. Discussion

We explored the feasibility of fusing S1 & S2 data streams with a MOGP approach for cloud-free VWC time series mapping. This study provides a potentially powerful research line that deserves to be carefully analyzed. In the following, time and frequency domain similarities in the S1 & S2 dataset (Section 4.1), MOGP modeling and assessment (Section 4.2), S1 & S2-based spatiotemporal mapping of VWC (Section 4.4), and finally advantages and opportunities for improvement of the fusion approach (Section 4.3) are discussed.

4.1. Time and Frequency Domain Similarities in the S1 & S2 Dataset

GEE proved to be an invaluable tool for processing and downloading Copernicus data quickly, efficiently and accurately. Cloud-processed time series of VWC derived from S2 data produced the typical phenological profile of winter wheat at the study site as was also presented by Caballero et al. [54]. The LAI mapping of winter wheat at the BVCR based on S1 radar data was explored by Caballero et al. [25], demonstrating the efficacy of merging distinct S1 acquisition geometries to retrieve wheat LAI in southern Argentina. In the present study, we analyzed the RVI for two distinct S1 orbits that allow having two radar channels to merge the S1 & S2 time series. Regarding the wheat growth cycle at the focused area, we found the same temporal trends for S1 RVI and S1 LAI GP model developed by Caballero et al. [25]. In Figures 3d and 4d an amplitude offset of RVI for orbit 68 and orbit 141 can be appreciated. These RVI differences, which are related to the mismatch of the local incidence angle, provide valuable information on the three-dimensional structure of the vegetation. The BVCR's representative crop rotation at the study site was faithfully reproduced by long time series of S2 GP VWC (see Figures 3a and 4a). The S2 GP VWC and S1 RVI time series follow the same temporal patterns, so three phenological cycles (corn-sunflower-wheat) can be captured at the study sites (see Figure 1). In addition, this time correspondence enabled us to gauge the spectral similarities in the S1 & S2 dataset. The frequency domain analysis determines the peak and position of the principal spectral components that are mainly related to crop rotation and phenology. Seeking to customize the response of the SM kernels we selected Q = 4 prioritizing the most representative spectral components in the S1 & S2 dataset (see Section 2.5).

4.2. MOGP Modelling and Assessment

We evaluated several MOGP kernels as well as the SOGP SM approaches aiming to select the best one for the spatiotemporal reconstruction of VWC maps. We presented a set of error metrics in Tables 2 and 3 for each MOGP kernel, but finally, we adopted the NRMSE for cross-model comparison. The poor capability of SOGP to reconstruct VWC in the absence of optical data can be easily observed for winter wheat ROI-1 and ROI-2. All latent values are remarkably underestimated, therefore, the true VWC profiles are entirely lost (see Figure 5). In the SOGP approach, the spectral mixture kernels are trained independently on each channel, which fails to account for the cross-spectral similarity between S1 & S2 time series. While it is true that other MOGP kernels such as CSM and SM-LMC reached an acceptably high performance for the 2020 winter wheat site, the CONV model was the only one able to tackle the VWC time series reconstruction for both averaged ROIs (see Figure 7). CONV makes use of the convolution theorem to model cross-channel dependencies in the S1 & S2 datasets by means of cross-convolution in the spectral domain. The cross-spectral similarity of the S1 & S2 time series, in this regard (see Section 4.1), is the backbone of the spectral mixture approach (see Figure 6). In terms of S1 & S2 dataset configuration, we assessed two or three-channel fusion models. Regarding the CONV model, superior results were found for both winter wheat averaged ROIs (see Tables 2 and 3) when the S1 & S2 dataset is fused with S1 RVI orbit 68 instead of S1 RVI orbit 141. We obtained $NRMSE_{(S2\&S1,orbit68)}$ = 14.97% and $NRMSE_{(S2\&S1,orbit141)}$ = 20.05% for winter wheat 2020 ROI-1 and a two-channel dataset. In the same way, $NRMSE_{(S2\&S1,orbit68)}$ = 14.61% and $NRMSE_{(S2\&S1,orbit141)}$ = 15.68% for ROI-2. When it comes to three-channel S1 & S2 datasets, the following scenarios were

encountered: (i) the accuracy of the CONV kernel increases for ROI-2 (wheat 2021), $NRMSE_{(S2\&S1,orbits68\&141)}$ = 10.1% and; (ii) a slight accuracy loss is reflected by the CONV model over the ROI-1 (wheat 2020), $NRMSE_{(S2\&S1,orbits68\&141)}$ = 16.1%. These results are directly connected to the fact that the number of S2 cloud-free acquisitions over ROI-1 and ROI-2 is different. Furthermore, they are unevenly spaced, so the S2 GP VWC time series have different frequency spectra in each case.

4.3. S1 & S2-Based Spatiotemporal Mapping of Vegetation Water Content

The outstanding reconstruction results delivered by the CONV model over the two selected subsets of the study site highlight its ability to fuse EO S1 & S2 data for cloud-free crop trait mapping purposes. Thanks to the guidance of the radar data stream, CWV maps were reconstructed by MOGP even in the absence of optical data. Accurate reconstructed VWC maps were obtained for both studied subsets when a CONV model was trained on a per-pixel basis. The land cover spatiotemporal heterogeneity was correctly captured thanks to this strategy. We focused exclusively on the mapping of winter wheat paddocks, nevertheless, other crop types are present in the scenes such as pasture and legumes and even more differ across multiple crop seasons. The CONV model was able to accurately reconstruct the VWC maps over all parcels, regardless of the land cover type (see Figures 8 and 9). It suggests that the MOGP technique can be generically applied, as long as there is sufficiently complementary information present in the radar signal. At the same time, as a Bayesian nonparametric probabilistic ML regression algorithm, MOGP provides an automatic mechanism to construct and calibrate uncertainties. Uncertainty maps offer the opportunity to assess the confidence of predictions and construct reliability maps at pixel level [76].

4.4. Advantages and Opportunities for Improvement of the Fusing Approach

The S1 & S2 time series fusing approach presented here offers attractive and powerful opportunities to be further exploited. Firstly, there is the actual feasibility of successfully implementing cloud-free VWC map reconstruction techniques by taking advantage of the all-weather availability of S1 radar data. Fusing S1 SAR and S2 optical imagery proved particularly useful for monitoring crops' VWC in southern Argentina, and can be easily extrapolated to high-latitude cloudy regions worldwide. Secondly, MOGP can also be used for gap-filling S2 time series by combining optical data from other EO systems like Landsat-8 or Sentinel-3. Likewise, also other optically-derived variables can be targeted that align well with radar data, such as LAI [29]. Furthermore, thirdly, the ever-increasing supply of emerging radar satellite constellations in different frequency bands poses a revolutionary paradigm [77]. Altogether, the Earth observation scenario for the next few years is extremely promising and requires further exploration of MOGP techniques.

On the downside, it is worth emphasizing that the training time was rather long (see Tables 2 and 3) when the data from S1 and S2 were combined to reconstruct the VWC maps (see Section 3.3). The long runtime constitutes the main bottleneck of the MOGP technique. Training MOGP algorithms is a challenging task as it involves a large number of hyperparameters to model all the inter-channel cross-correlations in the spectral domain. Some attempts were explored to further improve the results. Seeking to substitute the per-pixel optimization step Belda et al. [37] suggested optimizing a GP for an averaged ROI and then using the hyperparameters of the optimized model. This approach could reduce the long processing time of S1 & S2 datasets but is at a risk to account for the cropland's spatiotemporal variability. We had tested that approach; however, it appeared that the results in our context were unsatisfactory, and this path was therefore discarded. Follow-up research may attempt to address this limitation. Several alternative mechanisms can be explored to accelerate the training phase of MOGP. They can be divided into two groups: technical and theoretical solutions. Technical solutions include using a more powerful computer (RAM $\geq$ 64 GB), considering fewer observations for model training, reducing the number of spectral components, or deploying the code in a Graphics Processing Unit

(GPU) environment. Theoretical solutions include using a sparse model, e.g., as presented by Titsias [78], or a stochastic gradient descent [79].

5. Conclusions

Cloud-free optical imagery is usually scarce over cloud-prone agroecosystems, implying that crop monitoring is often limited to a few observations during key phenological development stages. The synergy of optical with complementary all-weather SAR data can provide valuable insights into specific agricultural areas, even in the presence of persistent cloud cover. In our study, we demonstrated that fusing time series of S1 SAR and S2 optical data through MOGP proved to be a powerful and innovative methodology to reconstruct cloud-free time series data streams over the entire growing season. Pursuing the development of a powerful fusion approach that learns the dependencies of S1 & S2 time series data, we applied a processing framework for selecting the best MOGP model. The S1 & S2 MOGP CONV model was validated with relatively high accuracy against S2 GP VWC retrieved data over two winter wheat fields belonging to the BVCR 2020 and 2021 crop campaigns (wheat 2020: $NRMSE_{(S2\&S1,orbits68\&141)}$ = 16.1% and wheat 2021: $NRMSE_{(S2\&S1,orbits68\&141)}$ = 10.1%). The CONV models were afterward applied iteratively at the pixel level to reconstruct removed S2 acquisitions. The reconstructed VWC maps in the absence of optical data showed spatiotemporal consistency and made it possible to accurately capture complete phenology curves. We conclude that the cross-correlation of the time series of S1 and S2 data can be exploited for the purpose of cloud-free large-scale reconstructing of optical-imagery-derived crop trait data streams. Further research must be conducted to deploy the MOGP strategy over other croplands and target other vegetation traits while keeping the runtime within acceptable limits.

Author Contributions: G.C., J.D. and J.V. proposed the general objectives and goals of the research; A.P., C.W., P.S.A. and A.C. designed the field campaigns and collected the in situ data; G.C., M.S.-D., L.O. and P.R.-M. analyzed the data and obtained the results; G.C. and K.B. wrote the paper; K.B., J.V. and J.D. reviewed the paper and supervised all the procedures. All authors have read and agreed to the published version of the manuscript.

Funding: This research was funded by the European Research Council (ERC) under the ERC-2017-STG SENTIFLEX project (grant agreement 755617) (K.B.) and Ramón y Cajal Contract (Spanish Ministry of Science, Innovation and Universities) (J.V.).

Data Availability Statement: Not applicable.

Acknowledgments: We would like to thank the Hilario Ascasubi Experimental Station (HAEE) of Argentina's National Institute of Agricultural Technology (INTA) for the in situ database used in this study. This research has been held out by the Fundación Carolina's 2021 doctoral program scholarship. This publication is also the result of the project implementation: "Scientific support of climate change adaptation in agriculture and mitigation of soil degradation" (ITMS2014+313011W580) supported by the Integrated Infrastructure Operational Programme funded by the ERDF. The research was also supported by the Action CA17134 SENSECO (Optical synergies for spatiotemporal sensing of scalable ecophysiological traits) funded by COST (European Cooperation in Science and Technology, www.cost.eu (accessed on 5 February 2023)).

Conflicts of Interest: The authors declare no conflict of interest.

Appendix A. Sentinel–1 & Sentinel–2 Acquisition Dates

Table A1. Sentinel–2 and Sentinel–1 acquisition dates corresponding to the winter wheat 2020 crop campaign at the BVCR. The (–) symbol means no acquisition. The (*) indicates the S2 removed images from the S1 & S2 dataset for model validation.

Winter Wheat 2020 Crop Campaign		
S2 Acquisition Date	**$S1_{(Orbit\ 68)}$ Acquisition Date**	**$S1_{(Orbit\ 141)}$ Acquisition Date**
-	2020-08-27	-
2020-08-29	-	-
-	-	2020-09-01
-	2020-09-02	-
2020-09-13 *	-	2020-09-13
2020-09-18 *	-	-
-	2020-09-20	-
2020-09-23 *	-	-
-	-	2020-09-25
-	2020-09-26	-
2020-09-28 *	-	-
-	2020-10-02	-
-	-	2020-10-07
-	2020-10-08	-
2020-10-13 *	-	-
-	2020-10-14	-
-	-	2020-10-19
-	2020-10-20	-
-	2020-10-26	-
-	-	2020-10-31
-	2020-11-01	-
2020-11-02 *	-	-
-	2020-11-07	-
-	-	2020-11-12
-	2020-11-13	-
2020-11-17 *	-	-
-	2020-11-19	-
-	-	2020-11-24
-	2020-11-25	-
2020-11-27 *	-	-
-	2020-12-01	-
-	-	2020-12-06
2020-12-07 *	2020-12-07	-
-	2020-12-13	-
-	-	2020-12-18
-	2020-12-19	-
2020-12-22	-	-
-	2020-12-25	-
-	-	2020-12-30
-	2020-12-31	-
-	2021-01-06	-

Table A2. Sentinel–2 and Sentinel–1 acquisition dates corresponding to the winter wheat 2021 crop campaign at the BVCR. The (–) symbol means no acquisition. The (*) indicates the S2 removed images from the S1 & S2 dataset for model validation.

Winter Wheat 2021 Crop Campaign		
S2 Acquisition Date	**$S1_{(Orbit\ 68)}$ Acquisition Date**	**$S1_{(Orbit\ 141)}$ Acquisition Date**
-	2021-08-16	-
-	2021-08-22	-
2021-08-24 *	-	-
-	-	2021-08-27
-	2021-08-28	-
-	2021-09-03	-
-	-	2021-09-08
-	2021-09-09	-
-	-	2021-09-20
-	2021-09-21	-
-	2021-09-27	-
-	-	2021-10-02
2021-10-03 *	2021-10-03	-
2021-10-08 *	-	-
-	2021-10-09	-
-	-	2021-10-14
-	2021-10-15	-
2021-10-18 *	-	-
-	2021-10-21	-
-	-	2021-10-26
-	-	2021-10-27
2021-11-02 *	2021-11-02	-
-	2021-11-08	-
-	2021-11-14	-
2021-11-17 *	-	-
-	-	2021-11-19
-	2021-11-20	-
-	2021-11-26	-
-	-	2021-12-01
-	2021-12-02	-
2021-12-07	-	-
-	2021-12-08	-
-	-	2021-12-13
-	2021-12-14	-
-	2021-12-20	-
2021-12-22	-	-
2022-01-01	2022-01-01	-

Appendix B. Hyperparameters of the CONV Models Trained over the Winter Wheat Test Sites

Table A3. Hyperparameters of the MOGP CONV model trained with the S2 GP VWC and S1 RVI orbits 68 and 141 time series over the winter wheat 2020 ROI-1.

Name	Range	Value
M[0].CONV.weight	$(1 \times 10^{-8}, \infty)$	[0.16140878 0.12014237 0.25099972]
M[0].CONV.variance	$(0.0, \infty)$	$[[4.57955225 \times 10^{-6}]\ [1.48168009 \times 10^{-5}]\ [4.89282973 \times 10^{-5}]]$
M[0].CONV.base_variance	$(1 \times 10^{-8}, \infty)$	[29.65490441]
M[1].CONV.weight	$(1 \times 10^{-8}, \infty)$	[0.18422568 0.12714211 0.09511325]
M[1].CONV.variance	$(0.0, \infty)$	[[0.00208712] [0.00021101] [0.00029573]]
M[1].CONV.base_variance	$(1 \times 10^{-8}, \infty)$	$[3.84536139 \times 10^{-6}]$
M[2].CONV.weight	$(1 \times 10^{-8}, \infty)$	[0.161608 0.36756376 0.38364755]
M[2].CONV.variance	$(0.0, \infty)$	$[[5.97699880 \times 10^{-6}]\ [8.28188220 \times 10^{-4}]\ [2.73658687 \times 10^{-3}]]$
M[2].CONV.base_variance	$(1 \times 10^{-8}, \infty)$	[55.15439607]
M[3].CONV.weight	$(1 \times 10^{-8}, \infty)$	[0.45055456 0.09223841 0.01531059]
M[3].CONV.variance	$(0.0, \infty)$	$[[3.78006500 \times 10^{-6}]\ [2.45277978 \times 10^{-7}]\ [3.81411018 \times 10^{-7}]]$
M[3].CONV.base_variance	$(1 \times 10^{-8}, \infty)$	[54.76679359]
Gaussian.scale	$(1 \times 10^{-8}, \infty)$	[0.07039943 0.05906305 0.03154559]

Table A4. Hyperparameters of the MOGP model trained with the S2 GP VWC and S1 RVI orbits 68 and 141 time series over the winter wheat 2021 ROI-2.

Name	Range	Value
M[0].CONV.weight	$(1 \times 10^{-8}, \infty)$	[0.05051712 0.27439207 0.38695247]
M[0].CONV.variance	$(0.0, \infty)$	$[[4.86858144 \times 10^{-6}]\ [7.13908231 \times 10^{-6}]\ [1.31486331 \times 10^{-3}]]$
M[0].CONV.base_variance	$(1 \times 10^{-8}, \infty)$	[34.01715996]
M[1].CONV.weight	$(1 \times 10^{-8}, \infty)$	[0.07826687 0.21647057 0.08729357]
M[1].CONV.variance	$(0.0, \infty)$	$[[2.67026775 \times 10^{-5}]\ [2.09623224 \times 10^{-6}]\ [3.66018092 \times 10^{-5}]]$
M[1].CONV.base_variance	$(1 \times 10^{-8}, \infty)$	[19.31982864]
M[2].CONV.weight	$(1 \times 10^{-8}, \infty)$	[0.5937755 0.30263363 0.22857684]
M[2].CONV.variance	$(0.0, \infty)$	$[[1.10220013 \times 10^{-4}]\ [1.21975560 \times 10^{-2}]\ [6.16156520 \times 10^{-6}]]$
M[2].CONV.base_variance	$(1 \times 10^{-8}, \infty)$	[49.46172915]
M[3].CONV.weight	$(1 \times 10^{-8}, \infty)$	[0.0563912 0.01698611 0.03144775]
M[3].CONV.variance	$(0.0, \infty)$	$[[2.51113006 \times 10^{-5}]\ [1.23150713 \times 10^{-5}]\ [1.27814011 \times 10^{-2}]]$
M[3].CONV.base_variance	$(1 \times 10^{-8}, \infty)$	[0.08717407]
Gaussian.scale	$(1 \times 10^{-8}, \infty)$	[0.04004209 0.06703326 0.0397214]

References

1. Verrelst, J.; Camps-Valls, G.; Muñoz-Marí, J.; Rivera, J.P.; Veroustraete, F.; Clevers, J.G.P.W.; Moreno, J. Optical remote sensing and the retrieval of terrestrial vegetation bio-geophysical properties—A review. *ISPRS J. Photogramm. Remote Sens.* **2015**, *108*, 273–290. [CrossRef]
2. Verrelst, J.; Malenovský, Z.; Van der Tol, C.; Camps-Valls, G.; Gastellu-Etchegorry, J.P.; Lewis, P.; North, P.; Moreno, J. Quantifying Vegetation Biophysical Variables from Imaging Spectroscopy Data: A Review on Retrieval Methods. *Surv. Geophys.* **2019**, *40*, 589–629. [CrossRef]
3. Quemada, C.; Pérez-Escudero, J.M.; Gonzalo, R.; Ederra, I.; Santesteban, L.G.; Torres, N.; Iriarte, J.C. Remote Sensing for Plant Water Content Monitoring: A Review. *Remote Sens.* **2021**, *13*, 2088. [CrossRef]
4. D'Urso, G.; Richter, K.; Calera, A.; Osann, M.A.; Escadafal, R.; Garatuza-Pajan, J.; Hanich, L.; Perdigão, A.; Tapia, J.B.; Vuolo, F. Earth Observation products for operational irrigation management in the context of the PLEIADeS project. *Agric. Water Manag.* **2010**, *98*, 271–282. [CrossRef]
5. Clevers, J.G.P.W.; Kooistra, L.; Schaepman, M.E. Estimating canopy water content using hyperspectral remote sensing data. *Int. J. Appl. Earth Obs. Geoinf.* **2010**, *12*, 119–125. [CrossRef]
6. Wocher, M.; Berger, K.; Danner, M.; Mauser, W.; Hank, T. Physically-based retrieval of canopy equivalent water thickness using hyperspectral data. *Remote Sens.* **2018**, *10*, 1924 [CrossRef]
7. Gerhards, M.; Schlerf, M.; Mallick, K.; Udelhoven, T. Challenges and Future Perspectives of Multi-/Hyperspectral Thermal Infrared Remote Sensing for Crop Water-Stress Detection: A Review. *Remote Sens.* **2019**, *11*, 1240. [CrossRef]

8. Bowman, W.D. The relationship between leaf water status, gas exchange, and spectral reflectance in cotton leaves. *Remote Sens. Environ.* **1989**, *30*, 249–255. [CrossRef]
9. Ustin, S.L.; Riaño, D.; Hunt, E.R. Estimating canopy water content from spectroscopy. *Israel J. Plant Sci.* **2012**, *60*, 9–23 [CrossRef]
10. Berger, M.; Moreno, J.; Johannessen, J.A.; Levelt, P.F.; Hanssen, R.F. ESA's sentinel missions in support of Earth system science. *Remote Sens. Environ.* **2012**, *120*, 84–90. [CrossRef]
11. Drusch, M.; Del Bello, U.; Carlier, S.; Colin, O.; Fernandez, V.; Gascon, F.; Hoersch, B.; Isola, C.; Laberinti, P.; Martimort, P.; et al. Sentinel-2: ESA's Optical High-Resolution Mission for GMES Operational Services. *Remote. Sens. Environ.* **2012**, *120*, 25–36 [CrossRef]
12. Amin, E.; Verrelst, J.; Rivera-Caicedo, J.P.; Pipia, L.; Ruiz-Verdú, A.; Moreno, J. Prototyping Sentinel-2 green LAI and brown LAI products for cropland monitoring. *Remote Sens. Environ.* **2021**, *255*, 112168. [CrossRef]
13. Delloye, C.; Weiss, M.; Defourny, P. Retrieval of the canopy chlorophyll content from Sentinel-2 spectral bands to estimate nitrogen uptake in intensive winter wheat cropping systems. *Remote Sens. Environ.* **2018**, *216*, 245–261. [CrossRef]
14. Brede, B.; Verrelst, J.; Gastellu-Etchegorry, J.P.; Clevers, J.G.; Goudzwaard, L.; den Ouden, J.; Verbesselt, J.; Herold, M. Assessment of workflow feature selection on forest LAI prediction with sentinel-2A MSI, landsat 7 ETM+ and Landsat 8 OLI. *Remote. Sens.* **2020**, *12*, 915 [CrossRef]
15. Verrelst, J.; Rivera, J.; Veroustraete, F.; Muñoz Marí, J.; Clevers, J.; Camps-Valls, G.; Moreno, J. Experimental Sentinel-2 LAI estimation using parametric, non-parametric and physical retrieval methods—A comparison. *ISPRS J. Photogramm. Remote. Sens* **2015**, *108*, 260–272 [CrossRef]
16. Estévez, J.; Salinero-Delgado, M.; Berger, K.; Pipia, L.; Rivera-Caicedo, J.P.; Wocher, M.; Reyes-Muñoz, P.; Tagliabue, G.; Boschetti, M.; Verrelst, J. Gaussian processes retrieval of crop traits in Google Earth Engine based on Sentinel-2 top-of-atmosphere data. *Remote. Sens. Environ.* **2022**, *273*, 112958 [CrossRef]
17. Torres, R.; Snoeij, P.; Geudtner, D.; Bibby, D.; Davidson, M.; Attema, E.; Potin, P.; Rommen, B.; Floury, N.; Brown, M.; et al. GMES Sentinel-1 mission. *Remote Sens. Environ.* **2012**, *120*, 9–24. [CrossRef]
18. Ulaby, F.T.; Aslam, A.; Dobson, M.C. Effects of Vegetation Cover on the Radar Sensitivity to Soil Moisture. *IEEE Trans. Geosci. Remote Sens.* **1982**, *GE-20*, 476–481. [CrossRef]
19. Karam, M.A.; Fung, A.K.; Lang, R.H.; Chauhan, N.S. A microwave scattering model for layered vegetation. *IEEE Trans. Geosci. Remote Sens.* **1992**, *30*, 767–784. [CrossRef]
20. Bousbih, S.; Zribi, M.; Lili-Chabaane, Z.; Baghdadi, N.; El Hajj, M.; Gao, Q.; Mougenot, B. Potential of Sentinel-1 Radar Data for the Assessment of Soil and Cereal Cover Parameters. *Sensors* **2017**, *17*, 2617. [CrossRef]
21. Rozenstein, O.; Siegal, Z.; Blumberg, D.G.; Adamowski, J. Investigating the backscatter contrast anomaly in synthetic aperture radar (SAR) imagery of the dunes along the Israel–Egypt border. *Int. J. Appl. Earth Obs. Geoinf.* **2016**, *46*, 13–21. [CrossRef]
22. Gao, S.; Niu, Z.; Huang, N.; Hou, X. Estimating the Leaf Area Index, height and biomass of maize using HJ-1 and RADARSAT-2. *Int. J. Appl. Earth Obs. Geoinf.* **2013**, *24*, 1–8. [CrossRef]
23. McNairn, H.; Kross, A.; Lapen, D.; Caves, R.; Shang, J. Early season monitoring of corn and soybeans with TerraSAR-X and RADARSAT-2. *Int. J. Appl. Earth Obs. Geoinf.* **2014**, *28*, 252–259. [CrossRef]
24. Zhang, Y.; Venkatachalam, A.S.; Huston, D.; Xia, T. Advanced signal processing method for ground penetrating radar feature detection and enhancement. In *Nondestructive Characterization for Composite Materials, Aerospace Engineering, Civil Infrastructure, and Homeland Security 2014*; SPIE: Bellingham, WA, USA, 2014; Volume 9063, pp. 276–289. [CrossRef]
25. Caballero, G.; Pezzola, A.; Winschel, C.; Casella, A.; Sanchez Angonova, P.; Orden, L.; Berger, K.; Verrelst, J.; Delegido, J. Quantifying Irrigated Winter Wheat LAI in Argentina Using Multiple Sentinel-1 Incidence Angles. *Remote Sens.* **2022**, *14*, 5867. [CrossRef] [PubMed]
26. Mattia, F.; Balenzano, A.; Satalino, G.; Lovergine, F.; Peng, J.; Wegmuller, U.; Cartus, O.; Davidson, M.W.J.; Kim, S.; Johnson, J.; et al. Sentinel-1 & Sentinel-2 for SOIL Moisture Retrieval at Field Scale. In Proceedings of the IGARSS 2018–2018 IEEE International Geoscience and Remote Sensing Symposium, IEEE, Valencia, Spain, 22–27 July 2018; pp. 6143–6146. [CrossRef]
27. Satalino, G.; Mattia, F.; Balenzano, A.; Lovergine, F.P.; Rinaldi, M.; De Santis, A.P.; Ruggieri, S.; García, D.A.N.; Gómez, V.P.; Ceschia, E.; et al. Sentinel-1 & Sentinel-2 Data for Soil Tillage Change Detection. In Proceedings of the IGARSS 2018–2018 IEEE International Geoscience and Remote Sensing Symposium, IEEE, Valencia, Spain, 22–27 July 2018; pp. 6627–6630. [CrossRef]
28. Veloso, A.; Mermoz, S.; Bouvet, A.; Le Toan, T.; Planells, M.; Dejoux, J.F.; Ceschia, E. Understanding the temporal behavior of crops using Sentinel-1 and Sentinel-2-like data for agricultural applications. *Remote Sens. Environ.* **2017**, *199*, 415–426. [CrossRef]
29. Pipia, L.; Muñoz-Marí, J.; Amin, E.; Belda, S.; Camps-Valls, G.; Verrelst, J. Fusing optical and SAR time series for LAI gap filling with multioutput Gaussian processes. *Remote Sens. Environ.* **2019**, *235*, 111452. [CrossRef] [PubMed]
30. Druce, D.; Tong, X.; Lei, X.; Guo, T.; Kittel, C.M.M.; Grogan, K.; Tottrup, C. An Optical and SAR Based Fusion Approach for Mapping Surface Water Dynamics over Mainland China. *Remote Sens.* **2021**, *13*, 1663. [CrossRef]
31. Caballero, G.; Delegido, J.; Verrelst, J. Estimación del LAI de la vegetación a partir de la sinergia Sentinel 1 -Sentinel 2. *ResearchGate* **2018**. [CrossRef]
32. Tona, C.; Bua, R. Open Source Data Hub System: Free and open framework to enable cooperation to disseminate Earth Observation data and geo-spatial information. *EGU Gen. Assem. Conf. Abstr.* **2018**, *20*, 13038.
33. Pipia, L.; Amin, E.; Belda, S.; Salinero-Delgado, M.; Verrelst, J. Green LAI Mapping and Cloud Gap-Filling Using Gaussian Process Regression in Google Earth Engine. *Remote. Sens.* **2021**, *13*, 403 [CrossRef]

34. Gorelick, N.; Hancher, M.; Dixon, M.; Ilyushchenko, S.; Thau, D.; Moore, R. Google Earth Engine: Planetary-scale geospatial analysis for everyone. *Remote Sens. Environ.* **2017**, *202*, 18–27. [CrossRef]
35. Kumar, L.; Mutanga, O. Google Earth Engine Applications Since Inception: Usage, Trends, and Potential. *Remote Sens.* **2018**, *10*, 1509. [CrossRef]
36. Rasmussen, C.E.; Williams, C.K.I. *Gaussian Processes for Machine Learning*; The MIT Press: New York, NY, USA, 2006.
37. Belda, S.; Pipia, L.; Morcillo-Pallarés, P.; Verrelst, J. Optimizing Gaussian Process Regression for Image Time Series Gap-Filling and Crop Monitoring. *Agronomy* **2020**, *10*, 618. [CrossRef]
38. Bonilla, E.V.; Chai, K.; Williams, C. Multi-Task Gaussian Process Prediction. *Adv. Neural Inf. Process. Syst.* **2007**, *20*. Available online: https://proceedings.neurips.cc/paper/2007/hash/66368270ffd51418ec58bd793f2d9b1b-Abstract.html (accessed on 21 February 2023).
39. Álvarez, M.A.; Rosasco, L.; Lawrence, N.D. Kernels for Vector-Valued Functions: A Review. *MAL* **2012**, *4*, 195–266. [CrossRef]
40. Goovaerts, P. *Geostatistics for Natural Resources Evaluation*; Oxford University Press: Oxford, UK, 1997.
41. Lin, Q.; Hu, J.; Zhou, Q.; Cheng, Y.; Hu, Z.; Couckuyt, I.; Dhaene, T. Multi-output Gaussian process prediction for computationally expensive problems with multiple levels of fidelity. *Knowl.-Based Syst.* **2021**, *227*, 107151. . [CrossRef]
42. Alvarez, M.A.; Ward, W.; Guarnizo, C. Non-linear process convolutions for multi-output Gaussian processes. In the 22nd International Conference on Artificial Intelligence and Statistics, Naha, Okinawa, Japan, 16–18 April 2019; pp. 1969–1977. Available online: https://proceedings.mlr.press/v89/alvarez19a.html (accessed on 21 February 2023).
43. de Wolff, T.; Cuevas, A.; Tobar, F. MOGPTK: The Multi-Output Gaussian Process Toolkit. *Neurocomputing* **2020**, *424*, 49–53. [CrossRef]
44. Kim, Y.; Jackson, T.; Bindlish, R.; Lee, H.; Hong, S. Radar Vegetation Index for Estimating the Vegetation Water Content of Rice and Soybean. *IEEE Geosci. Remote Sens. Lett.* **2012**, *9*, 564–568.
45. Rasmussen, C.E. Gaussian Processes in Machine Learning. In *Advanced Lectures on Machine Learning*; Springer: Berlin, Germany, 2004; pp. 63–71. [CrossRef]
46. Snee, R.D. Validation of Regression Models: Methods and Examples. *Technometrics* **1977**, *19*, 415–428. [CrossRef]
47. Love, B.C.; Jones, M. Bayesian Learning. In *Encyclopedia of the Sciences of Learning*; Springer: Boston, MA, USA; 2012; pp. 415–417. [CrossRef]
48. Wackernagel, H. *Multivariate Geostatistics: An Introduction with Applications*; Springer: Berlin, Germany, 2013.
49. Barry, R.P.; Hoef, J.M.V. Blackbox Kriging: Spatial Prediction without Specifying Variogram Models on JSTOR. *J. Agric. Biol. Environ. Stat.* **1996**, *1*, 297–322 [CrossRef]
50. Ver Hoef, J.M.; Barry, R.P. Constructing and fitting models for cokriging and multivariable spatial prediction. *J. Stat. Plan. Inference* **1998**, *69*, 275–294. [CrossRef]
51. Higdon, D. Space and Space-Time Modeling using Process Convolutions. In *Quantitative Methods for Current Environmental Issues*; Springer: London, UK, 2002; pp. 37–56. [CrossRef]
52. Casella, A.; Orden, L.; Pezzola, N.A.; Bellaccomo, C.; Winschel, C.I.; Caballero, G.R.; Delegido, J.; Gracia, L.M.N.; Verrelst, J. Analysis of Biophysical Variables in an Onion Crop (*Allium cepa* L.) with Nitrogen Fertilization by Sentinel-2 Observations. *Agronomy* **2022**, *12*, 1884. [CrossRef]
53. Caballero, G.R.; Platzeck, G.; Pezzola, A.; Casella, A.; Winschel, C.; Silva, S.S.; Ludueña, E.; Pasqualotto, N.; Delegido, J. Assessment of Multi-Date Sentinel-1 Polarizations and GLCM Texture Features Capacity for Onion and Sunflower Classification in an Irrigated Valley: An Object Level Approach. *Agronomy* **2020**, *10*, 845. [CrossRef]
54. Caballero, G.; Pezzola, A.; Winschel, C.; Casella, A.; Sanchez Angonova, P.; Rivera-Caicedo, J.P.; Berger, K.; Verrelst, J.; Delegido, J. Seasonal Mapping of Irrigated Winter Wheat Traits in Argentina with a Hybrid Retrieval Workflow Using Sentinel-2 Imagery. *Remote Sens.* **2022**, *14*, 4531. [CrossRef]
55. Berger, K.; Rivera Caicedo, J.P.; Martino, L.; Wocher, M.; Hank, T.; Verrelst, J. A Survey of Active Learning for Quantifying Vegetation Traits from Terrestrial Earth Observation Data. *Remote. Sens.* **2021**, *13*, 287 [CrossRef]
56. Settles, B. Active Learning Literature Survey. University of Wisconsin–Madison, Department of Computer Sciences. 2009. Available online: https://minds.wisconsin.edu/handle/1793/60660 (accessed on 21 February 2023).
57. Salinero-Delgado, M.; Estévez, J.; Pipia, L.; Belda, S.; Berger, K.; Paredes Gómez, V.; Verrelst, J. Monitoring Cropland Phenology on Google Earth Engine Using Gaussian Process Regression. *Remote Sens.* **2021**, *14*, 146 [CrossRef]
58. Reyes-Muñoz, P.; Pipia, L.; Salinero-Delgado, M.; Belda, S.; Berger, K.; Estévez, J.; Morata, M.; Rivera-Caicedo, J.P.; Verrelst, J. Quantifying Fundamental Vegetation Traits over Europe Using the Sentinel-3 OLCI Catalogue in Google Earth Engine. *Remote Sens.* **2022**, *14*, 1347. [CrossRef] [PubMed]
59. Verrelst, J.; Rivera-Caicedo, J.P.; Reyes-Muñoz, P.; Morata, M.; Amin, E.; Tagliabue, G.; Panigada, C.; Hank, T.; Berger, K. Mapping landscape canopy nitrogen content from space using PRISMA data. *ISPRS J. Photogramm. Remote. Sens.* **2021**, *178*, 382–395. [CrossRef]
60. Gutman, G.; Ignatov, A. The derivation of the green vegetation fraction from NOAA/AVHRR data for use in numerical weather prediction models. *Int. J. Remote Sens.* **1998**, *19*, 1533–1543. [CrossRef]
61. Gitelson, A.; Zur, Y.; Chivkunova, O.; Merzlyak, M. Assessing carotenoid content in plant leaves with reflectance spectroscopy. *Photochem. Photobiol.* **2002**, *75*, 272–281 [CrossRef]

62. Jia, K.; Liang, S.; Gu, X.; Baret, F.; Wei, X.; Wang, X.; Yao, Y.; Yang, L.; Li, Y. Fractional vegetation cover estimation algorithm for Chinese GF-1 wide field view data. *Remote Sens. Environ.* **2016**, *177*, 184–191. [CrossRef]
63. Song, W.; Mu, X.; Ruan, G.; Gao, Z.; Li, L.; Yan, G. Estimating fractional vegetation cover and the vegetation index of bare soil and highly dense vegetation with a physically based method. *Int. J. Appl. Earth Obs. Geoinf.* **2017**, *58*, 168–176. [CrossRef]
64. García-Haro, F.J.; Campos-Taberner, M.; Munoz-Mari, J.; Laparra, V.; Camacho, F.; Sanchez-Zapero, J.; Camps-Valls, G. Derivation of global vegetation biophysical parameters from EUMETSAT Polar System. *ISPRS J. Photogramm. Remote. Sens.* **2018**, *139*, 57–74 [CrossRef]
65. Lee, J.S.; Jurkevich, L.; Dewaele, P.; Wambacq, P.; Oosterlinck, A. Speckle filtering of synthetic aperture radar images: A review. *Remote. Sens. Rev.* **1994**, *8*, 313–340. [CrossRef]
66. Lee, J.S. Refined filtering of image noise using local statistics. *Comput. Graph. Image Process.* **1981**, *15*, 380–389. [CrossRef]
67. Pan, Z.; Hu, Y.; Cao, B. Construction of smooth daily remote sensing time series data: A higher spatiotemporal resolution perspective. *Open Geospat. Data Softw. Stand.* **2017**, *2*, 1–11. [CrossRef]
68. Savitzky, A.; Golay, M.J.E. Smoothing and Differentiation of Data by Simplified Least Squares Procedures. *Anal. Chem.* **1964**, *36*, 1627–1639. [CrossRef]
69. Neeff, T.; Dutra, L.V.; Dos Santos, J.R.; Freitas, C.C.; Araujo, L.S. Power spectrum analysis of SAR data for spatial forest characterization in Amazonia. *Int. J. Remote Sens.* **2005**, *26*, 2851–2864. [CrossRef]
70. Parra, G.; Tobar, F. Spectral Mixture Kernels for Multi-Output Gaussian Processes. *Adv. Neural Inf. Process. Syst.* **2017**, *30*. [CrossRef]
71. Ulrich, K.R.; Carlson, D.E.; Dzirasa, K.; Carin, L. GP Kernels for Cross-Spectrum Analysis. *Adv. Neural Inf. Process. Syst.* **2015**, *28*. Available online: https://proceedings.neurips.cc/paper/2015/hash/285ab9448d2751ee57ece7f762c39095-Abstract.html (accessed on 21 February 2023).
72. Alvarez, M.; Lawrence, N. Sparse Convolved Gaussian Processes for Multi-output Regression. *Adv. Neural Inf. Process. Syst.* **2008**, *21*. Available online: https://proceedings.neurips.cc/paper/2008/hash/149e9677a5989fd342ae44213df68868-Abstract.html (accessed on 21 February 2023).
73. van der Wilk, M.; Rasmussen, C.E.; Hensman, J. Convolutional Gaussian Processes. 2017. Available online: https://doi.org/10.48550/ARXIV.1709.01894 (accessed on 21 February 2023). [CrossRef]
74. Kingma, D.P.; Ba, J. Adam: A Method for Stochastic Optimization. *arXiv* **2014**. [CrossRef]
75. Tobar, F. Bayesian Nonparametric Spectral Estimation. *Adv. Neural Inf. Process. Syst.* **2018**, *31*. Available online: https://proceedings.neurips.cc/paper/2018/hash/abd1c782880cc59759f4112fda0b8f98-Abstract.html (accessed on 21 February 2023).
76. Verrelst, J.; Rivera, J.; Moreno, J.; Camps-Valls, G. Gaussian processes uncertainty estimates in experimental Sentinel-2 LAI and leaf chlorophyll content retrieval. *ISPRS J. Photogramm. Remote Sens.* **2013**, *86*, 157–167 [CrossRef]
77. Paek, S.W.; Balasubramanian, S.; Kim, S.; de Weck, O. Small-Satellite Synthetic Aperture Radar for Continuous Global Biospheric Monitoring: A Review. *Remote Sens.* **2020**, *12*, 2546. [CrossRef]
78. Titsias, M.K. *Variational Model Selection for Sparse Gaussian Process Regression*; University of Manchester: Manchester, UK, 2008.
79. Kiefer, J.; Wolfowitz, J. Stochastic Estimation of the Maximum of a Regression Function. *Ann. Math. Stat.* **1952**, *23*, 462–466. [CrossRef]

Fuentes de Financiación

El desarrollo de esta tesis doctoral ha sido posible gracias a la financiación económica recibida por parte de:

- La beca doctoral de Fundación Carolina (C.2021) para profesores de universidades de América Latina asociadas a la red Carolina , financiada por la Fundación Carolina de España.
- El proyecto SENTIFLEX financiado por el European Research Council (ERC) (ERC-2017-STG, grant agreement 755617–Katja Berger) y el contrato Ramón y Cajal (Ministerio de Ciencia, Innovación y Universidades del gobierno de España) de Jochem Verrelst.

Otros proyectos y contratos que han financiado actividades de divulgación científica realizadas en el marco del desarrollo de esta tesis doctoral:

- El Contrato Framework Partnership Agreement on Copernicus User Uptake. Courses, workshops and seminars in Europe and Latin America (FPA 275G/GRO/COPE/17/10042) financiado por la Comisión Europea.
- El proyecto RESSBIO (REmote Sensing Spectroscopy for wetlands BIOdiversity - PROMETEO–CIPROM/2021/049) financiado por la Conselleria de Innovación, Universidades, Ciencia y Sociedad Digital de la Generalitat Valenciana.

Los recursos naturales deben ser gestionados de forma sostenible para promover el desarrollo económico y minimizar el impacto ambiental. No existe un planeta B. ¿Qué estamos esperando?

VNIVERSITAT DE VALÈNCIA